Title of Thesis: Gas Kinematics of Galaxies in the Epoch of Reionization

Name: Siân Grace Phillips

A thesis submitted in partial fulfilment of the requirements of Liverpool John Moores University for the degree of Doctor of Philosophy

Month and Year of Submission for Examination: January 2026

Gas Kinematics of Galaxies in the Epoch of Reionization

Siân Grace Phillips

A thesis submitted to Liverpool John Moores University for the award of Doctor of Philosophy within the Astrophysics Research Institute

Supervised by

Dr Renske Smit

2025

Declaration

The work presented in this thesis was carried out at the Astrophysics Research Institute, Liverpool John Moores University. Unless otherwise stated, it is the original work of the author, and all published works referred to during the course of the research have been cited appropriately.

While registered as a candidate for the degree of Doctor of Philosophy, for which submission is now made, the author has not been registered as a candidate for any other award. This thesis has not been submitted in whole, or in part, for any other degree.

Siân Grace Phillips
Astrophysics Research Institute
Liverpool John Moores University
IC2, Liverpool Science Park
146 Brownlow Hill
Liverpool
L3 5RF
UK

Relevant Publications by the Author

Chapter Two is based on *Lessons Learned from Studying Hα Galaxy Kinematics with Mock JWST/NIRSpec IFU Observations at $z > 6$* by Siân Phillips (lead author), Francesca Rizzo, Mahsa Kohandel, Renske Smit and Andrea Pallottini (co-authors), accepted for publication in Monthly Notices of the Royal Astronomical Society.

Chapter Three is based on the forthcoming publication *REBELS-HR: Survey overview and multi-tracer morphologies* by Siân Phillips, Renske Smit and the REBELS collaboration.

Chapter Four is based on the forthcoming publication *REBELS-HR: Cold gas kinematics* by Siân Phillips, Renske Smit and the REBELS collaboration.

I was furthermore co-author on a number of relevant publications during the course of my PhD:

- Fisher, R., Bowler, R., Stefanon, M., Rowland, L., Algera, H., Aravena, M., Bouwens, R., Dayal, P., Ferrara, A., Inami, H., Ormerod, K., Pallottini, A., **Phillips, S.,** Smit, R., Sommovigo, L., *REBELS-IFU: Dust attenuation curves of 12 massive galaxies at $z \approx 7$*, 2025, MNRAS, 539, 109

- Algera, H., Rowland, L., Stefanon, M., Palla, M., Sommovigo, L., Inami, H., Bouwens, R., Aravena, M., Bowler, R., Dayal, P., De Looze, I., Ferrara, A., Fisher, R., Graziani, L., Heintz, K., Hodge, J., van Leeuwen, I., Pallottini, A., **Phillips, S.,** Schouws, S., Smit, R., van der Werf, P., *REBELS-IFU: Dust*

Build-up in Massive Galaxies at Redshift 7, 2025, arXiv:2501.10508, submitted to MNRAS.

- Rowland, L., Hodge, J., Bouwens, R., Mancera Piña, P., Hygate, A., Algera, H., Aravena, M., Bowler, R., da Cunha, E., Dayal, P., Ferrara, A., Herard-Demanche, T., Inami, H., van Leeuwen, I., de Looze, I., Oesch, P., Pallottini, A., **Phillips, S.,** Rybak, M., Schouws, S., Smit, R., Sommovigo, L., Stefanon, M., van der Werf, P., *REBELS-25: discovery of a dynamically cold disc galaxy at* $z = 7.31$, 2024, MNRAS, 535, 2068

- Molyneux, S., Smit, R., Schaerer, D., Bouwens, R., Bradley, L., Hodge, J., Longmore, S., Schouws, S., van der Werf, P., Zitrin, A., **Phillips. S.,** *Spectroscopic confirmation of a gravitationally lensed Lyman-break galaxy at* $z_{[CII]} = 6.827$ *using NOEMA*, 2022, MNRAS, 512, 535

In addition to:

- Schiavon, R., **Phillips, S.**, Myers, N., Horta, D., Minniti, D., Allende Prieto, C., Anguiano, B., Beaton, R., Beers, T., Brownstein, J., Cohen, R., Fernández-Trincado, J., Frinchaboy, P., Jönsson, H., Kisku, S., Lane, R., Majewski, S., Mason, A., Mészáros, S., Stringfellow, G. , *The APOGEE value-added catalogue of Galactic globular cluster stars*, 2024, MNRAS, 528, 1393

- **Phillips. S.,** Schiavon, R., Mackereth, J., Allende Prieto, C., Anguiano, B., Beaton, R., Cohen, R., García-Hernández, D., Geisler D., Horta, D., Jönsson, H., Kisku, S., Lane, R., Majewski, S., Mason, A., Minniti, D., Schultheis, M., Taylor, D. *APOGEE detection of N-rich stars in the tidal tails of Palomar 5*, 2022, MNRAS, 510, 3727

- Taylor, D., Mason, A., Schiavon, R., Horta, D., Nataf, D., Geisler D., Kisku, S., **Phillips, S.,** Cohen, R., Fernández-Trincado, J., Beers, T., Bizyaev, D., García-Hernández, D., Lane, R., Longa-Peña, P., Minniti, D., Muñoz, C., Pan, K., Villanova, S., *Is Terzan 5 the remnant of a building block of the Galactic bulge? Evidence from APOGEE*, 2022, MNRAS, 513, 3429

Dedication

For Mum, Grandad and Lucien
and in memory of Dad and Granny
with love and thanks

Acknowledgments

Firstly, to Renske Smit: it was my dream to work with you from as soon as I saw your presentation at EAS 2018, and I feel lucky that this dream came true having you as my mentor for this thesis. Your work on high redshift galaxies inspired me academically from the beginning, and your kindness, intelligence, and patience have taught me so much in these last few years. Thank you for everything.

Many thanks to Francesca Rizzo and Mahsa Kohandel for supervising the project that became Chapter 2. I will always remember my research visit with you both at the Cosmic Dawn Centre, and I really appreciate everything I have learned from our project, not only in terms of science but also communication and collaboration; it has made me a better researcher.

Thank you to the entire REBELS collaboration for inspiration, encouragement and many useful discussions, especially Mauro Stefanon, Katherine Ormerod, Lucy Astles, Lucie Rowland, Rebecca Fisher, Rebecca Bowler, Hiddo Algera and Rychard Bouwens. Thanks to all of the brilliant researchers I have had the privilege of learning from and alongside over the course of my PhD, including George Bendo and Andrea Pallottini.

Thank you to Mum and Dad, who as my teachers fostered my enthusiasm for learning, and as my parents gave me a life full of love and encouragement, and walks on the beach. Thank you to Grandad and Gran, for all the fun in my childhood and support in my adulthood, and for having me to stay with you during my degree. Thank you to Lucien for brightening my life over the past five years and for looking after me during difficult times. I love you all.

Thank you to all of my family and friends for everything. Thanks to my physics girls (and chemistry girl) Maha, Lauren, Serena, Ellie, Gabi, Tash, Trish and Harriet for helping me to survive physics undergrad. Thank you to my friends from home, Laura, Lewis, Huw, Libby, and Holly, for all the memories. Thank you to my brilliant friends at the ARI and in GoodGym for making me feel so at home in Liverpool.

‘There was a star danced, and under that was I born.’

Beatrice, Much Ado About Nothing, William Shakespeare

-for Mum

Abstract

The earliest galaxies formed during the first billion years after the Big Bang, producing the energetic photons required to initiate the Epoch of Reionization. Resolved observations of these sources enable us to build a picture of the evolutionary path from primordial density fluctuations to the development of galaxies such as our own. Kinematic analysis is a key probe into the mass budget of galaxies, the interstellar medium (ISM) properties affecting star formation, and the physical processes ongoing within galaxies including accretion, minor and major mergers, turbulence and feedback driven by stars or active galactic nuclei (AGN).

With the extraordinary synergistic capabilities of the Atacama Large (sub)Millimetre Array (ALMA) and the James Webb Space Telescope (JWST), we are in an unprecedented era of discovery in detecting primeval galaxies across a wide range of wavelengths and emission line tracers of the multiphase ISM. However, numerical simulations show that warm ionized gas and cold gas trace different regions of galaxies and yield different measurements of internal properties, leading to the question of how can we compare information obtained from varied tracers? Furthermore, how confident can we be in physically interpreting high-redshift observations that often suffer from the complications of poor angular and spectral resolution?

In this thesis, we address these challenges through kinematic analysis of realistic NIRSpec IFU mock observations derived from galaxies in the SERRA suite of cosmological zoom-in simulations. With these synthetic data we determine the robustness of dynamical information recovered from typical IFU observations, and test widely-used criteria for identifying disks and gaseous outflows at high redshift. We carry the lessons learned from this study into the second part of the thesis, where we present the first sample of galaxies from the Epoch of Reionization to have constraints on the cool gas kinematics and distribution and morphology of the dust-obscured star

formation, alongside NIRCam and NIRSpec IFU PRISM observations. We examine the morphology of the stars, gas and dust, and perform kinematic fitting to reveal an intriguing diversity of dynamical classifications, including rotation-dominated and dispersion-dominated galaxies, turbulent disks, and galaxies with signatures of merging activity and outflowing gas streams.

Contents

List of Figures

List of Tables

Chapter 1

Introduction

1.1 Cosmological Context

Our current standard cosmological paradigm is the Λ Cold Dark Matter model (ΛCDM: Peebles, 1984; Peebles and Ratra, 2003), of which the two main constituents are cold dark matter (CDM: 'cold' here referring to particles moving at non-relativistic speeds), and dark energy, represented by the cosmological constant Λ (Carroll, 2001). Dark matter and dark energy respectively comprise approximately 26% and 69% of the observed gravity in the Universe, compared to 5% accounted for by baryonic matter (Planck Collaboration et al., 2016). There is abundant evidence for the existence of dark matter, including the phenomenon of flat galaxy rotation curves (e.g. Rubin and Ford, 1970; Rubin et al., 1978; Rubin et al., 1980), whereby the velocities of bodies in orbit around the centres of galaxies remain constant out to very large radii, rather than decreasing with $v(R) \propto R^{-0.5}$ as would be expected from the equation:

$$v(R) = \sqrt{\frac{GM(R)}{R}} \tag{1.1}$$

leading to the conclusion that galaxies contain significantly more mass than is accounted for by the baryonic component. The gravitational effect of dark matter on visible matter is directly observable through gravitational lensing, an effect predicted in Einstein (1916), which causes photons to be deflected as they pass through spacetime that has been warped by the gravitational field of a nearby massive object (see e.g. the reviews Massey et al., 2010; Saha et al., 2024, and references therein). Observational evidence for dark energy comes from the study of distant supernovae;

these events are used as standard candles, so the discovery of distant supernovae with lower luminosities than would be expected was the first indication that the expansion of the Universe is accelerating, interpreted as the cosmological constant (Riess et al., 1998; Perlmutter et al., 1999).

The ΛCDM model assumes that gravity at cosmological scales is described by General Relativity (Einstein, 1915; Einstein, 1917), and is underpinned by the Cosmological Principle, which in simple terms states that the energy distribution of the Universe is statistically homogenous and isotropic at sufficiently large scales (Milne, 1933; Hawking and Ellis, 1973; Ellis and Harrison, 1974), where 'sufficiently large' refers to $\gtrsim$ 100Mpc. The Einstein (1915) field equation describing the spacetime geometry of a certain distribution of energy is given by:

$$\mathcal{G}_{\mu\nu} = \frac{8\pi G}{c^4}\mathcal{T}_{\mu\nu} \tag{1.2}$$

where $\mathcal{T}_{\mu\nu}$ is the tensor evaluating the effect of an energy distrubution on the curvature of spacetime, as described by Einstein's tensor:

$$\mathcal{G}_{\mu\nu} = R_{\mu\nu} - \frac{1}{2}g_{\mu\nu}R \tag{1.3}$$

where $R_{\mu\nu}$ is the Ricci tensor and R the scalar. The Friedmann Lemaître Robertson Walker (FLRW) metric:

$$d\tau^2 = g_{\mu\nu}dx^\mu dx^\nu = dt^2 - a^2(t)\Big\{\frac{dr^2}{1-kr^2} + r^2(d\theta^2 + sin^2\theta d\phi^2)\Big\} \tag{1.4}$$

governs the average evolution of the Universe's large-scale structure, being an exact solution of the Einstein field equations obtained assuming the Cosmological Principle. The Cosmological Principle is strongly supported by the highly isotropic nature of the cosmic microwave background (CMB: Penzias and Wilson, 1965; Dicke et al., 1965), relic radiation created by the process of protons and electrons recombining ('recombination') at $z \sim 1100$, when the Universe had cooled sufficiently following the Big Bang (Jones and Wyse, 1985). The observation of the CMB by the Planck satellite (Fig. 1.1) provides a stringent test of ΛCDM, measuring five of its six parameters to better than 1% precision. Assuming that the radiation is comprised of photons with a blackbody temperature of 2.7260 K (Fixsen, 2009), and neutrinos of very small mass, permits a comparison between the power spectrum (that is, the Fourier transformation of the matter correlation function) as measured by Planck

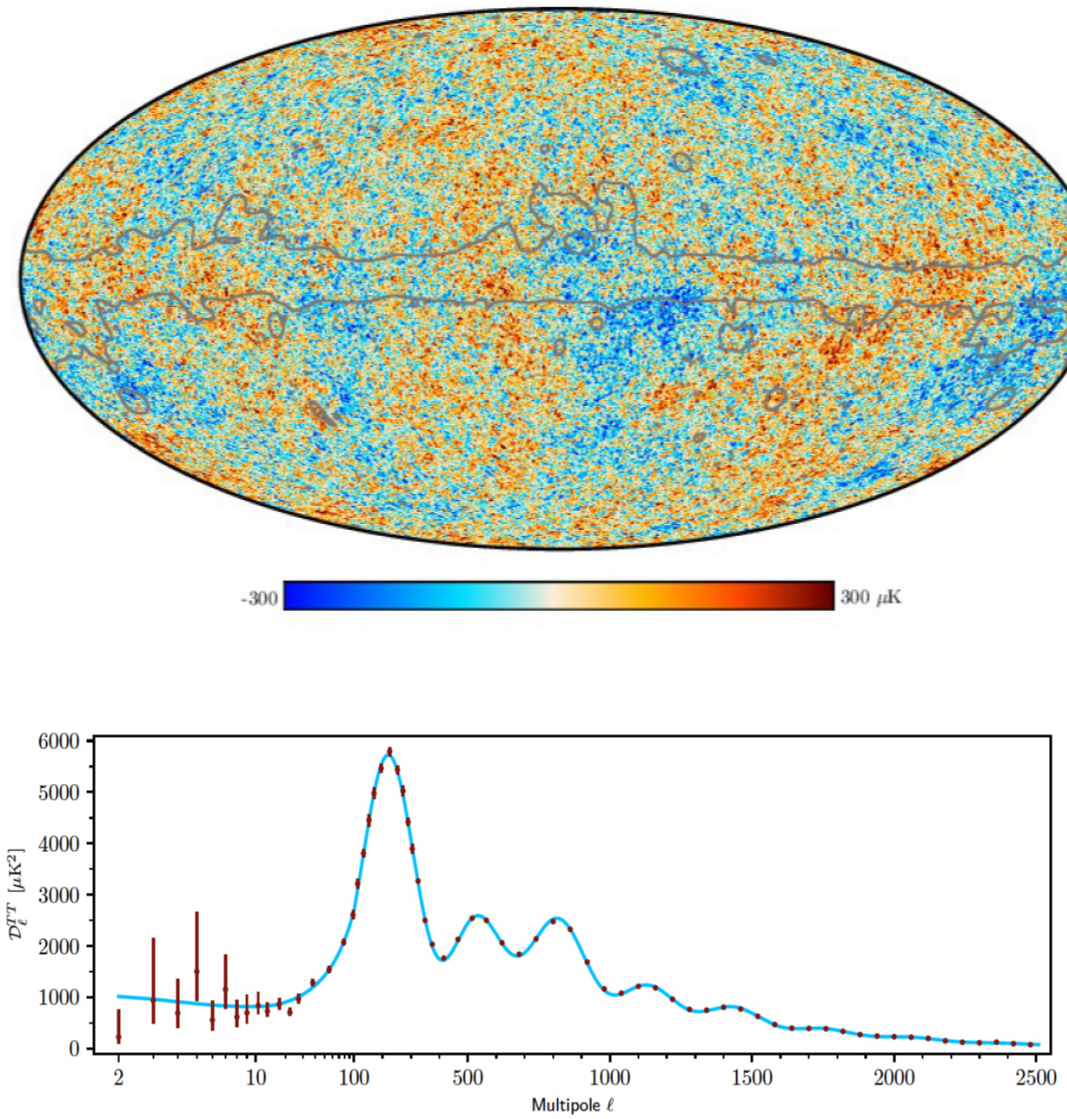

Figure 1.1: (*top panel*) Planck satellite skymap of the Cosmic Microwave Background radiation temperature distribution, with a grey line delineating the mask applied around the Galactic plane. (*bottom panel*) Foreground subtracted and frequency averaged angular power spectrum for temperature, plotted alongside the model prediction in blue. Figure credit: Planck Collaboration et al. (2020a)

with that predicted by ΛCDM, and the two agree exquisitely (See Fig. 1.1: Planck Collaboration et al. (2020a)).

However, despite this success, challenges to the model persist. The Hubble tension is the $> 5\sigma$ discrepancy between measurements of the Hubble constant (H_0) from Planck (Planck Collaboration et al., 2020b) and from a survey of Cepheid variables and Type Ia Supernovae by the SH0ES collaboration (Riess et al., 2022). The S_8 tension refers to the disagreement between the Planck best fit measurement of the parameter combination $S_8 = \sigma_8(\Omega_m/0.3)^{1/2}$ and the measurements from surveys of weak galaxy lensing (Efstathiou, 2025). These tensions could indicate the existence of new physics.

Recently, and primarily due to the James Webb Space Telescope[1] (JWST), an abundance of galaxies has been spectroscopically confirmed at $z > 11$ (e.g. Arrabal Haro et al., 2023; Castellano et al., 2024; Harikane et al., 2024; Zavala et al., 2024), which has been considered to be in tension with the ΛCDM model of hierarchical galaxy formation in which galaxies form from dark matter halos, which themselves evolve according to the initial power spectrum of density perturbations (Frenk et al., 1985). For instance, Boylan-Kolchin (2023) calculate that the star formation efficiency of baryons in halos would have to be close to unity in order to reproduce the stellar mass function determined by Labbé et al. (2023), in comparison to a star formation efficiency of $\sim 5 - 10\%$ in the Milky Way (Eke et al., 2005). However, by extending a model first presented in Cowley et al. (2017) to take into account the growth timescales of dust grains, Lu et al. (2025) argue that ΛCDM naturally predicts the observed population of very high redshift galaxies.

1.1.1 The Big Bang and Cosmological Inflation

The history of the cosmos begins with the Big Bang: see Fig. 1.2 for a schematic overview of the evolution of the Universe. The model of inflationary cosmology

[1]While I will refer to the telescope by its full name in this thesis, I would like to clarify my belief that its name is inappropriate considering that during his tenure as lead administrator at NASA, the namesake of the telescope presided over the implementation of federal policies expelling LGBTQ+ individuals from the workforce (Johnson, 2009).

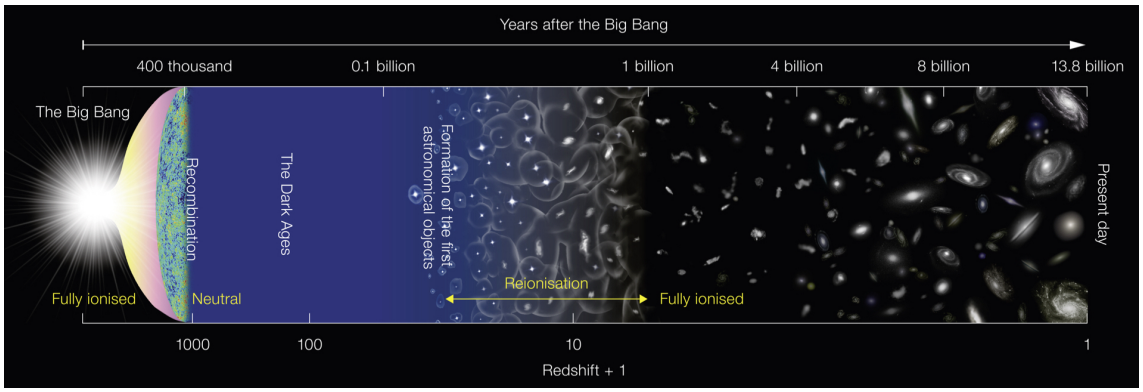

Figure 1.2: Schematic representation of the cosmic from the Big Bang to the present day, delineating notable cosmic epochs. Figure credit: NAOJ.

(Starobinsky, 1980; Guth, 1981) is an auxiliary theory to the Big Bang, and resolves certain problems associated with it; namely, the Horizon Problem and the Flatness Problem. The Horizon Problem (Misner, 1968) concerns the observational horizon, defined as the distance beyond which information cannot reach an observer on Earth. The horizon expands at the speed of light c, in direct proportion to time t. This evolution is more rapid than the expansion of the Universe's scale factor, which increases proportional to $t^{\frac{1}{2}}$ when the Universe is radiation dominated, and proportional to $t^{\frac{2}{3}}$ when the Universe is matter dominated. Thus, looking back in time, the observational horizon shrinks faster than the cosmic scale factor. It appears that the established laws of physics are valid for the entire Universe within our horizon, and as discussed in Sec. 1.1 the cosmic microwave background appears isotropic. Without inflation, this would not be expected, as regions on the sky separated by $> 1^\circ$ /200kpc / 200Mpc (comoving coordinates), would not have been in causal contact prior to decoupling, after which there is no interaction between matter and radiation.

The Flatness Problem (Hawking and Israel, 2010) refers to the observational result that the mean cosmic density is almost the critical density. Combining the matter-dominated Friedmann equation with the modern-day Friedmann equation gives:

$$R^2 = \frac{8\pi G\rho_0 R_0^3}{3R} - R_0^2 H_0^2[\Omega_0 - 1] \tag{1.5}$$

which, using

$$\Omega = \frac{8\pi G\rho}{2H^2} \text{ and } \rho = \rho_0(1+z)^3 \tag{1.6}$$

leads to the result

$$\Omega(z) = \frac{\Omega_0(1+z)}{(1+z\Omega_0)} \tag{1.7}$$

It then follows that at high redshifts, Ω is almost exactly 1. In the era of nucleosynthesis, at a redshift of $z = 10^8$, Ω equals unity within 10^{-12}, which implies an extremely flat Universe; such a result cannot be a coincidence.

Inflation proposes that immediately after the Big Bang, the density of all cosmic matter would have been so great that all matter would have been in causal contact and thermal equilibrium, subject to the same laws of physics. At 10^{-36}s following the Big Bang, then, the Universe experienced a very brief metric expansion at a speed far greater than c, such that cosmic expansion exceeded the expansion of the horizon. This resolves the Horizon Problem, and the solution of the Flatness Problem falls out naturally, as if at the instant of the Big Bang, the value of Ω was anything other than unity, inflation would have blown up the the size of the Universe to the extent that any curvature existing prior to inflation would no longer be observable.

1.1.1.1 The Cosmic Dark Ages

Cosmic inflation cooled the matter in the Universe until the point where it was cool enough for the combination of electrons and protons into hydrogen and helium atoms to become energetically favourable, in what is known as the Recombination Epoch. This phase transition caused the Universe to enter a period known as the Cosmic Dark Ages, in which there were no significant radiation sources, and the majority of cosmic hydrogen was neutral (Dayal and Ferrara, 2018). During this period, inhomogeneities in the dark matter density field grew gravitationally to form baryon-accreting non-linear structures, which acted as potential wells. Within these potential wells, accreted gas could cool, fragment, and condense to form stars and then galaxies, creating radiation sources.

1.2 The Reionization of the Universe

The formation of these sources of luminosity brought an end to the Cosmic Dark Ages and ushered in the Epoch of Reionization (EoR). During this period, ther-

monuclear reactions within the first stars generated ultraviolet radiation. Lyman continuum (LyC) photons with energy greater than the ionization energy of hydrogen, 13.6 eV, were able to begin the process of ionizing the neutral cosmic hydrogen. The EoR began at a redshift of $z \sim 30$ and was complete by $z \sim 6$, with the end point of reionization being well constrained by observations of quasars. The observed spectra of quasars from $z > 6$ display a trough, as predicted by Gunn and Peterson (1965), corresponding to neutral hydrogen in the intergalactic medium (IGM) absorbing quasar continuum emission. This feature is not seen in the spectra of quasars at $z \lesssim 6$, which suggests that by this time the hydrogen in the Universe had been fully ionized (e.g. Becker et al., 2001).

1.2.1 Understanding the Reionizing Contribution of Galaxies

There is ongoing debate around the main sources of the energetic photons that reionized the Universe. In the low-redshift Universe, active galactic nuclei (AGN) emit strongly at LyC frequencies, but they are not expected to contribute significantly to reionization as their population decreases rapidly as a function of redshift (Qin et al., 2017; Kulkarni et al., 2019; Faisst et al., 2022; Dayal et al., 2024). Star-forming galaxies are therefore considered the most likely candidates to have injected large amounts of highly energetic photons into the IGM during the EoR (e.g. Bouwens et al., 2015). However, uncertainty remains over which types of galaxies had the greatest impact, and how the efficiency of ionizing photon emission is affected by the diversity of physical properties among galaxies, included but not limited to the stellar mass, the dark matter halo mass, the star formation rate (SFR), the dust content, and the burstiness of the star formation history (SFH).

To quantify the ionizing photon contribution from galaxies, we must measure the following properties: (1) the number of galaxies producing LyC photons, (2) ξ_{ion}, the ionizing photon production efficiency, or the number of LyC photons produced per unit UV luminosity, and (3) f_{esc}, the fraction of ionizing photons created within a galaxy that are able to escape into the IGM (Gnedin and Madau, 2022).

Reionization is thought to have been brought about by the large population of faint galaxies, rather than having been driven by a small number of UV-bright galaxies,

or a small subset of bright Lyα emitters with high ξ_{ion} and f_{esc} (e.g. Lewis et al., 2022; Rosdahl et al., 2022). To confirm this model, it is necessary to well understand ξ_{ion} and f_{esc} across different galaxy populations; however, both parameters are highly uncertain. Escape fractions are challenging to determine as the IGM becomes opaque to ionizing photons after $z \sim 4$ (Madau, 1995; Inoue et al., 2014), so the LyC flux cannot be directly measured in the EoR. Studies of f_{esc} in the local Universe (e.g. Choi et al., 2020; Meštrić et al., 2021; Naidu et al., 2022) have found galactic features that correlate strongly with escape fraction, such that f_{esc} values can be inferred at high redshifts through measuring these secondary properties. Among these is the UV slope β_{UV}, as it has been found that bluer galaxies have higher escape fractions (Chisholm et al., 2022; Saldana-Lopez et al., 2023). The ionizing efficiency of a galaxy is a function of the shape of its ionizing spectrum, which is determined by the initial mass function (IMF), stellar metallicity, and binary star fraction. Analytic models generally assume $\log(\xi_{ion}/\text{Hz erg}^{-1})$ in the range 25.2-25.3 (Shivaei et al., 2018), which is consistent with ξ_{ion} values inferred from the UV spectral slope; however, variations in assumptions made about the aforementioned stellar population parameters can cause recovered ξ_{ion} values to vary by $2-3\times$ (Eldridge et al., 2017; Stanway and Eldridge, 2018). Some studies with JWST have found higher ionizing efficiencies of $\log(\xi_{ion}) \approx 25.5-26.0$ (e.g. Curtis-Lake et al., 2023; Atek et al., 2024). These results, together with local constraints on f_{esc}, and the large population of star-forming galaxies revealed with JWST at $z > 9$, lead Muñoz et al. (2024) to posit that there is a photon budget crisis, with too many ionizing photons being produced and reionization being ended too early. This crisis is not reproduced by other works, such as Simmonds et al. (2024) and Begley et al. (2024), who find no evidence for over- (or under-) production of ionizing radiation relative to what would be required to reproduce the observed timeline of reionization. Kreilgaard et al. (2024) investigate the population distribution of f_{esc} by applying hierarchical Bayesian inference to the ratio of LyC to non-ionizing UV flux for a sample of galaxies at $z \sim 3.5$, and find that the best-fitting distribution is exponential. As models generally assume a constant f_{esc}, an exponential distribution could alleviate such a 'budget crisis' as it suggests that at any time, only a small fraction of sources may be producing ionizing radiation.

1.2.1.1 Reionizing Bubbles

In simulations, reionization originates around overdensities (e.g. Trac and Cen, 2007; Hutter et al., 2021), a scenario which is supported by observational results (e.g. Castellano et al., 2016; Endsley and Stark, 2022). Therefore, ionized bubbles form around LyC emitters, growing and merging until the last remaining regions of neutral hydrogen disappear. As the expected size distribution of ionized bubbles is determined by the clustering of the dominant source population (e.g. McQuinn et al., 2007; Hassan et al., 2018), the distribution of bubbles traces the reionization process itself. Hayes and Scarlata (2023) empirically demonstrate the growth of ionizing bubbles over time through studying a sample of 23 galaxies with JWST and finding that bubble size is smaller for galaxies at $z > 7.5$ compared to at lower redshift. A large-scale simulation study by Lu et al. (2024) suggests that high-redshift bubble observations must be interpreted through the framework of inhomogeneous reionization simulations, as they find that bubble size distribution around observable galaxies and overdensities differs significantly from that across the whole cosmic volume.

1.3 Galaxies from First Light to Present Day

In general terms, a galaxy may be defined as a dark matter halo containing a long-lived system of stars, dust, gas and black holes, with higher mass galaxies frequently containing a central supermassive black hole.

The gas reservoir from which the first stars formed would have been primordial, consisting only of hydrogen, helium, and trace amounts of lithium produced by Big Bang Nucleosynthesis (Alpher et al., 1948). These pristine stars are known as Population (Pop) III stars. The existence of Pop III stars has not yet been observationally confirmed, and it is challenging to do so, in part because direct collapse black holes or a second generation of enriched stars may have a spectral signature similar enough to that which would be expected for Pop III stars that these objects could be confused for each other (Nakajima and Maiolino, 2022). Pop II stars, those enriched by the metals produced in the first stars and ejected into the ISM by their deaths, are the oldest yet observed, and Pop I stars are those with solar metallicities.

It is not straightforward to define the observable properties of the first galaxies in such a way as to permit their positive identification. One could define that a galaxy must be pristine to be considered first-generation, with zero metallicity. However, this definition is insufficient, as most first galaxies may already be metal-enriched by the first supernovae and contain Pop II stars (Greif et al., 2010; Maio et al., 2011).

1.3.1 The Birth of Stars and Galaxies

Baryons falling into dark matter potential wells are shock-heated to the virial temperature of their host halo. This system is prevented from reaching equilibrium by dissipative cooling, which enables further collapse (Silk, 1977). The first galaxies would not have had access to the most efficient cooling mechanisms: line emission from collisionally-excited atoms and molecules, and continuum radiation, due to their extremely low metallicity content; metal-rich species offer more efficient cooling due to their greater number of electronic levels. Radiative cooling would therefore have been dominated by vibrational and rotational transitions of molecular hydrogen and, above $\gtrsim 10^4$K, Lyα emission, the $2p \rightarrow 1s$ transition of hydrogen (Dayal and Ferrara, 2018).

Once the baryonic gas has cooled sufficiently to form a centralised structure, clumps begin to form according to gravitational instabilities. The gas is in constant flux, with flows driven by gravity and radiation, and giant molecular clouds build up at the points where flows converge (Chevance et al., 2023). These clouds have a complex, filamentary internal structure and are highly turbulent. Their sizes are governed by the Jeans length, which sets the scale beyond which perturbations are unstable,

$$\lambda_J = \left(\frac{\pi c_s^2}{G\rho}\right)^{1/2} = c_s t_{ff} \tag{1.8}$$

where c_s is the speed of sound in the medium, ρ is the density, and t_{ff} is the local free fall time (e.g. Truelove et al., 1997). These GMCs can have masses in the range $10^4 - 10^6 M_\odot$, and local collapses occur in sufficiently massive clouds around overdensities where the energy densities from gravity exceed those from kinetic, magnetic and thermal effects, seeding star formation (McKee and Ostriker, 2007).

1.3.2 The Origin of the Elements

In astronomy, hydrogen and helium are considered 'primordial', and all heavier elements are considered 'metals' as they were not produced in the Big Bang (other than lithium, in trace amounts) and were created subsequently through stellar processing. See Fig. 1.3 for a schematic view of the production mechanisms of each element in the Solar neighbourhood. The metallicity, Z, is defined in terms of the ratio of the mass of metals to the total baryonic mass, which is dominated by hydrogen and helium:

$$Z = \frac{M_{metals}}{M_{baryons}}$$

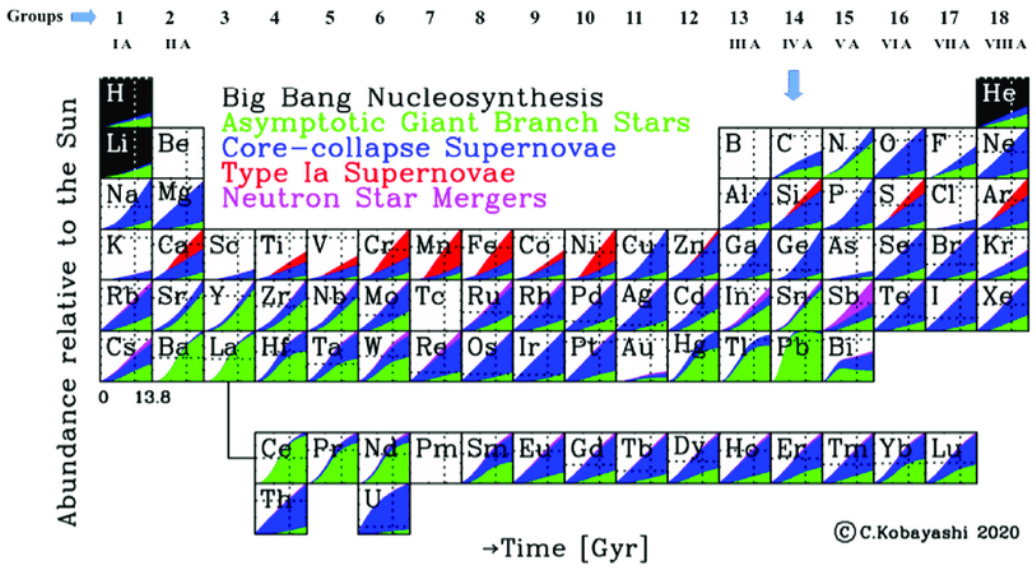

Figure 1.3: This representation of the Periodic Table is labeled with the origins of each element in the Solar neighbourhood. The square representing each element is a plot showing the relative contribution of various formation mechanisms to that element's abundance over time, which increases from left to right. The vertical lines are plotted at the formation time of the Sun and the horizontal lines represent Solar abundances. Figure Credit: Kobayashi et al. (2020).

1.3.2.1 Big Bang Nucleosynthesis

In the microseconds immediately following the Big Bang, the Universe consisted of a 'primordial soup' of fundamental particles including neutrinos, electrons and quarks, with a density so high that photons were trapped for 400,000 years until the Epoch of Recombination when free electrons and nuclei combined to form neutral atoms (Peebles, 1993).

During the ensuing expansion and cooling of the Universe, quarks became bound into neutrons and protons, which were initially held in equilibrium via interactions such as

$$p + e^- \longleftrightarrow n + \nu_e$$

until the temperature fell to $\sim 10^{10} - 10^9 K$, at which point the equilibrium shifted in favour of a higher proportion of protons, due to their lower mass. The ratio was controlled by:

$$n/p = e^{-(m_n - m_p)c^2/kT}$$

decreasing with temperature until 1s after the Big Bang (Johnson et al., 2020), at which point the Universe was cool and dilute enough to halt neutron/proton conversions and kickstart nuclear fusion which produced hydrogen, helium and trace amounts of lithium, until the Universe cooled too far to allow this to continue, minutes later. ^{4}He is very unlikely to be created by direct combination, as this would require a four-body interaction between two protons and two neutrons, so its formation pathway has an intermediate stage, the deuterium ^{2}H nucleus, which can produce stable helium nuclei through combining with ^{3}H or ^{3}He (Alpher et al., 1948). The deuterium bottleneck effect delayed the progress of nucleosynthesis, as the binding energy of deuterium is 2.23 MeV, corresponding to a temperature of $T = 2.6 \times 10^{10} K$; at the temperatures in the first seconds of cosmic time, the high number density of dissociating photons with energies exceeding 2.23 MeV destroyed deuterium instantaneously as it formed.

1.3.2.2 The Emergence of Metals

Metals are created through stellar nucleosynthesis and highly energetic stellar events, notably supernovae and neutron star mergers, as outlined in the following.

At the point where the entire luminosity radiated by a star is supplied by nuclear fusion, and gravitational contraction has ceased to contribute significantly to the energy output of the star, it begins its life on the main sequence (MS) as a Zero-Age Main Sequence (ZAMS) star (Mengel et al., 1979). During the main sequence phase, which lasts for the majority of the stellar lifetime, helium is created from the nuclear fusion of hydrogen via the proton-proton (pp) chain, which is the dominant mechanism in low-mass stars and can function in zero metallicity conditions:

$$4p \rightarrow {}^{4}\mathrm{He} + 2e^{-} + 2\nu_{e}$$

and the Carbon-Nitrogen-Oxygen (CNO) cycle which dominates higher mass stars, relying on existing metals to process hydrogen into helium (Adelberger et al., 2011). The luminosity of a MS star is proportional to temperature:

$$L_{pp} \propto T^{4}$$

$$L_{CNO} \propto T^{18}$$

and to mass:

$$L \propto M^{\alpha}$$

leading to the main-sequence lifetime relation

$$T_{MS} \propto M/L \propto M^{(1-\alpha)}$$

where $\alpha \sim 3.5$ (Salaris and Cassisi, 2005). Therefore, the main-sequence lifetime decreases significantly with increasing stellar mass.

As a star runs out of hydrogen to burn, it leaves the main sequence, and the next phase in its life depends on its mass. Low mass ($< 2M_{\odot}$) stars undergo electron degeneracy in the helium core, initiating the 'Helium Flash', a sudden release of nuclear energy (e.g. Schwarzschild and Härm, 1962; Mocák et al., 2010), from which the star transitions to the Asymptotic Giant Branch (AGB) phase. Intermediate mass stars ($2\mathrm{M}_{\odot} < \mathrm{M} < 8\mathrm{M}_{\odot}$) reach this stage without undergoing the Helium Flash, as the internal temperature is not high enough to ignite the carbon and oxygen that are the main components of their cores (e.g. Arcones and Thielemann, 2023).

AGB stars consist of thin shells of burning hydrogen and helium surrounding the electron-degenerate core, and are characterised by recurrent thermonuclear flashes

that instigate convective mixing, inducing nucleosynthesis (Herwig, 2005). AGB stars create approximately half of all light elements such as carbon, nitrogen and fluorine (Kobayashi et al., 2020). In high-mass stars ($> 8M_{\odot}$), the central temperature is high enough for carbon, neon, oxygen and silicon fusion. The energy from nuclear fusion balances the energy lost through radiation and neutrino emission, and therefore as each fuel is exhausted, the stellar core contracts, becoming hotter and denser, until finally a core of iron group elements is produced, and fusion ceases as the nuclear binding energy per nucleon is maximal for the iron group. The iron core begins freefall at $\sim 0.25c$ from the combined effects of electron capture and photodisintegration acting to remove energy it requires to maintain pressure (e.g. Woosley and Janka, 2005). This is halted by the repulsion of the strong nuclear force when the density is almost twice that of the atomic nucleus, launching a shock wave which ignites nuclear fusion in the outer shells in a core collapse supernova. These supernovae eject α elements into the ISM (Timmes et al., 1995; Kobayashi et al., 2006), while Type Ia supernovae, the explosions of white dwarf stars in binary systems, produce half of the iron-peak elements (e.g. Kobayashi and Nomoto, 2009). Heavier elements are produced in catastrophic events such as the merging of neutron stars. Approximately half of all elements heavier than iron are produced by the rapid neutron-capture process (r-process), which is the only source of elements beyond lead and bismuth, and is initiated by catastrophic events such as neutron star mergers (Thielemann et al., 2017).

1.4 Star Formation and the Initial Mass Function

As illustrated in the previous section, the mass of a star is the key parameter determining its properties and evolution. The distribution of the birth masses of stars is called the Initial Mass Function (IMF) and is a fundamental quality in understanding galaxy characteristics. As the IMF is not directly observable, it must be described through modelling assumptions, which introduces a significant uncertainty. The shape of the IMF, and whether it is bottom-heavy (dominated by lower-mass stars) or top-heavy (dominated by higher-mass stars), is dependent on factors including gas temperature and density, metallicity, stellar multiplicity and turbulence (e.g.

the review article Hennebelle and Grudić, 2024).

The IMF is generally parameterised as one of three models. The first of these is the Salpeter (1955) linear power law,

$$\frac{dN}{dM} \propto M^{-\alpha}$$

where $\alpha = 2.35$.

The Kroupa (2002) formalism models the IMF as a broken power law function, with $\alpha = 2.3$ at $0.5 - 150\mathrm{M}_\odot$, $\alpha = 1.3$ at $0.08 - 0.5\mathrm{M}_\odot$, and $\alpha = 0.3$ at $< 0.08\mathrm{M}_\odot$.

Chabrier (2003) model the IMF with a log-normal distribution below $1\mathrm{M}_\odot$, alongside a variation to account for stellar multiplicity.

These three models have been found to be similarly successful at describing observations, but as they were calibrated on stellar systems in the Local Group, there is considerable debate over how applicable these relations are further back in cosmic time. This is a particularly relevant question considering the extremely massive galaxies that have been observed at high redshift, as the IMF is central to calculating stellar mass from the light profile of a galaxy (the mass/light, M/L relation: e.g. Liang et al., 2025). Indeed, Woodrum et al. (2024) study the properties of a sample of 21 galaxies observed by NIRCam by fitting the spectral energy distribution using varying parameterisations of the IMF, and demonstrate that these are able to fit the SED equivalently well, while yielding stellar masses that are smaller by a factor of 3 than those obtained from the Chabrier (2003) model.

Hutter et al. (2025), using the ASTRAEUS simulations, test the effect of an evolving IMF, which becomes increasingly top-heavy with increasing gas density, and find that this boosts the population of UV-bright galaxies at $z > 10$ compared to the Salpeter (1955) IMF, and is able to reproduce the observed UV luminosity functions at $z = 5 - 15$. This is in agreement with the result obtained by Katz et al. (2022) from the SPHINX simulations, that a top-heavy IMF reproduces observed high $[\mathrm{OIII}]_{88}/[\mathrm{CII}]_{158}$ fractions in the Epoch of Reionization.

1.4.1 Star Formation across Cosmic Time

The star formation rate (SFR) of an individual galaxy quantifies the efficiency of that galaxy at forming stars, and is dependent on multiple factors, such as the

galaxy's cold gas reservoir and internal properties. The cosmic star formation rate density (SFRD) measures global star formation across the Universe. Star formation rates are measured in numerous ways, notably through integrated galactic light in the UV and FIR regions, and nebular recombination lines.

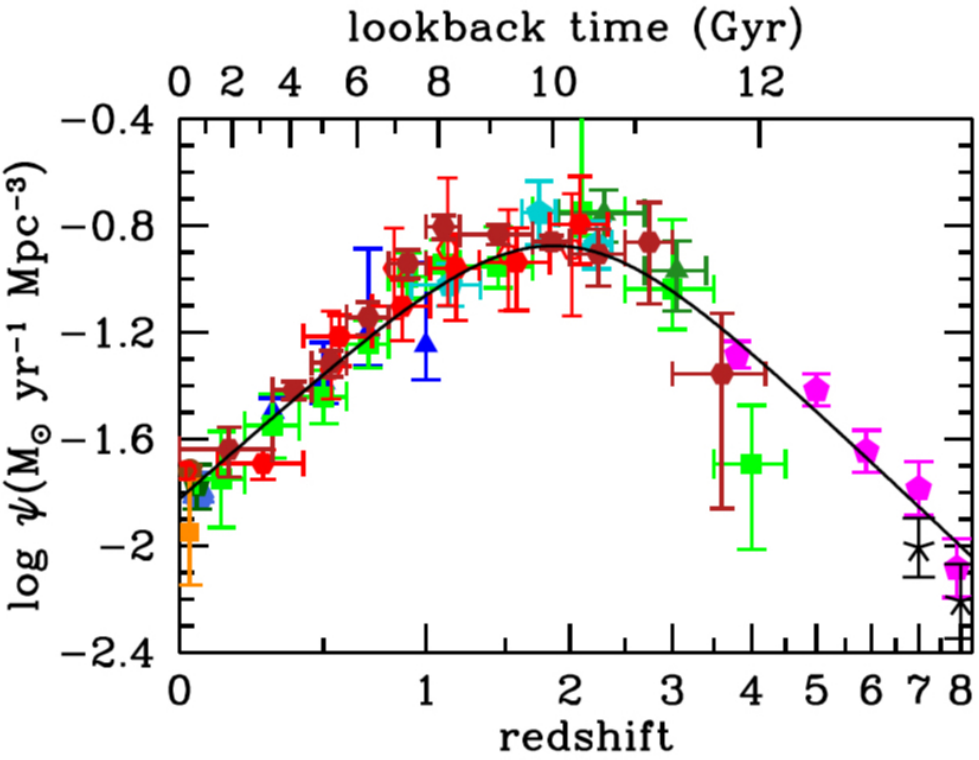

Figure 1.4: The evolution of star formation with redshift as measured by rest-frame far ultraviolet (blue, teal, green, lime and magenta points) and infrared (orange, scarlet and crimson points) observations. Figure Credit: Madau and Dickinson (2014).

In the UV regime ($\sim 1250 - 2500$Å) young stars dominate the integrated spectrum, and luminosity can be converted to SFR assuming some IMF. With a Salpeter IMF function (Salpeter, 1955), the composite spectrum is approximately flat at UV wavelengths, and therefore SFR scales linearly with UV luminosity (Kennicutt, 1998). The FIR continuum can also be used as a tracer of emission from young stars and therefore the SFR, as a significant proportion of their radiation is absorbed by dust and re-emitted at longer wavelengths (Kennicutt, 1998; Elbaz et al., 2011). Emission lines, such as Hα, directly probe the ionizing flux of massive (> 10 M$_\odot$) stars with < 20 Myr lifetimes, and these lines therefore provide a 'snapshot' view of

the SFR that is not affected by the SFH (e.g. Kennicutt, 1983).

Fig. 1.4 reproduces the well-known plot from Madau and Dickinson (2014) illustrating the relationship between SFRD and redshift. SFRD increases from the highest redshift up to a peak at cosmic noon, $z \sim 2$, and then decreases exponentially to the present day. The SFRD can be considered as a composite of the halo mass function and the distribution of SFR as a function of halo mass. In the early Universe, star formation is limited by the build-up of dark matter haloes. Star formation reaches a peak at cosmic noon, and thereafter quenching through feedback and gas exhaustion becomes more significant (Schaye et al., 2010). At the highest redshifts, the SFRD is dominated by low mass galaxies, with massive galaxies becoming increasingly significant over time. The main contribution to the present-day SFRD is attributed to galaxies in the mass range $10^{10-10.5} M_{\odot}$ as the more massive galaxies are quenched more efficiently by AGN (Vogelsberger et al., 2014). Up to $z \leq 4$, the SFRD is dominated by dust-obscured SF (e.g. Magnelli et al., 2011; Bouwens et al., 2016). Algera et al. (2023) test the impact of dust-obscured SF at $z \sim 7$, finding that it contributes $\sim 30\%$ to the SFRD already at this early redshift.

1.5 Galaxy Kinematics across Cosmic Time

The evolution of galaxies is governed by a complex interplay of physical processes such as merger activity, smooth gas accretion from the cosmic web, and feedback-driven gaseous outflows. These processes leave distinct dynamical signatures, and therefore to understand galactic mass assembly and dust formation mechanisms requires comprehensive, synergistic consideration of resolved kinematics, as presented in this thesis. In this section, I motivate the power of kinematics as a tool for understanding galaxy environments and physics across cosmic time. In Figure 1.5 I show an example from Kohandel et al. (2019) of the integrated spectra and morphology of a simulated galaxy from the SERRA simulations (Pallottini et al., 2022) in the following dynamical stages: merger, stable disk, and disturbed disk.

1.5.1 Galactic Disks

Following the natal collapse of a galaxy, and any major merger events that it subsequently experiences, angular momentum gained from the tidal fields of nearby mass concentrations drives the gas to settle into a disk structure (e.g. Tinsley, 1980; Sellwood, 2014). At low to intermediate redshifts ($z \lesssim 4$) resolved kinematic surveys of galaxies with integral field spectroscopy (IFS) have supported the model of galaxies growing in mass through smooth gas accretion from the cosmic web, and confirmed that the majority of star forming galaxies have rotation-dominated kinematics with regular disky velocity fields (e.g. Genzel et al., 2008) and display kinematic properties consistent with an 'inside-out' formation mechanism (Förster Schreiber et al., 2009). Surveys up to $z \sim 2.5$ consisting of hundreds of star forming galaxies with resolved kinematics, lying on a tight main sequence between stellar mass and SFR, find that $\sim 70 - 80\%$ of the sample is rotation-dominated (Wisnioski et al., 2015; Wisnioski et al., 2019; Stott et al., 2016). Some criteria for the positive identification of a disk are presented in Wisnioski et al. (2015). These include the v/σ ratio, alongside the presence of a smooth, continuous velocity gradient along a single axis, with the region of steepest velocity gradient coinciding with the peak of the velocity dispersion distribution, and the centre of the potential as represented by the continuum centre. The v/σ measurement is the ratio of rotational velocity to velocity dispersion, and quantifies the degree of rotational support possessed by a system. The v/σ threshold at which an object is considered to be rotation-dominated varies between $1 - 3$ according to different authors, while $v/\sigma = \sqrt{3.36}$ corresponds to equal contributions to the support of a turbulent disk from rotation and random motion (Förster Schreiber and Wuyts, 2020).

Übler et al. (2019) study the ionized gas kinematic properties of a sample of 175 galaxies between $0.6 < z < 2.6$, finding that the intrinsic velocity dispersion, and thus the turbulence of the interstellar medium, increases as a function of redshift. Velocity dispersion is the main driver of disk instability, and thus the degree of rotational support (according to v/σ) decreases as a function of redshift over this interval. This result is in line with expectations from the hierarchical model of galaxy formation, according to which galaxies at high redshift should be more turbulent than lower redshift analogues, due to more intense merger activity, gas accretion,

and internal feedback at early times (Conselice et al., 2008; Hayward and Hopkins, 2017; Romano et al., 2021). However, recent results have identified a significant population of disk galaxies, including resolved dynamically cold objects, at $z > 3$ (e.g. Smit et al., 2018; Rizzo et al., 2020; Rizzo et al., 2021; Lelli et al., 2021; Rowland et al., 2024). This result, which simulations typically fail to reproduce (Pillepich et al., 2019; Simons et al., 2019), indicates that galactic turbulence is a weaker function of redshift in this epoch than would be expected from extrapolating lower-redshift relations, such as that from Übler et al. (2019). However, caution must be applied in comparing results from low and high redshift regimes, as this often means comparing results from warm and cold gaseous tracers respectively; see Section 1.5.4.

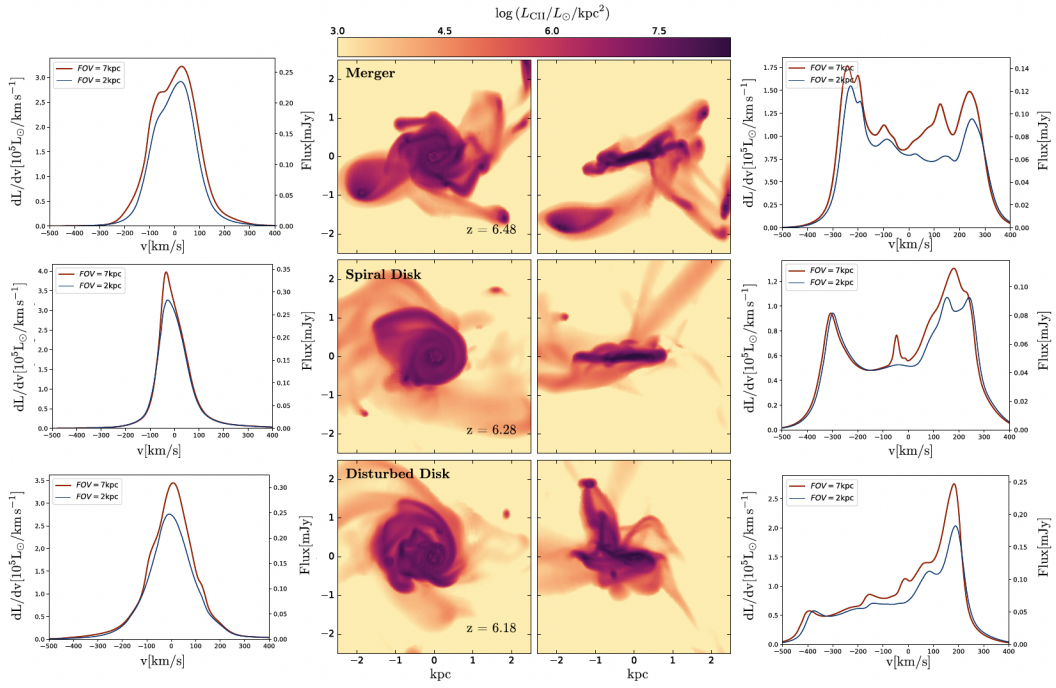

Figure 1.5: Left column: [CII] spectrum for the face-on inclination of a galaxy 'Althea' from the SERRA simulations in three distinct evolutionary stages. Centre: Face-on and edge-on images of the galaxy in each stage. Right: As the left column, for the edge-on inclination. Figure Credit: Kohandel et al. (2019).

1.5.2 The Impact of Mergers

According to the hierarchical galaxy formation model, galaxies grow through mergers, triggered by the merging of their dark matter haloes (Blumenthal et al., 1984). Mergers are catastrophic events with varied and profound consequences for the galaxies involved. According to simulations, mergers redistribute angular momentum within the interacting systems, causing gravitational instabilities in the ISM and funnelling gas into the galactic centre (e.g. Hernquist, 1989; Blumenthal and Barnes, 2018). This is hypothesised to boost star formation by introducing a supply of pristine gas (Hani et al., 2018) or by redistributing the existing gas content (Thorp et al., 2019), and this framework appears to be borne out by observations revealing merger galaxies to have an enhanced SFR (e.g. Ellison et al., 2008). SFR enhancement is observed to begin at a separation of 150kpc (Patton et al., 2013), and to peak around the time of coalescence (Ferreira et al., 2025). Such an inflow of gas towards the centre should also increase the accretion of the supermassive black hole (SMBH) and correspondingly provide a kick to AGN activity. However, this is difficult to confirm; some observations report AGN enhancement in merger galaxies (e.g. Marian et al., 2020; Pierce et al., 2022), while others find no evidence of this phenomenon (e.g. Shah et al., 2020; Lambrides et al., 2021). From simulations, Quai et al. (2023) find that mergers heighten SMBH accretion, while Sharma et al. (2024) do not find evidence that mergers grow the SMBH. Disagreement between various studies may be, at least in part, attributable to variations in definitions and selection criteria, with analysis of an observational sample by Treister et al. (2012) finding that only the most luminous AGN are driven by mergers ($\sim 4\%$ at $L_{bol} = 10^{43}\text{ergs}^{-1}$, rising to $\sim 90\%$ at $L_{bol} = 10^{46}\text{ergs}^{-1}$).

Identifying galaxy mergers can pose an observational challenge. Mergers are identified in the early stage of their interaction through their proximity as a close pair (Patton et al., 2000), and in the late phase are identified just pre- or post- coalescence (Conselice et al., 2003) through merger-induced gravitational instabilities. Hashimoto et al. (2019) identify a source as a major merger at $z = 7.15$ through spatially decomposing the [OIII] and [CII] spectra into two distinct peaks separated by $\sim 200\text{kms}^{-1}$ and each associated with a corresponding rest-UV clump.

With JWST observations, Duan et al. (2025) probe pair fractions, merger rates,

and mass accretion rates in the redshift range $4.5 < z < 11.5$, finding pair fractions increase up to ~ 0.2 at $z = 8$, followed by a flat evolution period up to the upper limit of their redshift coverage. Furthermore, they find that mergers contribute around half of galaxy assembly at high redshift, broadly consistent with the result from Robaina et al. (2010) that major mergers between $> 5 \times 10^{10}$ $M_\odot$ galaxies are the main driver of massive red sequence growth. Galaxy merger events evidently contribute significantly to galaxy evolution at high-redshift, and constraining the disk and merger fractions provides insight into mass assembly mechanisms. The merger and disk fractions do not, however, sum to 1; galaxies are significantly more complex than this, with many or even most at high redshifts not belonging to either category. Even within the framework of simple dynamical classifications we must also consider dispersion dominated galaxies (see the following, Section 1.5.3) - though indeed, these could represent a clumpy, chaotic stage in the process of galaxy merging (Bournaud et al., 2011).

1.5.3 Dispersion-Dominated Galaxies

Dispersion-dominated galaxies are those where the average velocity dispersion, after applying corrections for instrumental broadening and beam smearing, exceeds the inclination-corrected rotation velocity (Förster Schreiber et al., 2009). Compared to rotation-dominated systems, in general dispersion-dominated galaxies are younger and exhibit lower stellar mass, dynamical mass, and metallicity, along with a higher gas fraction, as described in Newman et al. (2013) where it is suggested that they may be 'seeds' for the development of rotational systems. As they are often compact in nature, it is possible that they could in fact be small rotationally-supported systems that appear dispersion-dominated due to instrumental effects obscuring the rotation, or that we could be seeing a clump or some internal structure of an approximately face-on disk, where the surrounding material is too low in surface brightness to be detected (Förster Schreiber et al., 2009).

Interpretations of dispersion-dominated galaxies that consider them as real physical phenomena and not observational artefacts include that they could be an early stage in galaxy evolution with higher gas fractions and lower masses, or the result of dissipative major mergers (Law et al., 2007).

1.5.4 Comparing Gaseous Tracers

Warm, ionized tracers such as Hα and [OIII] that are frequently used to measure ISM properties at $z < 3$ are shifted to the observed mid infrared for sources at higher redshifts. At $z > 6$ characterising the ISM from optical and near infrared photometry is challenging due to uncertainties in redshifts, dust extinction and rest frame optical nebular emission line properties. Kinematic characterizations of galaxies in the first billion years are sparse, and have previously been dominated by cold gas observations from facilities like ALMA. However, JWST now provides access to warm gas in galaxies from this era, and it is therefore crucial in understanding the difference between information provided by cold and warm gas, thus facilitating meaningful comparisons between results obtained from different tracers. Several recent studies have looked into this; Rizzo et al. (2023) assemble a sample of galaxies between $0 < z < 4$ from archival ALMA observations, and in Rizzo et al. (2024) they use this sample, along with other results from the literature, to determine that the evolution of turbulence is a much weaker function of redshift when cold gas tracers are used compared to warm gas. Kohandel et al. (2024) used galaxies from the SERRA simulations (Pallottini et al., 2022) to examine the discrepancy between warm and cold gas dynamics by comparing the velocity dispersion (σ) and rotational support (v/σ) measurements obtained from Hα and [CII]. They find that the values of σ and v/σ measured depend strongly on the gas tracer, with the warm gas v/σ values being systematically lower than for cold gas. Furthermore, v/σ is not a significant function of redshift irrespective of the tracer employed, but is instead strongly dependent on galaxy mass, particularly in the case of warm gas observations, as shown in Figure 1.6. For SERRA galaxies and other simulations (Ejdetjärn et al., 2022), the main difference between cold and warm gas dynamics is due to the presence of outflows. While cold [CII] gas traces the disk component, Hα traces both the disk and the outflow. This concept is considered and developed in greater depth in Chapter 2.

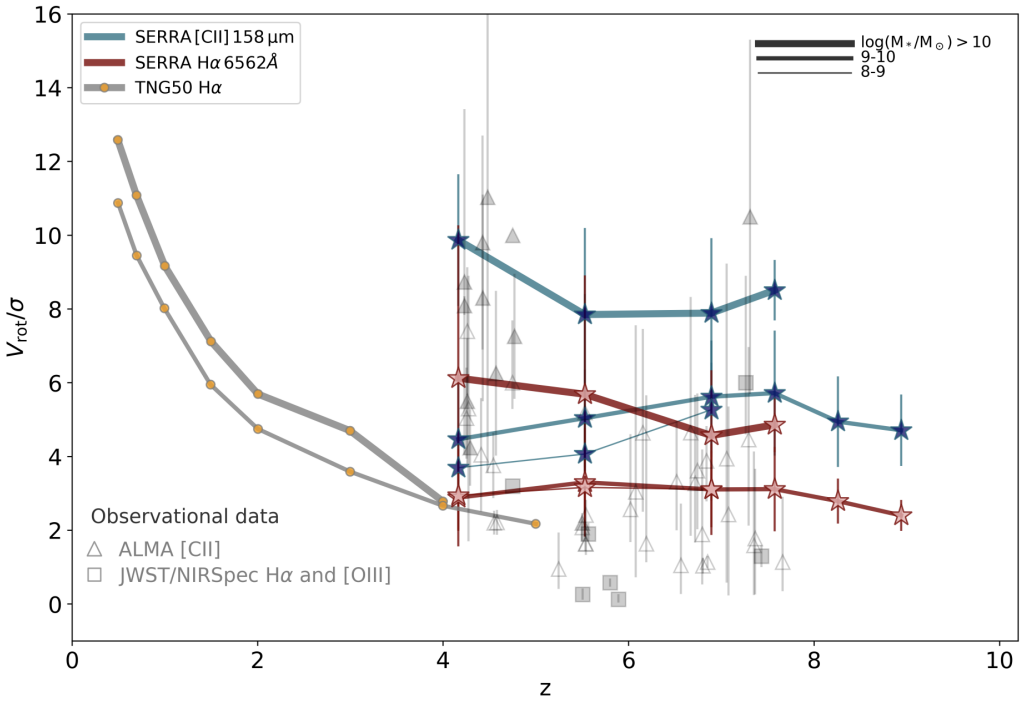

Figure 1.6: From this plot, we see that the rotational support is higher when measured with cold gas compared to warm gas tracers, and has a relatively flat evolution with redshift. Figure Credit: Kohandel et al. (2024).

1.6 Complementary Analysis Techniques

To understand galactic mass assembly and dust formation mechanisms requires comprehensive, synergistic consideration of resolved kinematics alongside dust detections and resolved spectral energy density (SED) fitting, to truly benefit from the multi-tracer view of early galaxies now available from our most powerful observatories. In this section I introduce some complementary techniques employed in this thesis.

1.6.1 Galactic Morphology

Morphology concerns a galaxy's visual appearance, and due to its efficiency at classifying galaxies in large samples, it is an important first-order probe of diversity within a galactic population. Morphometric measurements include the effective radius, the asymmetry, the ratio between the radial scale length and vertical scale height, and the Sérsic index n, where $n = 0.5$ represents a Gaussian profile, $n = 1$ an exponential profile, and $n = 4$ a de Vaucouleurs profile. Sérsic index distributions differ

significantly between distinct morphological groups, but n is not capable of cleanly delineating disky and spheroidal galaxies (Kartaltepe et al., 2023). Parameterising asymmetry can provide insight into the ongoing dynamical processes within a galaxy, with interactions and mergers increasing asymmetry (Conselice et al., 2000). Morphology and kinematics are deeply interconnected and therefore synergistic tracers of galactic structure and physics. Candidate disks are morphologically identified through a flattened, extended light profile (Robertson et al., 2023; Vega-Ferrero et al., 2024), and kinematic follow-up can then confirm their diskiness. Comparing the morphologies of diverse tracers reveals whether stellar UV, dust, and emission line components are co-spatial, and if not, then kinematic analysis could shed light on the physical processes that could be driving the morphological differences and offsets between them (e.g. Ginolfi et al., 2020; Pizzati et al., 2020).

1.6.2 Continuum Mapping

Mapping the FIR continuum in a galaxy reveals the locations of dust-obscured star formation. Observational evidence indicates a significant level of dust obscured star formation in the first $\sim$ billion years (e.g. Schouws et al., 2022). Using a [CII]-selected galaxy sample at $z \gtrsim 5$, van Leeuwen et al. (2024) forward-model the UV luminosity function, finding that obscured SF contributes $> 3\%$ of the total SFRD at $z \sim 5$, and $> 10\%$ at $z \sim 10$.

Additionally, the dust mass can be converted to a molecular hydrogen mass (e.g. Scoville et al., 2013; Schinnerer et al., 2016), which is intrinsically connected to the SFR as the gas reservoir for star formation. The dust-to-gas conversion is not straightforward, however, as continuum emission depends on various factors such as the temperature and emissivity of the dust grains (Groves et al., 2015).

1.6.3 Spectral Energy Distribution Fitting

The SED of a galaxy may consist of photometry, spectroscopy, or both, and is a measure of the total electromagnetic radiation emitted by that galaxy as a function of wavelength or frequency. An example SED is illustrated in Figure 1.7.

SED fitting is a very powerful tool that can yield many important properties of a galaxy, including the star formation rate, star formation history, stellar mass

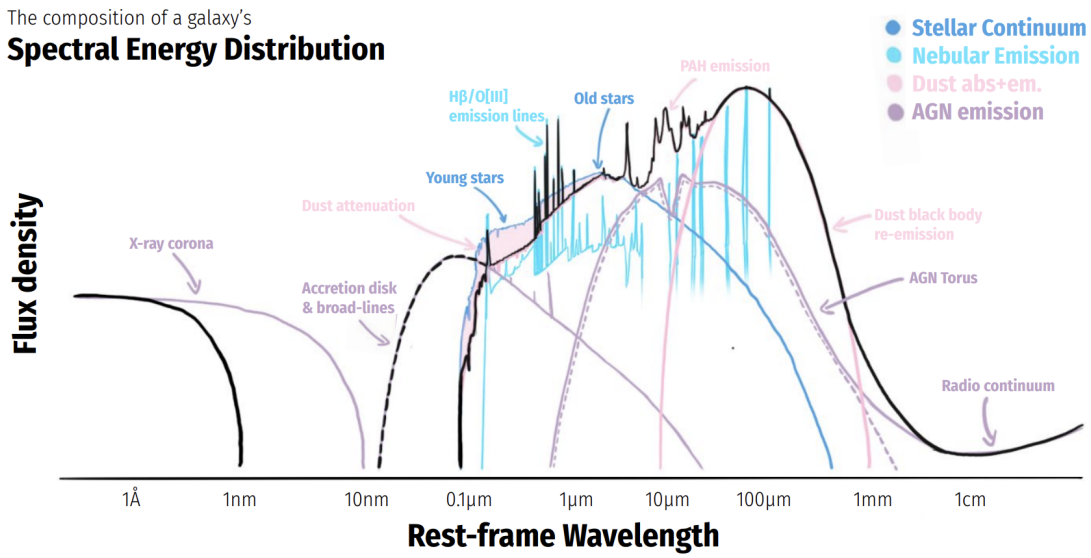

Figure 1.7: This is an illustration of an example spectral energy distribution, showing the various components contributing to the galaxy emission across the wavelength spectrum. Figure credit: Iyer et al. (2025)

and metallicity, as well as the quantity and properties of dust and gas present (Iyer et al., 2025). SED fitting depends on a number of assumptions regarding physical properties. These include the stellar initial mass function (IMF): the dust attenuation, which depends on dust/star geometry (Calzetti, 2001) and is generally accounted for by assuming a certain attenuation curve: and the nebular emission from the continuum and recombination lines, which is particularly relevant at low metallicities and young ages, and therefore at high redshift (Anders and Fritze-v. Alvensleben, 2003). Measuring star formation rates is complicated by the lack of reliable age measurements due to the age-dust-metallicity degeneracy, and is also affected by the choice of dust and SFH priors (Conroy, 2013). Galaxies with high SFRs can contain 'hidden' populations of older stars, which have a relatively high mass to light ratio (Papovich et al., 2001). This is expected to be less problematic at higher redshifts, where the stellar populations are universally younger, but Giménez-Arteaga et al. (2023) and Giménez-Arteaga et al. (2024) show that the effect of outshining by younger stellar populations remains significant at $5 < z < 9$ and would lead to underestimating the total stellar mass. A solution to this, employed by Giménez-Arteaga et al. among others, is to perform resolved SED fitting where data quality allows. Furthermore, Pacifici et al. (2023) note that uncertainties and

biases are introduced by the choice of fitting code employed.

1.7 Observing Facilities and Surveys Relevant to this Thesis

In the following subsections I provide brief descriptions of the technological specifications and capabilities of the observatories which provided the data that this thesis makes use of.

1.7.1 The Hubble Space Telescope

The Hubble Space Telescope (Polidan, 1991; Dalcanton, 2009, HST:) is a telescope that was launched into low Earth orbit in 1990, with a 2.4m primary mirror and multiple science instruments. One of these is the Wide Field Camera 3 (Baggett et al., 2008; Kimble et al., 2008, WFC3:), a powerful dual channel camera sensitive to wavelengths from ultraviolet to infrared. The ultraviolet/visible light (UVIS) channel has a silicon-based CCD detector with a 160×160 arcsec field of view, while the infrared (IR) channel has a HgCdTe detector with 123 × 137 arcsec field of view. WFC3, simultaneously with the Advanced Camera for Surveys (ACS) has been used to image galaxies in the distant universe, expanding upon the legacy of the Hubble Deep Fields.

1.7.2 The James Webb Space Telescope

The James Webb Space Telescope (JWST: Lightsey et al., 2012; Rigby et al., 2023) is a telescope launched in 2021 into orbit around the second Lagrange point, with a hexagonal mirror of 6.5m diameter, composed of 18 hexagonal segments. Its science payload consists of the following instruments:

- Mid-Infrared Instrument (MIRI), which provides imaging and spectroscopy in the wavelength range $4.9 - 27.9\mu$m
- Near-Infrared Camera (NIRCam), which is capable of imaging and wide-field slitless spectroscopy in across two channels: short wavelength ($0.6 - 2.3\mu$m) and long-wavelength ($2.4 - 5\mu$m)

- Near Infrared Imager and Slitless Spectrograph (NIRISS) which offers slitless spectroscopy, high-contrast interferometric imaging, and imaging for light in the wavelength range $0.6 - 5\mu$m

- Near Infrared Spectrograph (NIRSpec) which performs near-infrared spectroscopy from $0.6 - 5.3\mu$m across four observing modes: imaging spectroscopy with the integral field unit, multi-object spectroscopy with the micro-shutter assembly, single object spectroscopy with fixed slits, and bright object time series spectroscopy with the wide aperture.

JWST, with its unprecedented resolution and sensitivity at high redshift (Robertson, 2022), is opening up a new window into the first galaxy populations, allowing the study of both their stellar morphology through rest-frame near-infrared and optical imaging, and emission line kinematics with warm, ionized gas (e.g., Hα, [OIII]).

1.7.3 The Atacama Large Millimetre/Submillimetre Array

The Atacama Large Millimetre/submillimetre Array (ALMA: Hills and Beasley, 2008; Wootten and Thompson, 2009) is a radio interferometer consisting of 66 antennae in total, made up of 50× 12m antennae in the main reconfigurable array, 12× 7m antennae in the Atacama Compact Array (ACA) and 4× 12m antennae in the Total Power Array (TPA). It is located on the Chajnantor plateau in the Chilean Atacama desert, at an elevation of over 5000m, where it benefits from exceptionally dry atmospheric conditions.

The advent of ALMA ushered in a new era of high-redshift astrophysics, offering unprecedented sensitivity. With ALMA, the point source sensitivity was improved by 10-100× relative to what was possible previously, and the spectral line sensitivity by 10-20×. The various configurations available from the 12m array offer an angular resolution range between 10 miliarcseconds to a few arcseconds, and its ten bands offer near-continuous frequency coverage between 35-950 GHz. This has enabled ALMA to be used effectively for spectral scanning experiments to confirm the redshifts of distant galaxies, leading to its designation as a 'redshift machine' (Smit et al., 2018; Schouws et al., 2023). For a comprehensive review of the observational capabilities and notable scientific discoveries of ALMA in the field of high-redshift

galaxies, see Hodge and da Cunha (2020).

1.8 Recent Results and Outstanding Questions

Recent observations reveal massive galaxies already established within the first 1-2 billion years of cosmic time, including a $3 \times 10^{11} M_{\odot}$ star-forming galaxy at $z = 6.9$ (Strandet et al., 2017; Marrone et al., 2018), a $10^{9} M_{\odot}$ galaxy at $z = 10.6$ (Oesch et al., 2016; Bunker et al., 2023), and massive $\sim 10^{11} M_{\odot}$ passive galaxies at $z = 3-5$ (Glazebrook et al., 2017; Valentino et al., 2020; Carnall et al., 2023b). Such sources are predicted by certain models (Mason et al., 2015; Mashian et al., 2016), but their prevalence is far higher in observations than would be expected from galaxy formation simulations. This discrepancy is not simply accounted for by cosmic variance, as Baker et al. (2025) demonstrate through comparing the abundance and properties of quiescent galaxies from the JWST Advanced Deep Extragalactic Survey (JADES: Eisenstein et al. (2023)) spectroscopy with predictions from the Full-hydro Large-scale structure simulations with All-sky Mapping for the Interpretation of Next Generation Observations (FLAMINGO: Schaye et al. (2023)) simulations.

How are galaxies becoming quiescent or mini-quenched on short timescales? The population of massive galaxies at high redshift spotlights long-standing questions on how such bright galaxies form. In particular, the relatively high number density of quiescent galaxies prompts questions over which processes could be responsible for driving star formation and its cessation on such short timescales. SF within galaxies is regulated by a complex interplay of physical processes, driven by gas cooling and aggregating into giant molecular clouds which then fragment into stars, and counteracted by a variety of feedback processes whose relative contributions to suppressing star formation are yet poorly constrained. There is a diverse range of such mechanisms active across different timescales and spanning a wide parameter space of galaxy masses. External effects such as ram pressure stripping and tidal interactions quench SF over long (>100Myr) timescales, while at <50Myr scales, SF is internally regulated by feedback driven by active galactic nuclei or supernovae (e.g. Binney and Tabor, 1995; Arjona-Gálvez et al., 2024).

Observations from Spitzer-IRAC suggested that $z > 6$ galaxies generally exhibit

high specific star formation rates (e.g. Kim et al., 2012), while JWST finds a diverse range of star formation histories (e.g. Endsley et al., 2024). JWST provides a window into faint sources, and has enabled the discovery of low mass quiescent galaxies at $z = 5.2$ (Strait et al., 2023) and $z = 7.3$ (Looser et al., 2024) which appear to have been internally quenched, having rapidly ceased SF after a starburst phase, alongside numerous post-burst candidates identified with NIRCam imaging (e.g. Endsley et al., 2023; Trussler et al., 2024).

Simulations (e.g. Dome et al., 2024) find that bursty star formation at $z = 4 - 8$ results in mini-quenched galaxies in the mass range $M_* = 10^7 - 10^9 M_\odot$, with the main causes of mini-quenching being stellar feedback, insufficient gas accretion, and intergalactic interactions. However, the observed population of mini-quenched galaxies indicates that quenching is occurring on a shorter timescale than simulations are able to reproduce (e.g. Gelli et al., 2024).

How are galaxies becoming metal enriched at redshifts as high as $z \sim 14$?

Presented in Carniani et al. (2025), the galaxy JADES-GS-z14-0 has been spectroscopically confirmed at $z = 14.1796$ (Carniani et al., 2024), and is extremely luminous, with $M_{UV} = -20.81$, its UV emission dominated by stars. Schouws et al. (2024) perform a blind line scan with ALMA and detect the [OIII]88μm line at 6.6σ at a luminosity which shows the galaxy is consistent with the local $L_{[OIII]}$−SFR relation, while Schouws et al. (2025) find a non-detection of [CII]158μm. These results, in combination with the non-detection of dust, lead to the galaxy being characterised as having a high ionization parameter, low gas density and a low dust and gas fraction, a profile indicative of strong feedback effects. The ALMA and JWST observations combined in Carniani et al. (2025) yield a metallicity of $Z = 0.17 Z_\odot$, an extraordinary level of enrichment for such an early time in cosmic history. With JWST and ALMA synergy, we are discovering a significant population of chemically enriched galaxies in the Epoch of Reionization (e.g. Curti et al., 2023; Scholtz et al., 2025), suggesting that chemical evolution progressed rapidly at early times (Nakazato et al., 2023).

Why are some galaxies in the EoR dusty and metal-rich while others are dust-free, UV-bright 'Blue Monsters'?

JWST has revealed a population of bright ($M_{UV} \sim -21$), massive galaxies with

steep UV spectral slopes at very high ($z > 10$) redshift (e.g. Castellano et al., 2022; Whitler et al., 2023). There are various scenarios proposed to explain this phenomenon in simulations. These include the process of dust being ejected from galaxies through stellar radiation pressure, or that galaxies appear blue due to a spatial offset between their dust and UV emission (Ziparo et al., 2023). Ferrara et al. (2025) test whether limited dust production and dust destruction can account for the presence of Blue Monsters, and conclude that to explain observational results it is necessary to have a mechanism to remove dust, such as outflows.

What are the physical origins of observed [CII] haloes?

The [CII] line, arising from the collisional excitation of C+ ions by atomic and molecular hydrogen and electrons, is a dominant coolant of the ISM and thus [CII] morphology is a powerful probe of the physical conditions in the ISM and potentially CGM.

Fujimoto et al. (2019) find [CII] emission to be more spatially extended than star-forming regions by a factor of ~ 5 for a sample of 18 galaxies at $z \sim 5-7$, using [CII] observations from ALMA and stellar continuum emission from HST. Fujimoto et al. (2020) extend this analysis to the ALPINE sample of 40 galaxies at $z \sim 4-6$, and Fudamoto et al. (2022) perform stacking analysis of [CII] emission lines and dust continua from REBELS galaxies at $z \sim 7$, again finding evidence of significantly extended [CII] halos. This is an intriguing observational result, as simulations capable of reproducing the dust and stellar continuum properties did not predict the extended [CII] structure (e.g. Pallottini et al., 2017b; Arata et al., 2019).

1.9 Thesis Outline

The focus of this thesis is on presenting a morpho-kinematic view of galaxies in the Epoch of Reionization through the study of emission lines and complementary tracers, demonstrating the powerful synergy of the multi-tracer information now available.

In Chapter 2, we investigate whether it is possible to identify galaxies hosting disks at $z > 6$ and derive their intrinsic properties, including the level of turbulence and the presence of outflows, with the typical observations available from the NIR-

Spec/IFU. In Chapter 3 we introduce the first sample of galaxies from the Epoch of Reionization from which we can measure the distribution and morphology of dust obscured star formation, along with resolved cool gas kinematics from [CII]. This chapter presents the data reduction processes employed for these ten galaxies, and provides an overview of their morphological properties. Chapter 4 explores the kinematic properties across the galaxy sample, classifying dynamical type as a probe of stellar mass build up. Chapter 5 outlines the main conclusions from this work, and the future research that it could inspire.

Chapter 2

Lessons Learned from Studying Hα Galaxy Kinematics with Mock JWST/NIRSpec IFU Observations at $z > 6$

2.1 Introduction

The evolution of galaxies is governed by a complex interplay of astrophysical phenomena including minor and major merger events, smooth gas accretion, and gaseous outflows driven by feedback from stars and active galactic nuclei (e.g. Dayal and Ferrara, 2018; Crain and van de Voort, 2023). These processes leave distinct dynamical signatures in a galaxy, and therefore the study of galaxy kinematics represents a unique probe of the mechanisms governing the mass assembly and growth of galaxies.

The James Webb Space Telescope (JWST) is opening up an unprecedented view into the first galaxy populations, allowing the study of both their stellar morphology through the analysis of rest-frame near-infrared or optical imaging, and their kinematics through stars (e.g. D'Eugenio et al., 2024), and emission lines (e.g., Hα, [OIII]) tracing the warm ionized gas. Early morphological analysis of JWST imaging suggested that the disk population at $z > 1.5$ is 10$\times$ greater than was seen by the Hubble Space Telescope (Ferreira et al., 2022). Disks have been discovered up to

$z \sim 9$ in the Cosmic Evolution Early Release Science Survey (CEERS, Finkelstein et al., 2023) using morphological criteria, whereby galaxies are classified as potential disks if they display flattened, extended light distributions (e.g. Robertson et al., 2023; Vega-Ferrero et al., 2024). The disk fraction estimated from a large sample of CEERS galaxies is 60% at $z = 3$ and $\sim$ 30% at $z = 6 - 9$ (Kartaltepe et al., 2023). Kinematic information is crucial for positively confirming that visually identified disk candidates are indeed rotational systems (e.g. Wisnioski et al., 2015; Simons et al., 2019; Rizzo et al., 2022; Wang et al., 2024). One widely employed metric used to quantify the degree of rotational support in a galaxy is the ratio of rotational velocity to velocity dispersion, v/σ, where the velocity dispersion measures the turbulence of the ISM through the broadening of the spectral line (Li et al., 2023; Nelson et al., 2024; De Graaff et al., 2024). A value of $v/\sigma \geq 3$ is considered an indicator of a settled disk (Förster Schreiber and Wuyts, 2020), and $v/\sigma \geq 10$, typical of local galaxies, indicates a dynamically cold disk.

Galaxy kinematic studies using warm ionized gas tracers, most notably Hα, at intermediate redshifts ($0.5 \lesssim z \lesssim 3.5$) have found that the velocity dispersion within galaxies increases, and the v/σ ratio decreases, as a function of redshift (Wisnioski et al., 2015; Turner et al., 2017; Johnson et al., 2018; Übler et al., 2019; Birkin et al., 2024) such that galaxies at $z \geq 2.5$ have $v/\sigma < 2$ (e.g. Wisnioski et al., 2015; Turner et al., 2017). This is in agreement with simulations (e.g. Ceverino et al., 2017; Hung et al., 2019). For instance, using TNG50 simulations, Pillepich et al. (2019) find that at $z < 5$, disks traced by Hα become significantly more turbulent with increasing redshift.

Cold gas observations of galaxies, especially [C II]-158μm and CO observations with the Atacama Large Millimetre/Submillimetre Array (ALMA), are characterised by lower velocity dispersion and a greater degree of rotational support (i.e., $v/\sigma \sim 10$) at $z = 0.5 - 6$ (Jones et al., 2017; Neeleman et al., 2020; Rizzo et al., 2020; Rizzo et al., 2021; Fraternali et al., 2021; Tsukui and Iguchi, 2021; Lelli et al., 2021; Lelli et al., 2023; Rizzo et al., 2023; Roman-Oliveira et al., 2023), but see Spilker et al. (2022). Marginally resolved kinematic characterisations of sources in the Epoch of Reionization (EoR) indicate that disk structure may already be present at these early times (Smit et al., 2018; Posses et al., 2023; Parlanti et al., 2023), while the

high resolution observations presented in Rowland et al. (2024) reveal the earliest dynamically cold disk yet discovered, with v/$\sigma \sim 10$ at $z = 7.31$.

Rizzo et al. (2024) examine the discrepancy between warm and cold gas dynamics by comparing the velocity dispersion and v/σ measurements using spatially resolved CO, [CI] and [CII] observations from the ALPAKA sample at $z = 0.5 - 3.5$ (Rizzo et al., 2023) and from the literature (Girard et al., 2019; Girard et al., 2021; Bacchini et al., 2020; Fraternali et al., 2021; Rizzo et al., 2021; Lelli et al., 2021; Lelli et al., 2023; Roman-Oliveira et al., 2023) with trends from observations and models of warm ionized gas. They find that Hα yields measurements of σ (v/σ) that are higher (lower) than those from cold gas by a factor of ~ 3.

This observational result is in accord with theoretical work by Kohandel et al. (2024), using the SERRA zoom-in cosmological simulations (Pallottini et al., 2022). Kohandel et al. (2024) compare simulated velocity dispersion and v/σ values obtained from Hα and [CII] at $z = 4 - 9$, finding that the velocity dispersion from [CII] is a factor of $2 - 3\times$ smaller, on average, than the Hα value. They find that v/σ does not strongly evolve with redshift, and show that the tracers probe different galactic regions. [CII] traces the disk, as [CII] originates from the cold neutral medium and is found around molecular clouds (Vallini et al., 2015; Pallottini et al., 2017b; Olsen et al., 2021), while Hα traces both the disk and surrounding ionized gas, such as outflowing or inflowing streams (see also Ejdetjärn et al., 2022; Ejdetjärn et al., 2024). This contamination of warm gas kinematics by the non-circular motion of gas surrounding the galaxy is primarily responsible for the difference between kinematics as measured by cold and warm gas tracers.

Hence, cold gas observations provide a less biased estimate of the disk velocity dispersion, rotational velocity and circular velocity. To benefit from the synergy between JWST and ALMA, it is imperative to be able to interpret the difference in kinematic measurements from warm and cold gas. To illustrate this point, the galaxy COS-3018 was identified as a disk from ALMA observations (Smit et al., 2018; Parlanti et al., 2023), while Scholtz et al. (2025) interpret the system as a merger based on hot gas tracers available through NIRSpec. However, as discussed in Rizzo et al. (2022), it is challenging to obtain high resolution and SNR observations at z > 4 with ALMA, the primary facility currently available for observing galaxies in cold

gas. Existing ALMA high-resolution surveys of galaxies at $z > 4$ are therefore biased towards bright, massive galaxies with high star formation rates (e.g. Le Fèvre et al., 2020; Bouwens et al., 2022; Li et al., 2024). The JWST/IFU allows some redress of this bias towards extreme sources at $z > 4$, as it is capable of observing normal galaxies from this redshift range in warm gas, and thus greatly extends the accessible redshift range for warm gas kinematics. Recent studies analyze the kinematics of individual objects in the EoR at high resolution with the G395H grating (R $\sim$ 2700). They identify a galaxy group with indications of merger activity in its constituent galaxies at $z = 6.34$ (Jones et al., 2024), a candidate unsettled, turbulent disk at $z = 6.9$ (Arribas et al., 2024) and a lensed galaxy with a velocity gradient that could be indicative of rotation or merger activity at $z = 9.11$ (Marconcini et al., 2024). In the context of such progress, the aim of this chapter is to understand whether we can robustly identify galaxies hosting disks at $z > 6$ and derive their intrinsic properties, including the level of turbulence and the presence of outflows, with the typical observations available from the JWST/NIRSpec IFU.

To achieve this, we create idealised and realistic mock NIRSpec observations for two galaxies from the SERRA simulations (Pallottini et al., 2022), which form part of the sample studied in Kohandel et al. (2024). These are representative massive disk galaxies ($\sim 10^{10} M_\odot$) at redshift $z = 6 - 7$, chosen based on the comparison between the kinematics as measured by Hα and [CII] (see Section 2.2.1). One appears to host strong outflows, while the other shows no sign of non-circular motion. They act as case studies for which we examine the dynamical properties that can be recovered from observations using state-of-the-art analysis techniques. The structure of the chapter is as follows: in Section 2.2 we introduce the suite of simulations our target galaxies are drawn from, and establish their properties. In Section 2.3 we outline the process by which both idealised and realistic mock NIRSpec observations are created from the simulation outputs. In Section 2.4 we describe the methods we use to analyse the data. The results are discussed in Section 2.5 and summarised in Section 2.6.

Table 2.1: Properties of the SERRA galaxies derived directly from the simulations.

Name	z	$M_\star$ $[10^{10}M_\odot]$	M_{gas} $[10^9M_\odot]$	$L_{H\alpha}$ $[10^9L_\odot]$	$L_{[CII]}$ $[10^9L_\odot]$	SFR $[M_\odot yr^{-1}]$	$r_{eff,H\alpha}$ [kpc]	$r_{eff,[CII]}$ [kpc]	$\sigma_{[CII]}$ $[km\,s^{-1}]$	$\sigma_{H\alpha}$ $[km\,s^{-1}]$	$(v/\sigma)_{[CII]}$	$(v/\sigma)_{H\alpha}$
Opuntia	6.07	1.2	4.5	1.8	0.3	19	1	0.7	26.8	58.6	8.8	4.1
Narcissus	6.82	1.0	4.1	23	1.1	38.4	0.8	0.8	20.8	23.9	11.9	10.4

2.2 SERRA Simulations

SERRA is a suite of high resolution ($\simeq 10^4 M_\odot$, $\simeq 20$ pc) zoom-in cosmological simulations which tracks the formation and evolution of galaxies at $z > 4$ (Pallottini et al., 2022). These simulations model the interactions between radiation, gas, stars, and dark matter within a cosmological framework, using the adaptive mesh refinement code RAMSES (Teyssier, 2002; Rosdahl et al., 2013). Combined with the zoom-in technique, this provides the spatial and temporal resolution necessary for studying small-scale processes, including star formation and feedback (e.g. from SN and stellar winds: Pallottini et al., 2017b), chemical evolution (non-equilibrium chemistry up to molecular hydrogen formation: Grassi et al., 2014; Pallottini et al., 2017a), and radiative effects (e.g. photoionization and photoevaporation: Decataldo et al., 2019; Pallottini et al., 2019).

In post-processing (cf. Lupi et al., 2020; Katz et al., 2024), the SERRA simulations can be used to analyze line emission across multiple wavelengths using realistic, observational-like pipelines (Zanella et al., 2021; Rizzo et al., 2022), to provide detailed insights into the physical conditions of high-redshift galaxies. [CII] and Hα line emission in SERRA is computed using the CLOUDY spectral synthesis code (Ferland et al., 2017), accounting for the turbulent structure of molecular clouds (Vallini et al., 2018; Pallottini et al., 2019). For each emission line, simulated integral field unit observations are created from the output of the zoom-in simulations in the form of hyperspectral data cubes (Kohandel et al., 2019; Kohandel et al., 2020). These are cubic regions with two spatial and one spectral dimension, centred on target galaxies, upon which the velocity-dependent line surface brightness is modeled using Gaussian kernels to account for ISM temperature and internal turbulence.

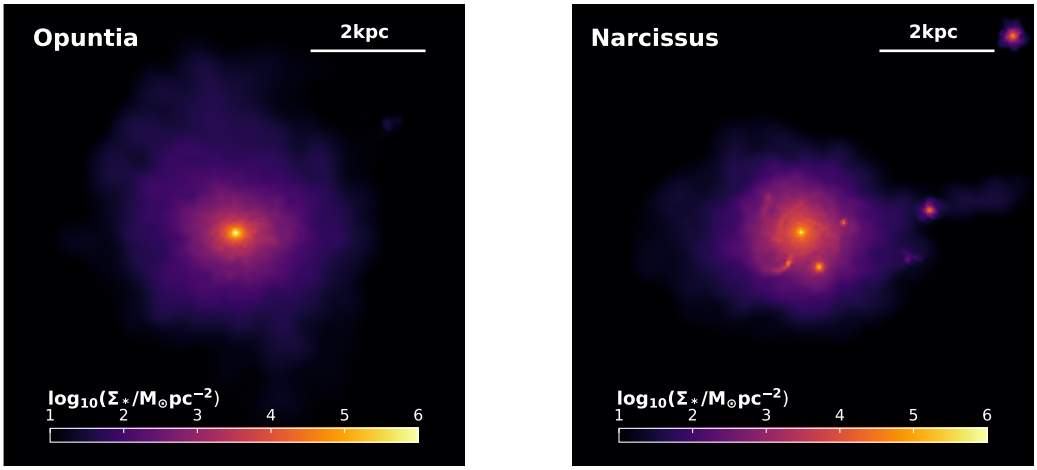

Figure 2.1: Maps of stellar distribution, with a colorbar showing the stellar mass density per unit area. The field of view is 8kpc × 8kpc, corresponding to $\sim 1.4''$ $\times 1.4''$ at $z = 6.07$ (Opuntia, $M_\star = 1.2 \times 10^{10} \mathrm{M}_\odot$) and $\sim 1.5''$ $\times 1.5''$ at $z = 6.82$ (Narcissus, $M_\star = 1.0 \times 10^{10} \mathrm{M}_\odot$).

2.2.1 Target Sources

In this chapter, we consider two simulated star-forming galaxies from the SERRA suite as representative case studies: 'Opuntia' at $z = 6.1$ (SFR $= 19\ \mathrm{M}_\odot \mathrm{yr}^{-1}$, $M_\star = 1.2 \times 10^{10} \mathrm{M}_\odot$) and 'Narcissus' at $z = 6.8$ (SFR $= 38.4\ \mathrm{M}_\odot \mathrm{yr}^{-1}$, $M_\star = 1.0 \times 10^{10} \mathrm{M}_\odot$). These galaxies were selected from the Kohandel et al. (2024) sample ($\simeq 3000$ galaxies at $4 \leq z \leq 9$) based on their kinematic properties, as each hosts a dynamically cold disk. From this sample, Kohandel et al. (2024) find that 60% of sources are dynamically cold in [CII].

We selected our two target galaxies based on their contrasting multi-wavelength kinematic properties. Narcissus, introduced in Kohandel et al. (2024), is an EoR galaxy that maintained a cold disk for over ten dynamical times, showing consistent v/σ in both [CII], a tracer of cold gas, and Hα, which traces the warm ionized component. The second galaxy, Opuntia, was previously analysed in Rizzo et al. (2022) and displays a significantly warmer ionized gas component (see intrinsic[1]

[1]In Kohandel et al. (2024), the intrinsic $\sigma_{\mathrm{em-line}}$ is defined as the luminosity-weighted average velocity dispersion, calculated using moment-2 and moment-0 maps of the respective emission line. The rotational velocity V_{rot} is estimated using the galaxy's circular velocity, given by $V_c = (GM_{\mathrm{dyn}}/r_d)^{1/2}$ where $M_{\mathrm{dyn}} = M_* + M_g$ represents the dynamical mass within the desired field of view, and r_d is the disk effective radius, defined as the radius containing 50% of the gas mass.

values in Table 2.1). This contrast in the cold and warm gas kinematics of high-redshift galaxies has been found to be a signature of outflows (see Kohandel et al., 2024; Kohandel et al., 2025).

To give an overview of the galaxies, in Figure 2.1 we show their stellar distributions. The stellar mass is strongly centrally concentrated in Opuntia, while Narcissus additionally hosts pockets of high stellar density. The most relevant global properties for the galaxies are recorded in Table 2.1. Narcissus has a high Hα luminosity, leading to an offset relative to widely-used $L_{H\alpha}$-SFR calibrations such as that presented in Kennicutt (1998). This offset is not unexpected for galaxies in the EoR, as the Kennicutt (1998) relation assumes solar metallicity and continuous star formation over 100 Myr. In contrast, SERRA galaxies form stars in relatively metal-poor bursty episodes (Pallottini et al., 2022), which can enhance the ionizing photon production per unit SFR and thus increase the predicted Hα luminosity (Kohandel et al., in prep). Similar excesses have been reported in other zoom-in simulations (e.g. SPHINX, Katz et al. (2019)), where low metallicity and bursty star formation systematically raise line luminosities.

As shown in Pallottini et al. (2022), the $L_{[CII]}$-SFR relation of SERRA galaxies is consistent with $z \sim 4$ observations (e.g. Carniani et al., 2018), and similar to the relations at $z = 0$ for starburst galaxies (De Looze et al., 2014; Herrera-Camus et al., 2018) albeit with a larger scatter (0.48 dex), which can cause individual galaxies to appear above (Opuntia) or below (Narcissus) the average of the relation.

2.3 Creating Mock Observations

Our ability to reliably derive disk kinematic properties in the presence of significant non-circular motions is limited by the spectral resolution, angular resolution, and signal to noise ratio. In order to test the effect of varying SNR and angular resolution on the feasibility of recovering the main properties of disks at $z > 4$ and the presence of non-circular motions driven by outflows, we create both realistic mock NIRSpec and idealised observations from the two simulated galaxies. The simulated datacubes have a native spectral pixel size of 10.1 $\mathrm{km\,s^{-1}}$ and spatial pixel size of ~ 0.03 kpc, corresponding to an angular resolution of $\sim$ 0.005 arcsec at the redshifts of our

targets. The field of view is 8 × 8 kpc ($\sim 1.4''$ ×$1.4''$ for Opuntia, $\sim 1.5''$ ×$1.5''$ for Narcissus). We use the simulation output to create idealised and mock NIRSpec observations using the general formula:

$$\text{processed cube} = (\text{simulated cube} \otimes \text{PSF} \otimes \text{LSF}) + \text{noise}\,, \tag{2.1}$$

where $\otimes$ represents a convolution operator, PSF is the Point Spread Function, and LSF is the Line Spread Function. Different PSFs, LSFs, and noise approximations are used for the idealised (Sec. 2.3.1) and realistic (Sec. 2.3.2) cases.

2.3.1 Idealised Data

We do not perform any spatial or spectral rebinning, in order to preserve the high intrinsic resolution in the creation of idealised observations, and so permit a comparison of the information recoverable from realistic mock NIRSpec observations and observations with ideal data quality. We convolve with a small PSF so as to maximise the number of resolution elements sampling the galaxy and therefore test the impact of resolution on our ability to recover kinematic properties from Hα. The process of creating the idealised data is outlined in the following.

1. The pixel size ($\sim 0.005''$) and the spectral pixel size (10.1 $\mathrm{km\,s^{-1}}$) are not changed from the simulation output.

2. The data were convolved with a PSF and LSF (eq. 2.1). The PSF is formed from a 2D Gaussian with Full Width at Half Maximum (FWHM) of 3 pixels $\approx 0.016''$. The LSF has a FWHM equivalent to twice the spectral pixel size.

3. We add noise taking a realization from a normal distribution, setting a high S/N ratio of 50 in an aperture of equivalent size to the PSF at the outer extent of the galaxy, so as to maximise signal while still providing a noise background to facilitate kinematic fitting.

2.3.2 Realistic mock NIRSpec Data

The process of creating the mock observations was to interpolate the data to the spectral and angular pixel scale of NIRSpec, and then to add a realistic realisation

of noise. The highest spectral resolution mode of JWST/NIRSpec, designed for kinematic characterisation of distant galaxies, has a resolution $R \simeq 2700$ (Jakobsen et al., 2022), which may not be sufficient to accurately measure velocity dispersion values below ~ 50 km s^{-1}, as a single spectral resolution element has a width of $\approx 111/\sqrt{8ln(2)} = 47.1$ km s^{-1}, and the instrumental LSF may here introduce strong uncertainties (e.g. Lelli et al. (2023), and see De Graaff et al. (2024) in which the LSF of the NIRSpec dispersers is found to be a strong function of the target light profile, with the measured LSF being up to 2× lower than reported by STScI - see their Appendix A.) The pixel scale of JWST is $\sim 0.1''$/pixel, equating to ~ 0.6 kpc/pixel at $z = 6$, and in IFU mode the FoV is $\sim 3.0'' \times 3.0''$ (Böker et al., 2022). To simulate detector noise we ran the JWST Exposure Time Calculator (ETC: Pontoppidan et al., 2016) on a blank scene, using the grating G395H, which provides the best spectral resolution for Hα at our target redshifts. The readout pattern employed is NRSIRS2, which offers an improvement in the handling of correlated noise compared to traditional readout methods through regular sampling of reference pixels, and is particularly effective for long exposures of faint sources (Rauscher et al., 2012; Birkmann et al., 2022). The detector parameters are informed by the set-up utilised to perform integral field spectroscopy on galaxies at $z > 8$ in GTO Cycle 1 Programme 1262 (PI Luetzgendorf). The specific details of creating the idealised and mock observations are described in the following.

1. Spectral binning to achieve a spectral pixel size equivalent to that of the ETC-generated noise cube for each galaxy, which had a value of 32.3 km s^{-1} (Narcissus) and 35.8 km s^{-1} (Opuntia). Spatial binning to a pixel scale of $0.05''$/pixel, representing dithered observations.

2. Convolution with a simulated PSF and LSF for NIRSpec/G395H. The PSF is created with the same dithered pixel size of $0.05''$, using the python package `WebbPSF` (Perrin et al., 2012; Perrin et al., 2014), and the LSF is a Gaussian profile with full width at half maximum equivalent to λ/R, where λ is the redshifted wavelength of Hα and R is the resolution corresponding to this wavelength, with a value of 3600.8 (3223.9) for Narcissus (Opuntia).

3. Addition of noise. The ETC-generated noise cube was scaled by a multiplica-

tive factor to reach a SNR of 5 in an aperture with the same area as the PSF at the outer extent of the galaxy. The region referred to here as the 'outer extent of the galaxy' is indicated with dotted lines in Figure 2.2, from which it is apparent that the region does not have a uniform flux. To account for this, we use the flux of the entire region to estimate the average signal within a PSF-sized aperture. We dropped 10,000 apertures at random positions on random slices of the ETC-generated noise cube, plotted the flux measurements in a histogram and took the standard deviation of the distribution as N.

We fitted the emission line spectrum of the galaxy with a Gaussian profile and extracted the centre (μ) and standard deviation (σ) of the fitted Gaussian. We used these measurements to create a spectral subcube of the data in the region $\pm 2\sigma$ of the emission line centre. From this subcube we extracted the signal within a PSF-sized aperture at the outer extent of the galaxy, S, and hence obtained the scaling factor by which we multiplied the noise before adding it to the galaxy data. We then estimate the exposure time that would be required to achieve a similar observation of a real target. To do this, we input the properties of our mock observations to the ETC, including the luminosity and effective radius, and calculate the SNR obtained at various exposure times. We find that an SNR of 5 is achievable in an aperture at the outer extent of the galaxy in 7236 seconds for Narcissus (using a detector set-up of 6 groups/integration, 4 integration/exposure, and 4 dithers) and in 57597 seconds for the fainter Opuntia (using a detector set-up of 28 groups/integration, 1 integration/exposure, and 28 total dithers). However, the exposure time required to obtain the same SNR can vary strongly as a result of small differences in target galaxy sizes and emission line widths, the latter being particularly relevant for galaxies with strong velocity gradients or outflow components, as is the case here. Therefore, for our results to translate reliably to real observations, in Section 5.1 we consider the effect on our recovered kinematic measurements of changing the SNR, rather than the exposure time.

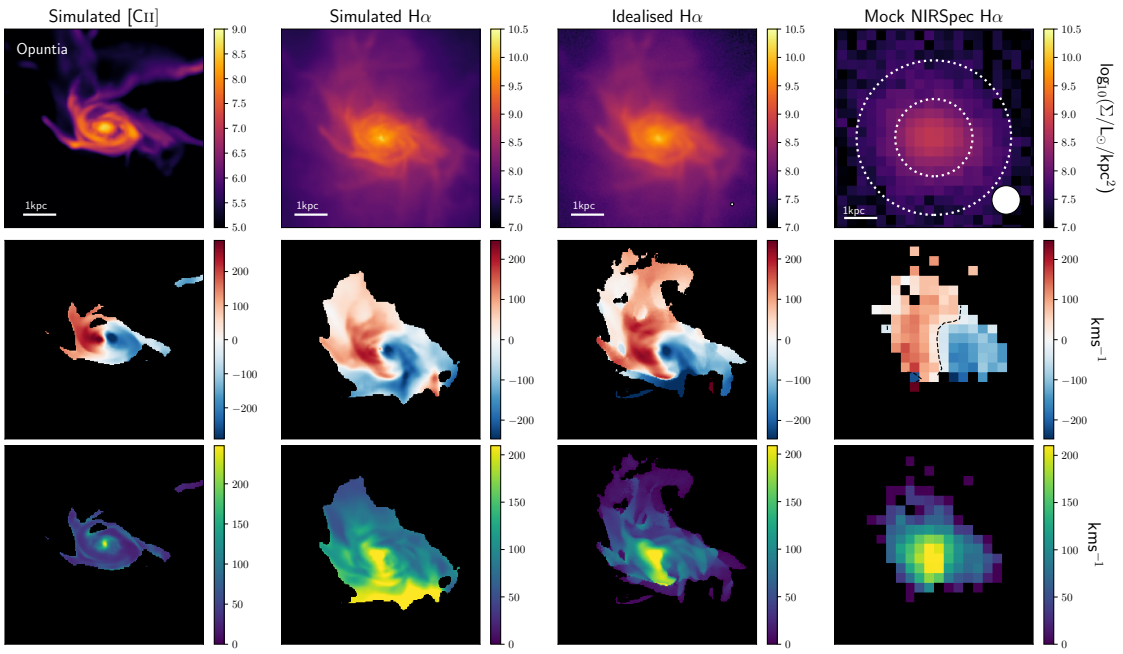

(a) Opuntia

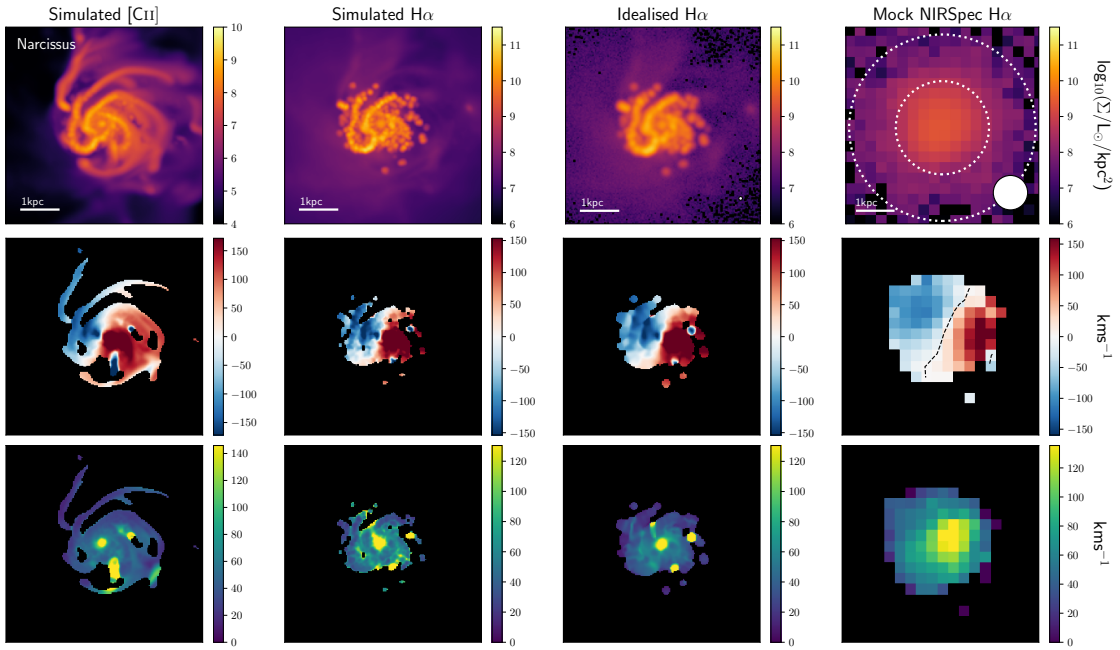

(b) Narcissus

Figure 2.2: Moment maps derived from Opuntia (top three rows) and Narcissus (bottom three rows). The $v = 0$ isophote is plotted on the mock NIRSpec moment-1 maps and dotted lines indicate the region representing the 'outer extent of the galaxy' in the mock NIRSpec moment-0 maps. PSFs are shown for the derived data.

2.4 Kinematic Analysis

2.4.1 Qualitative analysis of the moment maps

Moment maps are typically used to obtain evidence on the dynamical state of a galaxy. For instance, the presence of a continuous, smooth gradient in the moment-1 map is used as a criterion in the identification of disks Wisnioski et al. (e.g. 2015), but it is not sufficient. At marginal resolution, non-circular bulk motion of gas and interactions between merging systems can mimic certain disk characteristics (Simons et al., 2019).

Figure 2.2 shows the moment-0, -1, and -2 maps derived from Opuntia and Narcissus inclined at 60°, respectively depicting integrated spectral intensity, line-of-sight velocities, and velocity dispersion. The [CII] and Hα emission maps in the first and second columns are obtained directly from the simulations. The third and fourth columns show the idealised warm gas observation and a realistic mock NIRSpec/IFU observation as described in Section 2.3, for which the moment-1 and -2 maps are masked at 25σ (in the idealised case) and 5σ (in the mock NIRSpec case).

For Opuntia, the [CII] moment maps trace the dynamically cold central disk, which has a smooth velocity gradient and a centrally peaked velocity dispersion distribution. Opuntia appears far more extended in Hα, where we still see the central disk structure but also the diffuse gas surrounding it. In the mock NIRSpec/IFU observation, the moment-1 map shows the smooth gradient indicative of a disk. However, the velocity gradient is not only tracing the disk structure itself. The comparison with the intrinsic simulated Hα maps (second column) clearly shows that the velocity gradient in this case is tracing both the disk and the surrounding gas. Hence, at the angular resolution of the JWST observations, the diffuse component dominates and mimics the emission originating from the outer extent of the galaxy. The deviation of the $v = 0$ isophote from a straight line in the centre of the moment-1 map provides an indication of the presence of non-circular motion (e.g. Arribas et al., 2024; Übler et al., 2024). However, this method can be misleading in the case of limited resolution (Rizzo et al., 2022) or sub-optimal masking (see Appendix A.1). Traced by [CII], we see that the central disk of Narcissus is encircled by extended filamentary structures. From their morphology in the moment-0 map alone, these

could be interpreted as inflowing or outflowing gaseous streams, but the moment-1 map appears to contradict this scenario as the filaments reproduce the velocity gradient of the inner disk. We therefore consider them to be gravitationally bound to the disk, and perhaps best described as 'cold gas spiral arms'. For Narcissus, the structure traced by cold and warm gas appears similar; according to both, Narcissus has a strong axial asymmetry in the [CII] and Hα distributions. Its irregular structure comprises multiple off-centre clumps clearly visible in the moment-2 maps, which could represent satellites or localised clumps of star formation. While there is a velocity dispersion peak coincident with the galactic centre, the flux is not centrally concentrated and is instead weighted to the south of the galaxy. In the mock NIRSpec/IFU moment-1 map we again see a smooth, disky velocity gradient, though here it is indeed tracing disk structure. The high-velocity dispersion clumps are no longer resolved, and appear merged into a single off-centred region.

2.4.2 Kinematic Modelling with ^{3D}Barolo

Kinematic fitting to the simulated IFU observations is performed using the software ^{3D}BAROLO (Di Teodoro, 2015; Di Teodoro and Fraternali, 2015), which fits 3D tilted ring models (Rogstad et al., 1974) to emission line datacubes. ^{3D}BAROLO creates mock realizations of rotating disk models defined by kinematic and geometrical parameters, notably including rotational velocity, velocity dispersion, inclination angle, position angle, and the coordinates of the disk centre. The disc model is created as a series of concentric thin rings, with circular velocity being constant across all rings, while each has an independent value for radius, position angle, and rotational velocity. The gas emission in each ring is generated in 6D (three spatial and three velocity dimensions) and projected into the 3D data cube. This is done using a Monte Carlo process, in which the space is randomly populated with emitting gas clouds by a stochastic function, and line profiles are built from these. Before comparing the data with the model, ^{3D}BAROLO convolves the model with a Gaussian component which approximates the observational PSF to account for the impact of beam smearing. The model is then compared to the data on a ring-by-ring basis. ^{3D}BAROLO outputs model cubes convolved with the beam, as well as moment maps and major and minor axis position-velocity (PV) diagrams,

which are 2D velocity profiles extracted along the major and minor kinematic axes of a source. To perform fitting with ^{3D}BAROLO, we provide estimated values for certain parameters motivated by measurements and assumptions of the underlying physics, as described in the following.

Kinematic Parameters. The rotation velocity and velocity dispersion are allowed to vary between 10-300 $\mathrm{km\,s^{-1}}$, with initial parameter estimates of 250 $\mathrm{km\,s^{-1}}$ and 50 $\mathrm{km\,s^{-1}}$ respectively, informed by measurements for rotating disk candidates at similar redshifts (Smit et al., 2018; Posses et al., 2023; Rowland et al., 2024).

Geometrical Parameters. Since the goal of this project is to constrain the impact of data quality on the feasibility of deriving dynamical properties, it is a 'proof of concept' study and we therefore did not consider it necessary to fit the inclination angle from the data as if we had no *a priori* knowledge of the galaxy properties. We therefore fix the inclination angle to 60° for both galaxies. To confirm the validity of this decision, we re-run the fitting routine for the mock NIRSpec observation of each galaxy, supplying 60° as the initial estimate of the inclination angle but allowing the parameter to vary. The inclination angles are then fitted as 63° for Opuntia and 62° for Narcissus.

Position angle is left to be fitted. The `Z0` parameter, controlling the scale height of the disk, is fixed at 0.001″ for each observation as we assume a thin disk. We experiment with altering the assumed disk thickness and confirm that this has very little effect on the fitted model, as the rotating disk features are consistent between thin and thick discs and the uncertainties introduced by the thin disk assumption is not significant compared to the errors on the velocity measurements; see Appendix A.2 for a discussion. Assumed disk thickness mainly affects the inclination angle (Roman-Oliveira et al., 2023) which for our purposes is fixed.

Resolution Elements. The radial separation (`RADSEP`) was set so as to obtain the maximum possible number of independent measurements without oversampling. The value of `NRADII` is then the number of independent tilted rings that could be placed along the extent of the galaxy at a separation of `RADSEP` $\approx$ FWHM. For the realistic mock NIRSpec observations, `NRADII` is 2.

In Appendix A.3 we present representative channel maps of each datacube along with the best fitting model from ^{3D}BAROLO.

2.5 Results

In this section, we introduce evidence for the presence of disks in our sample (Section 2.5.1), and examine the impact of observational effects on the recovered kinematics and related measurements: turbulence and rotational support (Section 2.5.2). We use our mock observations to comment on the validity of current techniques used for outflow identification (Section 2.5.3), and furthermore we test the impact of the biases in our kinematic measurements on the recovered dynamical masses (Section 2.5.4).

2.5.1 Disk Identification

We use the position angle fitted by ^{3D}BAROLO to the mock NIRSpec observations and idealised Hα and [CII] observations to define the kinematic axis as measured by each tracer. Each measured axis is plotted over the corresponding galaxy in Figure 2.3. We extract the major PV diagrams along these kinematic axes, and the minor PV diagrams along the orthogonal axes. In Figure 2.4, we show the contours of the data (black) and the disk model (red). PV diagrams provide evidence for determining the kinematic properties of galaxies, with a rotating disk showing a characteristic signature in its PV diagrams (Fraternali et al., 2002; De Blok et al., 2008; Neeleman et al., 2020). The minor axis diagram of a rotating disk is symmetric about the axes defining the systemic velocity and the centre, and the major axis diagram displays an S-shape (Rizzo et al., 2022). For a rotating disk with no outflows, inflows, or other sources of non-virial motions, there should be no emission outside of the S-profile, and therefore the quadrants unoccupied by the S-profile are referred to as 'forbidden regions'.

For Opuntia, it is possible to discern a disk-like S-shaped distribution in the major-axis PV diagram of both the idealised and realistic mock NIRSpec cases, though it is significantly less distinct in the mock NIRSpec diagram due to the lower resolution. In the idealised case, it is clear that there are non-circular motions present as there is emission not reproduced by the rotating disk model visible in the so-called forbidden regions (e.g. the emission region in the negative quadrant of the major axis PV diagram, indicated with an arrow). In the mock NIRSpec case, the rotating disk

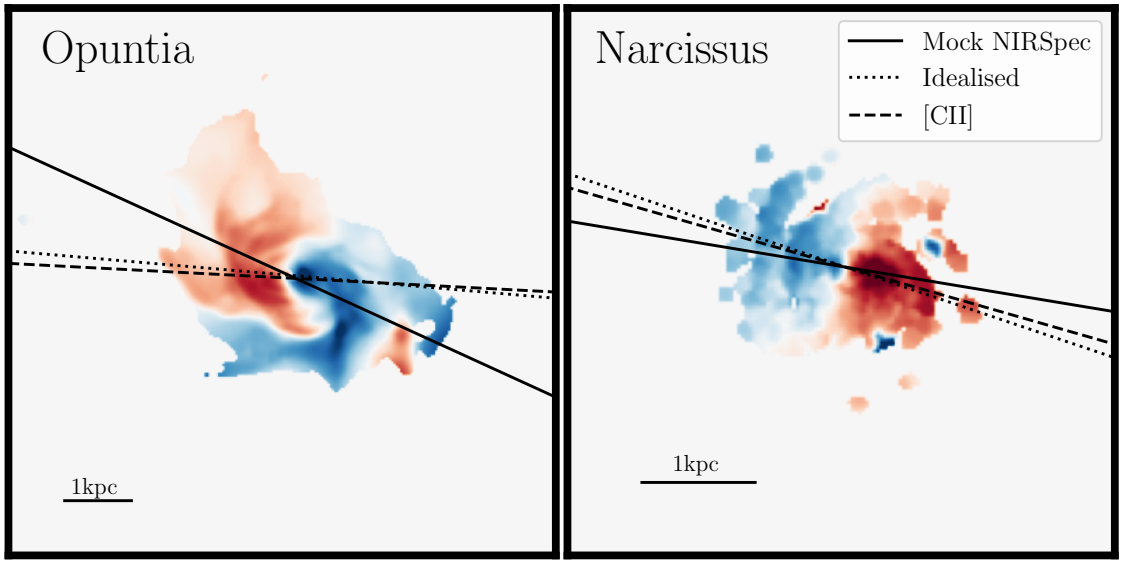

Figure 2.3: Kinematic axes obtained from ^{3D}BAROLO fitting (section 2.4.2), measured from the realistic mock NIRSpec observations, along with idealised Hα and [CII] observations, overlaid on the intrinsic Hα moment-1 maps.

model is able to well reproduce the overall emission in the bright inner region, but the agreement between the data and disk model worsens for the faint emission (the outermost contour line), in both the major and minor axis PV diagrams.

In Narcissus, it is evident that the major axis PV diagrams are heavily luminosity-weighted to one side, inconsistent with what would be expected for an axisymmetric disk. In the idealised case there is a small peak that could potentially be associated with an outflow, extending below the disk profile S-shape in the inner region, at approximately -350 km s^{-1} (indicated on Figure 2.4 with an arrow), and a similar feature is also visible in the minor axis diagram (again indicated by an arrow).

The agreement between data and model in the mock NIRSpec PV diagrams is poorer still for Narcissus than for Opuntia. Despite Narcissus being less influenced by non-circular motions, the asymmetry of the Hα distribution and the presence of bright clumps lead to a significant discrepancy between data and disk model along both the major and minor axis. From the mock NIRSpec observations, both galaxies would be identified as disks, Opuntia with $v/\sigma = 2.1$, and Narcissus with $v/\sigma = 3$ (Table 2.2). However, neither would be classified as cold disks, despite Narcissus being a dynamically cold disk, and Opuntia being a disk with strong rotational support (i.e. v/$\sigma > 5$) in simulated Hα.

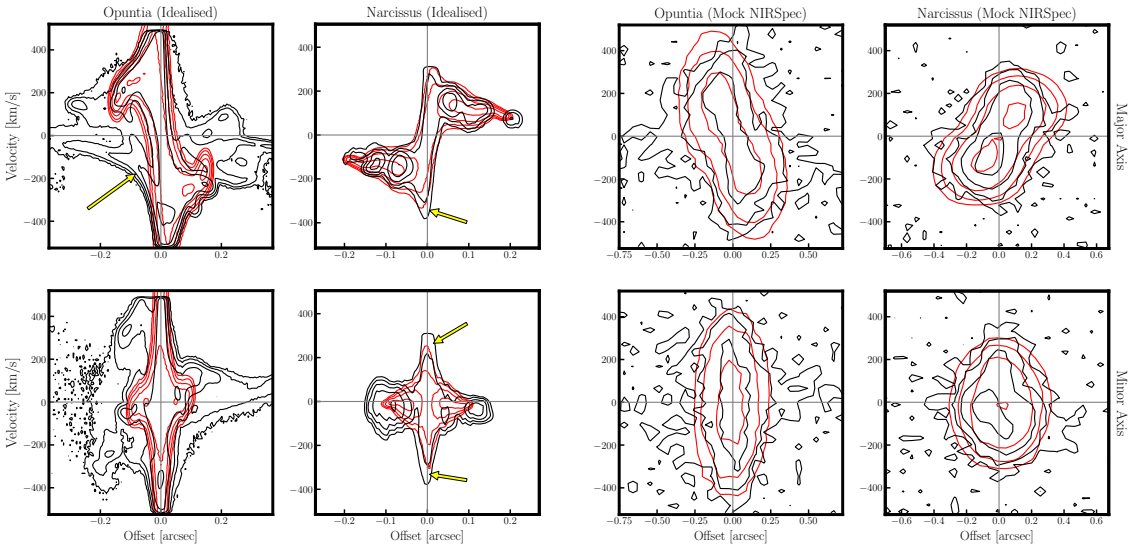

Figure 2.4: Position-Velocity diagrams for the idealised observations (left) and mock NIRSpec observations (right), where the major axis diagrams are extracted along the axes shown in Figure 2.3. Contour levels are at $3^n\sigma$, where n=[1, 2, 3, 4, 5] and the σ value used to define the contours is the RMS value of noise-dominated regions in the diagrams. Black contours trace the data, and red contours represent the disk model. Arrows indicate regions of the PV diagrams that deviate from the expected profile for a disk.

It is evident that the presence of non-circular gas motion in Opuntia, and of irregular disk structure in Narcissus, affects the shapes of their PV diagrams. We therefore examine the ensuing consequences for their disk classification according to the PVSplit method, a dynamical classification technique introduced in Rizzo et al. (2022). PVSplit analysis is based on three empirical parameters that quantify the symmetric and morphological properties of the major and minor PV diagrams. These are P_{major}, a measure of the asymmetry of the major axis PV diagram with respect to the axis defining systemic velocity, P_V, which quantifies the distribution of emission peaks along the velocity axis, and P_R which is similarly defined along the radial axis. The accuracy of PVSplit in separating mergers and disks is demonstrated in Rizzo et al. (2022) for mock ALMA observations at SNR $\geq$ 10 where at least 3 independent resolution elements can be laid along the galactic major axis. Figure 2.5 shows where Narcissus and Opuntia fall on the PVSplit parameter space in relation to the plane of best division between disk and non-disk systems, as defined by Roman-Oliveira et al. (2023) using the support-vector machine method to maximize the distance separating the disk and non-disk galaxy samples pre-classified by Rizzo et al. (2022), which are also plotted on the PVSplit diagram. Opuntia is classified as a disk, while Narcissus is classified as non-disk.

In summary, the comparison between the data and disk model reveals that the two galaxies might not be identified as regular rotating disks from realistic NIRSpec/IFU observations. This result indicates that despite the limited angular and spectral resolution, the mock observational data is not accurately reproduced by an axisymmetric disk model, and rather we see that the presence of non-circular motions in Opuntia and of asymmetries in Narcissus are identifiable through discrepancies with respect to the disk model.

We tested the effect on our recovered rotational velocity and velocity dispersion of changing the SNR from $\sim$ 5 to SNR$\sim$ 3 and $\sim$ 10, finding that the velocity measurements are robust for both galaxies across the entire S/N range. The kinematic measurements recovered at SNR$\sim$ 3 and SNR$\sim$ 10 are presented in a table in Appendix A.4.

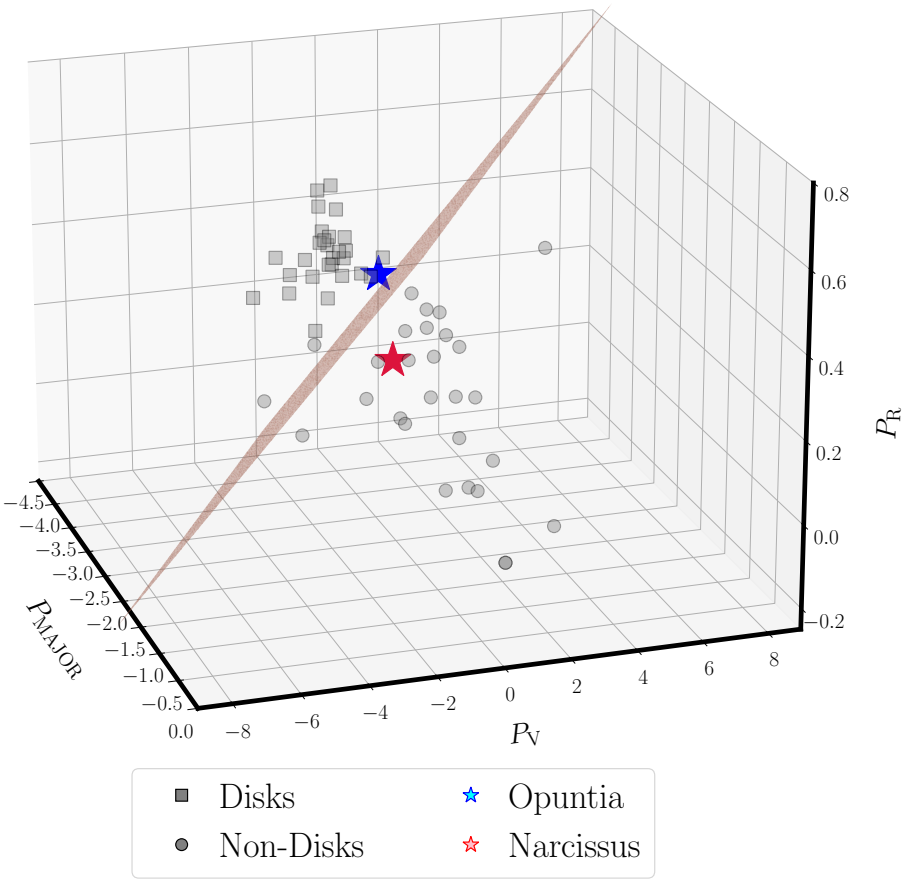

Figure 2.5: Narcissus and Opuntia are here plotted in the PVSplit parameter space alongside simulated disks and non-disks (Rizzo et al., 2022). Narcissus occupies the non-disk region of parameter space, while Opuntia is close to the plan of division between the disk and non-disk populations (Roman-Oliveira et al., 2023). Uncertainties in the PVSplit fitting, propagated from uncertainties in e.g. the fitted centre and position angle from ^{3D}BAROLO, tend to act towards the non-disk region.

2.5.2 Quantifying Biases in Measured Turbulence and Rotational Support

From the ^{3D}BAROLO fitting described in Sections 2.4.2 and 2.5.1, we extracted the rotation velocity and velocity dispersion profiles. We thus obtained the radial average values of σ and v/σ, which we computed as the ratio between the maximum rotation velocity and the average velocity dispersion across the individually fitted rings. Considering each of these in comparison to the intrinsic [CII] measurement gives insight into the extent to which the presence of non-circular motions under the conditions of lower spectral and angular resolution amplifies the disparity between the turbulence and rotational support measured from warm and cold gas. Figure 2.6 shows the comparison between these values and their analogues calculated directly from the simulations in both [CII] and Hα, as described in Section 2.2.1. The values are tabulated for both the idealised and realistic mock NIRSpec data in Table 2.2. In the following, we describe the comparison of velocity measurements extracted from our idealised and mock observational data with those from the intrinsic simulated Hα and [CII]. This comparison is performed to probe the impact of the gas tracer, without introducing complexity through observational effects acting on the reference values themselves.

In the case of Narcissus, less dominated by non-circular motions, the Hα σ and v/σ values from the realistic mock NIRSpec and idealised cases are consistent with each other, but $\sim 3\times$ higher and $\sim 3\times$ lower respectively than the intrinsic Hα measurement, which is close to the intrinsic [CII] measurement. We thus interpret the difference with respect to the intrinsic value as due to the assumption of an axisymmetric disk that we adopted to derive the kinematics, since it is apparent in both the high and low resolution observations.

For Opuntia, in the idealised case, the measured $\sigma_{\mathrm{H}\alpha}$ is $1.8\times$ higher than the intrinsic $\sigma_{\mathrm{H}\alpha}$ and $4.0\times$ higher than $\sigma_{[\mathrm{CII}]}$. The idealised v/$\sigma_{\mathrm{H}\alpha}$ measurement is $1.1\times$ lower than the intrinsic v/$\sigma_{\mathrm{H}\alpha}$ and $2.3\times$ lower than v/$\sigma_{[\mathrm{CII}]}$. For the mock NIRSpec observations, the measured $\sigma_{\mathrm{H}\alpha}$ is $2.3\times$ higher than the intrinsic $\sigma_{\mathrm{H}\alpha}$ and $5.1\times$ higher than $\sigma_{[\mathrm{CII}]}$. The mock v/$\sigma_{\mathrm{H}\alpha}$ measurement is $2.0\times$ lower than the intrinsic Hα measurement, and $4.2\times$ lower than v/$\sigma_{[\mathrm{CII}]}$. These comparisons illustrate the extent to which the non-circular gas component artificially increases the turbulence

Table 2.2: The maximum values of rotational velocity and the average values of the velocity dispersion for each galaxy, as ascertained with ^{3D} BAROLO, alongside the intrinsic measurements.

	$v_{rot,\ max}$ $[km\ s^{-1}]$	$\langle\sigma\rangle$ $[km\ s^{-1}]$	v/σ
Opuntia (Idealised)	410^{+89}_{-85}	108^{+5}_{-5}	$3.8^{0.8}_{0.8}$
Opuntia (Mock NIRSpec)	290^{+25}_{-28}	136^{+10}_{-14}	$2.1^{+0.2}_{-0.3}$
Opuntia (Intrinsic Hα)	240.3	58.6	4.1
Opuntia (Intrinsic [CII])	235.8	26.8	8.8
Narcissus (Idealised)	261^{+23}_{-27}	68^{+3}_{-3}	$3.8^{+0.5}_{-0.5}$
Narcissus (Mock NIRSpec)	193^{+14}_{-17}	62^{+10}_{-11}	$3^{+0.9}_{-0.6}$
Narcissus (Intrinsic Hα)	248.6	23.9	10.4
Narcissus (Intrinsic [CII])	247.5	20.8	11.9

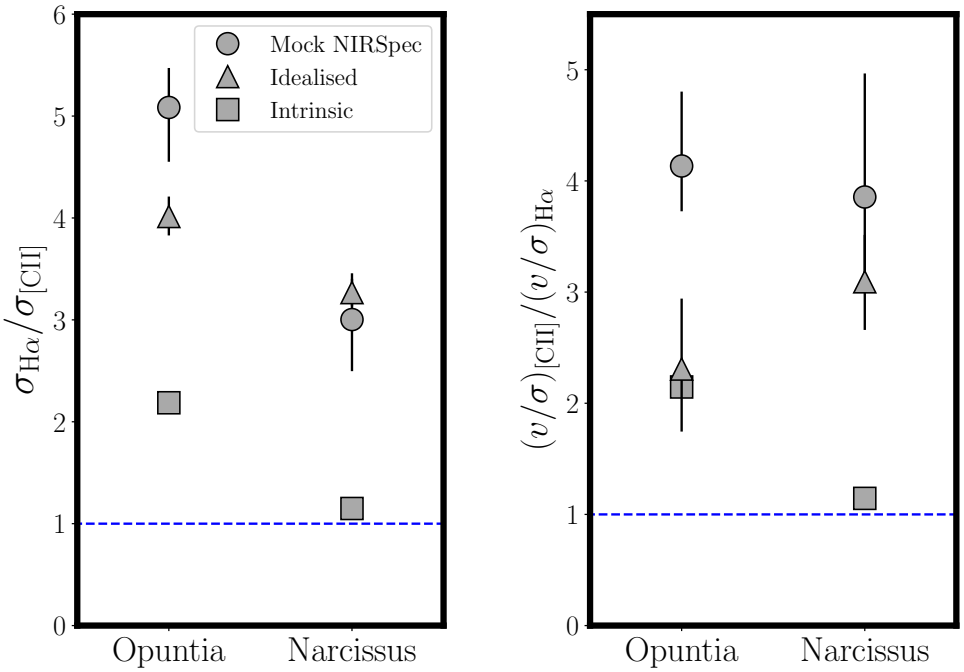

Figure 2.6: v/σ and σ values from the intrinsic, idealised and mock NIRSpec Hα measurements as a function of the intrinsic measurement obtained from cold gas.

and decreases the rotational support as measured by hot gas relative to cold gas intrinsically. For both the idealised and the mock NIRSpec observations, a rotating disk model is not able to well reproduce the data. In the idealised case, this is very clear, whereas for the mock NIRSpec case, we ascertain the disagreement between data and model from indications based on the fitting in the lower SNR outer regions of the galaxies, and the PVSplit results. Given the limited constraints available for the mock NIRSpec observations, making improvements to the modelling by adding, for example, non-circular motions, will not improve fitting due to the high number of parameters to be fitted relative to the available observational constraints. The higher turbulence and lower rotational support measured from the mock NIRSpec observations compared to the idealised observations motivates the conclusion that the lower resolution of the mock NIRSpec observations, as well as a residual beam smearing effect (e.g. Bosma, 1978; Begeman, 1987; Di Teodoro and Fraternali, 2015; Zhou et al., 2017) and contamination by non-circular motions, leads to artificially inflated values of the velocity dispersion. Under the assumption of a rotating disk, ^{3D}BAROLO tries to reproduce the diffuse gas in non-circular motions by increasing the velocity dispersion, and therefore the measured σ values are biased upwards.

2.5.3 Recovering Outflow Properties from Observations

Opuntia has a significantly more turbulent Hα component, a phenomenon which was connected to the presence of outflows in Kohandel et al. (2024), and further developed in Kohandel et al. (2025). Due to the complex geometry of outflow host candidates, it is challenging to positively attribute non-circular motion of gas observed in galaxies to the presence of outflows (for a review of outflow detection techniques see Veilleux et al., 2020). However, in this section we treat the presence of outflows in Opuntia as confirmed, a result which will be analysed in forthcoming work on outflows in simulations. To understand the properties of the gas surrounding the disk in Opuntia, we separate the disk and non-disk emission in the idealised case using the disk model fitted by ^{3D}BAROLO. From the disk model, we create a disk mask consisting of all pixels included in the disk model on a channel-by-channel basis, and we invert this to create a non-disk mask. We apply these masks in turn to the Opuntia idealised observation, yielding two separate datacubes consisting of

only disk emission and only non-disk emission. Maps of these separate emission components are presented in Appendix A.5. In Figure 2.7 the integrated spectrum of the idealised observation is plotted in black, and its disk and non-disk components in purple and pink respectively. From this, we additionally show the PV diagrams for each component extracted along the same axis as was used for the PV diagram of the unmasked idealised observation. We see that the integrated spectrum of the entire idealised observation has a Gaussian profile. The non-disk emission component shows a similar Gaussian profile with a lower amplitude and full width at half maximum, and the integrated spectrum of the disk component exhibits a characteristic double-horned peak profile.

In literature, a widely used technique to identify outflows is fitting a double Gaussian profile to the emission line spectrum of a galaxy, comprising one narrow component representing virial motion, and one broad component associated with outflows (e.g. Carniani et al., 2015; Maiolino et al., 2017; Herrera-Camus et al., 2021, out of many examples.) In Appendix A.6 we attempt to fit a two-component Gaussian composite line profile to the integrated spectrum of the mock NIRSpec observations, and find that the fitted Gaussian peaks do not conform to the broad and narrow shapes that would generally be considered indicative of the presence of outflows. Concas et al. (2022) criticise the oversimplifying assumptions inherent in the double Gaussian fitting outflow detection method, which does not account for observational effects which may artificially give rise to a non-Gaussian emission line profile that could include broad wings. Concas et al. (2022) caution that this method may result in the identification of outflows where none are present.

Our results as presented in Figure 2.7 add an additional caveat; this method may also fail to identify outflows where they are in fact present. The integrated spectrum of the idealised observation does not display the profile of a double Gaussian with a narrow and a broad component despite hosting diffuse emission, likely due to outflows, which dominates the emission from the galaxy. This component is only revealed by the 3-dimensional analysis made possible by the IFU, and thus our result indicates a challenge for confirming outflows from integrated or slit spectroscopy.

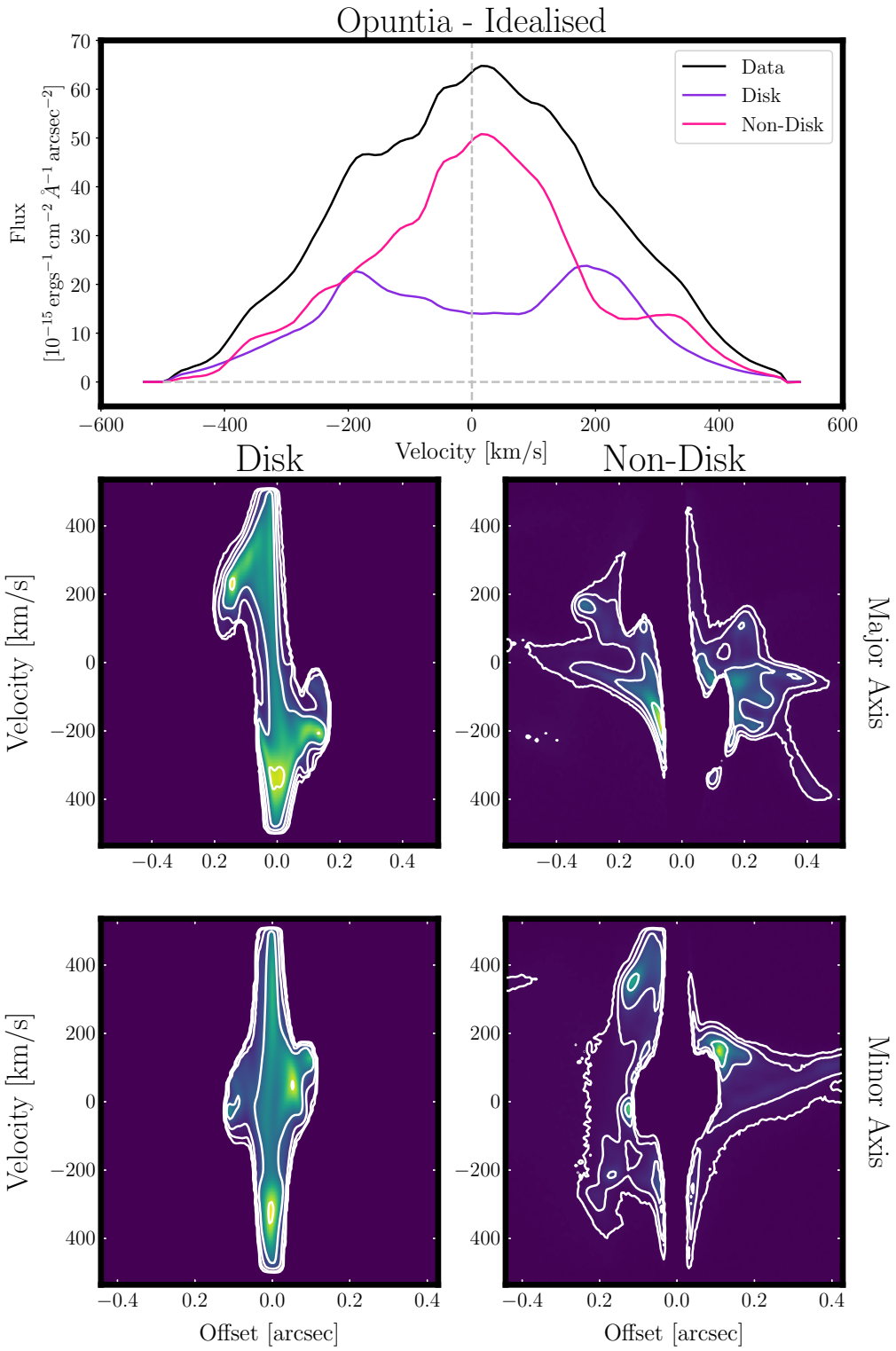

Figure 2.7: *Top Figure:* Idealised Opuntia spectrum (black line), total flux split into a disk (purple line) and non-disk (pink line) component.

Second Row: Major axis PV diagrams for the disk and non-disk components, extracted along the idealised observation axis identified in Figure 2.3. Contour levels are at $3^n\sigma$, beginning at $n = 1$.

Third Row: As above for the minor axis PV diagrams.

2.5.3.1 Considering Disk and Non-Disk Emission at Low Resolution

Applying the method described above to separate the idealised observation of Opuntia into a disk and a non-disk component and then comparing the summed emission in each gives a ratio of the disk to non-disk emission of 1:1.9. If we apply the same method to separate the emission components in the mock NIRSpec observation of Opuntia, we obtain a disk to non-disk emission ratio of 1:0.3, signifying the extent to which low resolution causes non-disk emission to appear part of the disk. Appendix A.4 provides the fitted channel maps and residuals for both the idealised and mock NIRSpec observations. Residuals may be thought of as identifying the non-disk emission; however, in the mock NIRSpec case and for real observations with low SNR, this would be an over-interpretation of the data, as with decreasing SNR it becomes more challenging to distinguish real emission from noise.

2.5.4 Implications for Dynamical Mass

The observational and modelling biases that affect kinematic measurements may consequently impact the estimates of the total mass budget within a galaxy. The rotational velocity is, in fact, a tracer of the galactic gravitational potential (Φ), which additionally depends on the pressure support provided by random motion within the gas (i.e. σ) (Binney and Tremaine, 1987; Cimatti et al., 2020).

$$\frac{1}{\rho}\frac{\partial \rho\sigma^2}{\partial R} = -\frac{\partial \Phi}{\partial R} + \frac{v_{\rm rot}^2}{R}, \tag{2.2}$$

where R is the radius and ρ is the gas volumetric density. This equation can be rewritten as $v_{\rm circ}^2 = v_{\rm rot}^2 + v_A^2$, where $v_{\rm circ}$ is the circular velocity, defined by $v_{\rm circ}^2 = R\partial\Phi/\partial R$ and $v_{\rm A}$ is the asymmetric drift correction

$$v_A^2 = -R\sigma^2 \frac{\partial \ln(\rho\sigma^2)}{\partial R}. \tag{2.3}$$

When the galaxy is dynamically cold ($V/\sigma \gtrsim 10$), the asymmetric drift term is negligible and $v_{\rm rot} \approx v_{\rm circ}$. In this case, to estimate the order of magnitude of the total mass enclosed up to outermost observable radius $R_{\rm out}$, we assume spherical symmetry and define the dynamical mass as

$$M_{\rm dyn} = \frac{R_{\rm out} v_{\rm circ}^2}{G} \approx \frac{R_{\rm out} v_{\rm rot}^2}{G}\,. \tag{2.4}$$

For galaxies with low rotation support ($V/\sigma < 10$), the asymmetric drift correction should be applied to obtain an unbiased estimate of the total gravitational potential. For a galaxy disc where the gas thickness does not depend on radius, and for an exponential surface brightness profile $\Sigma = e^{-R/R_{gas}}$, the asymmetric drift term can be written as

$$v_A^2 = -2R\sigma^2 \frac{\partial ln(\sigma)}{\partial R} + \frac{R\sigma^2}{R_{\mathrm{d,\ gas}}}, \tag{2.5}$$

where $R_{\mathrm{d,\ gas}}$ is the scale radius of the disc (Roman-Oliveira et al., 2024).

Both Opuntia and Narcissus have low rotation support estimated from the mock NIRSpec observations, so the asymmetric drift term will be non-negligible. Despite this, we calculate dynamical mass using both the asymmetric drift-corrected and uncorrected formalisms to quantify the accuracy of the dynamical mass measurements in the case in which the measured σ values are overestimated. The process by which dynamical masses are calculated is expounded on in Appendix A.7. In Table 2.3, we show the total masses within 1kpc measured directly from the simulations, including stars, gas and dark matter, which are $1.8 \times 10^{10}\mathrm{M}_{\odot}$ and $2.1 \times 10^{10}\mathrm{M}_{\odot}$ for Opuntia and Narcissus respectively.

For the idealised observations, the dynamical masses obtained without the asymmetric drift correction are a factor of 1.3× (Opuntia) and 2.3× (Narcissus) lower than the intrinsic values derived directly from the simulations (see Table 2.3). When the asymmetric drift correction is included the dynamical mass estimate becomes 1.1× below the intrinsic value for Opuntia, within 1σ uncertainty, and is unchanged at 2.3× below for Narcissus, within 4σ uncertainty.

For the mock NIRSpec observations, the dynamical masses obtained without the asymmetric drift correction are a factor of 1.4× (Opuntia) and 2.6× (Narcissus) lower than the intrinsic values derived directly from the simulations (see Table 2.3). When the asymmetric drift correction is included the dynamical mass estimates are 1.3× above and 2.1× below the intrinsic values, within 1 and 4σ uncertainties, for Opuntia and Narcissus respectively.

Therefore, we see that including the asymmetric drift correction in general acts to minimize the discrepancies in the measured dynamical mass with respect to the intrinsic values. However, the result that applying the asymmetric drift correction does not change the measured dynamical mass for the idealised Narcissus observa-

Table 2.3: Mass values within 1kpc measured from the simulations, the mock NIRSpec observations, and the idealised observations.

Environment	Opuntia	Narcissus
Intrinsic $M_\star$ [10^{10} $M_\odot$]	1.1	1.0
Intrinsic M_{gas} [10^{10} $M_\odot$]	0.24	0.41
Intrinsic M_{DM} [10^{10} $M_\odot$]	0.49	0.72
Intrinsic M_{total} [10^{10} $M_\odot$]	1.8	2.1
Idealised M_{dyn} [10^{10} $M_\odot$] [a]	$1.4^{+0.3}_{-0.3}$	$0.9^{+0.3}_{-0.4}$
Idealised M_{dyn} [10^{10} $M_\odot$] [b]	$1.7^{+0.3}_{-0.3}$	$0.9^{+0.3}_{-0.4}$
Mock NIRSpec M_{dyn} [10^{10} $M_\odot$] [a]	$1.3^{+0.5}_{-0.5}$	$0.8^{+0.3}_{-0.3}$
Mock NIRSpec M_{dyn} [10^{10} $M_\odot$] [b]	$2.3^{+0.6}_{-0.6}$	$1.0^{+0.3}_{-0.3}$
Idealised integrated spectra M_{dyn} [10^{10} $M_\odot$]	$3.22^{+0.3}_{-0.3}$	$2.5^{+1.5}_{-1.5}$
Mock NIRSpec integrated spectra M_{dyn} [10^{10} $M_\odot$]	$4.27^{+0.6}_{-0.6}$	$1.6^{+0.6}_{-0.6}$

[a] Approximating rotational velocity and circular velocity as equivalent: $v_{rot} \sim v_c$.

[b] Applying the correction for asymmetric drift (equation 2.5).

tions shows that the presence of an asymmetric light distribution can lead to bias in the dynamical mass.

The literature shows that the physical assumptions inherent in dynamical mass calculations can lead to over- or under- estimating the mass of a system, as illustrated by Simons et al. (2019) and Kohandel et al. (2019) using simulations. Our results suggest that despite the indication from our tests that observations overestimate the velocity dispersion, the dynamical mass obtained after correcting for the asymmetric drift acts as a reasonable proxy for the total mass enclosed up to the observable radius, at least in the axisymmetric case as exemplified by Opuntia. It must be noted that the measurement of inclination angle would present a further challenge to the measurement of dynamical mass in observations of real galaxies. If we assume an error of ± 10 degrees on our inclination angle of 60°, this introduces a further $+15\%/-10\%$ error on our measured dynamical masses according to the relation $\mathrm{M_{dyn}sin^2}(i) \sim$ constant.

2.5.4.1 Estimating Dynamical Mass from Integrated Spectra

We test the method employed by Kohandel et al. (2019) of measuring dynamical mass from the full width at half maximum of the emission line, according to the equation:

$$M_{\mathrm{dyn}}^{\mathrm{est}} = \left(\frac{\mathrm{FWHM}^2}{\gamma^2 \mathrm{sin}^2(i)}\right)\left(\frac{R}{G}\right) , \tag{2.6}$$

where θ is the inclination angle of the galaxy, R is the galactic radius, G is the gravitational constant, and we follow Capak et al. (2015) in assuming a value of 1.32 for the parameter γ, a constant controlled by line profile and galaxy properties. This method yields the following dynamical mass estimates: $3.22^{+0.3}_{-0.3} \times 10^{10}\mathrm{M}_{\odot}$ and $4.27^{+0.6}_{-0.6} \times 10^{10}\mathrm{M}_{\odot}$ (Opuntia) and $2.5^{+1.5}_{-1.5} \times 10^{10}\mathrm{M}_{\odot}$ and $1.6^{+0.6}_{-0.6} \times 10^{10}\mathrm{M}_{\odot}$ (Narcissus) in the idealised and mock NIRSpec case respectively. Conversely to the other methods discussed in this section which underestimate the total mass within 1 kpc for these galaxies, estimating dynamical mass from the emission line overestimates the mass in the case of Opuntia (though Narcissus is consistent within 1σ). This effect is understood through the results presented in Section 2.5.3, in which we see that the information recovered from integrated spectra may be contaminated by effects such as outflows, with no clear way to separate out the two velocity components.

2.6 Summary and Conclusions

In this work, we created idealised and realistic mock NIRSpec observations for two star-forming galaxies, Opuntia and Narcissus at $z = 6.1$ and 6.8 respectively, from the SERRA simulations. They were selected as case studies as both are disks with $v/\sigma \approx 10$ from [CII] kinematics, but they have different warm gas kinematics. For one galaxy (Narcissus), the v/σ measured from Hα is similar to that from [CII], while for the other (Opuntia) the Hα v/σ is a factor of 2 lower.

Our aim was to assess how reliably we may expect to recover kinematic information from JWST/NIRSpec IFU observations, and whether we are able to identify galactic features such as rotating disks and outflowing gas using kinematics at such redshifts. The comparison of the idealised and realistic mock NIRSpec/IFU observations provides insight into the extent to which the spectral and spatial resolution and the S/N ratio impact the measured kinematic parameters, while comparing kinematic measurements from both sets of mock observations with those from the intrinsic Hα simulations allows us to examine the validity of the implicit assumptions made when performing kinematic fitting.

Our main conclusions are summarised below.

- At $z \geq 6$, we determine that it is possible to recover complex structure from disk galaxies having a contribution from gas in non-circular motions, or strong asymmetries, at the resolution and SNR typical of NIRSpec/IFU observations, through discrepancies between the data and a rotating disk model.

- Non-circular motions can be robustly identified by leveraging the information contained in the data cubes and the PV diagrams.

- Non-circular motions and asymmetries contribute significant biases to measurements of turbulence and hence rotational support (Figure 2.6). We see that for Narcissus, which has a strong axial asymmetry, the assumption of an axisymmetric disk leads to a factor of ~ 3 inflation in the measured turbulence, irrespective of spatial and spectral resolution. For Opuntia, which is affected by non-circular motions, the lower spatial and spectral resolution available in mock NIRSpec observations biases the measured turbulence to 2.3$\times$ higher than its intrinsic value.

- The recovered dynamical mass appears to be robust for axisymmetric systems despite biases in $v_{\rm rot}$ and σ, with the value measured from our mock NIRSpec observations being within 1σ of the total baryonic+DM mass for Opuntia. Disk asymmetry presents a further challenge for dynamical mass recovery, with both the idealized and mock NIRSpec observations for Narcissus yielding values for dynamical mass that are $\sim 2\times$ lower than the intrinsic total mass.

- We present a caveat to the method of identifying outflows via the fitting of a double-Gaussian profile consisting of a narrow and a broad component to the galaxy integrated spectrum by illustrating (Figure 2.7) that the integrated spectrum of Opuntia, a galaxy that appears to host strong outflows, does not reproduce this profile, and its outflows are only recoverable through a 3-dimensional analysis.

In conclusion, we show that at the spatial and spectral resolution and S/N ratio that may be expected for NIRSpec/IFU observations of individual galaxies at $z > 6$, disk galaxies with strongly asymmetric structure, and those hosting significant outflows, are measurably distinct from the standard rotating disk model. For this to be apparent, we show that it is necessary to leverage the entire three-dimensional spatial and spectral information contained within the IFU data, rather than collapsing those data into 2-dimensional maps or inspecting 1-dimensional spectra. We stress the importance of comparing the different kinematic results obtained from Hα and [CII], using synergistic warm and cold gas observations in building characterisations of galaxy kinematics.

Chapter 3

REBELS-HR: Introducing the Sample

3.1 Introduction

Galactic morphology is a consequence of the astrophysical processes controlling how galaxies form, and is therefore of great importance in understanding galactic evolution. Morphology is one of the most fundamental and accessible observables in galactic astronomy, and therefore has a long history. The Hubble tuning fork diagram was originally devised by Hubble (1926) as a classification system that groups together galaxies sharing certain morphological characteristics, and is still widely used in the present day. The two primary galaxy types comprising the tuning fork are ellipticals, typically red in colour and showing little structure, and spirals, which are further subcategorised according to the presence or absence of bars, and the tightness of their spiral arms. As photometry was developed, it became possible to measure quantitatively the light profiles of galaxies in the local Universe. This led to the elucidation of the de Vaucouleurs profile (de Vaucouleurs, 1948) describing the light distribution within massive ellipticals, and the Sérsic profile (Sérsic, 1963) which is a more general formalism.

The Hubble Deep Fields (Williams et al., 1996) and subsequent even deeper imaging campaigns, such as the Great Observatories Origins Deep Survey (GOODS: Giavalisco et al., 2004), the Hubble Ultra Deep Field (Beckwith et al., 2006) and the Cosmic Evolution Survey (COSMOS: Scoville et al., 2007), were revolution-

ary to galaxy formation research, and provided a wealth of morphological targets. This was complemented by the detection of a significant population of high-redshift galaxies through the Lyman Break technique (Steidel and Hamilton, 1993), which identifies galaxies as high-redshift if they are seen to drop out of filters bluewards of the Lyman continuum discontinuity at 912Å (Giavalisco, 2002).

However, at $z \gtrsim 3$, it becomes challenging to study morphology with HST, as the rest frame optical is redshifted beyond the wavelength range of WFC3, and rest frame UV light must be used instead. The rest-UV traces young stars, and so is expected to be biased towards the location of actively star forming regions. Moreover, dust extinction is $\sim 2-5\times$ higher at rest-frame 1500Å compared to 5000Å, depending on the attenuation law (e.g. Salim and Narayanan, 2020). Rest-optical light is therefore considered more reliable for morphological measurements, as it is expected to be a better tracer of the stellar mass. Comparative studies of morphological properties as measured in the rest-optical and rest-UV have been performed by e.g. Rawat et al. (2009), who found that rest-UV measurements yield higher ellipticities, and lower Sérsic indices which could lead to an overestimation of the merger fraction. A similar study by Bond et al. (2011) found that the morphological differences between the two tracers are small, though more significant for star forming than passive galaxies. At $z \gtrsim 7$ HST has only far-UV coverage, and can only marginally resolve the typically compact galaxies present in this epoch without lensing (e.g. Grazian et al., 2012). In the context of these historical limitations, the improved angular resolution and wider wavelength coverage provided by JWST has been transformative. HST's F160W band can probe rest-optical light to $z \sim 2.8$, while JWST's F444W band is capable of these measurements at $z \sim 9$, revealing the rest-optical view of Epoch of Reionization galaxies and extending the timeline over which we can probe the evolution of morphological properties.

3.1.1 The Evolution of Morphology and Structure across Cosmic Time

With HST observations, the Hubble sequence is seen to be in place out to $z \sim 1$, with the majority of the galaxy population being classical ellipticals and spirals below this redshift (e.g. Glazebrook et al., 1995; Ravindranath et al., 2004), and

above, the frequency of irregular and interacting galaxies increases (e.g. Lee et al., 2013), with peculiar galaxies becoming more common than spirals and ellipticals at $z \sim 1.5$.

With JWST, we obtain a starkly different picture of how high-redshift galaxies are structured. Ferreira et al. (2022) re-examine galaxies previously observed with HST in the SMACS 0723 cluster field, and find that galaxies at $z > 3$ are smoother and more symmetrical than they appeared in HST imaging, with disks comprising $\sim 50\%$ of the sample at $z \sim 3-6$, a tenfold increase. Similar results are obtained by Jacobs et al. (2023) from a sample of $0.8 < z < 5.4$ galaxies, finding that the population is more irregular than local galaxies, but less clumpy and asymmetrical than HST rest-UV. Ferreira et al. (2023) extend this work, performing visual classification on a sample of 3956 CEERS/CANDELS galaxies at $1.5 < z < 6.5$ and find that the Hubble sequence is already in place, to some extent, at $z \sim 6$. They identify disk galaxies as dominating the low and high sSFR populations, contributing the majority of total galaxy stellar mass at $z < 4$, suggesting that most stars were formed in a disk or peculiar galaxy. Quantitative support for this interpretation is provided by Ormerod et al. (2024), who fit a Sérsic profile to each source from a sample of massive galaxies ($\log(M_*/M_\odot) > 9.5$ at $0.5 < z < 8$, finding that Sérsic indices decrease with increasing redshift, while SFGs typically maintain $n = 1$. However, despite the difference in galaxy population statistics inferred from JWST and HST imaging, Treu et al. (2023) find that the morphologies of their sample of 19 LBGs at $z > 7$ do not change significantly as a function of wavelength, such that they would be similarly classified in both rest-UV and rest-optical.

The new frontier of imaging in the Epoch of Reionization furthermore provides the opportunity for rest-UV and rest-optical morphologies to be compared to morphologies from emission lines and dust in the earliest galaxies (e.g. Zanella et al., 2024; Posses et al., 2025). This is the major focus of the following chapter.

3.2 Sample Selection

The 10 galaxies analysed in this work represent the first sample of galaxies where we can study resolved dust-obscured star formation, along with cool gas ([CII])

kinematics in the EoR. The REBELS-HR sample includes one optically dark 'ALMA only' galaxy, but is otherwise comprised of some of the most luminous cold gas and dust reservoirs from the REBELS ALMA large survey (and pilot programs) of UV-bright Lyman break galaxies, representing typical main sequence galaxies just above the z∼7 stellar mass function knee, with SFR 50−100 $M_{\odot}$/yr. In this section we introduce the criteria under which the sample was selected.

3.2.1 The Reionization Era Bright Emission Line Survey (REBELS)

The effectiveness of spectral scanning to detect the [CII] line in luminous galaxies with well constrained photometric redshifts was demonstrated in Smit et al. (2018).

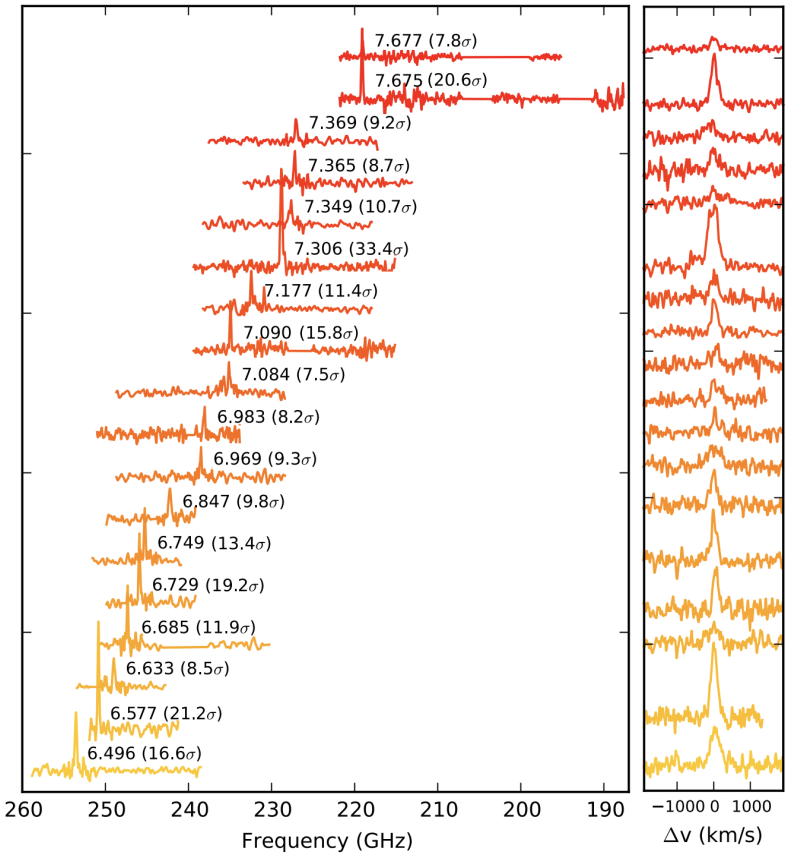

Figure 3.1: This plot shows the [CII] emission lines detected across the REBELS galaxies through spectral scanning, from which their redshifts were spectroscopically confirmed. Figure credit: Bouwens et al. (2022)

Previously, ALMA had discovered only a relatively small number of [CII] emitters

above $z \sim 6$, and even where [CII] emission was observed, it was generally faint. The method of spectral scanning targeted at UV-bright sources has yielded some of the brightest [CII] emitters in the Epoch of Reionization, with Smit et al. (2018) and Schouws et al. (2022) acting as successful pilots motivating the Reionization Era Bright Emission Line Survey (REBELS), a large ALMA programme which extends the technique to higher redshifts and a greater number of targets (Bouwens et al., 2022, : see Figure 3.1). The REBELS LP searched for [CII] emission in 40 UV bright galaxies selected from deep, wide-area optical and near-IR observation fields from ground-based telescopes, covering an area of seven square degrees - particularly the 2 deg^2 COSMOS/UltraVISTA field (Scoville et al., 2007; McCracken et al., 2012).

The sample was built from catalogues of these search fields; full details of how the 40 galaxies that make up the REBELS sample were selected are provided in the survey paper, Bouwens et al. (2022). To summarise, a compilation was created of galaxies photometrically identified as high-redshift candidates across multiple surveys (Bowler et al., 2014; Bowler et al., 2017; Bowler et al., 2020; Stefanon et al., 2017; Stefanon et al., 2019; Stefanon et al., 2022; Endsley et al., 2021; Schouws et al., 2023). The optical, near-IR and Spitzer/IRAC fluxes of these galaxies were then measured independently by three different members of the REBELS team using three different photometric procedures, and redshift likelihood distributions were measured using three different fitting codes. A fourth team member re-derived a redshift likelihood distribution for each of the three photometric sets, using different SED templates, resulting in six different realisations of the redshift likelihood distribution for each source from which the mean was taken to provide a maximally robust photometric redshift estimate. The likelihood of observing an ISM-cooling line in each galaxy was calculated using an $\mathrm{SFR_{UV}/L_{[CII]}}$ conversion factor of $2 \times 10^7 L_\odot/(M_\odot yr^{-1})$ (De Looze et al., 2014). The sources were then ranked by this probability, from which the final sample was chosen, consisting of 20 galaxies at $6.5 < z < 7.2$, 16 galaxies at $7.2 < z < 8.5$ and 4 galaxies at $7.8 < z < 9.4$ to ensure sufficient redshift coverage for luminous ISM reservoirs to be studied as a function of z. Appendix B of Bouwens et al. (2022) provides information on the distribution of the REBELS sample in parameter space. The median stellar mass was derived as $M_* = 10^{9.25-9.8} M_\odot$, between 0.4dex lower and 0.1dex higher than the ALPINE

survey (Le Fèvre et al., 2020). The median UV-continuum slope, $\beta = -1.98$, consistent with other measurements at $z \sim 7$ (-1.98 $\pm$ 0.07 in Bowler et al., 2017). The median EW([OIII]+Hβ is 638 Å, consistent with the median EW of 759^{+112}_{-113} measured at $z \sim 6.75$ by Endsley et al. (2021). In light of these consistent properties in common with other $z \sim 7$ galaxy surveys, the UV-bright LBGs comprising the REBELS sample may be considered representative of the typical galaxy population at the bright end of the UV luminosity function.

Of the 40 galaxies in the LBG sample, 25 were detected in [CII], and an additional three companion galaxies were serendipitously detected (REBELS-12-2, REBELS-29-2 and REBELS-39-2). To these [CII] detections we add 5 pilot galaxies to reach 33 positive [CII] detections from the full REBELS sample. The non-detected galaxies may be faint in [CII], or their emission may be out of redshift range of the spectral scan. Of these, 18 are also detected in dust continuum (Inami et al., 2022).

Study of the REBELS galaxies has provided a wealth of information on galactic structure, evolutionary processes, and dust build up in the Epoch of Reionization. The survey now benefits from extensive follow-up observations with JWST across many sources, as well as multiple ALMA programmes targeting other spectral lines or achieving higher resolution observations of particularly interesting targets, the focus of this chapter.

3.2.2 REBELS High Resolution Sample (REBELS-HR)

The REBELS high resolution sample (REBELS-HR) consists of 10 galaxies at redshifts between $6.5 < z < 7.7$ selected from the REBELS sample and its pilots. We here note that although REBELS-25 is part of the REBELS-HR sample, and is included in discussion and analysis covering the full sample, we do not perform a detailed individual analysis of its morphology and kinematics in this work as we do for the other nine REBELS-HR galaxies as it is already the focus of such a study, presented in Rowland et al. (2024).

Of the ten REBELS-HR galaxies, three are REBELS pilots and were the most luminous [C II] emitters at the time of their publication: REBELS-P6 (COS-2987: Smit et al. (2018)), REBELS-P7 (UVISTA-Z-019: Schouws et al. (2023)) and REBELS-

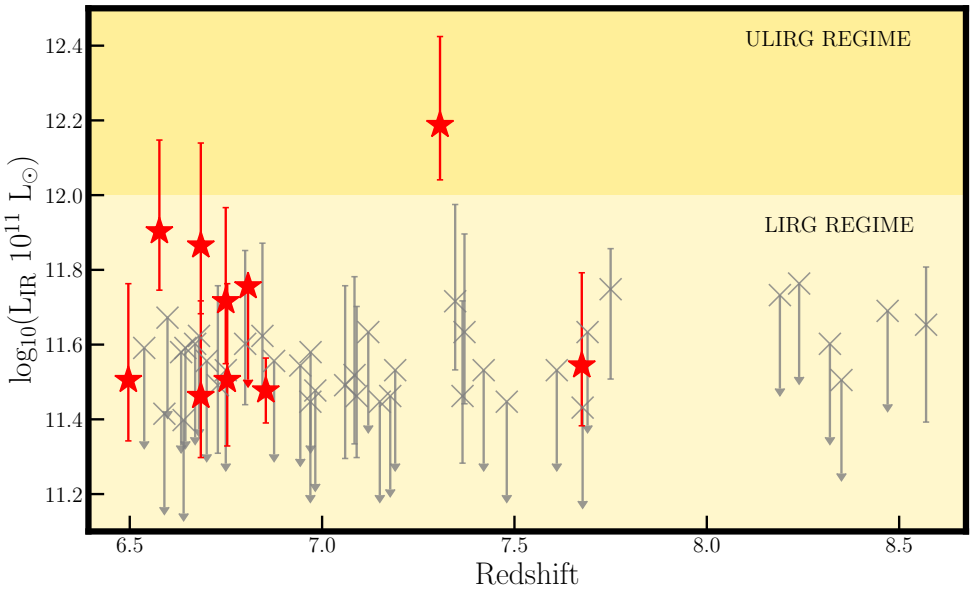

Figure 3.2: Infrared luminosity of the REBELS-HR galaxies (red stars) in comparison to the rest of the REBELS sample (grey crosses), with shading distinguishing the regions of parameter space representing 'Luminous Infrared Galaxies' (LIRGs) and 'Ultra-Luminous Infrared Galaxies' (ULIRGs).

P8 (COS-3018: Smit et al. (2018)). The galaxies comprising the rest of the sample were selected for follow up observations as some of the most luminous [C II] emitters in the REBELS sample, while REBELS-29 was of a lower [C II] luminosity but could be efficiently targeted with REBELS-29-2 in a single primary beam (Fudamoto et al., 2021). Within the REBELS sample the most [C II]-luminous sources are typically also dusty, such that their total SFR scales well with $L_{\rm CII}$ (Bouwens et al., 2022). Figure 3.2 shows the infrared luminosity of the REBELS-HR galaxies alongside the rest of the REBELS sample. All would be classified as Luminous Infrared Galaxies (LIRGs) but only one, REBELS-25, is an Ultra-Luminous Infrared Galaxy (ULIRG). The target selection properties of the REBELS-HR galaxies - namely, their photometric redshifts, co-ordinates, and UV luminosities, are listed in Table 3.1 along with references to publications in which they are analysed.

Figure 3.3 shows the luminosity of these galaxies in [CII]. REBELS-38 is the brightest [CII] emitter from the sample, at $L_{\rm CII} = 1.70^{0.16}_{0.15} \times 10^9 L_\odot$, closely followed by REBELS-25.

The pilots COS-2987 and COS-3018 are among the faintest in [CII] from the REBELS

Table 3.1: Target selection information for the REBELS-HR sample.

REBELS ID	ALMA Source ID	RA	Dec	z_{phot}	M_{UV}	References
REBELS-05	XMM1-1591	02:18:11.51	-05:00:59.3	$6.68^{+0.18}_{-0.17}$	-21.6 ± 0.2	1, 7, 8, 12, 13, 14
REBELS-08	XMM1-67420	02:19:35.13	-05:23:19.2	$6.71^{+0.13}_{-0.10}$	-21.8 ± 0.4	5, 7, 12, 13, 14
REBELS-18	UVISTA-Y-001	09:57:47.90	02:20:43.7	$8.20^{+0.63}_{-0.37}$	-22.5 ± 0.1	2, 4, 7, 8, 12, 13, 14
REBELS-25	UVISTA-Y-003	10:00:32.32	01:44:31.3	$7.40^{+0.22}_{-0.19}$	-21.7 ± 0.2	2, 4, 7, 12, 13, 14
REBELS-29	UVISTA-Z-004	10:01:36.85	02:37:49.1	$6.82^{+0.13}_{-0.11}$	-22.3 ± 0.1	1, 5, 6, 7, 8, 12, 13, 14
REBELS-29-2	UVISTA-Z-004	10:01:36.93	02:37:56.4	$6.82^{+0.13}_{-0.11}$	···	6
REBELS-38	UVISTA-Z-349	10:02:54.05	02:42:12.0	$6.67^{+0.16}_{-0.10}$	-21.9 ± 0.2	5, 7, 8, 12, 13, 14
REBELS-P6	COS-2987030247	10:00:29.86	02:13:02.19	$6.66^{+0.14}_{-0.14}$	-24.3 ± 0.1	3, 8, 10
REBELS-P7	UVISTA-Z-019	10:00:29.89	01:46:46.4	$6.80^{+0.05}_{-0.06}$	-24.0 ± 0.2	8, 9, 10
REBELS-P8	COS-3018555981	10:00:30.19	02:15:59.8	$6.76^{+0.07}_{-0.07}$	-24.2 ± 0.1	3, 8, 10

[1] Bowler et al. (2014), [2] Stefanon et al. (2017), [3] Smit et al. (2018), [4] Stefanon et al. (2019), [5] Endsley et al. (2021), [6] Fudamoto et al. (2021), [7] Bouwens et al. (2022), [8] Inami et al. (2022), [9] Schouws et al. (2022), [10] Witstok et al. (2022), [11] Rowland et al. (2024), [12] Algera et al. (2025), [13] Fisher et al. (2025), [14] Rowland et al. (2025)

Table 3.2: Physical properties of the REBELS-HR sample.

REBELS ID	z_{spec}	$L_{[CII]}$ $[10^8 L_\odot]$	L_{IR} $[10^{11} L_\odot]$	$\log(M_*/M_\odot)$	SFR_{UV+IR} $[M_\odot yr^{-1}]$	f_{obs}
REBELS-05	6.4963	$6.9^{+0.8}_{-0.9}$ [a]	$3.2^{+1.9}_{-1.2}$ [d]	$9.42^{+0.1}_{-0.1}$ [a]	52^{+22}_{-15} [d]	0.77 ± 0.22 [e]
REBELS-08	6.7495	$7.4^{+1.1}_{-1.1}$ [a]	5.2^{+3}_{-2} [d]	$9.33^{+0.07}_{-0.06}$ [a]	79^{+37}_{-25} [d]	0.80 ± 0.34 [e]
REBELS-18	7.6750	$10.7^{+0.8}_{-0.9}$ [a]	$3.5^{+2}_{-1.3}$ [d]	$9.71^{+0.06}_{-0.04}$ [a]	69^{+24}_{-16} [d]	0.66 ± 0.15 [e]
REBELS-25	7.3065	$15.9^{+1.1}_{-1.1}$ [a]	$15.4^{+8.4}_{-5.2}$ [d]	$9.3^{+0.12}_{-0.14}$ [a]	199^{+101}_{-63} [d]	0.93 ± 0.21 [e]
REBELS-29	6.6847	$4.86^{+0.64}_{-0.64}$ [b]	$2.21^{+1.85}_{-1.01}$ [b]	$9.69^{+0.07}_{-0.05}$ [a]	59^{+20}_{-14} [d]	0.61 ± 0.16 [e]
REBELS-29-2	6.6813	$8.56^{+1.13}_{-1.13}$ [b]	$7.33^{+4.63}_{-3.08}$ [b]	< 10.4 [b]	< 76.3 [b]	> 0.97 [f]
REBELS-38	6.5770	$17.0^{+1.6}_{-1.6}$ [a]	$8.0^{+4.5}_{-2.9}$ [d]	$9.75^{+0.09}_{-0.06}$ [a]	114^{+54}_{-35} [d]	0.86 ± 0.23 [e]
COS-2987	6.8075	$2.83^{+0.69}_{-0.69}$ [c]	≤ 2.1 [c]	$9.23^{+0.1}_{-0.05}$ [c]	<84 [d]	> 0.37 [c]
UVISTA-Z-019	6.7534	$7.69^{+0.55}_{-0.55}$ [c]	$3.1^{+18.1}_{-1.8}$ [c]	$9.5^{+0.2}_{-0.2}$ [c]	52^{+23}_{-16} [d]	0.74 ± 0.22 [e]
COS-3018	6.8537	$3.97^{+0.31}_{-0.31}$ [c]	$0.99^{+0.68}_{-0.23}$ [c]	$9.1^{+0.2}_{-0.1}$ [c]	< 94 [d]	$0.31^{+0.52}_{-0.04}$ [c]

[a] Algera et al. (2025), [b] Fudamoto et al. (2021), [c] Witstok et al. (2022), [d] Inami et al. (2022), [e] Bowler et al. (2024), [f] Fudamoto et al. (2021)

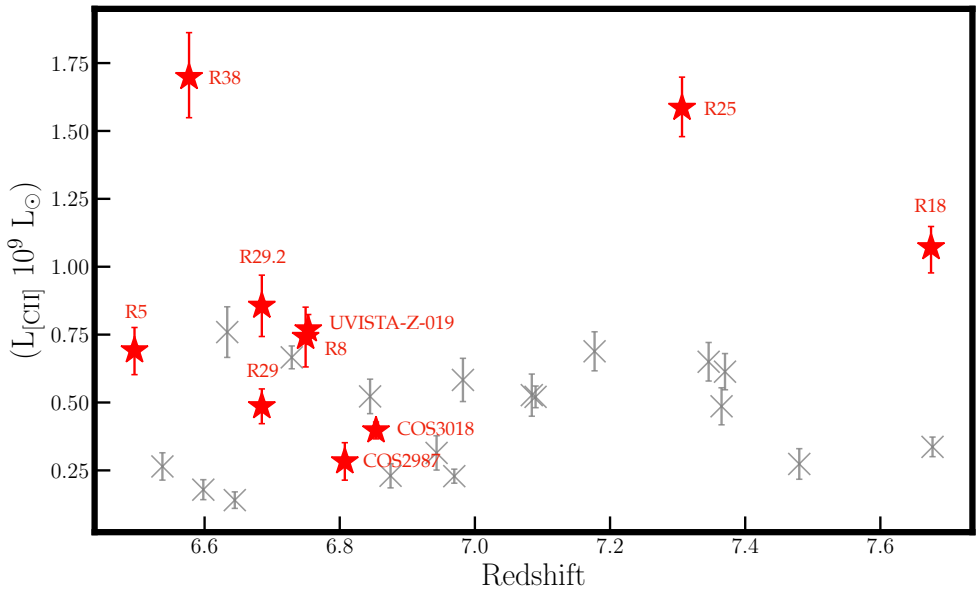

Figure 3.3: $L_{\rm CII}$ for the REBELS-HR galaxies (red stars) in comparison to the rest of the sample (grey crosses). The REBELS-HR galaxies are generally more luminous in CII than the rest of the sample, excepting the pilots and REBELS-29, due to the selection criteria for the HR sample.

sample, which demonstrates the extraordinary success of the REBELS programme in identifying [CII]-luminous galaxies at $z > 6$, as these pilots were the brightest [CII] lines found in optical/near-IR selected galaxies from the EoR at the time of their discovery (Smit et al., 2018). Smit et al. found that these two galaxies, selected as [OIII] + Hβ emitters to place an extra constraint on the redshift probability distribution, were consistent with the local SFR-$L_{[\rm CII]}$ relation, in contrast to similar observations of Lyα selected [CII] emitters that placed their sources significantly below it (e.g. Ouchi et al., 2013; Pentericci et al., 2016).

The REBELS galaxies and the high resolution subset REBELS-HR, despite their brightness in [CII], are still representative of normal star forming galaxies in the Epoch of Reionization, as is apparent from Figure 3.4 where the galaxies are placed on the star forming main sequence according to Santini et al. (2017) and are seen to be consistent.

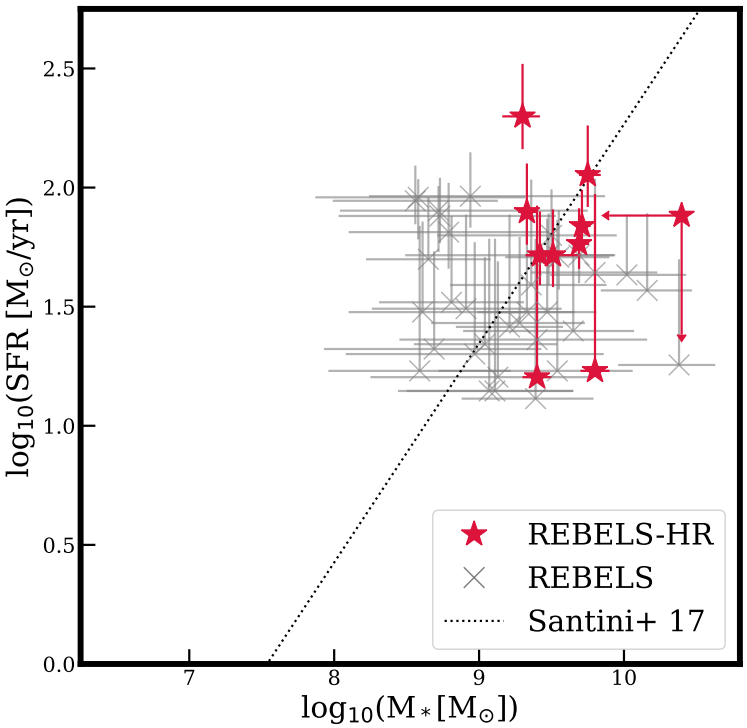

Figure 3.4: The REBELS and REBELS-HR galaxies are here placed on the star-forming main sequence, represented by the dotted line (Santini et al., 2017). We see that the REBELS galaxies, including the high resolution sample, are consistent with the star-forming main sequence and may be considered 'normal star forming galaxies'.

3.3 Data

The [CII] observations of the REBELS-HR sample are of uniquely high resolution for the redshift range, improving even on that achieved by the CRISTAL survey (Herrera-Camus et al., 2025) which similarly consists of high-resolution follow-up of galaxies from the ALMA Large Program to INvestigate [CII] at Early times (ALPINE) LP (Le Fèvre et al., 2020) at $4 < z < 6$. In addition to the [CII] observations, each member of the REBELS-HR sample, bar COS-2987, has been detected in the dust continuum. The sample furthermore benefits from NIRSpec and NIRCam coverage.

This section describes the conditions under which the observations were taken.

3.3.1 ALMA Data

A summary of the ALMA observations considered in this work is provided in Table 3.3. All galaxies were observed in Band 6. The angular resolution ranges from 0.1″ (REBELS-25) to 0.4″ (REBELS-38) and the observing conditions were generally favourable, with the average precipitable water vapour (PWV) being within the range of 0.4mm (REBELS-25) to 2.3mm (REBELS-18). The characteristic resolution in kpc of the observations is shown in comparison to the general REBELS sample, and lower-redshift galaxy kinematics surveys in Figure 3.5.

3.3.2 JWST Data

REBELS-5, REBELS-8, REBELS-25, REBELS-29 and REBELS-38 have been observed by the NIRSpec IFU in PRISM mode as part of the program 1626 (PI: Mauro Stefanon) with an exposure time of 1750.668 seconds, and REBELS-18 as part of the program 2659 (PI: John Weaver) with an exposure time of 5952.268s.

The program 6480 (PI: Sander Schouws) has obtained NIRCam imaging in multiple filters for REBELS-8, REBELS-18, REBELS-29 (inc. REBELS-29-2), REBELS-38, and UVISTA-Z-019. Each galaxy is observed in four filters between F070W-F444W, with an exposure time of 1245.464s in the bluest filter, and 773.046s in the reddest filter. COS-2987 and COS-3018 have NIRCam imaging in filters between F090W and F444W from the Public Release IMaging for Extragalactic Research survey

Table 3.3: ALMA observation details for the REBELS-HR sample. We show the bin width in MHz of the processed datacube and the beam size corresponding to the weighting scheme employed. We also show key details of the observing strategy, including the integration time, baseline length range, average angular resolution, average precipitable water vapour, and the codes of the projects from which the data originate. The Principal Investigators of the programmes are listed in the footnote.

REBELS ID	$\Delta\nu_{\rm obs}$ [MHz]	Weighting: $A_{\rm beam}$ [arcsec^2]	Int. Time [s]	Baseline [m]	Ang. Res. [arcsec]	PWV [mm]	Project Codes
REBELS-05	12	Natural: 0.35 × 0.28	14515.200	15.1-2100	0.2	1.2	2022.1.01131.S[a]
REBELS-08	12	Natural: 0.36 × 0.31	12852.000	15.1-1400	0.2	1.4	2022.1.01131.S[a]
REBELS-18	4	Natural: 0.4 × 0.39	13305.600	15.3-1400	0.3	2.3	2022.1.01131.S[a]
REBELS-25	11.7	Natural: 0.14 × 0.13	15603.840	41.3-3600	0.1	0.4	2021.1.01603.S[b]
REBELS-29	8	Natural: 0.27 × 0.26	33747.839	15.3-2500	0.2	1.2	2022.1.01131.S[a]
REBELS-29-2	15.625	Briggs(0.8): 0.22 × 0.2	33747.839	15.3-2500	0.2	1.2	2022.1.01131.S[a]
REBELS-38	15.625	Natural: 0.58 × 0.49	4475.520	15.3-740.7	0.4	0.95	2022.1.01131.S[a]
COS-2987	Combined 24	Combined Natural: 0.35 × 0.28	10402.56 25855.2	15.1-1397.8 15.1-2517.3	0.3 0.18	0.85 0.9	2018.1.01359.S[c] 2021.1.01159.S[d]
UVISTA-Z-019	12	Natural: 0.39 × 0.35	14364.000	15.0-1400	0.25	1.8	2019.1.01611.S[a]
COS-3018	23.4	Briggs(0.8): 0.35 × 0.29	45964.799	15.1-1400	0.3	1.2	2017.1.00604.S[a]

[a] Renske Smit, [b] Jacqueline Hodge, [c] Manuel Aravena, [d] Ana Nascimento

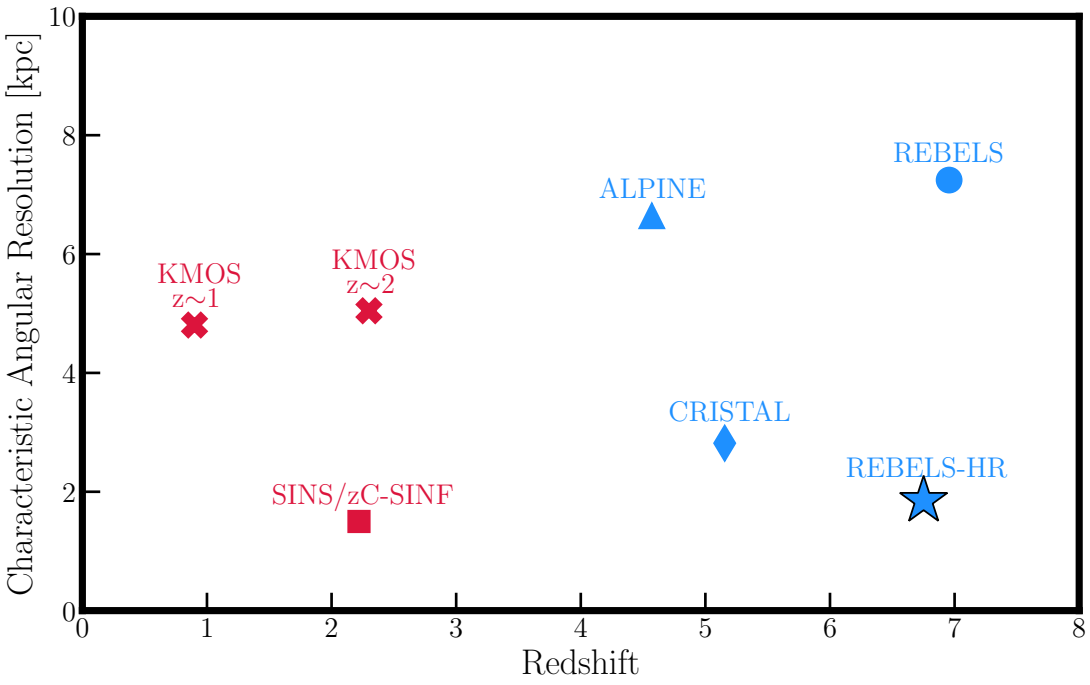

Figure 3.5: The REBELS-HR sample is here placed in context with other galaxy kinematic surveys to show the typical angular resolution achievable across redshifts. Warm gas (Hα, [OIII]) surveys are plotted in red (KMOS: Wisnioski et al. (2015) and Wisnioski et al. (2019) and SINS/zC-SINF: Förster Schreiber et al. (2009)), and cold gas ([CII]) surveys in blue (ALPINE: Le Fèvre et al. (2020), CRISTAL: Herrera-Camus et al. (2025), REBELS: Bouwens et al. (2022).

(PRIMER: PI James Dunlop).

3.3.3 ALMA Data Reduction with CASA

We reduce our ALMA data using the Common Astronomy Software Application (CASA) (McMullin et al., 2007), version 6.5.4. In this section we detail the process of data reduction, and justify decisions made where relevant. The flowchart in Figure 3.6 illustrates a basic overview of the data reduction steps set out below.

Telescope data are calibrated via an automated calibration pipeline, and subjected to a rigorous quality assurance testing procedure. The first stage (QA0) considers observational metadata at the Execution Block level. Data are then processed through a basic calibration and imaging pipeline, and checked for array and antenna performance parameters. Data meeting the frequency and spatial set-up, angular

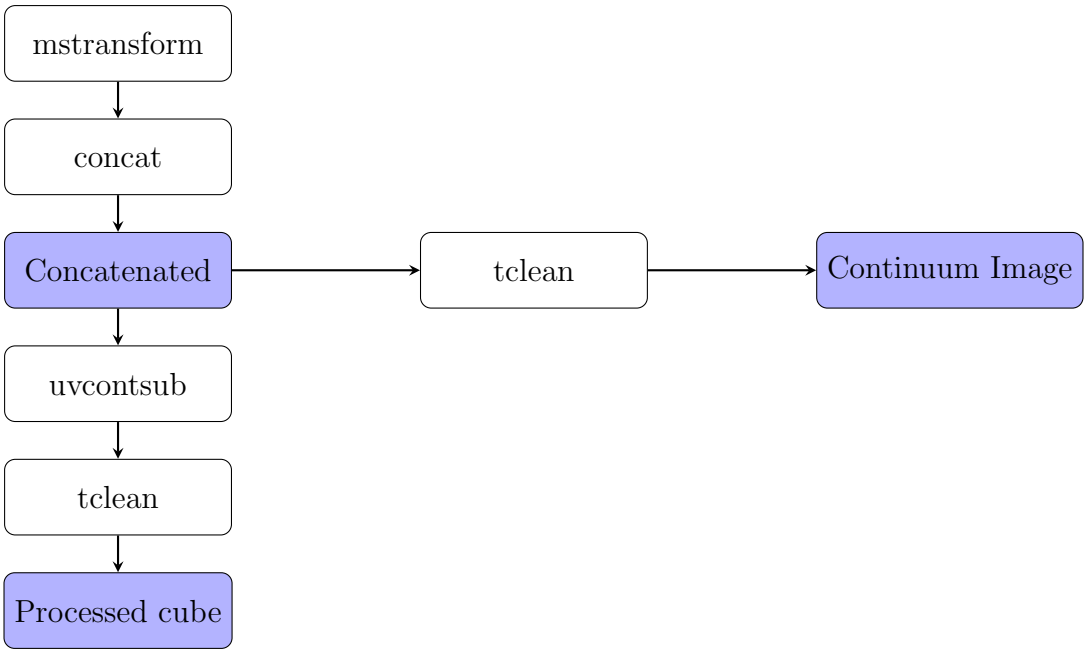

Figure 3.6: Simplified flowchart showing the steps involved in our data reduction procedure.

resolution, and sensitivity requirements of the science goal are marked as 'QA2-pass' and delivered to the PI as science-ready.

We download the QA2 package from the ALMA Science Archive[1] and run `scriptForPI.py` to recover the data in the form of calibrated measurement sets (.ms files). We isolate the science target from the calibrators using the task `mstransform`, by specifying the science field ID. We additionally limit the `datacolumn` parameter to 'corrected' to exclude uncalibrated data.

We then combine the science measurement sets into a single .ms file using `concat`. We do not set `freqtol`, a parameter determining the interval of tolerance in frequency space for data to be considered as belonging to the same SPW ID, as some frequency shift is expected due to the rotation of the Earth, nor `dirtol`, the direction shift tolerance for data to be associated with a common field, as this is not necessary for our data.

At this point, a continuum image can be created using the `tclean` routine (see our discussion of the cleaning procedure in Section 3.3.3.1), or the data can be continuum-subtracted using the `uvcontsub` task and then cleaned to produce a spectral line datacube, consisting of two spatial axes and one spectral axis. To run

[1] https://almascience.nrao.edu/aq/

`uvcontsub`, we exclude a full SPW covering the spectral line, and fit the continuum in the remaining SPWs. We have control over the order of the polynomial fitted to the continuum, using zeroth order as default and thereby fitting a constant to the continuum which is then subtracted from the data. The product of this task is a continuum-subtracted cube which is then used for imaging the line emission.

3.3.3.1 Data cleaning

The `tclean` task within CASA forms images from visibilities in the so-called UV-plane (Fourier space). It is based on the 'CLEAN' algorithm (Högbom, 1974) which represents the radio sky as a limited number of point sources in an otherwise blank field of view, and then iteratively determines the positions and strengths of the point sources.

There are a number of parameters within `tclean` that can be set to customise the cleaning process, as detailed in the following.

`specmode` is the parameter controlling the spectral definition mode. We set this to 'mfs', or 'multi-frequency synthesis', for continuum imaging, and 'cube' for spectral line imaging.

The size of each pixel in physical units is controlled by `cell`, which we set such that the FWHM of the beam is sampled by 5-8 pixels.

The parameter `weighting` controls how signals from different baselines are incorporated, and is tuned through the `robust` parameter, which can vary between 2 (natural weighting) and -2 (uniform weighting). Natural weighting makes no adjustment for the distribution of antennae, and as shorter baselines are more densely sampled than longer baselines, this results in a stronger weighting towards shorter baselines and consequently a poorer spatial resolution. Uniform resolution gives equal weight to all parts of the UV-plane irrespective of the sampling. This improves angular resolution, but also decreases SNR as the less well-sampled outer edge of the UV-plane is noisier. Briggs weighting (Briggs, 1995) offers a compromise through tuning of the `robust` parameter; decreasing the value of `robust` upweights outer antennae to compensate for the lower density of signal in this region. Setting the `robust` parameter therefore becomes a matter of finding a compromise between sensitivity and spatial resolution on a case-by-case basis. We prioritise SNR and

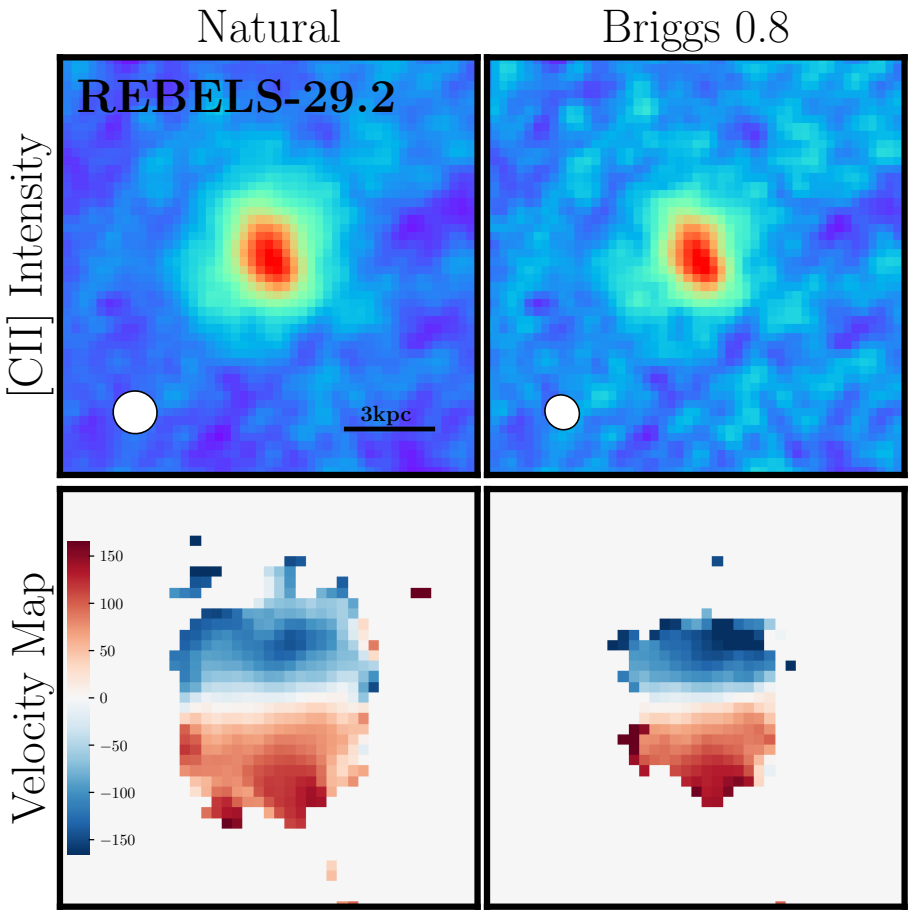

Figure 3.7: A comparison of REBELS-29-2 intensity and velocity maps under different weighting schemes: natural weighting, which gives equal weight to all baselines, and Briggs-0.8 weighting, which gives some upweighting to longer baselines.

employ natural weighting for the majority of our galaxies, but use a Briggs 0.8 weighting scheme for two of our galaxies, REBELS-29-2, for which the SNR is sufficiently high to permit the increase in spatial resolution, and COS-3018, for which we prioritise spatial resolution due to its clumpy internal structure. We show in Figure 3.7 the effect of different weighting scheme on the intensity and velocity maps of REBELS-29-2.

The `gridder` parameter is used to select the gridding convolution model used to resample visibilities onto a regular UV-grid, which will then have an inverse fast Fourier transform (FFT) applied to it. We use standard gridding, which is a prolate spheroid convolution function.

We use the `tclean` routine without any cleaning cycles to create dirty images of the continuum and the spectral line. Fourier transforming sampled visibilities directly from the UV-plane yields the true sky brightness convolved with the point spread function, or dirty beam, which has the form of a Gaussian with sidelobes. To extract the true image, we must clean the data. We first perform deconvolution to create a dirty image which will be contaminated by artefacts from the dirty beam. The `deconvolver` parameter controls the minor cycle algorithm that produces output models and restored images from residual images and PSFs. We use the `hogbom` deconvolver, which is adapted from the algorithm introduced in Högbom (1974). We identify a region on the dirty image containing clean components, and define a mask around it. Performing cleaning cycles will then convolve the clean components with the dirty beam, and subtract these from the data. This process is repeated on the residuals until the side lobes are lower than a certain noise level, which is set by the user with the parameter `threshold`. We set this threshold at $3\times$ RMS, where RMS is the root mean square of the dirty image. The sky brightness map recreated in this manner is then convolved with the clean beam; this is a Gaussian model that has been fitted to the main component of the dirty beam. The product of this convolution step is the final, clean image.

For most of the galaxies in the sample, we choose to use the high-resolution data exclusively, but we additionally test the effect of combining the lower and higher resolution ALMA observations. For COS-2987 we combine higher and lower resolution data from two observing projects. Figure 3.8 shows a comparison between

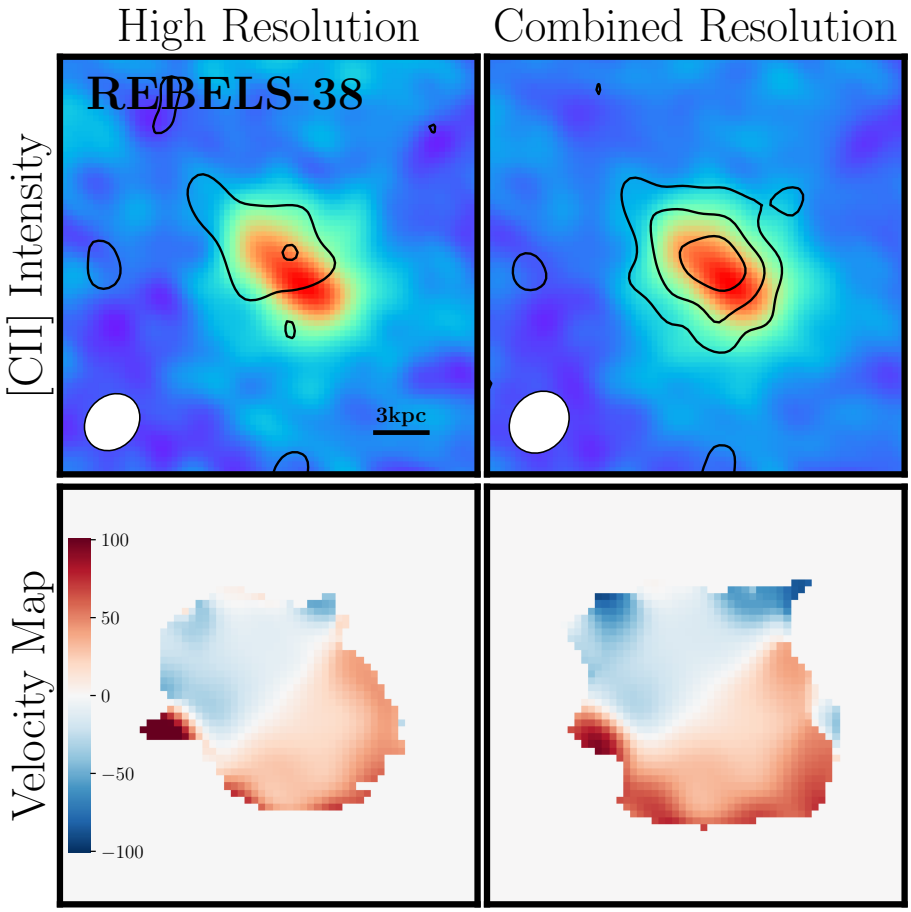

Figure 3.8: A comparison of REBELS-38 intensity and velocity maps with only the high-resolution data, and with the high and low resolution data combined. Black contours on the intensity maps represent the dust.

the high resolution (2022.1.01131.S) and the combined high and low resolution (2022.1.01131.S + 2019.1.01634.L) observations for REBELS-38. We see that the [CII] emission is similar between the two, but the dust (black contours) is significantly better sampled when the low resolution observations are included, as the lower resolution programme involved spectral scanning over a frequency range either side of the emission line, including more of the dust continuum emission.

3.3.4 Astrometry with Gaia

We perform astrometric corrections on the NIRCam and NIRSpec imaging available for our targets to ensure that we can accurately compare the co-spatiality of our separate emission components. We describe the process in the following.

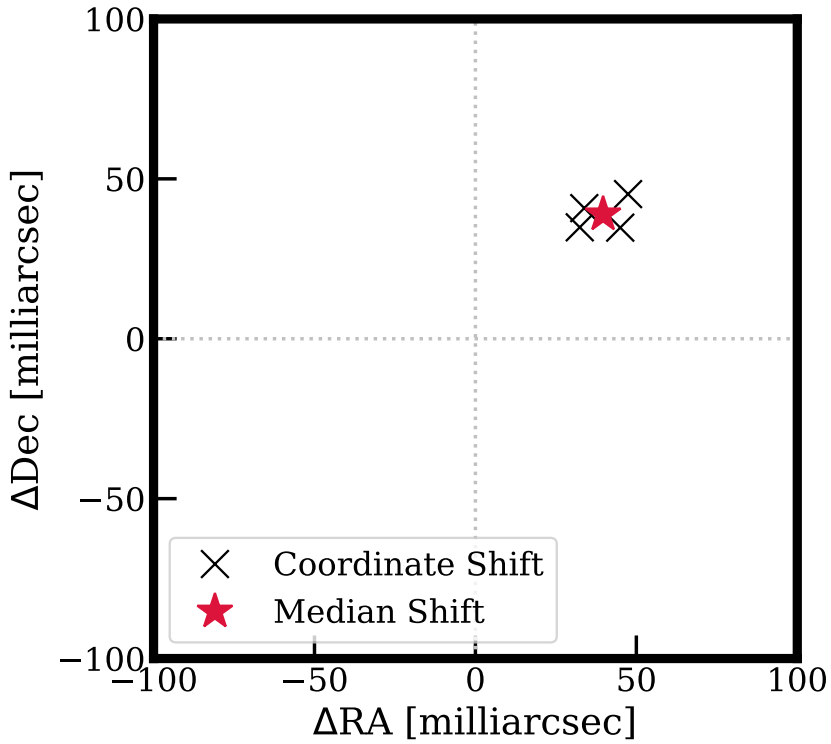

Figure 3.9: The co-ordinate shift between the centres of Gaia stars according to a 2D Gaussian fit, and their co-ordinates from Gaia DR2 corrected for proper motion (black crosses), with the median co-ordinate shift illustrated by a red star.

3.3.4.1 NIRCam Astrometric Corrections

For each galaxy covered by NIRCam observations, we perform co-ordinate matching within `ds9` (Smithsonian Astrophysical Observatory, 2000) to identify all stars from the Gaia DR2 catalogue (Gaia Collaboration et al., 2018) occurring in the field. We record the co-ordinates of these stars at the time of their observation, along with their proper motions, and use the proper motion information alongside the time elapsed between the Gaia and NIRCam observations to calculate the coordinates of the stars on the sky at the time of the NIRCam observations.

We visually examine each star to exclude any that are oversaturated, or have a close companion, so that the set of astrometric stars for each galaxy consists only of point sources. We fit 2D Gaussian profiles to these point sources, and extract the central co-ordinates of these fitted models. The difference between the fitted co-ordinates and the proper-motion corrected Gaia co-ordinates provides the astrometric correction. We find the median astrometric correction taking into account

all available stars, which is less biased by any outliers than the mean. The median co-ordinate shift is applied to the NIRCam imaging, an example of which is shown for REBELS-29 in Figure 3.9.

3.3.4.2 NIRSpec Astrometric Corrections

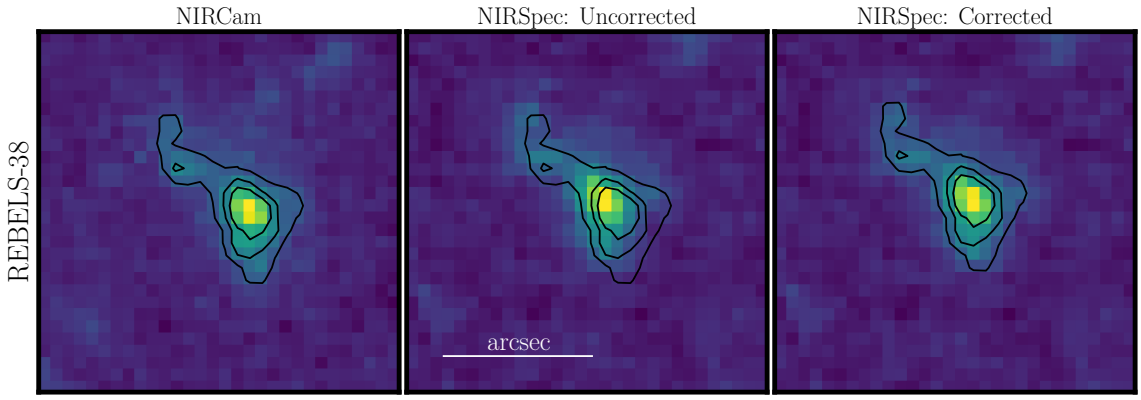

Figure 3.10: NIRCam F444W imaging shown with its associated contours (left), overplotted on the NIRSpec PRISM datacube collapsed over the F444W wavelength range prior to (centre) and following (right) astrometric correction.

To verify the astrometry of the NIRSpec IFU, we compare the NIRCam F444W imaging, following the application of the correction detailed in the previous section, to the NIRSpec PRISM datacube collapsed over the wavelength range covered by the F444W filter. We do not apply a convolution to the NIRCam image as the PSFs are similar between the NIRSpec imaging and the F444W filter. We overplot the contours from the F444W image on the collapsed NIRSpec image, and apply a co-ordinate shift to match the underlying emission to the contours. This shift defines the astrometric correction, as shown for REBELS-38 in Figure 3.10.

3.4 Morphological Fitting

For each galaxy, we derive and compare morphologies and physical properties as measured by each available tracer.

We create and fit integrated spectra from the [CII] line emission to obtain measurements of the spectral line FWHM and integrated line flux, among other mea-

Table 3.4: Galaxy [CII] and Continuum Flux Measurements for the REBELS-HR sample excluding REBELS-25.

REBELS ID	ν [GHz]	FWHM [km/s]	$F_{\text{Line (integrated)}}$ [mJy km/s]	$F_{\text{Line (peak)}}$ [mJy]	F_{cont} [μJy]
REBELS-05	253.53	278 ± 16	788 ± 60	2.7 ± 0.1	59 ± 10
REBELS-08	245.23	187 ± 12	498 ± 41	2.5 ± 0.1	36 ± 10
REBELS-18	219.08	151 ± 8	623 ± 45	3.9 ± 0.2	178 ± 26
REBELS-29	247.31	224 ± 11	656 ± 42	2.8 ± 0.1	49 ±7
REBELS-29-2	247.41	340 ± 16	922 ± 57	2.5 ± 0.1	258 ±16
REBELS-38	250.82	201 ± 11	1190 ± 84	5.6 ± 0.3	105 ±22
COS-2987	243.43	187 ± 17	201 ± 24	1.01 ± 0.08	···
UVISTA-Z-019	245.13	205 ± 14	1027 ± 91	4.7 ± 0.3	62 ±13
COS-3018	241.99	387 ± 20	346 ± 24	0.84 ± 0.04	63 ±7

surements recorded in Table 3.4. To do this, we first create a circular spatial mask covering the visible extent of the [CII] emission on the target galaxy, and plot the integrated spectrum of the spectral line cube with this mask applied. We fit the resulting spectrum with a Gaussian profile, and extract the line centre (μ) and FWHM ($\sigma\sqrt{8ln(2)}$). We create a subcube of the spectral line with a limited frequency range between $\mu-$FWHM and $\mu+$FWHM, and generate a temporary intensity map, from which we extract the signal in a background region.

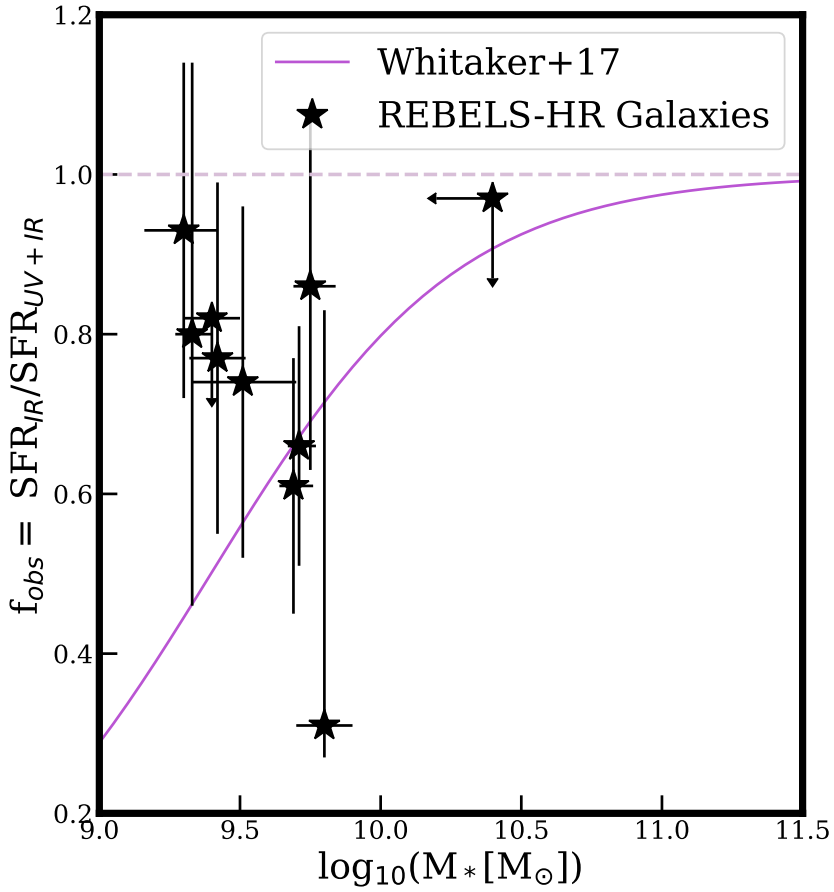

Figure 3.11: The distribution of the obscuration fraction with stellar mass for the REBELS-HR sample. The f_{obs}/M_* relation (solid purple line) is the best fitting relation derived by Whitaker et al. (2017) between $0.5 < z < 2.5$.

The standard deviation of this background region represents the noise, and we create a refined mask for the spectral line cube that requires signal $> 3\sigma$ within the previously defined circular aperture mask. We apply this new mask to the spectral line

cube and extract the integrated spectrum, which we fit with a Gaussian line profile. To measure the flux of the spectral line, we integrate under the fitted Gaussian. We generate the final [CII] intensity map from the ±FWHM spectral range.

To obtain morphological properties, we perform two dimensional fitting using the GALFIT algorithm (Peng et al., 2002) in both the rest-UV and rest-optical for each galaxy covered by the NIRSpec IFU, and for the remaining galaxies we use F200W and F444W NIRCam imaging as the rest-UV and rest-optical respectively. We preferentially define morphological properties from rest-optical imaging as this contains the majority of the stellar emission, with less bias towards unobscured star forming regions (see Section 3.1) except for REBELS-29. In this case, we elect to use the rest-UV to define the morphology, as this galaxy hosts a bright clump in the rest-optical which strongly biases the fitting away from the main body of the galaxy. The rest-frame optical/UV light does not represent an accurate tracer of the underlying morphology for the galaxies with the highest dust obscuration fractions (f_{obs}, see Table 2.1 and Figure 3.11). For REBELS-29-2 and REBELS-38, therefore, we perform Galfit fitting to the continuum emission. In Figure 3.12 we illustrate the necessity of this approach for the galaxy REBELS-38, which has $f_{obs} = 0.86 \pm 0.23$ (Bowler et al., 2024). The axis fitted to the continuum emission is similar to that fitted to the spectral line emission, while the axis fitted to the rest-optical light is visibly offset due to partial obscuration by dust.

Details of the specific model fitted in each case are provided in the following subsections, where we introduce each individual galaxy with a brief literature review and present our results. Morphological measurements for the galaxy sample are recorded in Table 3.6. In the following (Figures 3.13-3.21), we present the [CII] emission line spectrum for each galaxy alongside its Galfit fitting results, and cutouts of the multi-wavelength imaging. These cutouts show the comparative morphologies of the dust, cool [CII] gas, and young unobscured stars in the UV and rest-optical, alongside hot gas traced by Hα where available.

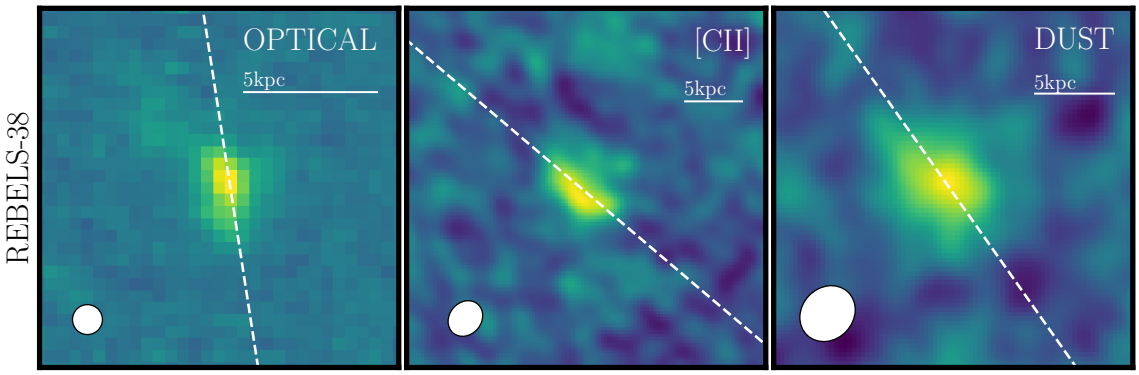

Figure 3.12: A comparison of the major axis fitted to the rest-optical (left), [CII] (centre) and continuum (right) emission for REBELS-38.

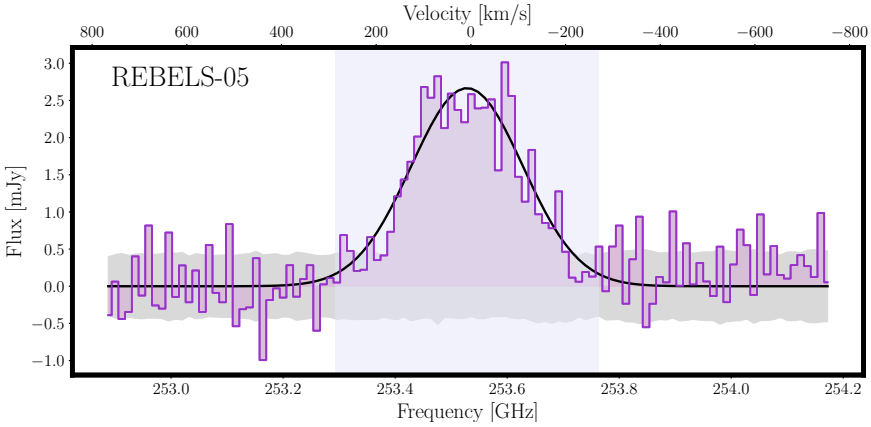

(a) Integrated spectrum and fitted Gaussian profile (black line). The vertical purple shaded region ±FWHM of the line centre represents the frequency range used to create the [CII] intensity map. The horizontal, grey shaded region is the error on the spectrum.

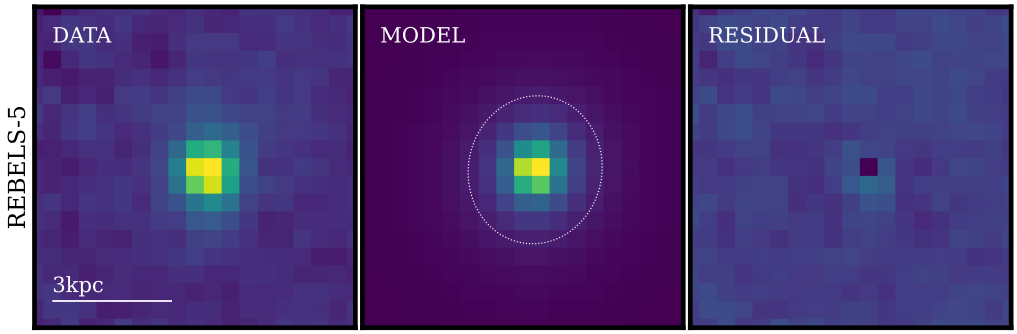

(b) The rest-optical image (from the NIRSpec IFU; left), the fitted Galfit model (centre) with a white dotted outline defined by the fitted parameters, and the residual (right).

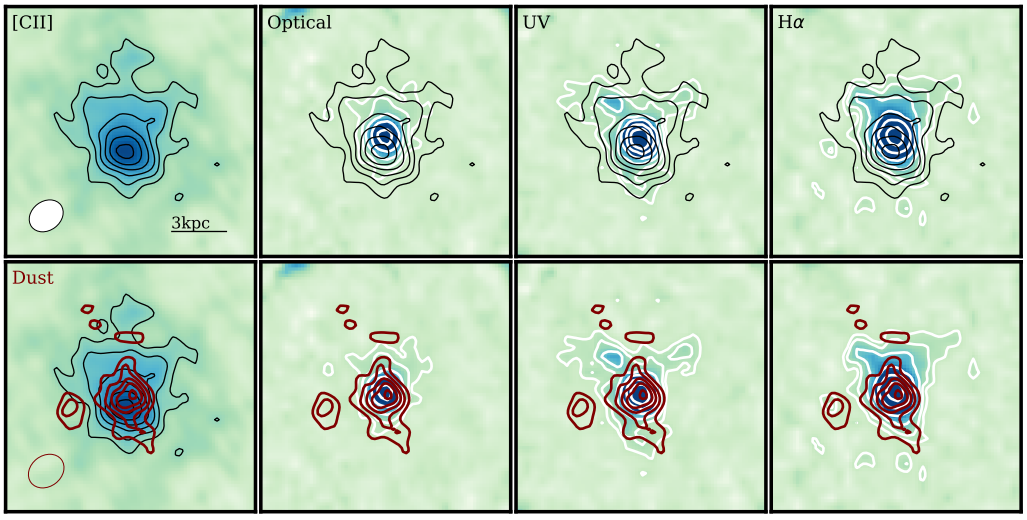

(c) Image cutouts: top row from left to right shows [CII] from ALMA, rest-optical, rest-UV and Hα maps from the NIRSpec IFU overlaid with white contours for the background emission and [CII] contours in black ($2^n\sigma$). Second row shows the same backgrounds, but overlaid with dust continuum contours in red (dust contours at 2-6σ).

Figure 3.13: REBELS-05 spectrum, morphological fitting and image cutouts.

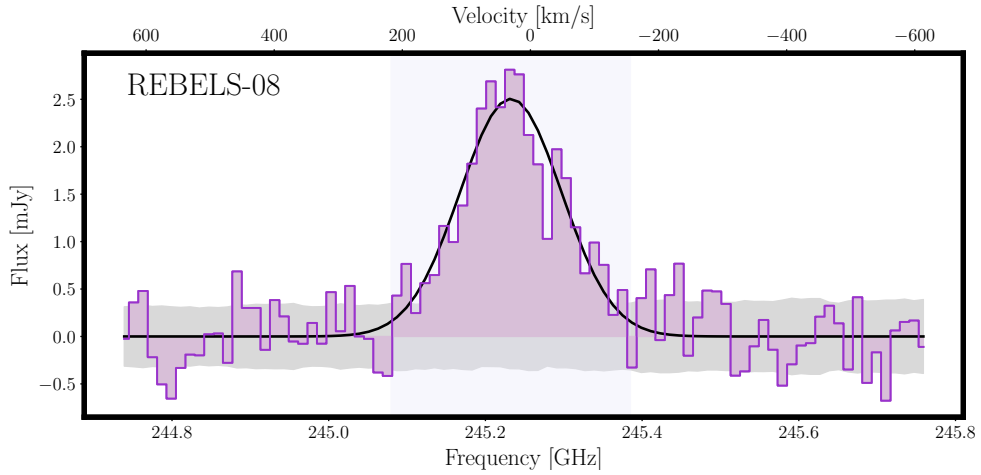

(a) As Fig. 3.13, for REBELS-08

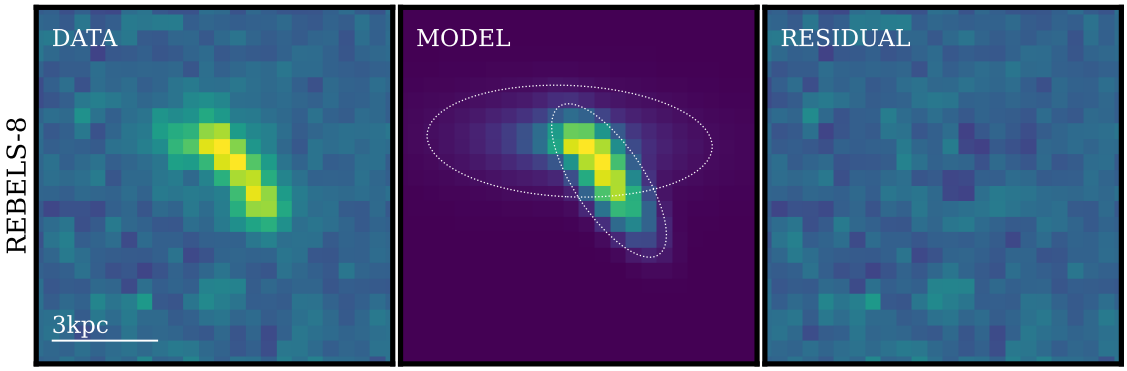

(b) As previous, for REBELS-08, showing the two-component fit representing the main galaxy component and diffuse emission.

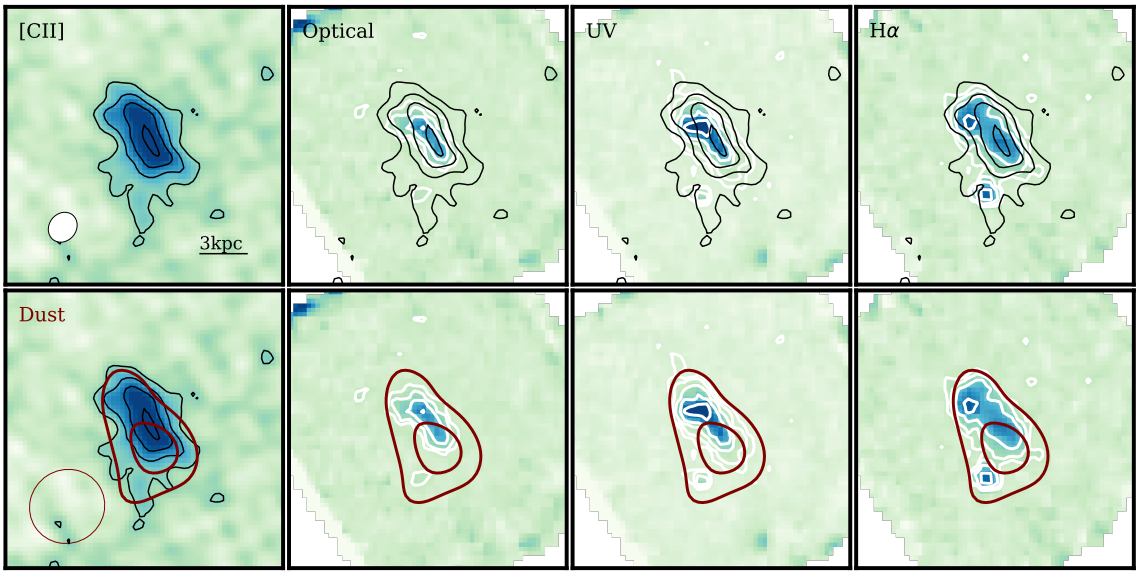

(c) As previous, for REBELS-08. [CII] contours at $5n$ σ, rest-optical, rest-UV and Hα contours at $2^n\sigma$, and dust contours at 2, 3 σ.

Figure 3.14: REBELS-08 spectrum, morphological fitting and image cutouts.

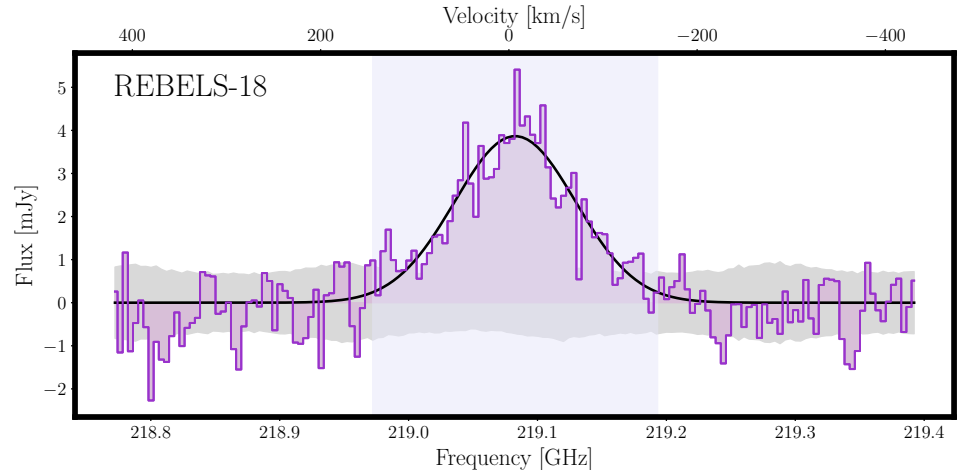

(a) As previous, for REBELS-18

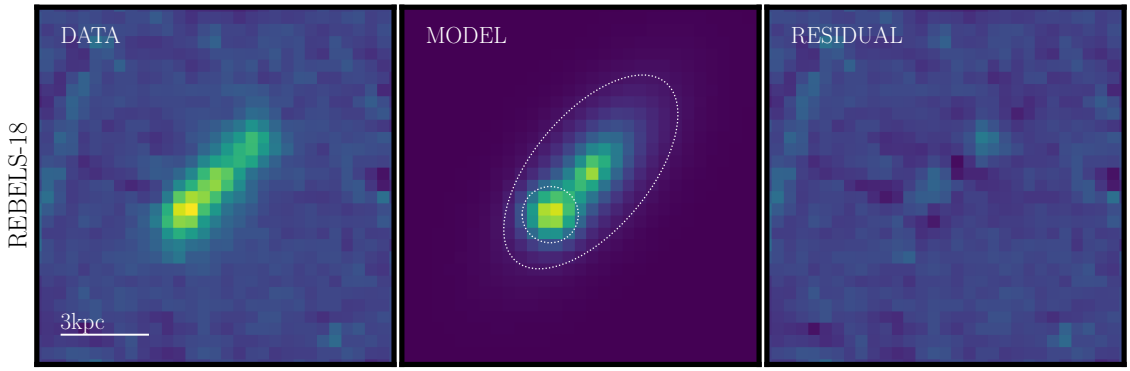

(b) As previous, for REBELS-18, showing the two-component fit representing the main galaxy component and a bright internal clump.

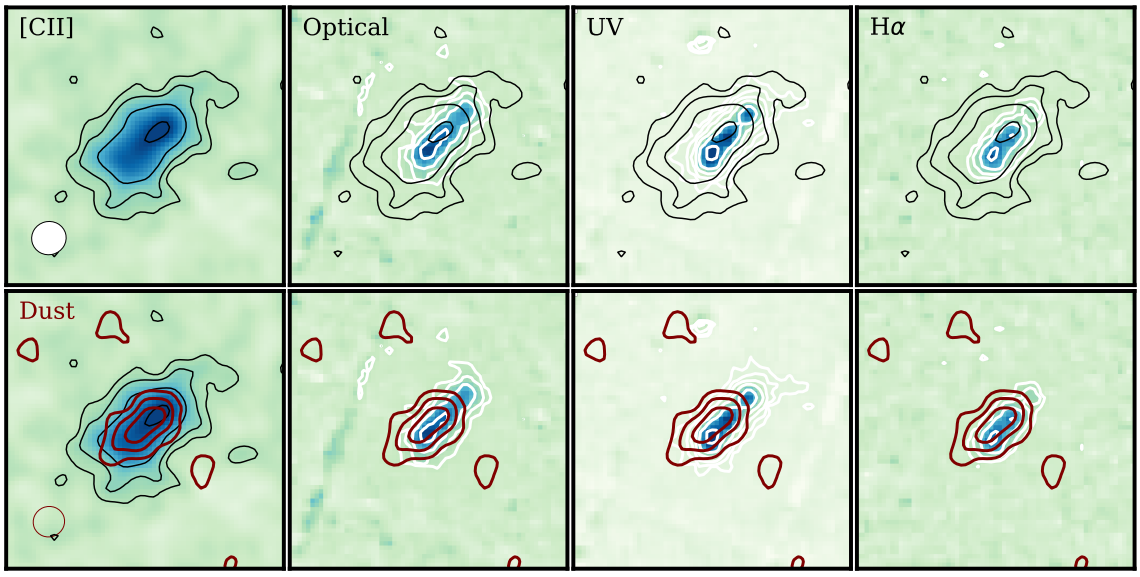

(c) As previous, for REBELS-18.

Figure 3.15: REBELS-18 spectrum, morphological fitting and image cutouts. Contours at $2^n\sigma$.

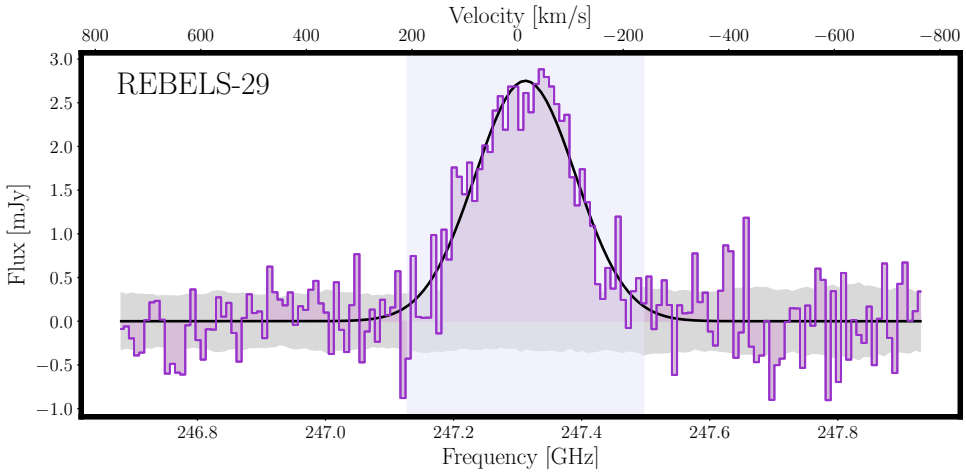

(a) As previous, for REBELS-29

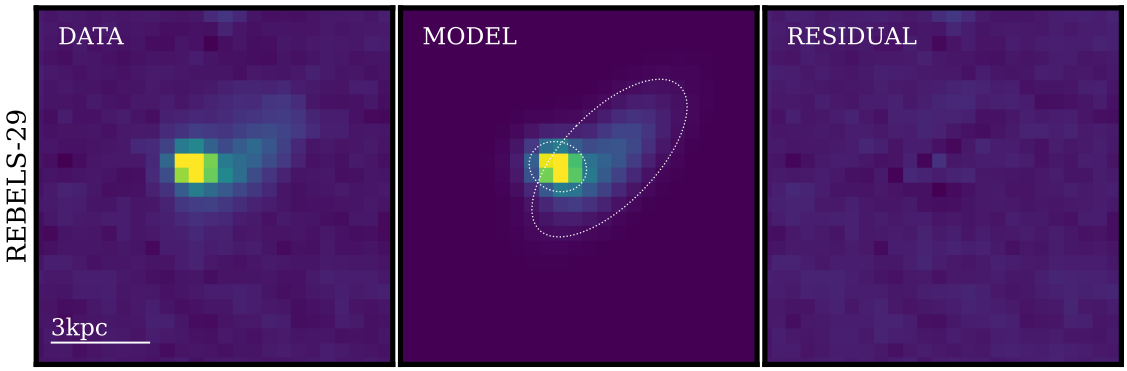

(b) Galfit fitting in the rest-UV for REBELS-29 , showing the two-component fit representing the main galaxy component and a bright internal clump.

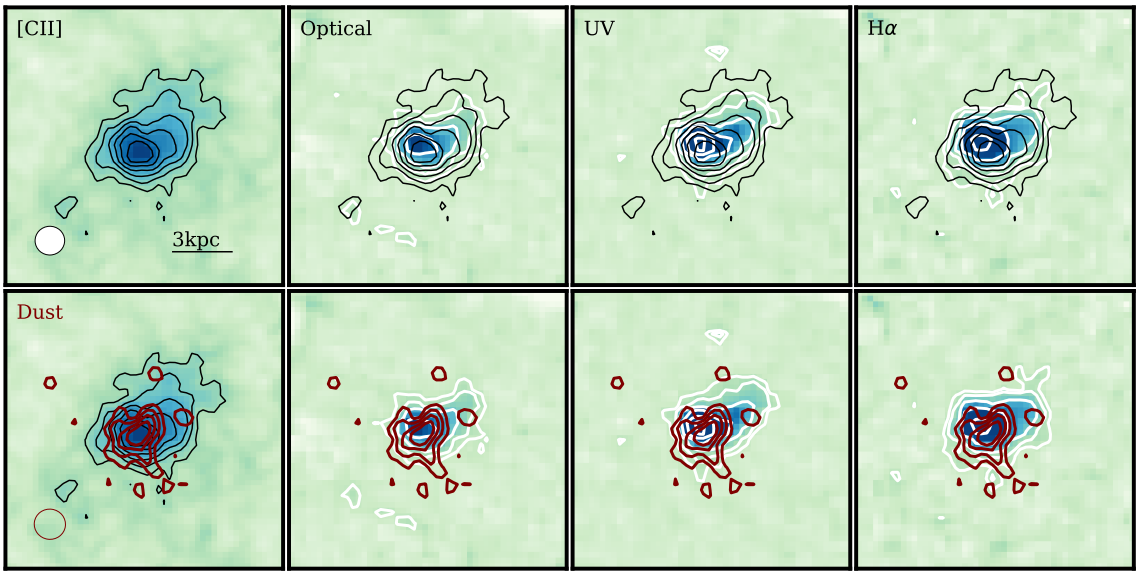

(c) As previous, for REBELS-29.

Figure 3.16: REBELS-29 spectrum, morphological fitting and image cutouts. [CII] contours begin at 3σ and increase in steps of 2σ. Rest-optical, rest-UV and Hα contours are at $2^n\sigma$, and dust contours at $2-5\sigma$.

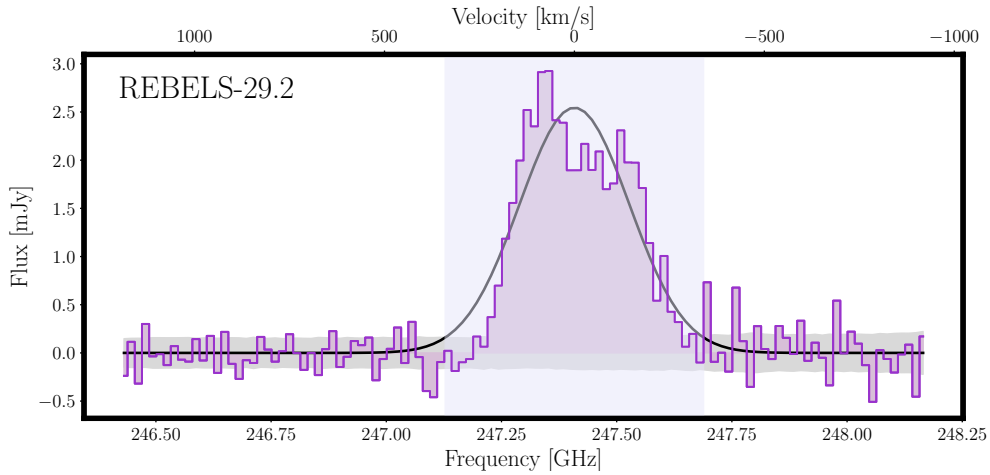

(a) As previous, for REBELS-29-2

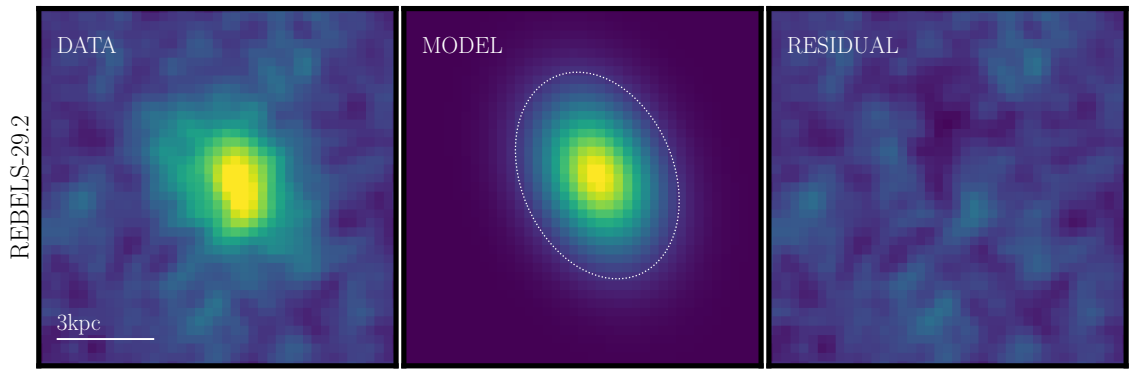

(b) Galfit fitting of a single component to the dust continuum for REBELS-29-2.

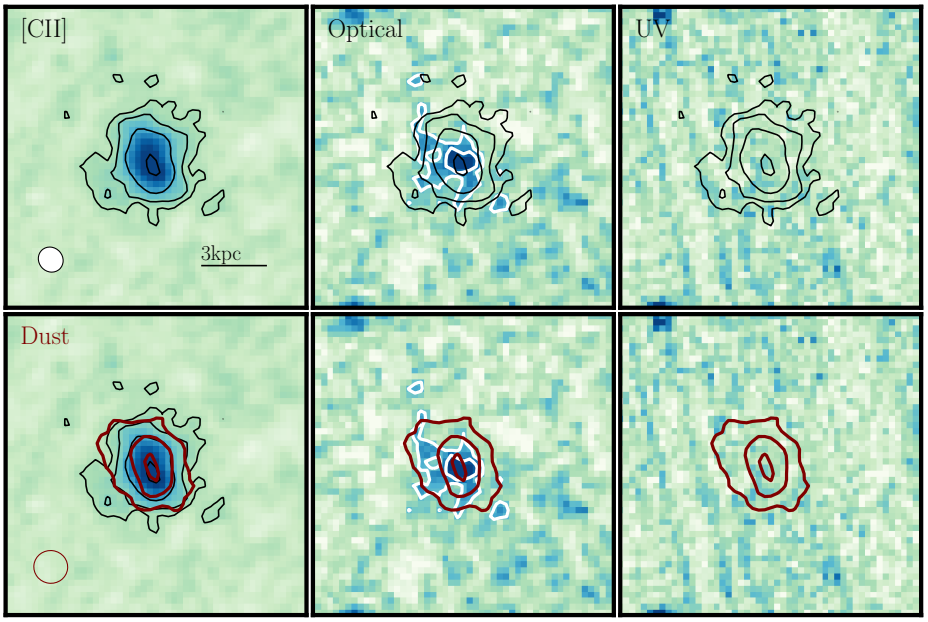

(c) As previous, for REBELS-29-2.

Figure 3.17: REBELS-29-2 spectrum, morphological fitting and image cutouts. [CII] and rest-optical contours are at $2^n\sigma$ and dust contours at $5n\sigma$.

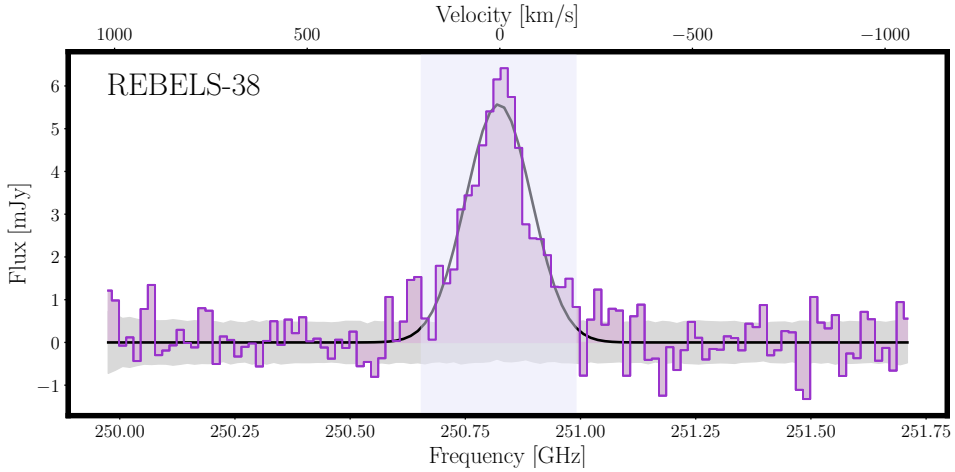

(a) As previous, for REBELS-38

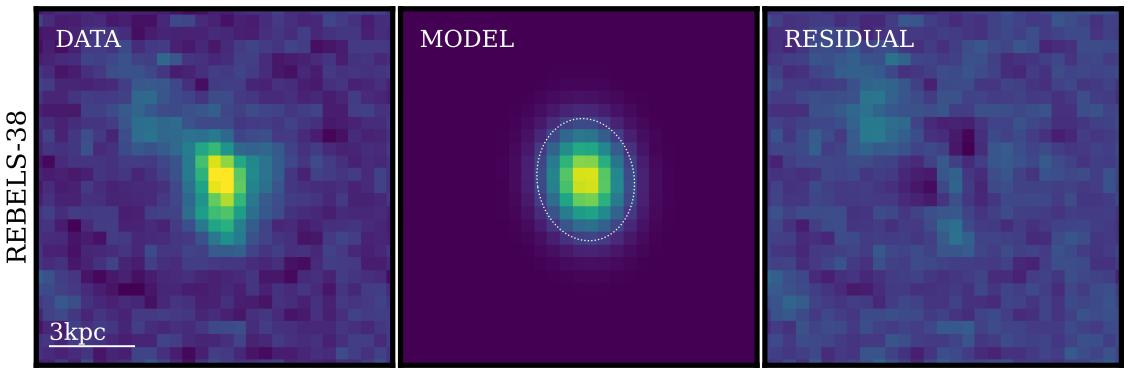

(b) As previous, for REBELS-38.

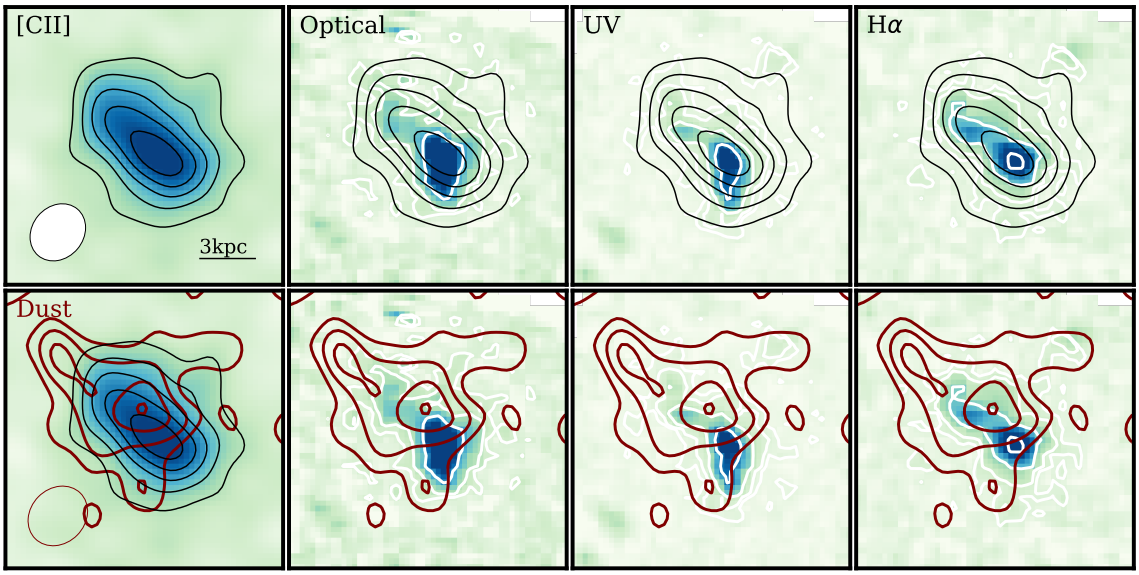

(c) As previous, for REBELS-38.

Figure 3.18: REBELS-38 spectrum, morphological fitting and image cutouts. [CII] contours are at $5n\sigma$, rest-optical, rest-UV and Hα contours at $3^n\sigma$, and dust contours at $1-4\sigma$.

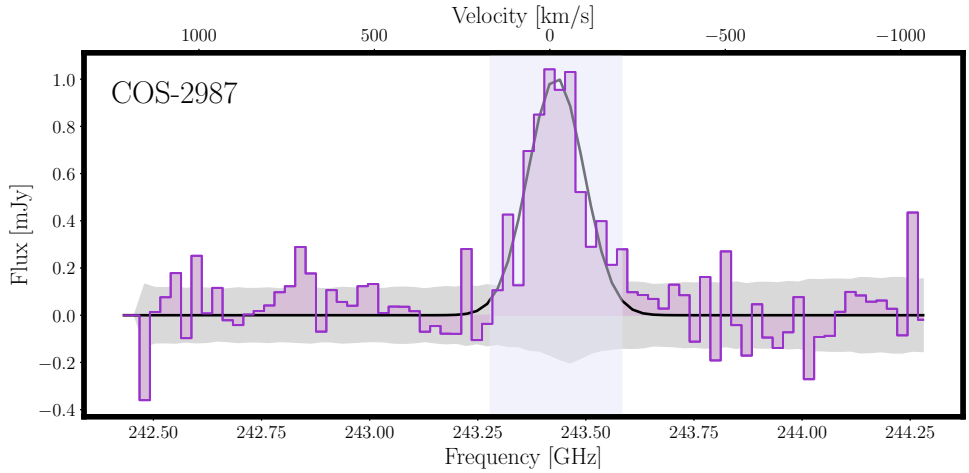

(a) As previous, for COS-2987

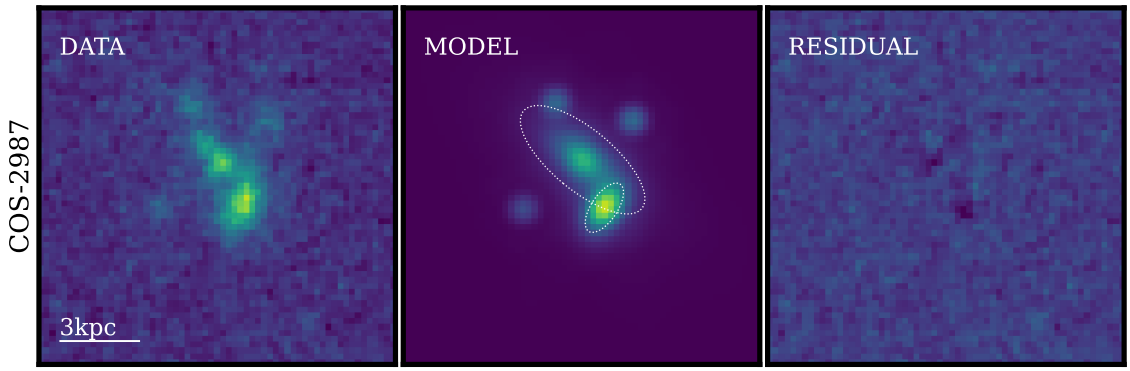

(b) The Galfit model consists of two Sérsic profiles fitting the rest optical emission (dotted white lines) and three PSF components representing two clumps and a foreground contaminant.

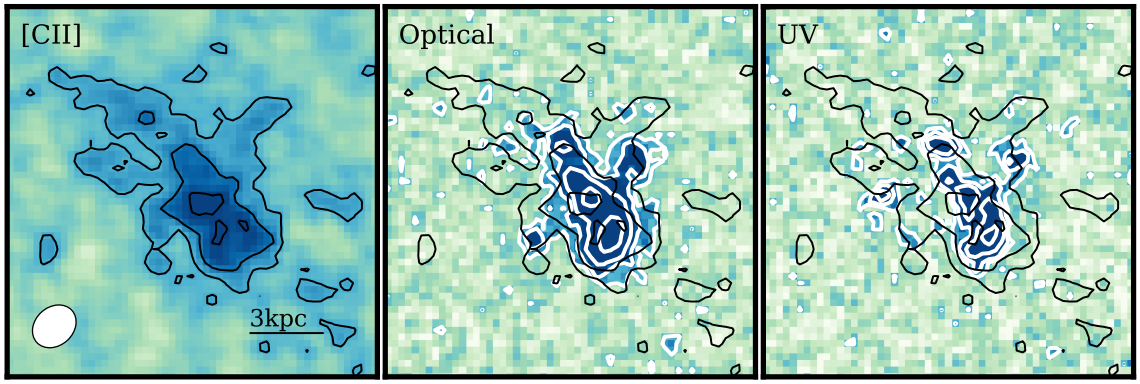

(c) As previous, for COS-2987, but showing NIRCam F444W band imaging for rest-optical and F200W for rest-UV. [CII] contours are at $2n\sigma$, rest-optical and rest-UV contours are at $2^n\sigma$.

Figure 3.19: COS-2987 spectrum, morphological fitting and image cutouts.

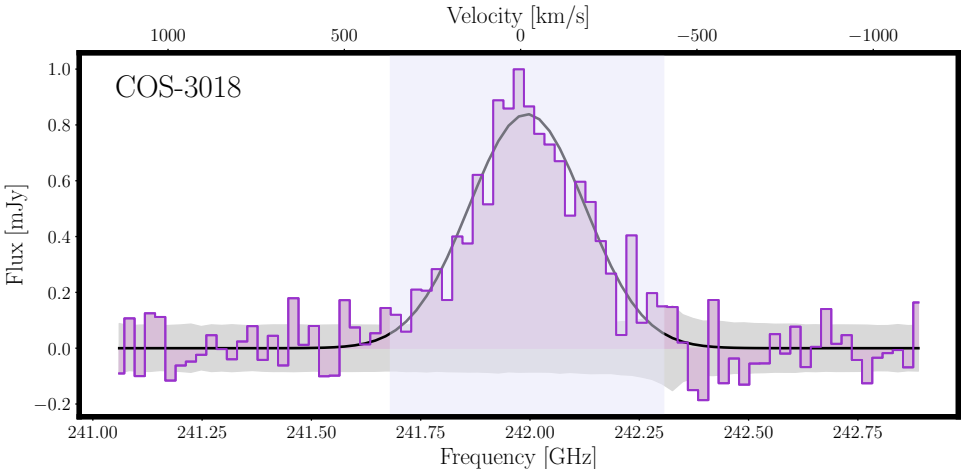

(a) As previous, for COS-3018

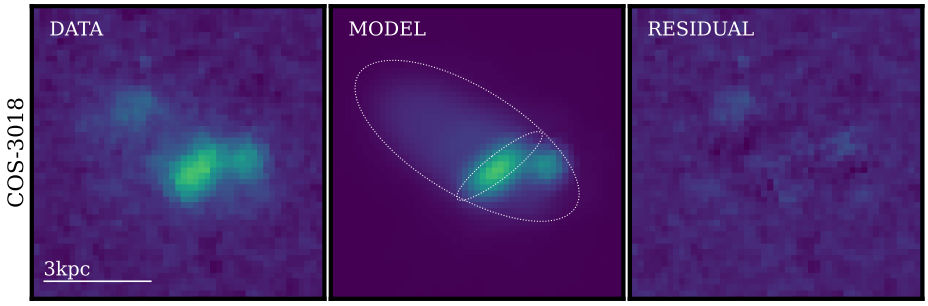

(b) The model fitted with Galfit in the rest-optical consisted of two Sérsic profiles (white dotted lines) and a PSF component covering the remaining clump.

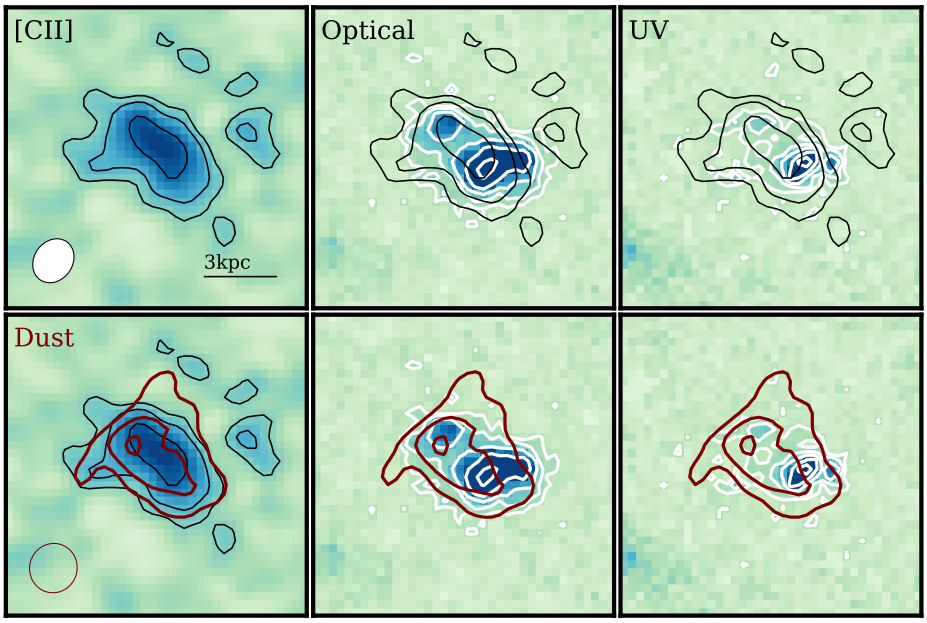

(c) As previous, for COS-3018.

Figure 3.20: COS-3018 spectrum, morphological fitting and image cutouts. Contours at $2^n\sigma$.

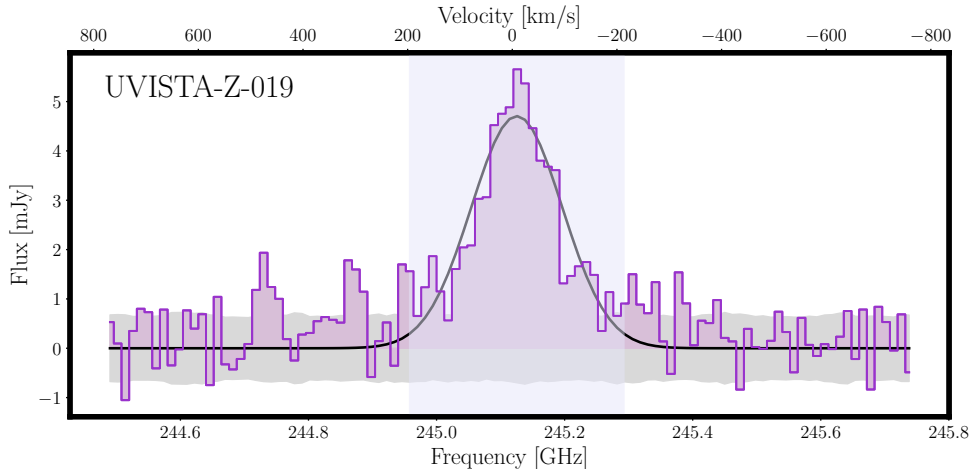

(a) As previous, for UVISTA-Z-019.

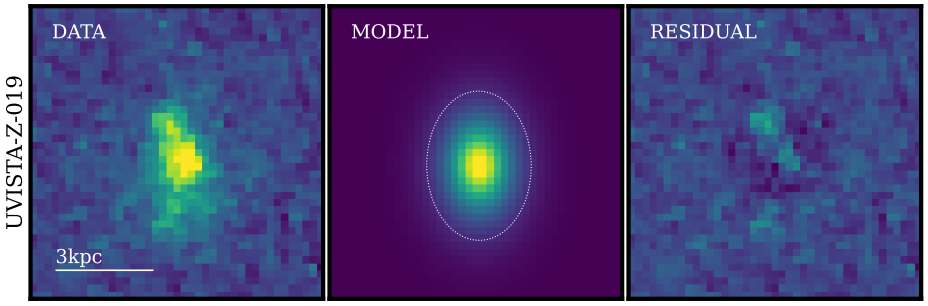

(b) As previous, for UVISTA-Z-019.

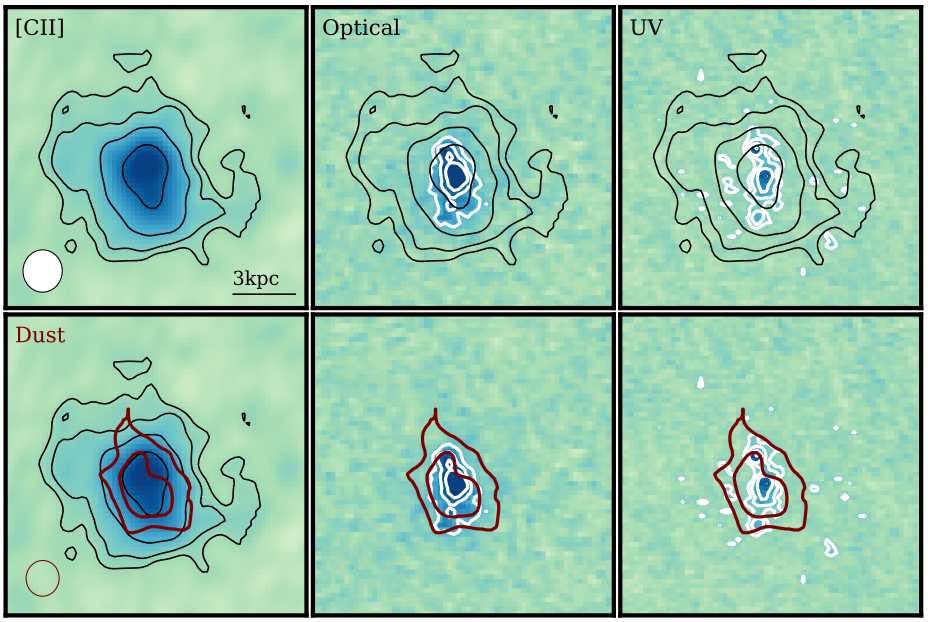

(c) As previous, for UVISTA-Z-019.

Figure 3.21: UVISTA-Z-019 spectrum, morphological fitting and image cutouts. Rest-optical contours are at $5n\sigma$, all other contours at $2^n\sigma$.

3.4.1 REBELS-05

REBELS-5 was first identified by Bowler et al. (2014) as ID 118717 from the tenth data release of the Ultra Deep Survey (UDS) taken by the ground-based United Kingdom Infra-Red Telescope (UKIRT) as part of the UKIRT Infrared Deep Sky Survey (UKIDSS: Lawrence et al. (2007)). The source was selected with a colour-colour LBG criterion, with Spitzer/IRAC imaging constraints on the strong (log EW(OIII+Hβ)/Å$=3.02$) rest-frame optical emission lines improving the robustness of the photometric redshift estimate. REBELS-5 was studied in Inami et al. (2022), where a spatial offset of $0.13'' \pm 0.04$ was found between the rest-UV and continuum components. Fisher et al. (2025) measure the dust attenuation curve and compare the best-fitting curve to Calzetti-like and Small Magellanic Cloud (SMC) dust extinction relations, finding that it lies between the two. Rowland et al. (2025) using strong line calibrations measure the metallicity as $12 + \log(\mathrm{O/H}) = 8.51 \pm 0.16$.

We present the [CII] spectrum and morphological measurements for REBELS-5 in Figure 3.13. We see a tentative extended wing of positive flux bluewards of the emission line in the spectrum, which could be interpreted as an indication of outflowing/inflowing gas streams.

We fit a single Sérsic profile to the rest-optical observation, which has no apparent clumps or diffuse emission regions. By comparing the contours from different emission components, we see that there is an offset between the [CII] centre and the centres of the other emission components, while the peak of the dust continuum appears aligned with the centres of the rest-optical, rest-UV and Hα emission. There is an extended emission filament visible in [CII] and not in other tracers towards the North, which is in the blue region of the velocity map (Figure 4.1) and could therefore correspond to the positive emission wing visible in the spectrum.

3.4.2 REBELS-08

REBELS-08 was identified in Endsley et al. (2021) with the source ID XMM1-88152. Fisher et al. (2025) identify a 2175Å UV bump feature in the dust attenuation curve of REBELS-08 at a 7.0σ confidence level. Out of the 12 REBELS galaxies analysed by Fisher et al., REBELS-08 displays the strongest UV bump, a feature

associated with the presence of polycyclic aromatic hydrocarbons (Shivaei et al., 2022; Schneider and Maiolino, 2024). Such a robust identification of the UV bump feature in a galaxy at $z = 6.75$ indicates that these small carbonaceous dust grains are produced on a short timescale, and are able to survive within the ISM of EoR galaxies (see also: Witstok et al., 2023). Fisher et al. (2025) recover a bump strength $B = 3.04^{+0.47}_{-0.44}$, comparable to the Milky Way's mean bump strength of $B = 3.0$ (Salim et al., 2018), where

$$B = A_{bump}/E(B-V)$$

and A_{bump} is the additional attenuation at 2175Å attributed to the presence of the bump. Fisher et al. additionally find that this galaxy, similarly to REBELS-05, has a best fitting dust attenuation curve lying between the Calzetti-like and SMC extinction relations. Inami et al. (2022) identify a considerable offset of $0.37'' \pm 0.07$ between the dust and UV peaks in this galaxy, and Rowland et al. (2025) derive a metallicity of $12 + \log(\mathrm{O/H}) = 8.22 \pm 0.22$.

We show the spectrum, Galfit fit and multi-wavelength image cutouts in Figure 3.14. We model the rest-optical morphology with two almost perpendicular Sérsic profiles, one fitting the main body of the galaxy and one fitting a diffuse emission component which is more extended. We see a bright clump in the rest-optical, rest-UV and Hα image cutouts aligned with the position of this diffuse component, which are absent from the [CII] map and dust continuum. The brightness of this clump dominates the rest-UV emission map, showing that this is likely to be a relatively young, unobscured star forming region. The presence of this star forming clump biases the locations of the rest-optical, -UV and Hα emission peaks, but it appears that their morphologies are otherwise broadly coincident with the [CII] and dust morphologies, while the dust peak is offset to the South (in agreement with Inami et al., 2022). A bright Hα clump is additionally visible in the South-West, with some indication of its presence in the rest-optical and (particularly) the rest-UV.

3.4.3 REBELS-18

This galaxy was first identified in Stefanon et al. (2017) where high redshift galaxy candidates were selected from deep NIR imaging over the COSMOS and UltraV-

ISTA fields using the Lyman break technique and excluding brown dwarf candidates. REBELS-18 was initially estimated to have a photometric redshift $z_{\rm phot} > 8.5$, and was notable for its extreme brightness, with a magnitude of 24.6 in the H_{160} filter. Fisher et al. (2025) find a steep dust attenuation curve for REBELS-18, consistent within errors with the SMC extinction relation. The metallicity is $12 + \log(\mathrm{O/H}) = 8.50 \pm 0.13$ (Rowland et al., 2025), and Inami et al. (2022) measure an offset of 0.19 ± 0.05 between the dust and rest-UV.

We show the [CII] spectrum, the Galfit morphological fit, and the image cutouts for REBELS-18 in Figure 3.15. We model the rest-optical emission with two Sérsic components representing the main galaxy body and an internal clump, or flux excess, to one side. While the [CII] emission peak is offset from the peaks of the other tracers, which are biased towards the bright clump, it appears well aligned with the main morphological Galfit component, although this is difficult to confirm without smoothing the JWST data to the ALMA beam.

3.4.4 REBELS-25

REBELS-25 was initially presented in Stefanon et al. (2017) and Stefanon et al. (2019) as a candidate LBG covered by the Drift And SHift (DASH: Momcheva et al. (2016) and Mowla et al. (2019)) mosaic, where it was identified as a multiple structure in the rest-UV, consisting of three sub-components.
This galaxy has been the subject of extensive and fruitful follow-up observation and analysis campaigns from which we have gained a strong understanding of its structure and governing physics. Hygate et al. (2023) study the [CII] observations made of this galaxy as part of the REBELS LP, finding a velocity gradient consistent with the rotating disk scenario, and excess [CII] emission in the emission line spectrum significantly offset (+ 500 km/s) from the line centre. They posit that this secondary [CII] component could indicate the presence of a merger component or an outflow, and estimate that in the merger scenario, this would represent an outflow with a deprojected atomic mass outflow rate of 120 $\mathrm{M}_\odot$/yr, and an atomic mass loading factor of $\gtrsim 1.0$.

Rowland et al. (2024) present analysis of follow-up high resolution [CII] and dust

continuum observations with ALMA. They find that the [CII] morphology is well-described by a near-exponential disk profile ($n = 1.3 \pm 0.2$), indicating that the clumpiness observed in the rest-UV is a result of dust obscuration and not intrinsic, and the secondary component identified in Hygate et al. (2023) is indeed likely to represent an outflow. Rowland et al. (2024) find that REBELS-25 is a dynamically cold rotating disk with $v/\sigma = 11^{+6}_{-5}$, making it the highest-redshift kinematically confirmed disk galaxy yet observed. Their measurement of the dynamical mass as $1.2^{+1.0}_{-0.6} \times 10^{11}$ $M_\odot$ indicates a strongly gas-dominated galaxy with little dark matter. REBELS-25 is also shown to host a UV-bump in Fisher et al. (2025), with a bump strength that is consistent within 1σ with the Milky Way. REBELS-08 and REBELS-25 are the only two galaxies in the Fisher et al. (2025) sample for which including a bump in the dust relation fitting yields a significantly better fit (according to the Bayesian Information Criterion). The metallicity is $12 + \log(\mathrm{O/H}) = 8.62 \pm 0.17$ (Rowland et al., 2025).

3.4.5 REBELS-29 and REBELS-29-2

REBELS-29 was identified in Bowler et al. (2014) (with ID 304384) and Endsley et al. (2021) (with ID COS-1224137), and has a metallicity of $12 + \log(\mathrm{O/H}) = 8.73 \pm 0.15$ (Rowland et al., 2025). REBELS-29 is studied in Fudamoto et al. (2021) alongside REBELS-12 as the [CII] imaging of both galaxies revealed an 'ALMA-only' dust-obscured companion galaxy coincident with the field. Fudamoto et al. (2021) record a spectral line detection significance of 9.7σ and dust detection significance of 9.2σ. The spectral lines of REBELS-29 and REBELS-29-2 are near-coincident in frequency, with an estimated velocity offset of 110 km/s between them. The discovery of REBELS-12.2 and REBELS-29-2 was significant as despite the identification of several galaxies at $z > 6$ with dust reservoirs, no heavily dust obscured EoR galaxies had previously been found.

Through SED analysis, Fudamoto et al. (2021) establish that REBELS-29-2 is consistent with being a lower luminosity analogue of a typical dusty star forming $z > 6$ galaxy, and estimate that $> 97\%$ of its star formation may be obscured, compared to $< 63\%$ for REBELS-29. This leads Fudamoto et al. (2021) to suggest that heavily dust obscured galaxies could contribute $10 - 25\%$ of the cosmic SFRD at $z > 6$,

though this is a highly uncertain figure as the estimate changes significantly depending on how clustering is accounted for, given that REBELS-29-2 (and REBELS-12.2) were identified as companion galaxies to the main targets.

The spectrum, morphological fitting, and image cutouts are shown in Figure 3.16 for REBELS-29. We fit the rest-UV emission with two Sérsic profiles, one ellipse modelling the extended elliptical light profile, and one smaller component, which models a bright clump. This clump dominates the emission more strongly in the rest-UV than the rest-optical, however, the higher S/N in the rest-UV allows for better modelling of the two components, motivating our decision to fit the rest-UV. This clump is the location of the emission peak across all of our available tracers, and the dust continuum is seen to be focused on the clump region, with no significant FIR emission across the extended body of the galaxy. This suggests that REBELS-29 could be a major merger system, with the apparent clump indicating the merging site. Inami et al. (2022) measure a modest offset between the UV and dust of 0.12 $\pm$ 0.14″, which appears consistent with the alignment of our components.

We show the spectrum of REBELS-29-2 and the single-component Sérsic profile we fit to the dust continuum in Figure 3.17. The spectrum appears to show a 'double horned peak' profile, which results from the presence of multiple line-of-sight velocities within the source. The double-peak structure seen in the spectrum is therefore evidence supporting the interpretation of REBELS-29-2 as a rotating disk galaxy, but other physical processes such as galaxy mergers can also give rise to this profile (Maschmann et al., 2023), so it is an inconclusive result in isolation. We show the image cutouts for the [CII] and dust emission, and the F444W and F200W NIRCam filters representing the rest-optical and rest-UV. While the morphology of the rest-optical emission is more compact and irregular than the [CII] and dust, the centres of all three components are reasonably well aligned. REBELS-29-2 is not detected in the rest-UV due to its high level of dust obscuration, and we therefore plot the dust and [CII] contours against a noise background in this case.

3.4.6 REBELS-38

REBELS-38 is identified in Endsley et al. (2021) from the COSMOS field (with ID COS-1304254), and is the brightest galaxy in [CII] of the REBELS-HR sample. REBELS-38 has the flattest dust attenuation slope out of their sample, as well as the highest molecular index after REBELS-25 (Ferrara et al., 2022; Inami et al., 2022). The molecular index is defined by $I_m = \frac{F_{158}/F_{1500}}{\beta-\beta_0}$ where F_{158} and F_{1500} are the flux densities at 158Å and 1500Å, and β_0 is the intrinsic UV slope. A high molecular index comes from a strong IR flux component compared to the UV flux, and is associated with galaxies having patchy dust obscuration, for example due to a multiphase ISM with both opaque dust-obscured star forming clumps, as well as a diffuse dust component that is relatively transparent to UV emission(Inami et al., 2022). A large offset is also found in Inami et al. of $0.57'' \pm 0.25$ between the UV and dust components, and the metallicity is $12 + \log(\mathrm{O/H}) = 8.28 \pm 0.18$ (Rowland et al., 2025).

There is a diffuse, extended emission component visible in the rest-optical, but the galaxy is still well-described by a single Sérsic profile (Figure 3.18). The [CII] emission centre is near-coincident to the rest-optical, rest-UV and Hα peaks. However, we see a strong offset between the dust continuum and all other emission components. The extended dust emission is stronger towards the faint rest-optical emission to the North-East, where [CII] is also detected.

3.4.7 COS-2987

COS-2987 was detected in [CII] through spectral scanning with ALMA between 241-245GHz, having been selected as a target through its blue rest optical colours in Spitzer, and extreme [OIII]+Hβ emission (Smit et al., 2018). The source was identified by Smit et al. as hosting a smooth velocity gradient in [CII] across the extent of the galaxy, which could be interpreted as evidence for a rotating disk, but the resolution was too low for this to be confirmed. Laporte et al. (2017) obtained deep spectra with XSHOOTER/VLT for COS-2987 as one of a sample of three bright [O III] emitting galaxies at $z \sim 7$ (also including COS-3018), from which they find tentative evidence that the emission lines they detect originate from separate

components. However, Carniani et al. (2018) include COS-2987 (and COS-3018) in a sample of normal $z > 5$ star forming galaxies for which they study the [C II] and UV morphologies, and do not find indication of a multiclump structure.

Posses et al. (2023) combine the low resolution [CII] observations from Smit et al. (2018) with higher resolution data from 3.6hr on source with ALMA, and analyse the morphology and kinematics. With this higher resolution data, they discover a complex internal structure with an extended arm shaped feature that could indicate a satellite in the process of being accreted. Posses et al. (2023) find that the disky velocity gradient persists at higher resolution, and their calculated v/σ is consistent with the rotating disk scenario. They determine the Toomre Q parameter to quantify the disk stability, with a value of $Q < 1$ indicating that the disk is susceptible to local gravitational collapse. Posses et al. (2023) estimate $Q = 0.44$ for COS-2987, which suggests that it could be a disk in a non-turbulent phase that is vulnerable to becoming clumpy. Parlanti et al. (2023) re-analyse this galaxy and their recovered velocity dispersion and v/σ ratio are in good agreement with the findings of Posses et al.

We gain further understanding of this source from its JWST observations. Harikane et al. (2025) measure a stellar mass of $\log(M_*/M_\odot) = 9.4 \pm 0.1$ from SED fitting to NIRCam imaging. Mawatari et al. (2025) present the NIRCam and NIRSpec [OIII]5008Å view of COS-2987, which identifies the galaxy as not a rotating structure, but a system of merger induced star forming clumps. They identify five distinct clumps, with two main clumps that are star forming with moderate dust attenuation, and three dust-free sub-clumps. This result does not necessarily present a conflict with the diskiness observed with ALMA, as one possible scenario (other than the ALMA observations being of insufficient spatial resolution to reveal the internal clumpiness) is that the cold and warm gas trace different environments within the galaxy. Usui et al. (2025) exploit the ALMA/JWST synergy to reveal a two-phase ionised gas structure within the galaxy. They compare the critical densities of the ALMA [OIII]88Å line with the NIRSpec [OIII]4346, 5008Å lines, finding that the density of the former is 3-4 orders of magnitude lower than the latter. This motivates the conclusion that they originate from physically different ionized gas phases, in contrast to the assumption commonly made for similar galaxies of a

homogenous ionized gas giving rise to all emission lines present. Usui et al. also measure a metallicity of $12 + \log(\mathrm{O/H}) = 7.67^{+0.11}_{-0.13}$.

The spectrum, morphological fitting and image cutouts for COS-2987 are shown in Figure 3.19. The spectrum appears to show positive flux to the lower-frequency side of the emission line peak, although at a similar level of significance to the noise. The Galfit model consists of two Sérsic profiles fitted to the rest-optical emission, and three PSF components representing the clumps surrounding the main emission component. The clump visible to the top left of the galaxy is a foreground contaminant which does not drop out in blue filters. We choose to model this clump instead of masking it out so as to better account for its contribution to the total observed flux. The [CII], rest-optical and rest-UV emission morphologies appear to be coincident, though the [CII] morphology has an extended wing to the North-East at the 2σ level not visible in the other tracers. COS-2987 is not detected in the dust continuum.

3.4.8 COS-3018

COS-3018 has been extensively studied since its discovery by Tilvi et al. (2013) as a candidate $z \sim 7$ Lyman Break Galaxy (LBG) from an area of 155 arcmin^2 in the CANDELS/COSMOS field, and independently by Bowler et al. (2014) through photometric redshift analysis of UltraVISTA data. It was part of a sample of LBGs analysed by Smit et al. (2015) to test a novel method of selecting star forming galaxies at $z \sim 6.6 - 6.9$ through IRAC colours, since sources at such redshifts would appear blue due to the presence of high equivalent-width [O III] emission.

The redshift of COS-3018 was spectroscopically confirmed by Smit et al. (2018), where its low-resolution velocity structure revealed a smooth gradient characteristic of a rotating disk. The kinematics were further characterised as representing a turbulent disk by Parlanti et al. (2023). Carniani et al. (2018) find the galaxy to be compact in [C II] with a considerably smaller UV emitting region, having no indication of a multiclump structure. Laporte et al. (2017), from ground-based observations, placed a 3σ upper limit on the 1907/1909 Å flux ratio of 0.6, which could be indicative of a very high gas density. Harikane et al. (2025) measure a stellar mass of $\log(M_*/M_\odot) = 9.8 \pm 0.1$ from SED fitting to NIRCam imaging. Scholtz

et al. (2025) analyse NIRCam and NIRSpec/IFS data of COS-3018, finding that the galaxy appears clumpy and complex in hot gas, and interpreting the system as comprising at least three components offset from each other in velocity space. Through SED fitting they characterise each of these components as a young starburst. They perform a search for AGN in the galaxy with optical emission line diagnostics and are not able to confirm the presence of an AGN, though emission line ratios are consistent with either the star forming or AGN host galaxy scenario. They measure an average metallicity of $12 + \log(\mathrm{O/H}) = 7.9 - 8.2$ across the three components.

Figure 3.20 shows the spectrum, Galfit fit, and image cutouts for COS-3018. There are three apparent clumps visible in the rest-optical morphology, which we represent as two Sérsic components and a PSF component. From the contour plots, we see that the [CII] and dust emission are broadly in agreement. There is evidently a secondary peak in the far-infrared continuum. There is an approximately coincident peak visible in the rest-UV emission map, but it becomes far brighter and more distinct in rest-optical. This is expected, as the clump is dust obscured and therefore reddened, and would be correspondingly more obscured at bluer wavelengths.

3.4.9 UVISTA-Z-019

UVISTA-Z-019 was identified in Schouws et al. (2023), the second pilot study carried out prior to the REBELS LP, where it is one of six galaxies spectroscopically confirmed in [CII] through spectral scanning with ALMA on galaxies from the COSMOS field with photometrically constrained redshifts. No significant velocity gradient was identified with these low angular resolution observations, and the maximum rotation velocity was constrained to $v\sin(i) < 50\mathrm{kms}^{-1}$, implying that the galaxy could be face-on, or dominated by dispersion. The [CII] emission displays a broad and a narrow component, which could variously be interpreted as the effect of an outflow, a minor merger, with the narrow component being the signature of an infalling galaxy, or a bright star forming clump. The indication of complex structure from the [CII] emission without any evidence of rotation in UVISTA-Z-019 inspired an ALMA follow-up campaign with 5 hours on-source. UVISTA-Z-019 is also detected significantly in the dust continuum, and Vallini et al. (2024) measure a metallicity of $\log(\mathrm{Z/Z_\odot}) = -0.43^{+0.24}_{-0.28}$.

We see the spectrum, morphological fitting and image cutouts for UVISTA-Z-019 in Figure 3.21. The spectrum clearly shows a narrow and a broad Gaussian component, which is widely recognised as a signature of gaseous outflows at high redshift, as we will examine more closely in Section 2.5.3. The rest-optical morphology appears to have a complex structure, but we approximate its light profile with a single Sérsic component which, despite not accounting for the complex morphology as is apparent from the over-subtraction visible in the residual map, is sufficient to provide a good approximation of the effective radius. From the contour maps, we see that the [CII], dust, rest-optical and rest-UV emission component peaks are all approximately coincident, although the [CII] emission is significantly more extended than the other components; this could be described as a [CII] halo (Fujimoto et al., 2019; Fujimoto et al., 2020), and is consistent with the scenario of UVISTA-Z-019 hosting significant outflows.

3.4.10 Emission Component Offsets

We calculate the offsets between the [CII], optical and UV emission and the dust continuum by measuring the distance between the peak pixels of each component, and compare our UV/dust offsets with those measured at lower resolution by Inami et al. (2022). These results are presented in Table 3.5. We find that our UV/dust offsets are consistent with those of Inami et al. with the exception of UVISTA-Z-019, for which our measured offset is $\sim 3\times$ higher. Inami et al. found that REBELS-38 had a high UV/dust offset of $0.6''$, and we also measure a significant, although lower, offset between the dust emission and the other components in this galaxy, while the peaks of the [CII] and optical emission are coincident. The majority of component offsets are smaller than the effective radius (Table 3.6) indicating that we are seeing different regions within a single galaxy, and not a merging system of galaxies with different physical properties. The offsets which are higher than the corresponding effective radius are the UV/dust offsets for REBELS-8, REBELS-38, UVISTA-Z-019, and COS-3018, the [CII]/dust offsets for REBELS-8 and REBELS-38, and the [CII]/optical offset for COS-2987. This could suggest that these galaxies contain minor or major merging activity, or host clumps distributed over the surface of the galaxy with varied star formation rates/histories.

Table 3.5: Emission component offsets for all REBELS-HR galaxies (excepting REBELS-25) shown alongside the Inami et al. (2022) UV/dust offsets, where available, for the purposes of comparison. Note that we do not detect COS-2987 in the dust continuum nor REBELS-29-2 in the rest-UV.

GALAXY ID	[CII]/dust [arcsec]	[CII]/optical [arcsec]	UV/dust [arcsec]	I22 UV/dust [arcsec]
REBELS-5	0.13 ± 0.09	0.16 ± 0.08	0.03 ± 0.1	0.13 ± 0.04
REBELS-8	0.3 ± 0.4	0.14 ± 0.08	0.43 ± 0.4	0.37 ± 0.07
REBELS-18	0.11 ± 0.07	0.25 ± 0.09	0.16 ± 0.1	0.19 ± 0.05
REBELS-29	0.0 ± 0.03	0.11 ± 0.08	0.14 ± 0.09	0.12 ± 0.14
REBELS-29.2	0.11 ± 0.03	0.11 ± 0.07	···	···
REBELS-38	0.34 ± 0.1	0.0 ± 0.09	0.38 ± 0.15	0.57 ± 0.25
COS-2987	···	0.32 ± 0.09	···	···
UVISTA-Z-019	0.24 ± 0.06	0.13 ± 0.05	0.37 ± 0.07	0.13 ± 0.04
COS-3018	0.2 ± 0.1	0.22 ± 0.06	0.5 ± 0.1	···

We plot the infrared luminosity and obscuration fraction for the sample against the measured UV/dust offset in Figure 3.22 and find a large spread in the distribution, with no clear trends evident within the data.

3.4.11 Consistency of Results

We perform morphological fitting with Galfit on both rest-UV and rest-optical imaging for every galaxy in the sample with the exception of REBELS-29-2, for which we are only able to fit the FIR continuum. We see some spread in the measured effective radii, and find that inclination angles are generally higher when measured

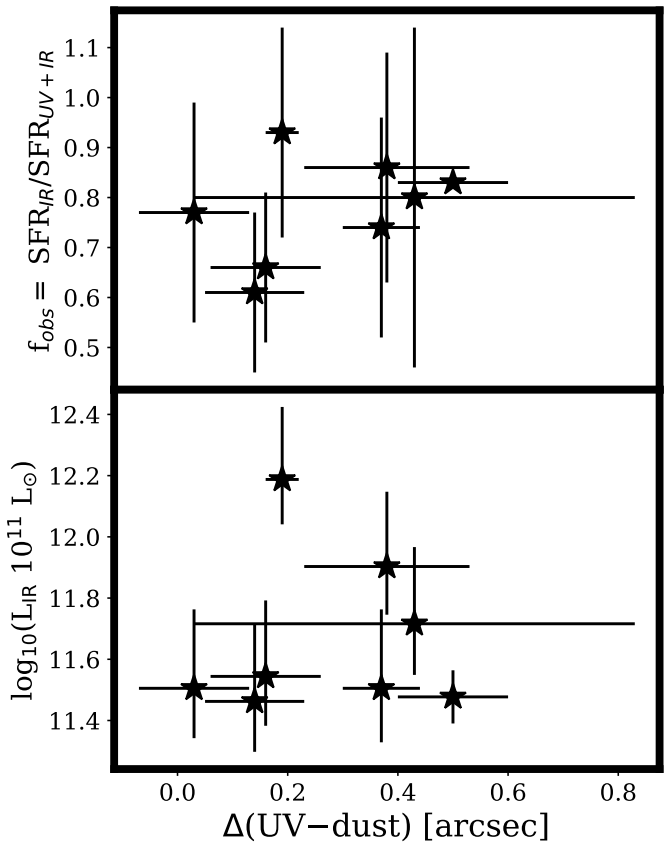

Figure 3.22: The obscuration fraction (top) and infrared luminosity (bottom) plotted against the UV-dust offset for all REBELS-HR galaxies.

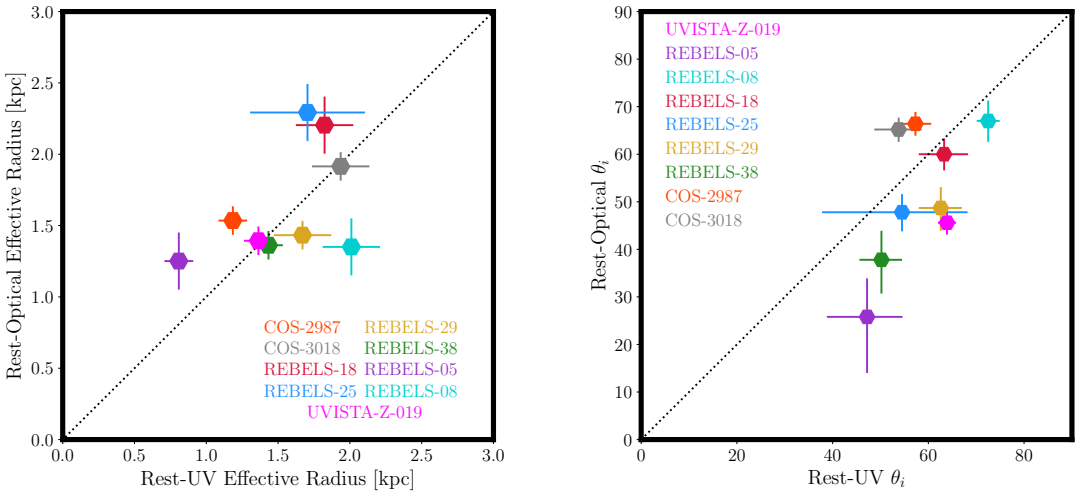

Figure 3.23: Comparison of effective radii (left) and inclination angles (right) measured using morphological fitting with Galfit for rest-UV and rest-optical imaging.

from the rest-UV, in comparison to the rest-optical. We do not find a systematic offset between the two tracers in measuring the effective radius, although our sample is too small to determine whether a systematic effect is in fact present. Most of our measurements in the rest-UV and rest-optical are consistent with each other within $1-2\sigma$, and we note that the errors are derived from Galfit and are likely underestimated (e.g. Suess et al., 2022).

3.5 Complexity of Clumpy High Redshift Systems

We observe a clumpy structure in the rest-UV for many galaxies in our sample. The presence of clumps in the rest-UV suggests isolated pockets of star formation which could be merger-induced (Harikane et al., 2025).

3.5.1 COS-3018

COS-3018 appears to have a clumpy structure across multiple tracers, and to understand its complex morphology we perform both integrated and resolved SED fitting on the NIRCam imaging obtained by the PRIMER survey. To measure the photometry, we run `Source Extractor` (Bertin and Arnouts, 1996) in dual image mode, where source detection is performed on one image and photometry on another to ensure that the signal is extracted in consistent apertures across all filters. To create a detection image for this purpose, we PSF-match the images in all filters to the reddest filter, F444W. We calculate the weighting for each filter as $w = \sigma^{-2}$ where σ is the noise, and the detection image is then obtained by dividing the sum of the weighted images by the sum of the weights:

$$I_{\rm det} = \frac{\Sigma w_i I_i}{\Sigma w_i}$$

Having thus measured photometry across all available filters, we fit the resulting SED with the software Bayesian Analysis of Galaxies for Physical Inference and Parameter EStimation (BAGPIPES: Carnall et al. (2018)).

We set the star formation rate as constant, with a fixed metallicity of 0.2, and allow the maximum age (the time since star formation began) and mass formed parameters to vary within a limited range. We employ the Calzetti dust law (Calzetti, 1997) and

Table 3.6: Measurements of galaxy morphological properties from rest-optical fitting, rest-UV fitting in the case of REBELS-29, and dust continuum fitting in the case of REBELS-29-2.

REBELS ID	$R_{\rm eff}$ [kpc]	θ_i [deg]	$\theta_{\rm PA}$ [deg]	RA J2000	Dec J2000
REBELS-05	1.3 ± 0.2	$25.8^{8.1}_{11.8}$	-10.2 ± 31.2	02:18:11.50	-05:00:59.22
REBELS-08	1.4 ± 0.2	$67.0^{4.3}_{4.4}$	33.7 ± 7.2	02:19:35.13	-05:23:19.38
REBELS-18	2.2 ± 0.2	$60.0^{3.3}_{3.4}$	-39.9 ± 5.4	09:57:47.90	02:20:43.72
REBELS-25	2.3 ± 0.2	$47.9^{3.8}_{4.0}$	-8.07 ± 8.13	10:00:32.33	01:44:31.25
REBELS-29	1.7 ± 0.2	$62.6^{4.4}_{4.6}$	-44.3 ± 9.2	10:01:36.84	02:37:49.27
REBELS-29-2	2.02 ± 0.02	$44.8^{0.8}_{0.8}$	23.1 ± 2.1	10:01:37.1	02:37:48.9
REBELS-38	1.4 ± 0.1	$37.8^{6.1}_{7.1}$	8.8 ± 15.3	10:02:54:04	02:42:12.18
COS-2987	1.5 ± 0.1	$66.4^{2.5}_{2.5}$	50.5 ± 4.4	10:00:29.86	02:13:2.15
UVISTA-Z-019	1.4 ± 0.1	$45.6^{2.4}_{2.5}$	0.6±4	10:00:29.89	01:46:46.33
COS-3018	1.9 ± 0.1	$65.2^{2.5}_{2.6}$	58.6 ± 4.1	10:00:30.18	02:15:59.89

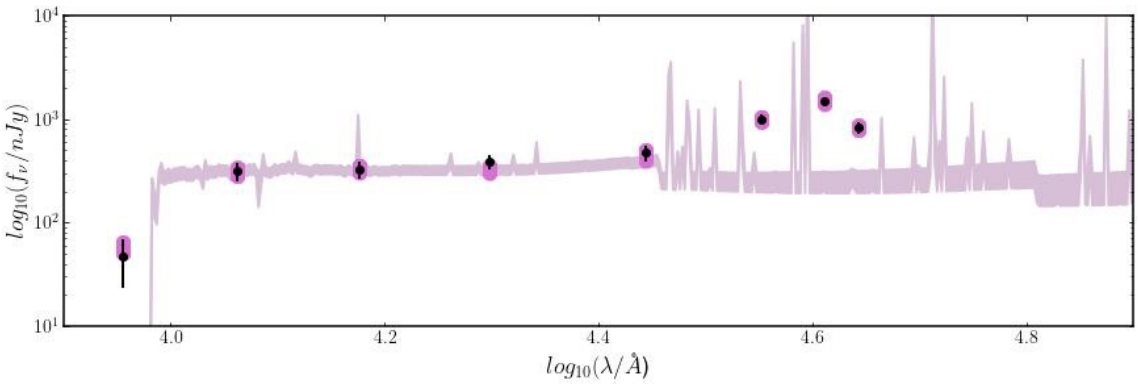

Figure 3.24: COS-3018 integrated light SED (black points) with fitted Bagpipes model (purple extended points) and inferred SED (lilac profile).

include a nebular component representing emission lines and the nebular continuum. Fitting the SED (Figure 3.24), the galaxy appears best described by a young burst model strongly dominated by emission lines, with an [OIII] + Hβ equivalent width of 3400Å. The best fitting model indicates that the galaxy formed most of its mass in a recent burst.

Even NIRCam imaging can suffer from the outshining effect, whereby bright young stellar populations outshine older ones, leading to a significant underestimate of the total stellar mass when it is derived from integrated SED fitting (Sorba and Sawicki, 2018; Giménez-Arteaga et al., 2023; Giménez-Arteaga et al., 2024). We test whether this effect is impacting our results by binning the photometric data using the Voronoi technique (Cappellari and Copin, 2003) which ensures a minimum threshold SNR per bin. We set this SNR threshold to 50 in the noise-weighted detection image, and measure the flux in each bin. We then run Bagpipes on this new photometric catalogue, and from the SED fitted to the photometry in each bin, we derive the resolved properties of the stellar population. From the integrated SED fit, we measure the mass formed as $\log_{10}(M_*/M_\odot) = 9.8^{+0.3}_{-0.4}$, which is in agreement with the value Harikane et al. (2025) obtain using the same method. The total mass formed that we obtain from the resolved SED fitting is consistent with the mass measurement from the integrated SED fit. This result indicates that outshining does not have a significant impact on COS-3018, which is as expected if the galaxy has indeed formed most of its mass in a recent burst. In Figure 3.25 and 3.26 respectively we show the resolved SFR/kpc^2 map, overlaid with dust and rest-UV

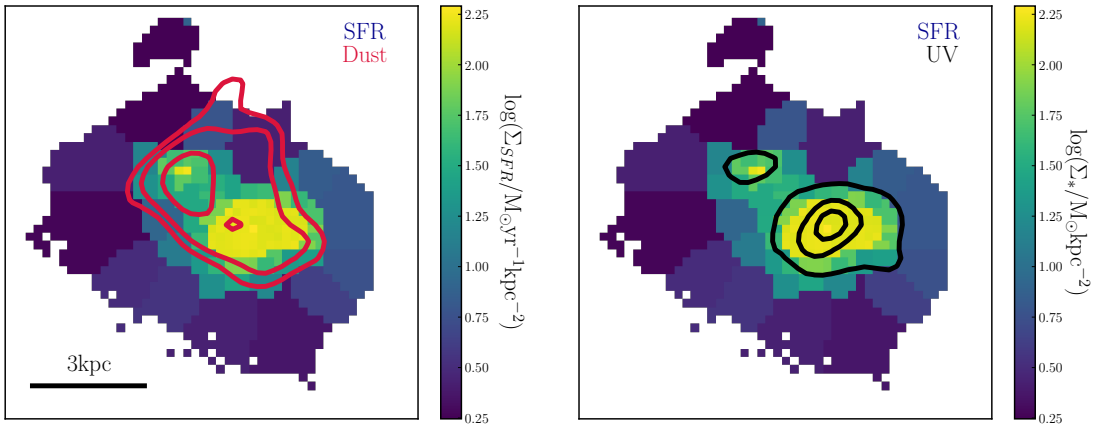

Figure 3.25: Resolved star formation rate per square kiloparsec, with contours representing dust (left) and rest-UV (right) emission.

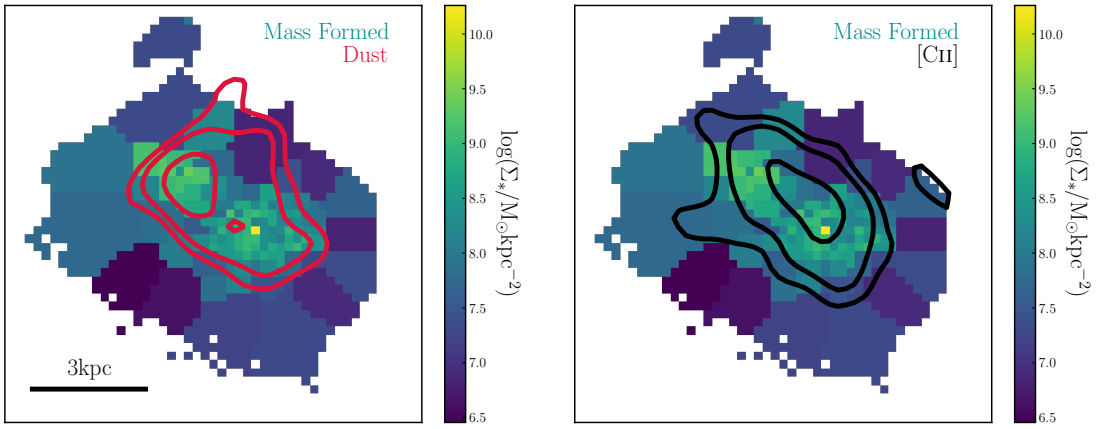

Figure 3.26: Resolved mass formed per square kiloparsec map, with contours representing the dust continuum (left) and [CII] (right).

contours, and the resolved mass formed/kpc^2 map, overlaid with dust and [CII] contours. The UV and SFR peaks are coincident, but the stellar mass is far less biased towards the UV bright peak, showing a smoother distribution across the extent of the source.

3.6 Summary and Conclusions

In this chapter we describe the observing strategy for, and present the global properties of, the ten-galaxy REBELS-HR sample. This is the first sample in the Epoch of Reionization for which we can measure the resolved cold gas kinematics alongside the distribution and morphology of obscured star formation through exploiting the synergy between ALMA, NIRCam, and NIRSpec IFU PRISM observations. We describe how we reduced the data, noting and justifying some key decisions made in the process, such as the weighting scheme applied.
We analyse the morphology of each individual galaxy, considering the distribution of various emission components and fitting the morphology with Galfit. Our main conclusions from this work are set out below.

- We find intriguing signatures of gaseous outflows in several sources, identifiable through the spectrum of the galaxy being best described by a double Gaussian peak profile with one broad and one narrow component. The strongest outflow signature is displayed by UVISTA-Z-019, but positive flux tails extending beyond the main emission line component are also visible in REBELS-5, REBELS-8, and COS-2987, in addition to the potential outflow feature identified in REBELS-25 by Hygate et al. (2023).

- We observe a clumpy structure across most galaxies in the sample in the rest-UV, indicative of concentrated pockets of intense star formation.

- We measure significant offsets between emission components across the REBELS-HR sample. In most cases, the offsets are within one effective radius, providing further evidence of clumpy internal structure. However, we do find offsets greater than the effective radius between components in multiple galaxies, which could be signatures of merging activity.

- Focusing on the separation between the rest-UV and dust continuum emission, we find that the emission from these components are spatially decoupled in four galaxies (REBELS-8, REBELS-38, UVISTA-Z-019, COS-3018), but with the low number statistics available in this study, we find no convincing relationship

between UV/dust offset and infrared luminosity or dust obscuration, instead finding a large scatter.

- In one galaxy, COS-3018, we perform resolved SED fitting to better understand the internal processes, and find that the galaxy appears to have undergone a recent strong burst of star formation contributing a significant fraction of the total stellar mass.

The morphological analysis of the REBELS-HR sample provides a first-order characterisation of the internal structure of the galaxies, from which we can infer some knowledge of the physical processes ongoing within them. This is crucial groundwork for the kinematic analysis we present in the following chapter.

Chapter 4

REBELS-HR: A Kinematic Analysis

4.1 Introduction

As we discuss in Section 3.1, JWST has discovered that the morphology of galaxies at $z > 3$ is smoother and more symmetrical than was expected from HST, and has identified a significant population of photometric disks at high redshifts up to and including in the Epoch of Reionization (e.g. Ferreira et al., 2022; Jacobs et al., 2023; Ferreira et al., 2023). While morphology is a crucial first-order probe of galaxy structure, particularly for large galaxy samples, we require spectroscopic follow-up to confirm the presence of disk structure. As yet, NIRspec surveys characterising individual galaxies in the Epoch of Reionization (e.g. the Galaxy Assembly with NIRSpec IFS: GA-NIFS survey, Perna (2023)) have not robustly confirmed a high proportion of disk galaxies among their samples, though Arribas et al. (2024) do identify a candidate turbulent disk from IFU observations at $z = 6.9$. Indeed, a NIRSpec analysis of the REBELS-HR galaxy COS-3018, characterised as a disk from low-resolution ALMA data in Smit et al. (2018), is re-interpreted by Scholtz et al. (2025) as a merging system on the basis of NIRSpec observations. These results evoke one of the key questions addressed in Chapter 2; how can we compare results between cold and warm gaseous tracers? Kinematic analyses of individual sources at $z > 3$ have confirmed that disk galaxies are not only present but can be dynamically cold at these redshifts (e.g. Neeleman et al. (2020) at $z \sim 4.3$, and Rowland et al.

(2024) at $z \sim 7.3$, the highest-redshift example so far). However, kinematic surveys are crucial in providing a picture of how common these dynamically cold systems are among the general galaxy population at high redshift. Lee et al. (2025b) perform kinematic analysis on the 32 galaxies of the CRISTAL sample at $4 < z < 6$ and find that $\sim 50\%$ have a disky structure, though they are characterised by a high velocity dispersion relative to lower-redshift counterparts, with a median $\sigma \sim 70$km/s and $v/\sigma \sim 2$. In this chapter we extend the statistical survey perspective of cold gas dynamical analysis into the $6 < z < 8$ redshift range.

We use the velocity measurements for the REBELS-HR galaxies to determine their dynamical mass, which is the sum of all gravitationally interacting matter within the enclosed radius, including dark and baryonic mass. Dynamical mass is therefore expected to be significantly higher than the stellar mass, though Gnerucci et al. (2011) find that the ratio of the two is smaller at $z \sim 3$ than in the local Universe. There is some uncertainty in the measurement of dynamical mass at high redshifts, particularly where it is estimated assuming a virialized system and the galaxy is actually a merger. Even minor mergers with a mass ratio of $\sim 10:1$ or higher disturb the kinematics of the system (Bournaud et al., 2005). From simulations, Simons et al. (2019) find that $\mathrm{M_{dyn}}$ can be overestimated by a factor of two for a merging system, while Kohandel et al. (2019) find that merging activity can lead to both under- and over- estimations of $\mathrm{M_{dyn}}$. Dynamical mass measurements obtained from galaxy kinematics, in combination with observational constraints on the stellar and gas mass, allow us to infer the properties of the dark matter halo. De Graaff et al. (2024) measure the dynamical mass of six JADES galaxies at $5.5 < z < 7.4$ and among these sources $\mathrm{M_{dyn}}$ is an average of $30\times$ higher than M_*, which is extreme in comparison to other surveys from the EoR, with the exception of Topping et al. (2022) which finds similarly high $\mathrm{M}_{dyn}/\mathrm{M}_*$ ratios at $z \sim 7$ for a sample of higher mass galaxies.

De Graaff et al. (2024) interpret their results as implying that either star formation is less efficient, leading to higher inferred gas masses, or that the galaxies are centrally dominated by dark matter. Collisionless dark matter-only cosmological simulations predict that dark matter halos should be organised in 'cusp' profiles, with density increasing steeply with decreasing radius, but local dwarf galaxies show 'core' density

profiles that flatten towards the centre (e.g. Moore, 1994), which has been viewed as a contradiction to ΛCDM (e.g. Hu et al., 2000), but the apparent challenge can be alleviated through strong stellar feedback acting to flatten a dark matter cusp (e.g. Pontzen and Governato, 2012; Read et al., 2016). Massive galaxies typically possess a low dark matter fraction within the effective radius, $f_{DM}(< R_{eff}) < 0.5$, which is often interpreted as evidence for a central dark matter core (Genzel et al., 2020; Danhaive et al., 2025). Roman-Oliveira et al. (2026) combine ALMA and JWST data to study the dark matter haloes of three galaxies at $0.5 < z < 3.5$ through matter decomposition of their rotation curves. Roman-Oliveira et al. (2026) derive $f_{DM} \sim 0.2$, broadly consistent with local galaxies and galaxies at $z = 1 - 3$, but from modelling the rotation curve decomposition, they find that the galaxies are well described by, or even cuspier than, standard Navarro-Frenk-White halos (Navarro et al., 1997).

Kinematic measurements can also be used to study the Tully-Fisher relation (Tully and Fisher, 1977), relating the stellar luminosity or mass to the circular velocity. The stellar mass Tully-Fisher relation represents the past average star formation to the halo mass.

4.2 Methods

We derive the intensity, velocity and velocity dispersion maps shown in Figures 4.1-4.9 through fitting a Gaussian profile to each spaxel within the galaxy and creating 2D maps of the resulting measurements of amplitude, μ and σ respectively. From visual inspection of these velocity maps we gain a qualitative insight into the dynamical classifications of the galaxies.

There are multiple codes that fit models to observations and extract physical and kinematic properties. Some of these codes fit models to the velocity field (e.g. KINEMETRY, Krajnović et al. (2006), DISKFIT, Sellwood and Spekkens (2015) + earlier examples) but we do not consider these codes because of the previously discussed uncertainties introduced by fitting to velocity maps which are dependent on data quality and certain arbitrary conditions such as masking (see Rizzo et al. (2022) and Appendix A.1). We instead choose to fit in 3D, the native space of the

datacubes. Among the plethora of 3D fitting codes, some of the most widely-used in literature are GALPAK3D (Bouché et al., 2015), DYSMAL (Cresci et al., 2009) and ^{3D}BAROLO (Di Teodoro et al., 2016). A comparison of the ability of these codes to recover the kinematics of galaxies between $z \sim 1-3$ is presented in Lee et al. (2025a), where it is found that all of the codes are capable of accurately recovering the rotational velocity across a range of SNR, resolution, mass and velocity dispersion regimes. However, the measurement of the velocity dispersion at lower SNR is more sensitive to the fitting template for the parametric codes (GALPAK3D and DYSMAL) and the SNR for the non-parametric ^{3D}BAROLO , highlighting the importance of optimising masking and priors/initial guesses for free parameters.
Our primary kinematic fitting code in this work is ^{3D}BAROLO , introduced in Section 2.4.2, which is widely used for high-redshift observations at typical resolution and sensitivity (e.g. Jones et al., 2021; Rizzo et al., 2023), which fits non-parametric tilted ring models to input spectroscopic datacubes. Our initial inputs to ^{3D}BAROLO are informed by the results of morphological fitting. We set the initial guesses for the central co-ordinate, inclination angle and position angle as the results from Galfit. We fix the inclination angle, but allow the central co-ordinates and position angle to vary as we do not expect these to be consistent between the morphological and kinematic fitting. Indeed, the co-incidence of the flux and kinematic centres, and of the morphological and kinematic position angles, are conditions for the positive identification of a disk against which we test candidate disk galaxies.

To validate the conclusions drawn from our kinematic fitting, we additionally fit our strongest disk candidates with `DysmalPy`[1](Davies et al., 2004b; Davies et al., 2004a; Cresci et al., 2009; Davies et al., 2011; Wuyts et al., 2016; Lang et al., 2017; Price et al., 2021; Lee et al., 2025a) and compare the two sets of velocity measurements against each other. `DysmalPy` is a forward modelling code specifically designed to analyse the kinematics of disk galaxies. It fits models comprised of a baryonic disk and dark matter halo and is capable of operating in 1D, 2D and 3D. We follow Lee et al. (2025b) in electing to perform 1D fitting as higher dimensional fitting has a higher SNR requirement and is more sensitive to the effects of non-circular

[1]https://www.mpe.mpg.de/resources/IR/DYSMALPY

motion. To fit in 1D, we supply a catalogue of rotational velocity and velocity dispersion measurements extracted from apertures placed along the kinematic major axis obtained from ^{3D}BAROLO , together with each aperture's offset from the centre.

4.3 Kinematic Fitting Results

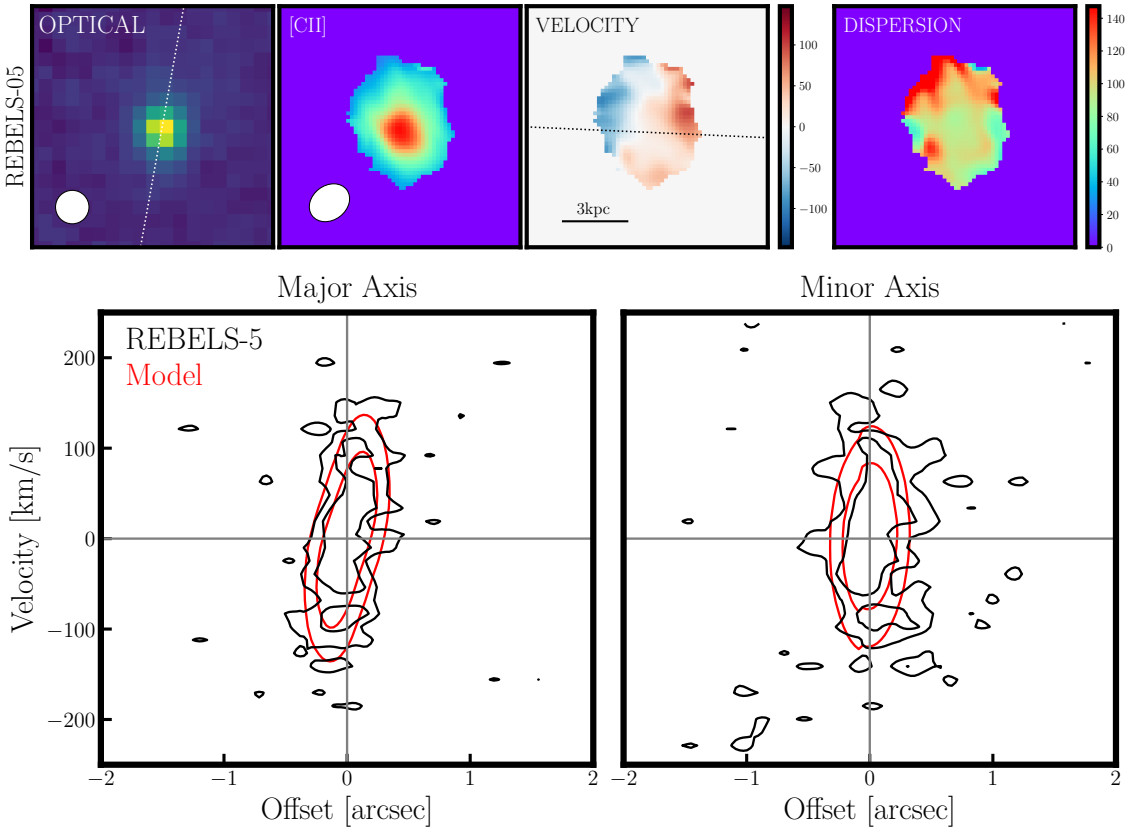

Figure 4.1: *Top row:* Left-to-right, we see the REBELS-5 optical imaging overplotted with the morphological axis measured by Galfit: the [CII] flux map: the velocity map overplotted with the kinematic axis measured by ^{3D}BAROLO : the velocity dispersion map from Gaussian fitting. *Bottom row:* Position-velocity diagrams extracted along the major (left) and minor (right) kinematic axes of the galaxy, with the observational data shown in black and the model in red, where the contours are drawn starting at 2 and increasing with 2 σ.

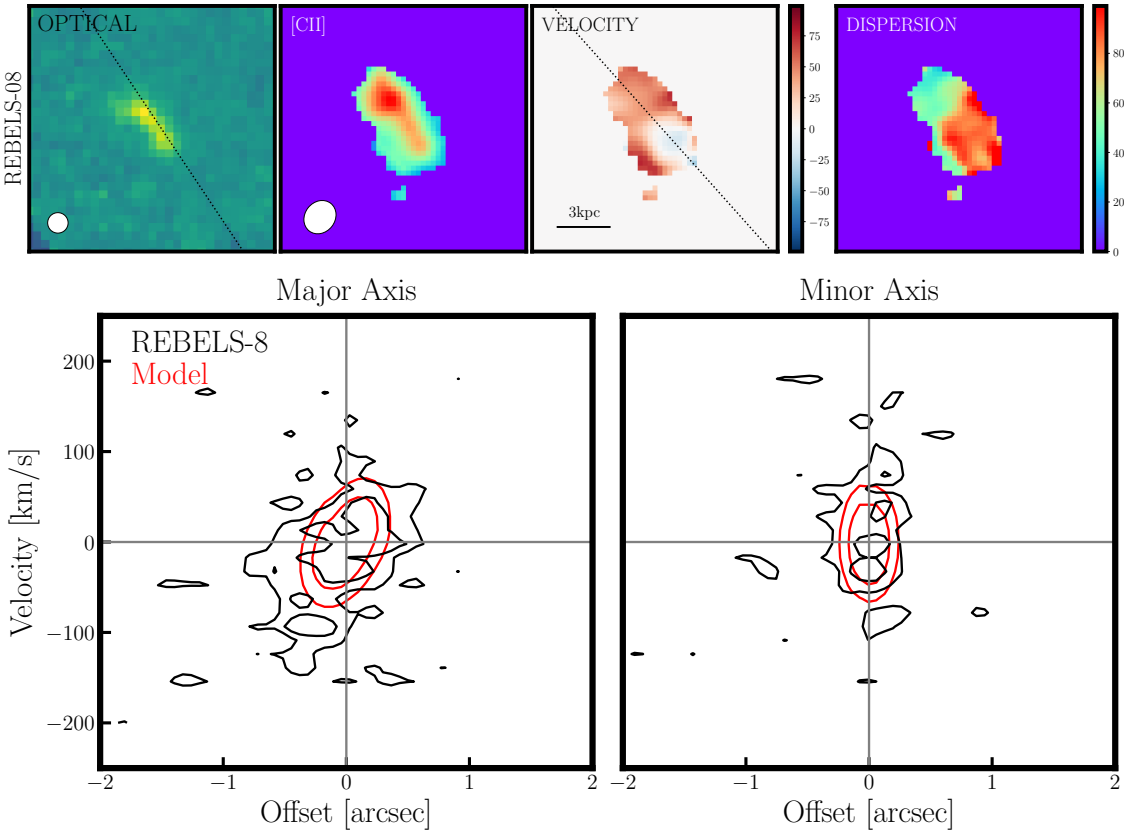

Figure 4.2: REBELS-8 velocity maps and position-velocity diagrams: see Fig. 4.1 for details.

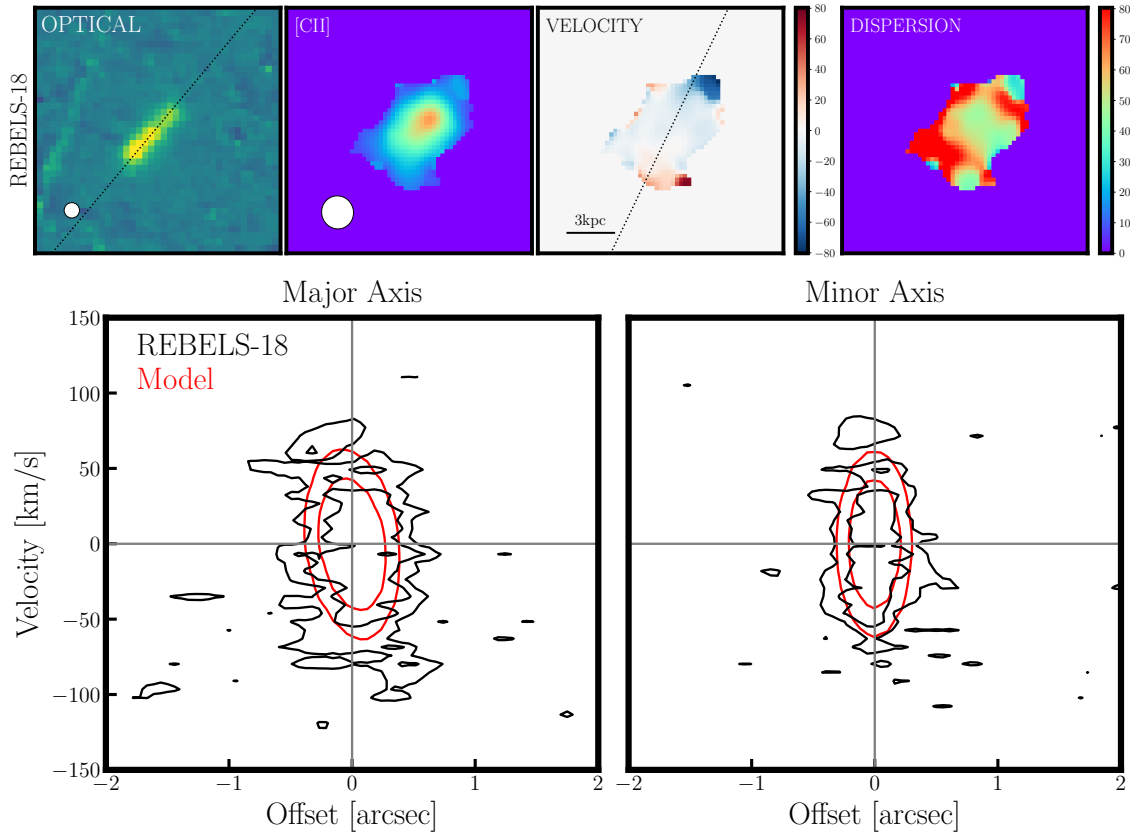

Figure 4.3: REBELS-18 velocity maps and position-velocity diagrams: see Fig. 4.1 for details.

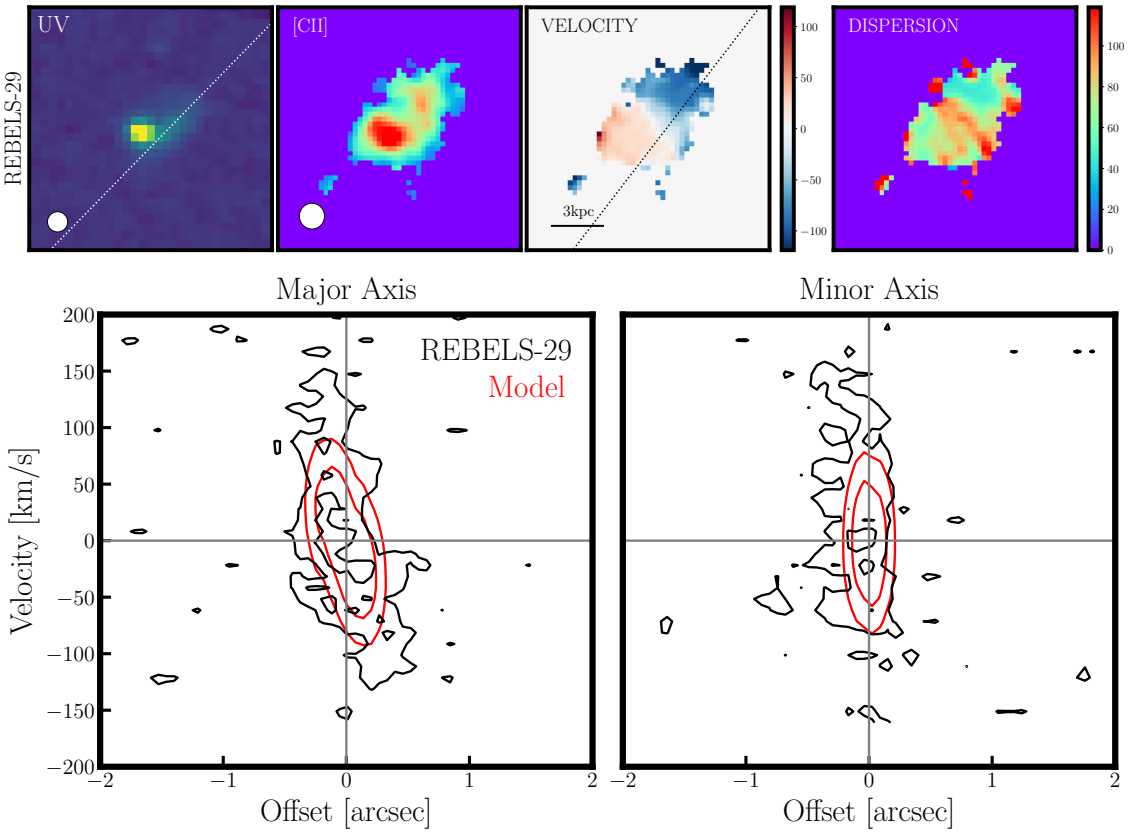

Figure 4.4: REBELS-29 velocity maps and position-velocity diagrams: see Fig. 4.1 for details, noting that we here show the rest-UV image in place of the rest-optical.

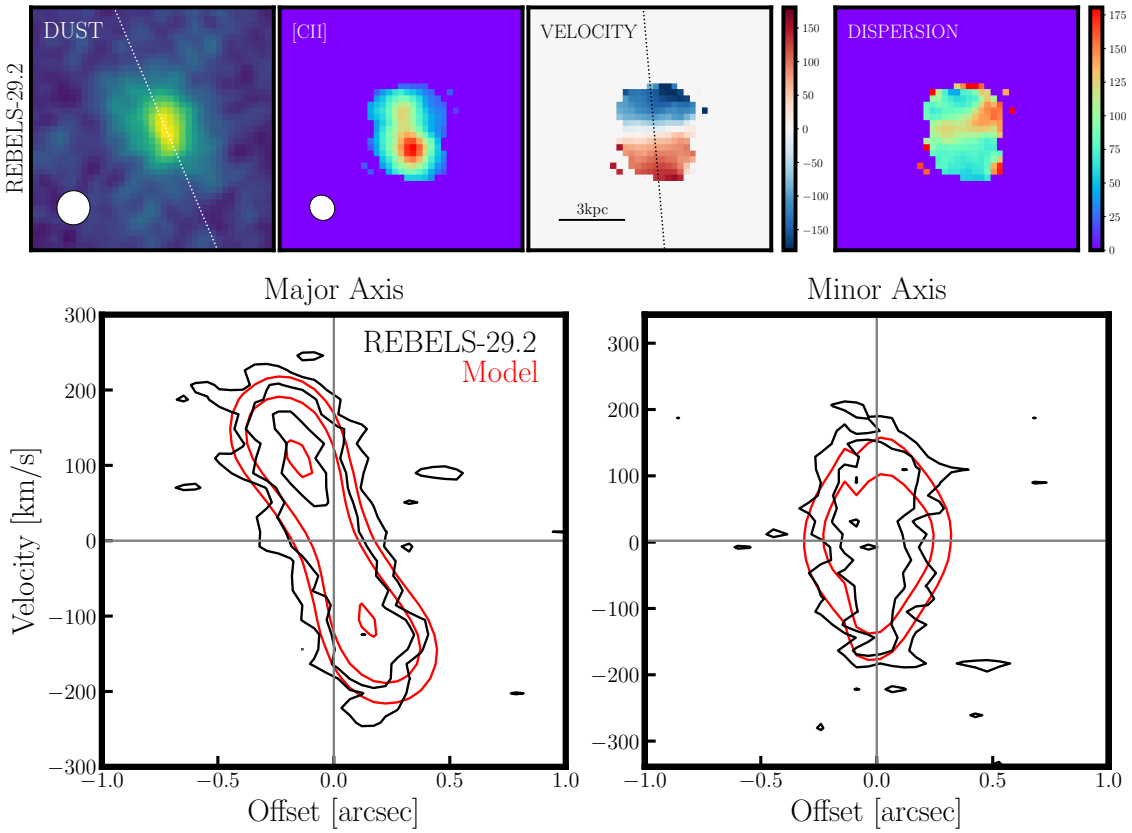

Figure 4.5: REBELS-29-2 velocity maps and position-velocity diagrams: see Fig. 4.1 for details, noting that we here show the FIR continuum image in place of the rest-optical.

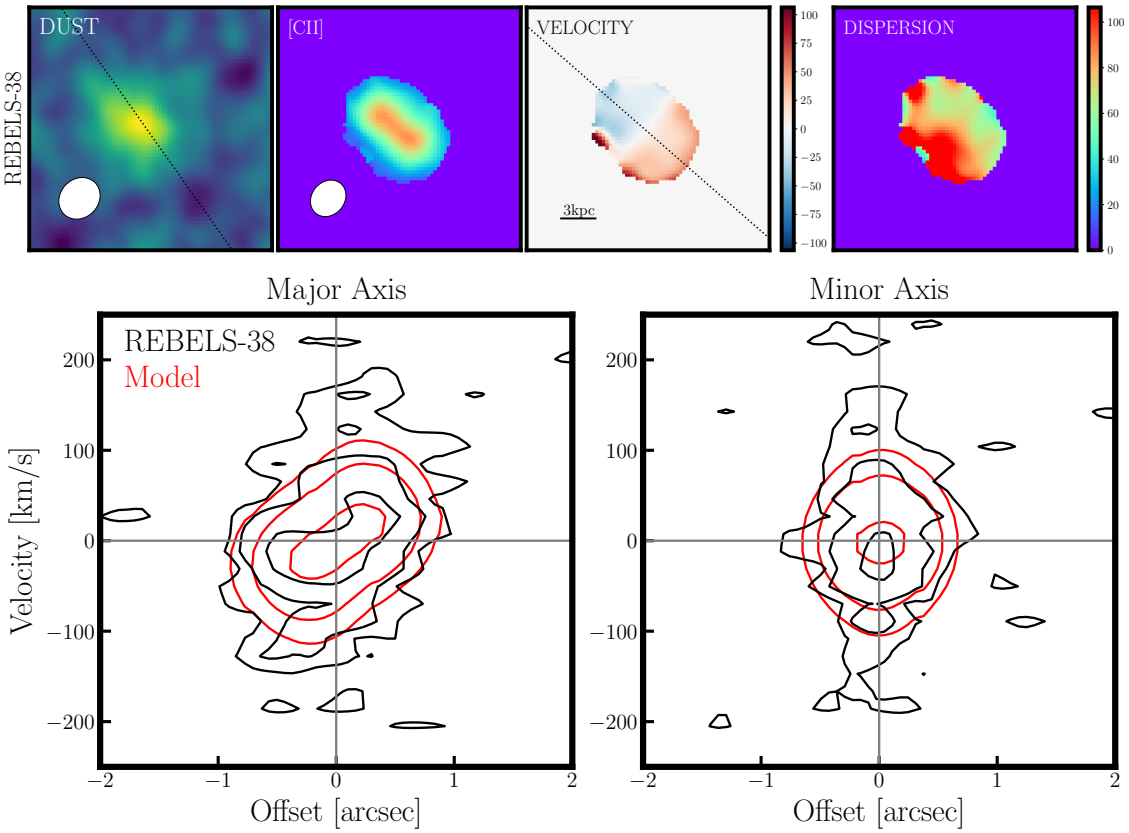

Figure 4.6: REBELS-38 velocity maps and position-velocity diagrams: see Fig. 4.1 for details, noting that we here show the FIR continuum image in place of the rest-optical.

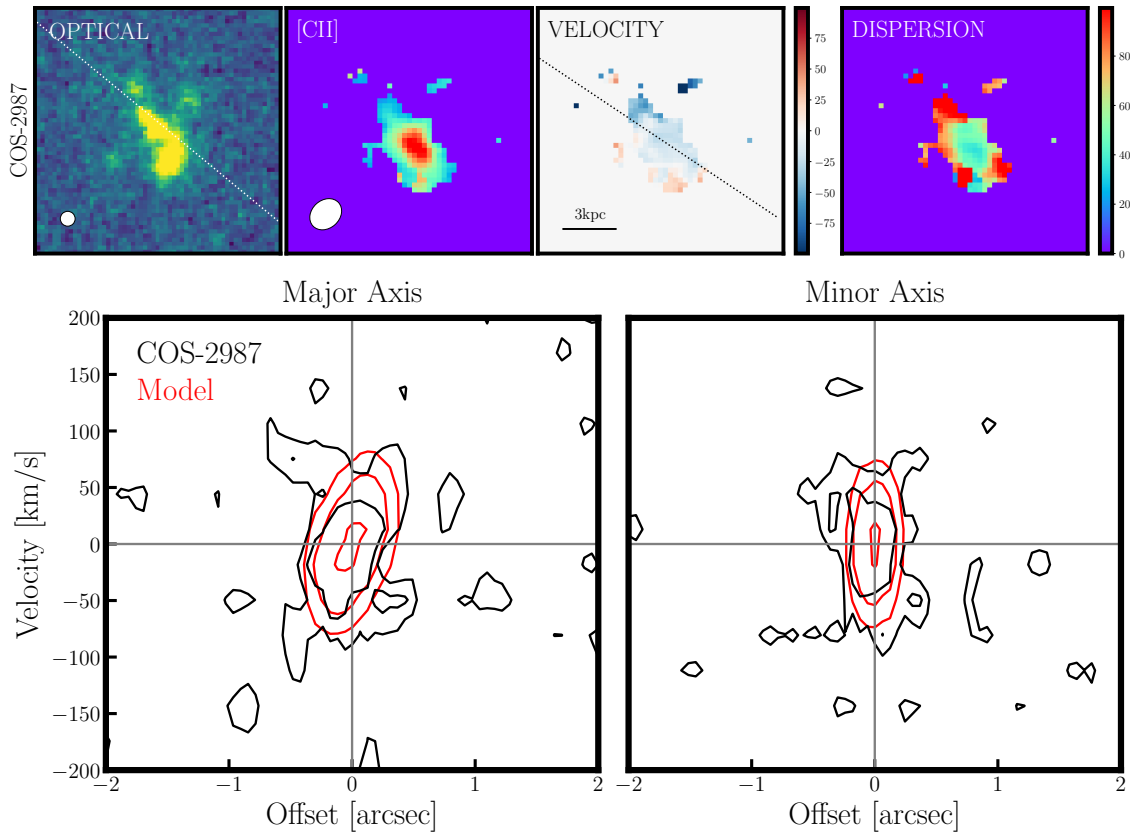

Figure 4.7: COS-2987 velocity maps and position-velocity diagrams: see Fig. 4.1 for details.

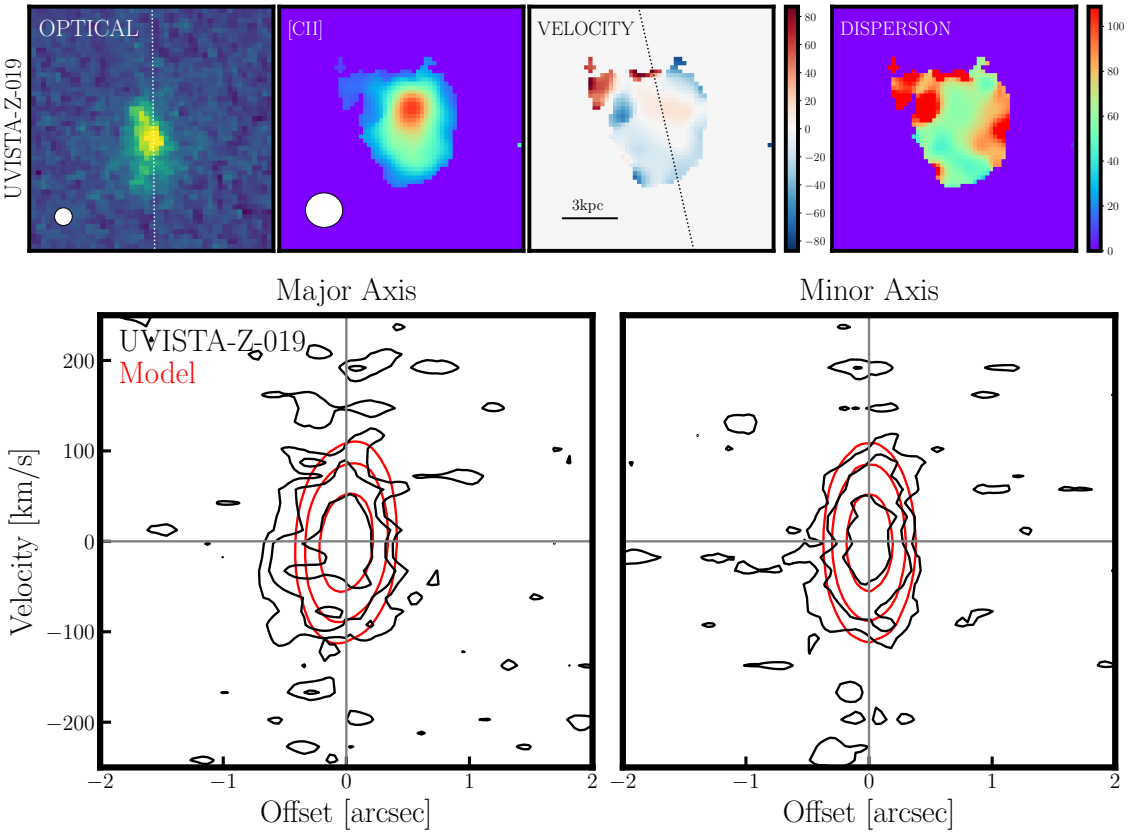

Figure 4.8: UVISTA-Z-019 velocity maps and position-velocity diagrams: see Fig. 4.1 for details.

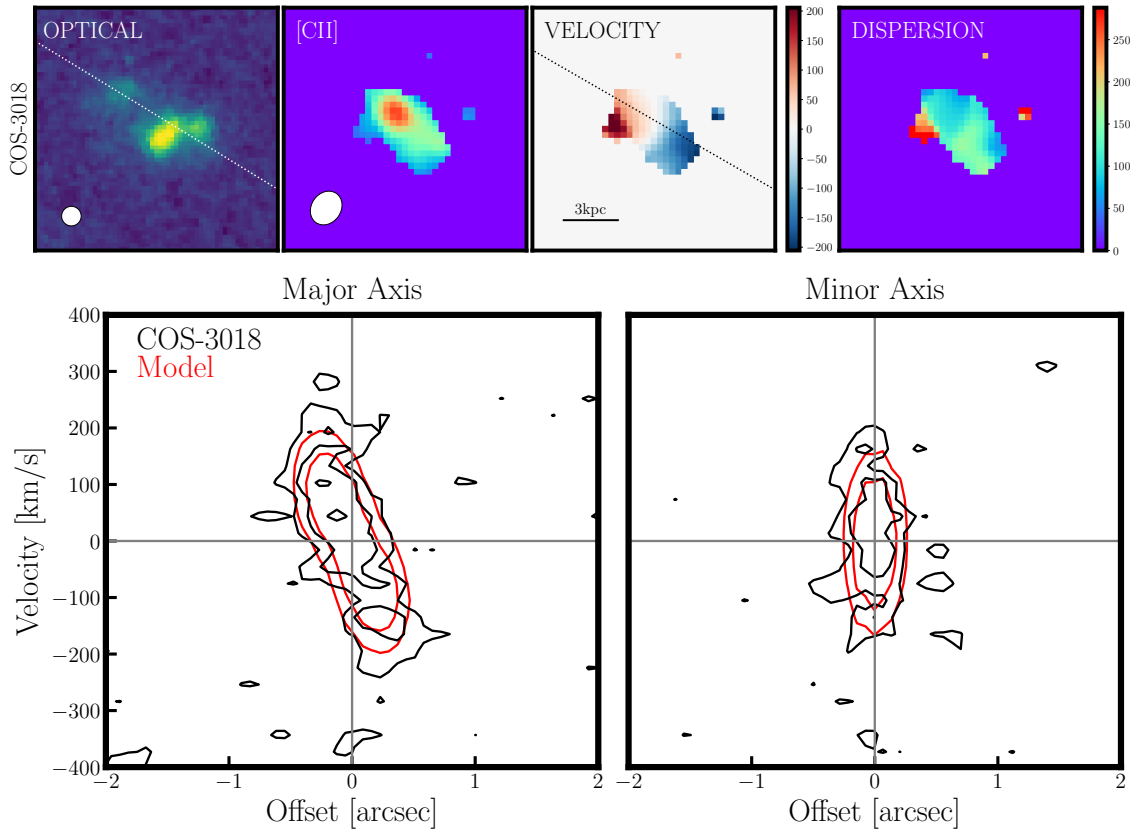

Figure 4.9: COS-3018 velocity maps and position-velocity diagrams: see Fig. 4.1 for details.

4.4 Galaxy Classification: Disks

Velocity maps are frequently used as indicators of a galaxy's dynamical type, with disk galaxies expected to display a smooth gradient in the velocity field. A set of five criteria for the positive identification of a disk based on its velocity maps was outlined by Wisnioski et al. (2015) for the KMOS^{3D} warm gas survey. These criteria were adapted for applicability to higher redshift [CII] kinematic analysis by Jones et al. (2021) for the ALPINE survey, in which a galaxy is typically considered a rotating disk candidate if three of the criteria are met, and is otherwise classified as a merging or disturbed system. The Jones et al. (2021) criteria for a disk galaxy are:

(a) A 1D velocity profile extracted along the kinematic major axis should exhibit a significant ($> 3\sigma$) slope.

(b) The average rotational velocity should be greater than the average dispersion in each fitted ring.

(c) The location of the average between the minimum and maximum of the velocity field should lie within one beamwidth of the velocity dispersion peak.

(d) The kinematic position axis should be within 30° of the morphological position axis.

(e) The location of the average between the minimum and maximum of the velocity field should lie within one beamwidth of the intensity peak.

In addition to these five morpho-kinematic conditions for the confirmation of disk structure, we consider two further proposed disk criteria. The first of these is the ratio of the maximum rotational velocity to the average velocity dispersion across all fitted rings ($v_{rot,\ max}/\langle\sigma\rangle$: hereafter and elsewhere v/σ). Secondly, we consider the results of fitting our PV diagrams with PVSplit (Rizzo et al., 2022), a code introduced in Section 2.5.1 which separates galaxies into the disk and non-disk parameter spaces on the basis of the symmetry and morphology of their PV diagrams. Therefore, for the sake of completeness, we test rotating disk candidates against the Jones et al. morpho-kinematic criteria in combination with the v/σ ratio, and the

PVSplit method.

Galaxies that we consider rotating disk candidates and so subject to these tests are all those with a v/σ ratio > 1. Galaxies with $v/\sigma < 1$ are considered dispersion-dominated and hence excluded from the disk classification. The results of the disk tests are provided below.

4.4.1 Morpho-kinematic Criteria

(a) The velocity profile extracted from the kinematic major axis exhibits a slope at $> 3\sigma$ significance for all galaxies except for COS-2987.

(b) The condition of the rotational velocity $v_{\rm rot}$ exceeding the velocity dispersion σ in every fitted ring is met for only three galaxies: REBELS-5, REBELS-29-2, and COS-3018. The rotational velocity exceeds the velocity dispersion in the majority of fitted rings for all galaxies except for COS-2987.

(c) For improved accuracy, we elect here to consider the fitted kinematic centre of the galaxy instead of the location of the average between the maximum and minimum of the velocity map. To measure the location of the velocity dispersion peak, we mask out the outer layer of pixels around the perimeter of the galaxy to negate edge effects. We then take the location of the pixel with the maximum velocity dispersion as representing the location of the σ peak. The separation between the kinematic centre and velocity dispersion peak is within the circularised beam diameter for two galaxies: REBELS-29-2 and COS-3018.

(d) The condition of the morphological and kinematic position axes being coincident within 30° is met for all turbulent disk candidates except for REBELS-5 and REBELS-38.

(e) We compare the locations of the fitted kinematic centre and the morphological centre fitted by Galfit, which we take to represent the intensity peak, while noting that the morphological centre is not measured from a uniform tracer across the sample of turbulent disk candidates. The kinematic and morphological centres are co-incident within one circularised beam radius for

REBELS-29-2, COS-2987 and COS-3018. The separation is between a circularised beam radius and circularised beam diameter for REBELS-8, REBELS-29 and REBELS-38, and approximately equal to the circularised beam diameter for REBELS-5.

Only two galaxies, REBELS-29-2 and COS-3018, pass every one of the morpho-kinematic criteria. However, every galaxy except for COS-2987 passes at least three criteria, which is all that is required of a galaxy to be classified as a disk in Jones et al. (2021).

4.4.2 Quantifying Rotational Support

The ratio of rotational velocity to velocity dispersion (v_{rot}/σ) quantifies the degree of rotational support within a system. Wisnioski et al. (2015) consider $v_{rot}/\sigma > 1$ as a criterion for the confirmation of a disk, but Förster Schreiber and Wuyts (2020) note that the chosen v_{rot}/σ threshold for disk identification can vary between 1-3 across various studies. The intermediate value of $\sqrt{3.36}$ represents equal contributions from rotational and random motion to the dynamical maintenance of a turbulent disk. In this work, we take a value of $v_{rot}/\sigma > 3$ as indicative of a dynamically cold disk and $v_{rot}/\sigma < 1$ of a non-disk, considering the parameter space $1 < v_{rot}/\sigma < 3$ as suggesting a turbulent disk. Furthermore, the v_{rot}/σ ratio itself is variously defined in literature (Wisnioski et al., 2015; Di Teodoro et al., 2016; Harrison et al., 2017; Swinbank et al., 2017; Turner et al., 2017; Lelli et al., 2018; Rizzo et al., 2020), with the two most commonly employed formalisms being the ratio between the maximum velocity and the mean velocity dispersion, and the ratio between the flat region of the rotation velocity curve and the velocity dispersion in the outer extent of the galaxy. We use the former definition in this work.

The ^{3D}BAROLO velocity measurements for our sample are recorded in Table 4.1, from which we see that REBELS-18 and UVISTA-Z-019 are dominated by turbulent random motions, and REBELS-29-2 is classified as a dynamically cold disk alongside REBELS-25, which was confirmed as the highest-redshift dynamically cold disk then discovered by Rowland et al. (2024). The other six galaxies fall within the parameter space occupied by galaxies with both random and rotational support, and from this evidence in isolation could be considered 'turbulent disks'.

4.4.3 PVSplit Results

The fitted position velocity diagrams provide a further diagnostic. As discussed in Section 2.5.1, a rotating disk galaxy hosting only rotational motion is expected to display an S-shaped major axis PV diagram with no emission outside of this region, and will also demonstrate symmetry in the minor axis PV diagram with respect to the axes defining the systemic velocity and the centre. Based on the morphology of the fitted PV diagrams, the algorithm PVSplit (Rizzo et al., 2022) classifies galaxies into disks and non-disks. Rowland et al. (2024) find that it classifies REBELS-25 as a disk, and in Figure 4.10 we place the remaining nine galaxies from the REBELS-HR sample on the PVSplit parameter space. Three galaxies are classified by this method as disks in addition to the confirmed disk REBELS-25: REBELS-29-2, a dynamically cold disk, REBELS-38, a turbulent disk, and REBELS-18 which is dispersion-dominated, as we will examine in Section 4.6.

4.5 Merging Systems

We test the galaxies that show potential signatures of merging activity to determine whether or not they are merging systems, and if so, whether they are minor or major mergers.

REBELS-8 is identified as a potential merger due to the low velocity ('blue') clump visible in its velocity map (Figure 4.2) which is spatially coincident with a region of high velocity dispersion. REBELS-29, though it displays a smooth and apparently disk-like velocity gradient (Figure 4.4), is considered a merger candidate due to its 'banana-shaped' optical, UV and Hα emission (Figure 3.16).

We consider REBELS-38, COS-2987 and COS-3018 to be potential merging systems due to their clumpy structure and irregular velocity dispersion distribution, which could be potentially attributed to the impact of merger activity.

To distinguish between major and minor mergers, we calculate the mass ratio of constituent components within a galaxy. Major mergers are considered to be those with a mass ratio between 1:1 and 1:3 (e.g. Shapiro et al., 2008; Hopkins et al., 2009) or 1:4 (e.g. Simons et al., 2019), with minor mergers being systems with $0.1 \lesssim M_1/M_2 \lesssim 0.25$. Simons et al. (2019) further define 'very minor' mergers as

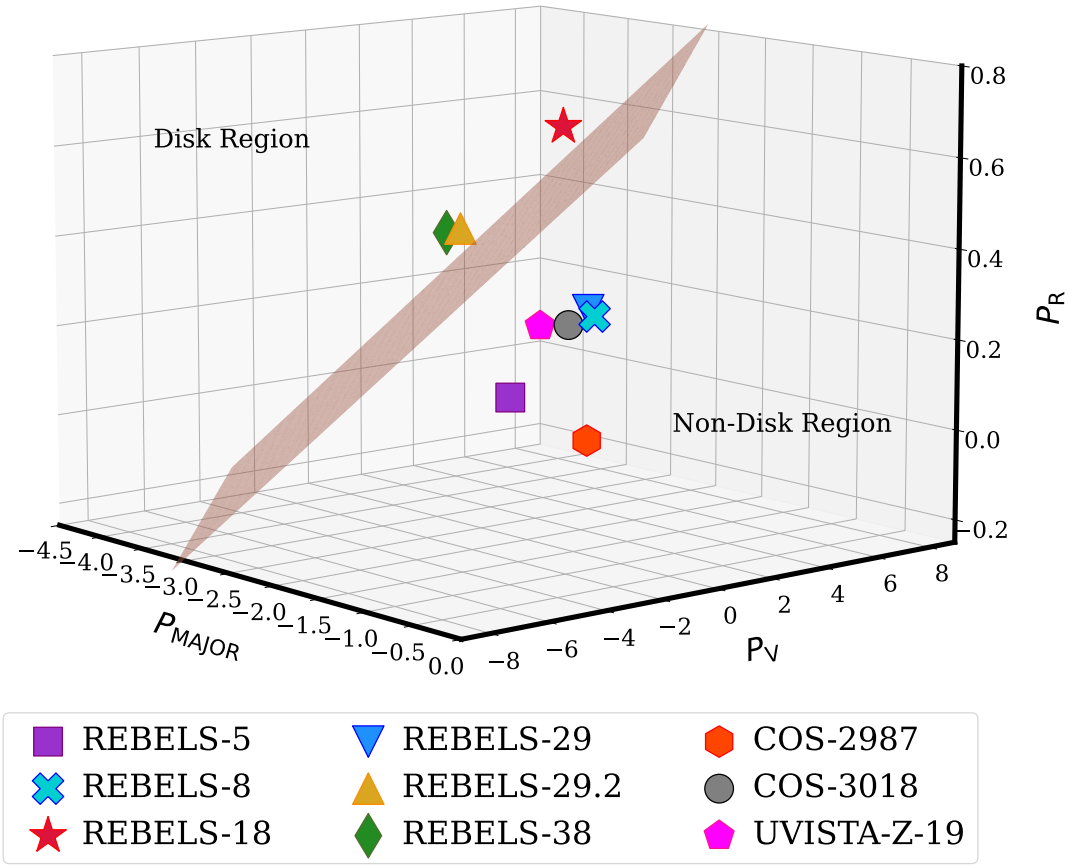

Figure 4.10: REBELS-HR galaxies placed on the PVSplit parameter space, showing the plane of best division between the disk and non disk regions. REBELS-25, not shown here, is classified as a disk by PVSplit (Rowland et al., 2024).

those with mass ratios between 1:10 and 1:30.

We estimate the mass ratio for REBELS-8 by extracting the spectrum over the region of the blue clump and fitting a double Gaussian profile with two peaks corresponding to the positions in velocity space of the clump and emission from the main component. We estimate the dynamical masses of the two components from Equation 2.6, using the FWHMs fitted to the two Gaussian components and the morphological inclination angle and radius (Table 3.6). We assume $R_{clump} = R_{galaxy}$ to obtain an upper limit on the mass ratio of 0.1, which would identify REBELS-8 as a minor merger. However, since the radius of the clump feature is expected to be lower than the galaxy radius, we can infer that the true mass ratio would likely indicate a 'very minor' merger.

For REBELS-29, it is not possible to define a mask from the velocity maps (Figure 4.4) that would separate the galaxy into distinct components. We therefore measure the luminosity ratio as a proxy for the mass ratio (e.g. Lambas et al., 2012). Given that the Galfit fitting to the rest-UV is more robust than that to the rest-optical, we calculate the luminosity ratio of the two components fitted by Galfit in the rest-UV. The measured $L_{1,UV}/L_{2,UV}$ ratio is 0.55, which would identify the galaxy as a major merger, albeit with the caveat that the rest-UV may not accurately trace the mass distribution.

For REBELS-38, COS-2987 and COS-3018, we estimate the contribution of potential mergers by comparing the disk and non-disk emission using the same method we employ in Appendix A.5. We isolate the disk emission by masking the data with the disk mask created by ^{3D}BAROLO , and the non-disk emission by applying the inverse mask alongside a spatial constraint to avoid incorporating background noise. We sum the flux of the disk and non-disk emission and use these measurements to calculate the disk:non-disk ratio. For these galaxies, the disk masking approach is preferable to the spectral fitting method employed for REBELS-8. In the case of REBELS-38, this is because the spectrum extracted over the high-velocity ('red') clump visible in the velocity map (Figure 4.6) does not have a sufficiently high SNR to robustly fit a double Gaussian profile to the galaxy and clump peaks.
In the case of COS-2987, it is because the galaxy hosts multiple high-dispersion clumps distributed across its extent (Figure 4.7).

The spectrum extracted over the region of the high-velocity ('red') clump present in COS-3018 (Figure 4.9) does, however, show a double Gaussian profile for which the SNR is high enough to permit fitting. We are therefore able to compare the merger ratio obtained for COS-3018 through both methods.

From the disk masking approach, we measure a non-disk/disk ratio of 0.07 for REBELS-38, 0.06 for COS-2987, and 0.1 for COS-3018. Fitting the spectrum extracted from the clump region of COS-3018 with a double Gaussian profile yields a dynamical mass ratio of 0.14. Comparing the classifications returned by these two methods for COS-3018, we see that they are broadly consistent in that both would identify the galaxy as a minor merger.

From this analysis, we would identify one major merger (REBELS-29), two minor mergers (REBELS-8 and COS-3018) and two galaxies that either host very minor mergers, or are complex systems comprising other sources of non-circular motion such as outflows (REBELS-38 and COS-2987).
Romano et al. (2021) measure the fraction of major mergers at $z = 4.5$ and $z = 5.5$ from morpho-kinematic analysis of the ALPINE galaxies, using low resolution ($\sim 1''$) [CII] observations, finding that the fraction is 0.44 at $z \sim 4.5$ and 0.34 at $z \sim 5.5$. Romano et al. derive a relation between the merger fraction and redshift by combining their results with lower redshift observations, and find that the evolution of the merger fraction over cosmic time takes the form of a rapid increase from $z \sim 0$ up to a peak at $z \sim 3$, followed by a gradual decrease with increasing redshift. Dalmasso et al. (2024) visually identify mergers from NIRCam imaging to measure the merger rate in the redshift range $4 < z < 9$, finding a redshift independent major merger fraction of $f_m = 0.11 \pm 0.04$. As we identify one major merger out of ten galaxies, our major merger fraction would be 0.1, and is therefore consistent with this result.

4.6 Dispersion-Dominated Galaxies

We classify REBELS-18 and UVISTA-Z-019 as dispersion-dominated galaxies on the basis of their lack of any observable velocity structure, and their v/σ ratios being < 1 (0.6 and 0.7 for REBELS-18 and UVISTA-Z-019 respectively). Newman et al.

(2013) observe that dispersion-dominated galaxies at $z \sim 2$ are typically small, while REBELS-18 is the second-largest galaxy in our sample by measured effective radius in the rest-optical and the size of UVISTA-Z-019 is representative of the sample (see Table 3.6). It is reasonable to expect that the small size of dispersion dominated galaxies at $z \sim 2$ does not translate to the EoR, where galaxies are typically smaller; no galaxy in the REBELS-HR sample has an effective radius as high as the threshold Newman et al. (2013) use to define a small galaxy ($R_{1/2} < 3$ kpc).

However, our kinematic fitting routine yields significantly different results for the two dispersion-dominated galaxies. ^{3D}BAROLO fits a disk model with a relatively low velocity dispersion of $35.5^{+4.4}_{-4.1}$ km/s for REBELS-18 (Table 2.2), below the sample median of 39.8 km/s, and based on the PV diagram morphology PVSplit categorises the galaxy as a disk. This is in contrast to UVISTA-Z-019, which has a high fitted velocity dispersion of $53.4^{+5.0}_{-4.7}$ and is categorised by PVSplit as a non-disk galaxy. We consider what could cause this difference in the fitting results between two galaxies that appear to show very similar properties from a visual inspection of their velocity fields (Figures 4.8 and 4.3), and attribute the discrepancy to the presence of a feature in UVISTA-Z-019 we associate with gaseous outflows, which we present in the following.

4.6.1 Candidate Gaseous Outflows in UVISTA-Z-019

The presence of broad wings in the tails of bright FIR lines is considered a signature of outflows at high redshift. AGN-driven outflows have been identified in this way (e.g. Maiolino et al., 2012), and strong evidence for outflows driven by star formation in galaxies at $z \geq 5$ has come from spectral stacking to reveal this feature. Through stacking the spectra of [C II] emitting galaxies, Gallerani et al. (2018) and Ginolfi et al. (2020) identify spatially and spectrally extended gas consistent with the presence of outflows. It is rare for outflows to be identifiable in a single source without spectral stacking, though Herrera-Camus et al. (2021) identify a broad Gaussian emission component aligned with the galactic minor axis, attributed to outflowing gas, in a normal star forming galaxy at $z \sim 5.5$.

At low resolution, Schouws et al. (2022) find intriguing evidence of complex structure within UVISTA-Z-019, with the [CII] emission in the centre of the galaxy showing

two distinct Gaussian components, one broad and one narrow. We find that this complex emission line structure persists at high resolution; from the [CII] morphology in Figure 3.21 we see that the galaxy exhibits a complex structure in [CII], being highly extended with a diffuse component visible on either side of the main galaxy. We identify the frequency ranges defining the red and blue wings of the emission line and plot the spectra of the components with signal of $> 2\sigma$ at these frequencies, confirming that double Gaussian fitting including a broad and narrow emission component provides a better fit, according to χ^2 values, than a single Gaussian. These spectra and their fitting profiles are shown in Figure 4.11.

We can furthermore associate the diffuse components of the [CII] morphology with the red and blue wings of the emission line, finding that the red wing is more extended but has a smaller velocity offset, while the blue wing has a more compact morphology but a high velocity offset from the emission line peak of the main body. We interpret this signal as a bimodal outflow signature, casting UVISTA-Z-019 as a potential high redshift analogue of M82 (Lynds and Sandage, 1963). This is particularly compelling in the context of JWST observations revealing a diverse range of star formation histories (e.g. Endsley et al., 2024), and finding that at least some galaxies in the early Universe are far less intensively star-forming compared to the picture we gained from Spitzer. For quenching to be as rapid as indicated by the star formation histories of the mini-quenched galaxies discovered by JWST (e.g. Strait et al., 2023; Looser et al., 2024), cold gas must be ejected through internal feedback, as we see in UVISTA-Z-019.

We follow the method of Hygate et al. (2023) in calculating an outflow velocity for each component according to

$$v_{out} \sim |\Delta v| + \frac{\mathrm{FW}_{10\%}}{2} \tag{4.1}$$

where $|\Delta v|$ is the difference in velocity between the centres of the emission line and outflow spectra, and $FW_{10\%}$ is the full width at tenth maximum of the outflow spectrum. We estimate a projected outflow velocity of $\sim$500 km/s for the red component, and $\sim$800 km/s for the blue component, comparable to the 900 km/s projected outflow velocity Hygate et al. (2023) calculate for REBELS-25. We obtain a lower limit on the mass contained within the outflows from their spectra using

Equation 2.6.

We fit Sérsic profiles to the morphology of each emission component to estimate their sizes, and given the masses, velocities and sizes we obtain the clearing timescale. It is cold gas that must be ejected in order to rapidly shut down star formation, but this is more difficult to remove with feedback from supernovae, and simulations generally predict outflows to be more present in hot gas (e.g. Gelli et al., 2024; Kohandel et al., 2024), so the outflows are likely to be stronger than we measure with only the [CII] view. However, our estimate indicates that the outflows are strong enough to remove all of the cold ISM gas within only 12 Myr, which suggests UVISTA-Z-019 could be a galaxy actively transitioning from a star-forming to a mini-quenched state.

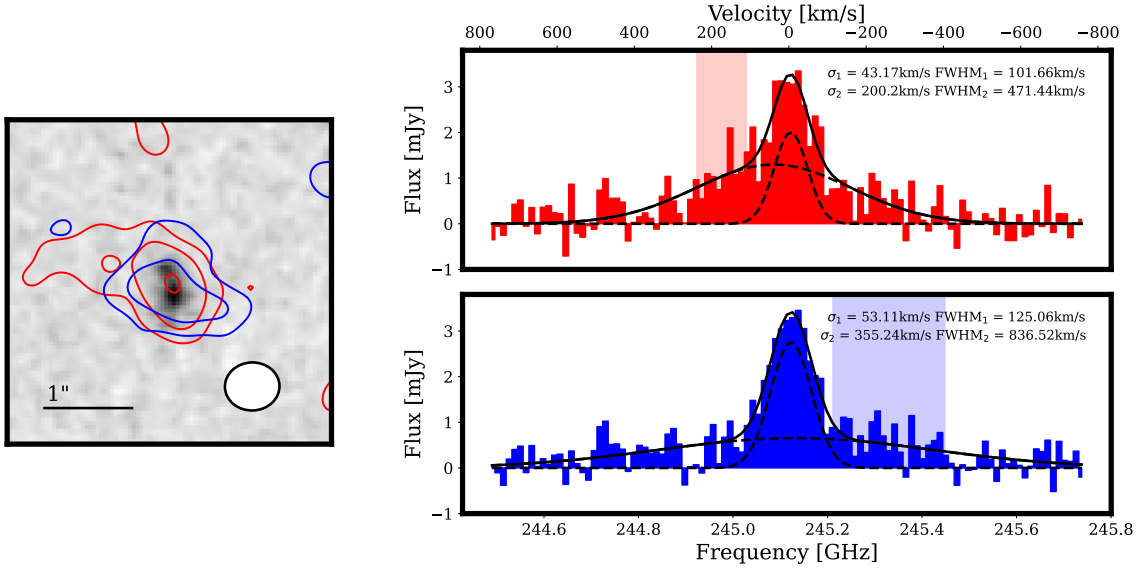

Figure 4.11: LHS: Rest-frame UV emission for UVISTA-Z-019 from the Hubble Space Telescope overlaid with $2^n\sigma$ contours from the red and blue wings of the emission line. RHS: Spectra representing the red wing (above) and the blue wing (below) of the emission line, and their Gaussian fits as black lines (composite: solid line, component fits: dashed line). The shaded region in each spectrum represents the frequency range of the wing.

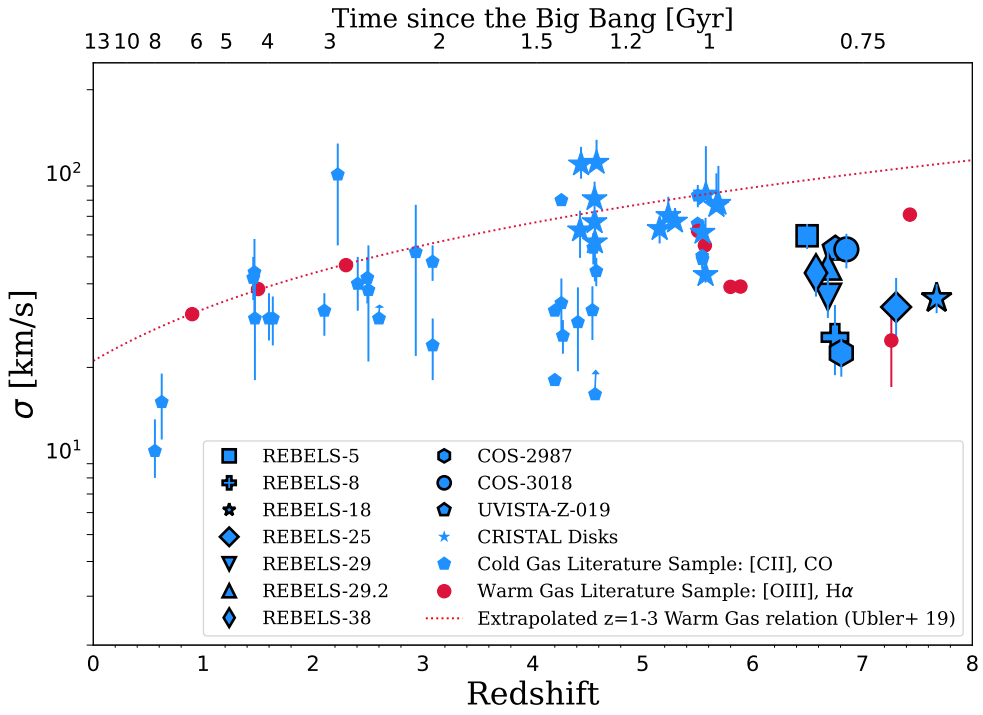

Figure 4.12: Velocity dispersion evolution with redshift in the context of literature samples. The cold gas literature sample is compiled from: Neeleman et al. (2020), Rizzo et al. (2020), Jones et al. (2021), Herrera-Camus et al. (2022), Pope et al. (2023), Rizzo et al. (2023), and Lee et al. (2025b). Warm gas data are from De Graaff et al. (2024), and the warm gas $\sigma - z$ relation is extrapolated from Übler et al. (2019).

4.7 Evolution of Velocity Measurements across Cosmic Time

In Figure 4.12 we see the velocity dispersion measurements for each of the REBELS-HR galaxies set in the context of literature sources and the extrapolated $\sigma - z$ relation established by Übler et al. (2019) at $z < 3$. Our measured velocity dispersions are significantly lower than would be expected from extending the Übler et al. (2019) relation to higher redshift. This is not unexpected, as this relation is calculated using warm gas observations, and as previously mentioned in Section 1.5 and explored in Chapter 2, it is not possible to make a direct 'apples-to-apples' comparison between kinematics measured by cold and warm gas. However, we note that the CRISTAL galaxies (Lee et al., 2025b) at $4 < z < 6$ appear to follow the relation,

with typically higher σ measurements than we obtain. This is somewhat surprising as the CRISTAL galaxies included in the comparison are the subset of the entire CRISTAL sample that have been identified as disks by Lee et al. (2025b), and so would be expected to have lower velocity dispersion measurements relative to the general galaxy population in this redshift range. However, considering the full literature sample of cold gas measurements we present in Figure 4.12, our results are consistent with there being little to no evolution in velocity dispersion as measured by cold gas tracers across cosmic time, though there is a large scatter.

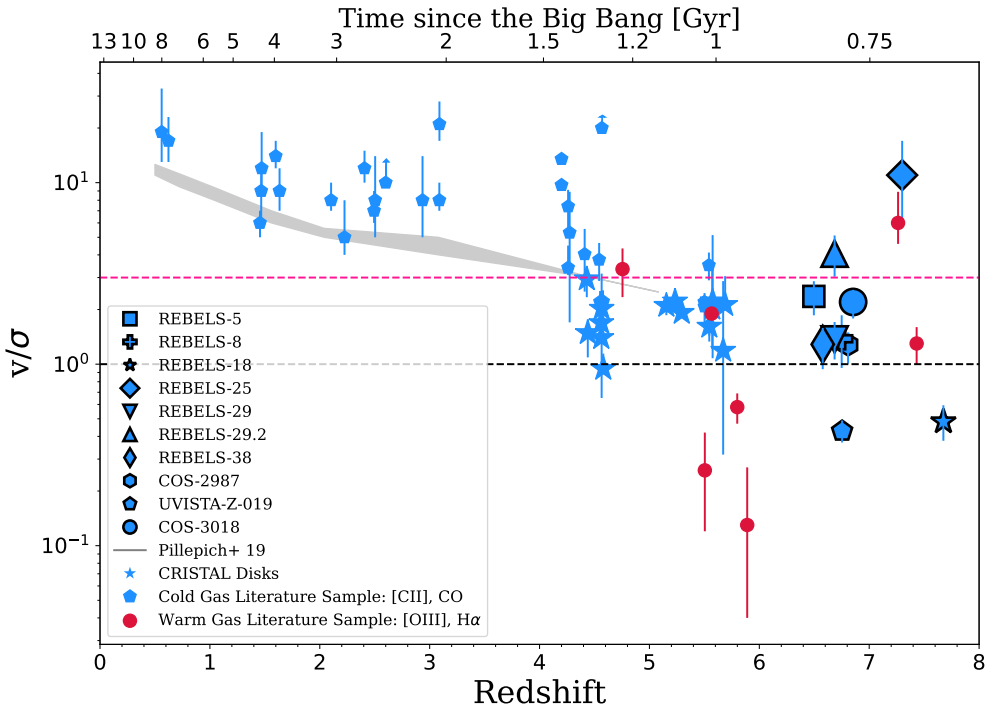

Figure 4.13: Evolution of the v/σ ratio over cosmic time in the context of literature samples. Our literature sources are as in Figure 4.12, and we plot the $v/\sigma - z$ relation established with the Illustris TNG simulations in Pillepich et al. (2019). The grey horizontal line represents $v/\sigma = 1$, the turbulent disk threshold, and the pink line $v/\sigma = 3$, the settled disk threshold in this work.

Figure 4.13 shows the evolution of the rotational velocity to velocity dispersion ratio v/σ across cosmic time, where v/σ quantises the degree of rotational support within a galaxy. We see that two of our galaxies are dynamically cold, and two of the galaxies are dominated by turbulent motions, with the majority of the sample occupying

Table 4.1: Velocity measurements fitted by 3DBarolo. v_{rot} is the maximum rotation velocity and σ is the average velocity dispersion across all fitted rings, with v/σ being the ratio between these values.

REBELS ID	v_{rot} [km/s]	σ [km/s]	v_{rot}/σ
REBELS-5	154^{+47}_{-41}	60^{+6}_{-6}	$2.5^{+0.8}_{-0.7}$
REBELS-8	42^{+7}_{-5}	$25.7^{+5.8}_{-5.3}$	$1.6^{+0.5}_{-0.4}$
REBELS-18	20^{+6}_{-5}	36^{+4}_{-4}	$0.6^{+0.2}_{-0.2}$
REBELS-25 [a]	374^{+86}_{-91}	33^{+9}_{-7}	11^{6}_{5}
REBELS-29	60^{+9}_{-7}	36^{+6}_{-6}	$1.7^{+0.4}_{-0.4}$
REBELS-29-2	212^{+27}_{26}	46^{+6}_{-5}	$4.6^{+0.8}_{-0.8}$
REBELS-38	95^{+18}_{-19}	44^{+5}_{-6}	$2.2^{+0.5}_{-0.5}$
COS-2987	38^{+6}_{-6}	23^{+3}_{-4}	$1.7^{+0.3}_{-0.4}$
UVISTA-Z-019	39^{+3}_{-2}	53^{+5}_{-5}	$0.7^{+0.1}_{-0.1}$
COS-3018	137^{+25}_{-20}	53^{+6}_{-6}	$2.6^{+0.6}_{-0.5}$

[a] Rowland et al. (2024)

the region of parameter space representing turbulent disks. Our results are consistent with the trend identifiable in the literature cold gas kinematics sample of the v/σ ratio decreasing with increasing redshift, with significant scatter. However, all of the CRISTAL disk galaxies are identified as turbulent disks, suggesting that there may not be significant evolution in cold gas measurements of the v/σ ratio between $z = 4$ and $z = 8$. As previously demonstrated in Figure 4.12, the measured velocity dispersion is low relative to the literature measurements using [CII] at $z \sim 4-6$, yet the v/σ measurements are consistent, which indicates that our measured rotational velocities are relatively low.

4.8 Dynamical Mass

For the dispersion-dominated galaxies, REBELS-18 and UVISTA-Z-019, we calculate dynamical mass according to the Cappellari et al. (2006) formalism:

$$M_{dyn} = K(n)\frac{r_e\sigma_0^2}{G} \tag{4.2}$$

where $K(n)$ is the virial coefficient, defined on the Sérsic index:

$$K(n) = 8.87 - 0.831n + 0.0241n^2$$

. For the rest of the sample, we calculate dynamical mass using the equation

$$M_{dyn}(< R) = k(R)\frac{Rv_{circ}^2(R)}{G} \tag{4.3}$$

evaluated at $R = r_e$, where $k(R)$ is the virial coefficient at radius = R. Price et al. (2022) derive the values of this coefficient across a range of measurements of the Sérsic index (n) and intrinsic axis ratio (q). We take k as 1.8, which corresponds to $n = 1$, an exponential disk, and $q = 0.2$, a typical assumption for a thin disk (e.g. van der Wel et al., 2014; Rowland et al., 2024).

In Figure 4.14 we show the comparison of the dynamical mass to the stellar mass and baryonic (stellar + gas) mass. We take the stellar mass from literature, and calculate the gas mass by converting the literature [CII] luminosity (Schouws et al., 2022; Algera et al., 2025; Harikane et al., 2025) to $M_{[CII]}$ using the relation $M_{[CII]} = \alpha L_{[CII]}$. There is a strong discrepancy among values of α derived in the

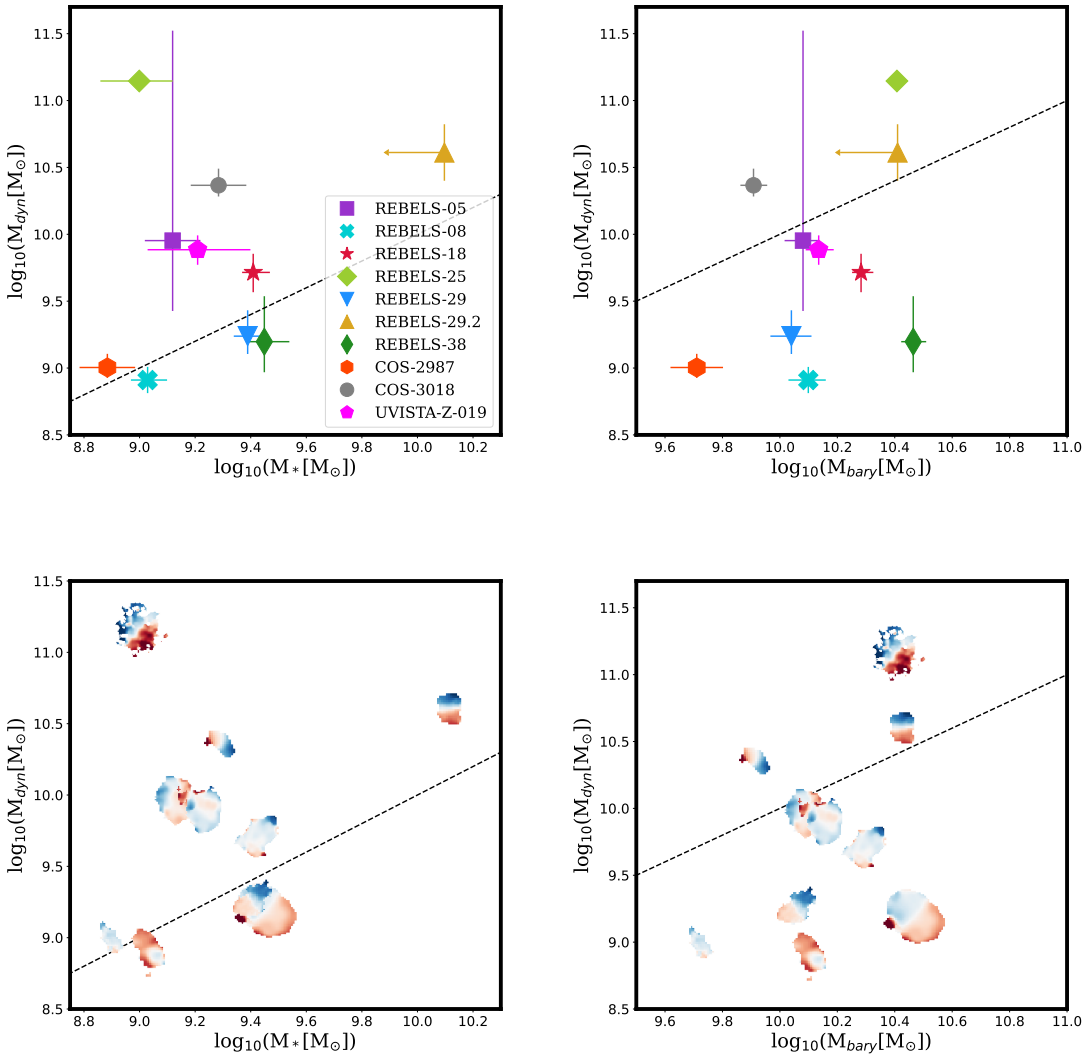

Figure 4.14: A comparison of the dynamical mass with the stellar (first column) and baryonic (second column) masses. The first and second rows show identical data, presented in the first row as points with associated errorbars, while in the second row the galaxies are represented by their velocity maps. The line of equality is plotted as a black dashed line.

literature, from $\alpha \approx 130 M_\odot/L_\odot$ measured by Madden et al. (2020) from observations of local and mainly low metallicity galaxies, to $\alpha = 7^{+4}_{-1} M_\odot/L_\odot$ from a study of dusty star forming galaxies at $z \sim 4.5$ (Rizzo et al., 2021). Simulations in the Epoch of Reionization tend to recover lower values in the range $\alpha = 10 - 18$ (Pallottini et al., 2017a; Vizgan et al., 2022). The physical origins from which these variations arise are briefly discussed in Aravena et al. (2024) and Algera et al. (2025). In this work, as in Algera et al. (2025), we adopt the commonly employed definition of $\alpha = 31^{+31}_{-15} M_\odot/L_\odot$ from Zanella et al. (2018).

We follow Posses et al. (2023) in evaluating the dynamical mass at the effective radius, and comparing this measurement to one half of the stellar/baryonic mass. The dynamical mass encompasses all gravitationally interacting matter within the galaxy, including stellar, gas and dark matter. The dynamical mass is therefore expected to be greater than the baryonic mass in all cases, but we find that this is not true for the REBELS-HR sample. Only COS-3018, REBELS-29-2 and REBELS-25 have a dynamical mass higher than their baryonic mass, and it is worth noting that of these three galaxies, two are dynamically cold disks and one is a turbulent disk with a relatively strong rotational gradient. Three of the galaxies, REBELS-08, REBELS-29 and REBELS-38, have higher stellar masses than dynamical masses, although they are within 1σ of the line of equivalence between M_{dyn} and M_*.

In Figure 4.15, we see the stellar mass fraction as a function of redshift, placing the REBELS-HR galaxies in context with the Wuyts et al. (2016) and Lee et al. (2025b) samples. We see that this could be interpreted as showing the stellar mass fraction decreasing with redshift, with a large scatter. For a galaxy to have a lower dynamical mass than baryonic mass is unphysical, but it is not unexpected for the *measurement* of the dynamical mass to be lower than the baryonic mass, particularly at high redshift where dynamical measurements become increasingly challenging as a result of limited resolution and SNR. There are many assumptions and uncertainties included in the calculation of both dynamical and baryonic mass, as we examine in the following.

4.8.1 Uncertainties in the Morphological Measurements

Both the rotation dominated and the dispersion dominated forms of the dynamical mass calculation require a measurement of the effective radius which we obtain from morphological fitting. The uncertainties introduced by morphological fitting are not limited to r_e, however, but are propagated throughout the kinematic fitting as we use the morphological centre, inclination angle and position angle to define the initial parameters supplied to ^{3D}BAROLO.

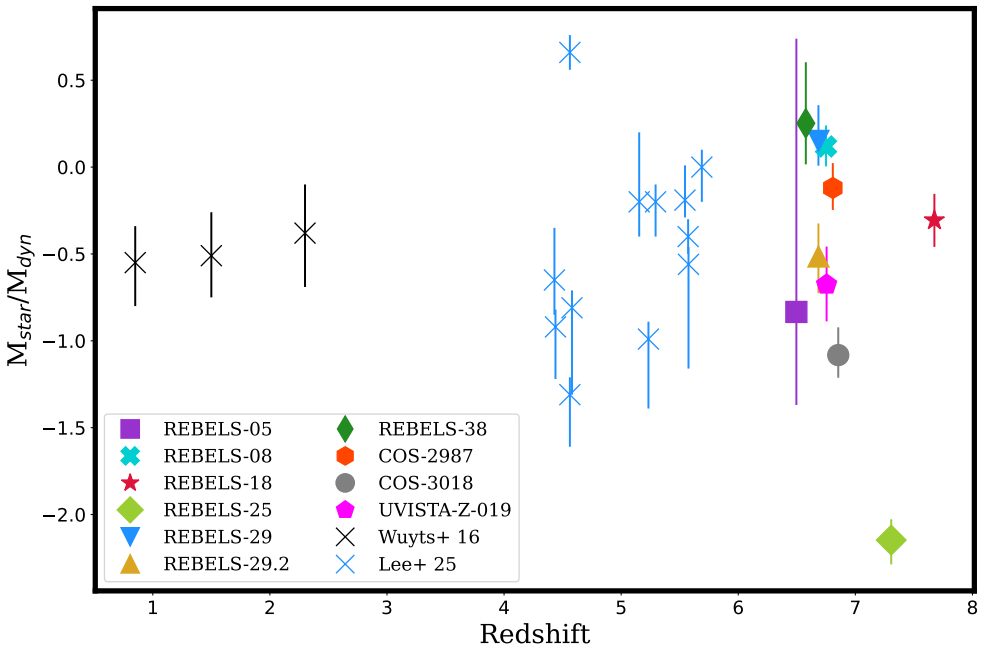

Figure 4.15: The ratio of dynamical mass to stellar mass plotted against redshift for the REBELS-HR sample and literature data from Wuyts et al. (2016) and Lee et al. (2025b), where the Wuyts+ data are median values across three redshift bins: $0.6 < z < 1.1, 1.3 < z < 1.7$ and $2.0 < z < 2.6$.

4.8.1.1 Morphological Tracer

We detail and justify the choice of tracer for each galaxy in Section 3.4. To summarise, we take the rest-optical as default to encompass the majority of stellar emission and avoid bias from young stars, but fit the rest-UV for REBELS-29 which is dominated by a bright clump in the rest-optical, and the FIR continuum for

REBELS-29-2 and REBELS-38 which both demonstrate high dust obscuration fractions of > 0.97 and 0.86 ± 0.23. respectively. The choice of tracer employed strongly impacts the results of morphological fitting, including the effective radius (see Fig. 3.23). There also appears to be a systemic effect on the measured inclination angle, with the rest-optical measurement appearing consistently lower than the rest-UV measurement across our sample (Fig. 3.23).

4.8.1.2 Inclination Angle

It is crucial to accurately estimate the inclination angle in order to obtain reliable results for other fitted kinematic parameters, but this is challenging, particularly in the case of limited angular resolution (e.g. Parlanti et al., 2023). There is a strong degeneracy between the inclination angle and the rotational velocity and velocity dispersion (e.g. Kohandel et al., 2019). To avoid encountering this degeneracy in our kinematic fitting, we choose to fix this parameter to the morphological measurement, but the underlying assumption of agreement between the morphological and kinematic inclination angles may not be valid for all of our galaxies (e.g. Epinat et al., 2008).

4.8.2 Uncertainties in the Kinematic Measurements

It is necessary to make certain assumptions about the internal structure of a galaxy in order to be able to fit a kinematic model to it, but these assumptions are a source of significant uncertainty, as we consider in the following.

4.8.2.1 Choice of Fitting Code: Comparing ^{3D}Barolo and DysmalPy

We extract the signal from a series of apertures of equivalent size to the PSF along the kinematic major axis of a selection of galaxies from the sample that show a rotational profile in the velocity map: REBELS-29-2, REBELS-38, and COS-3018, overlapping the apertures to oversample the data (see Figure 4.16). We fit a Gaussian profile to the signal extracted from each aperture to derive the rotational velocity and velocity dispersion at each position along the kinematic axis. We supply these data to `DysmalPy` after adding a quantity representing the systemic velocity to shift the velocity profile such that $v = 0$ at the central aperture.

We set the morphological position angle and inclination angle as fixed priors, and provide instrumental details such as the pixel scale and source details including the redshift of the galaxy. Our free parameters for this fit are the intrinsic velocity dispersion, for which we set the initial prior as the measurement from ^{3D}BAROLO and the fitting range between 5−300 $\mathrm{km\,s^{-1}}$: the effective radius, for which we set the morphological effective radius as the prior and a fitting range 1kpc either side of this measurement: and the dynamical mass, for which we use the baryonic mass as the prior.

We compare the velocity measurements fitted by `DysmalPy` and ^{3D}BAROLO in Appendix B.1. The velocity dispersions fitted by `DysmalPy` are consistent within 1σ with the ^{3D}BAROLO measurements for REBELS-29-2 and COS-3018, but only within 2σ for REBELS-38. This could be due to the asymmetric distribution of the velocity dispersion across the extent of this galaxy (Figure 4.6), particularly a high-dispersion clump at the edge of the galaxy which is coincident with the kinematic major axis. This is likely to affect the `DysmalPy` fit, which is 1D, to a greater extent than the 3D ^{3D}BAROLO fit.

We compare the rotational velocities measured by ^{3D}BAROLO and `DysmalPy` at the effective radius, rather than taking the rotational velocity at the outermost fitted ring of the galaxy as we do in Table 2.2, to ensure that the comparison is as fair as possible. The rotational velocity measured at the effective radius is systematically lower for the `DysmalPy` measurements, at 0.7×, 0.2× and 0.6× the ^{3D}BAROLO measurements for REBELS-29-2, REBELS-38 and COS-3018 respectively, which is surprising given that Lee et al. (2025a) find that rotational velocity measurements are robust between fitting codes and velocity dispersion is more affected by systematics. As the dynamical mass of a rotating disk system depends on rotational velocity to the second power, the difference in rotational velocities between the two fitting codes we test would be propagated into a large uncertainty in the dynamical mass.

4.8.2.2 Assumption of a Rotating Disk

Describing the kinematics of a galaxy with a tilted ring model, as ^{3D}BAROLO does, makes the assumption that the emitting matter is confined to a thin disc and that the

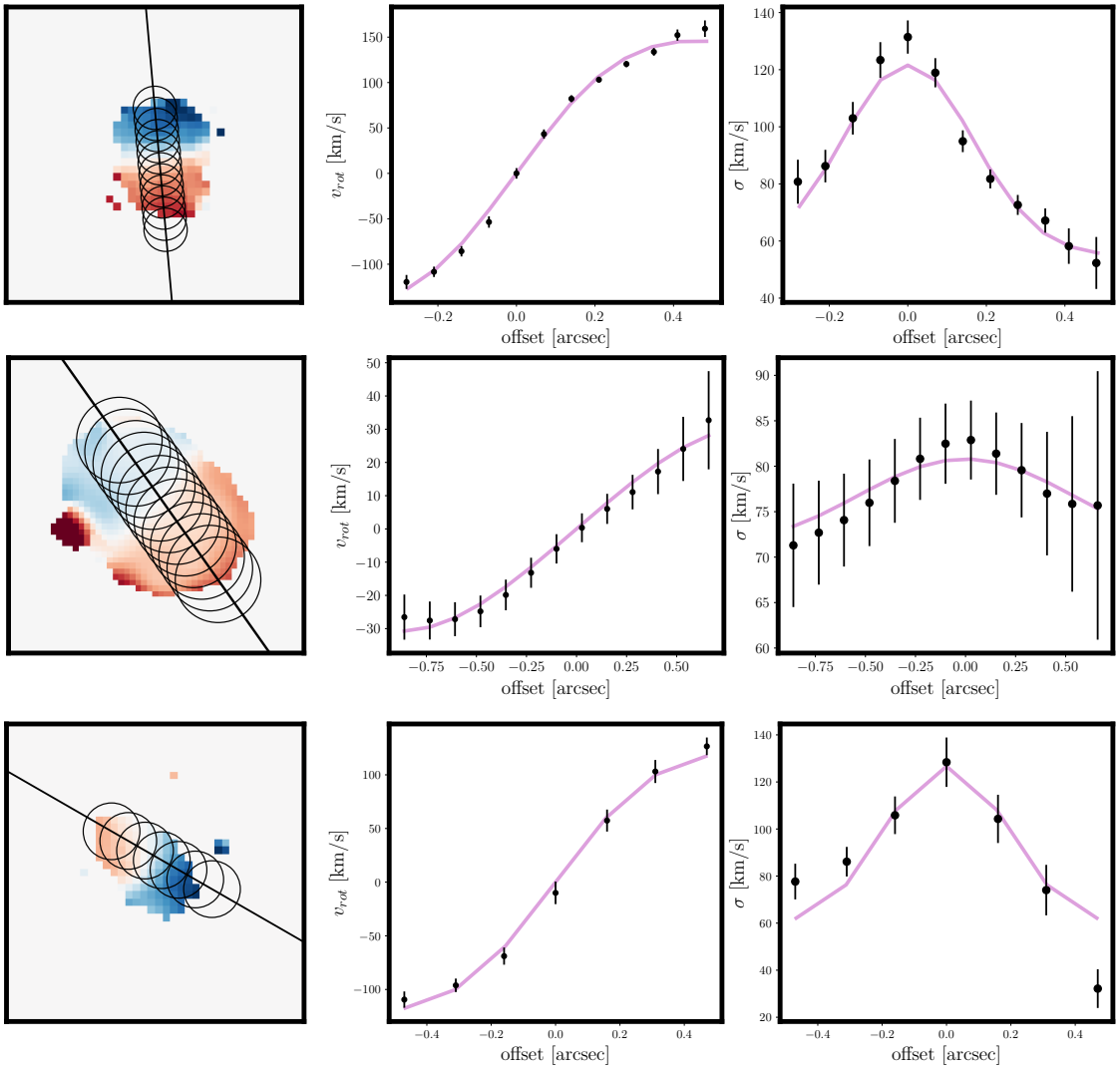

Figure 4.16: DysmalPy fits to disk candidate galaxies, showing the apertures from which we extract signal along the kinematic axis (LHS panels), the rotational velocity profile (central panels), and the velocity dispersion profile (RHS panels), where the extracted measurements are shown as black points and the model as a purple line connecting the points fitted by the model.

kinematics are dominated by rotational motion, such that each ring has a constant circular velocity which is a function of distance from the centre only. We furthermore invoke the rotating thin disk model to define the value of $k_{tot} = 1.8$ used in the calculation of dynamical mass for all of the galaxies excepting the dispersion-dominated REBELS-18 and UVISTA-Z-019. The rotating disk assumption is not uniformly valid across the sample, as we identify both dispersion-dominated galaxies with no discernable velocity structure, and multiple turbulent galaxies with little velocity structure, but we persist in fitting with a rotating disk model so as to quantify the lack of any such structure in these sources.

As the majority of the REBELS-HR galaxies are turbulent disks, we calculate the dynamical mass of these galaxies (REBELS-05, -08, -29, -38, COS-2987 and COS-3018) according to both the rotating disk formalism, as we present in Table 2.3, and the dispersion dominated formalism, shown in Appendix B.2. One method does not universally over- or under- estimate the dynamical mass in comparison with the other, but there is a median absolute difference of 0.4dex between the results of the two methods which indicates that this is a significant source of error.

4.8.3 Uncertainties on the Baryonic Mass

The unphysical situation of $M_{dyn} < M_{bary}$ could be resolved not only through an underestimation of M_{dyn}, but also through an overestimation of M_{bary}.
Stellar mass measurements for all galaxies excluding the pilots and the dust-obscured REBELS-29-2 are from Stefanon et al. in prep., with the measurements from this analysis being reported in Algera et al. (2025) and Rowland et al. (2025). The stellar masses in Stefanon et al. in prep. are estimated by fitting the extracted NIRSpec/IFU spectra with Bagpipes (Carnall et al., 2018), using the 2016 formalism of the Bruzual and Charlot (2003) stellar population models. The same method was used by Fudamoto et al. (2021) on rest-optical and NIR data from UltraVISTA (Scoville et al., 2007; McCracken et al., 2012) to establish an upper limit for the stellar mass of REBELS-29-2.
The stellar mass of UVISTA-Z-019 is recorded in Schouws et al. (2022) from fitting its UltraVISTA imaging with the fast code (Kriek et al., 2009) and Bruzual and

Charlot (2003) models, and the stellar masses of COS2987 and COS3018 are derived by Harikane et al. (2025) from fitting NIRCam SEDs with PROSPECTOR (Johnson et al., 2021).

4.8.3.1 Limitations of Measuring Stellar Mass with HST + NIRCam

The stellar masses of our REBELS-HR sample are all measured through SED fitting to HST/NIRCam imaging, as described above. However, Williams et al. (2024) note that there is some uncertainty, not adequately represented in the estimated error, in the interpretation of typically red, featureless HST/NIRCam SEDs for galaxies at $z > 3$. They find that adding photometry from the JWST Mid-Infrared Instrument (MIRI) leads to a decrease in the stellar mass fitted to the SED, and caution that without the long baseline provided by MIRI coverage, models tend to overestimate dust attenuation, resulting in a higher stellar mass by up to a factor of $3-5$ for a fixed rest-optical flux. Wang et al. (2025) also find that MIRI is critical for measuring the stellar mass of $z > 5$ galaxies, as without it stellar mass is overestimated by ~ 0.4dex in the mass range $M_* > 10^{10} M_\odot$.

4.8.3.2 Assumed Initial Mass Function

Stefanon et al. in prep. and Schouws et al. (2022) assume a Chabrier (Chabrier, 2003) initial mass function (IMF) while Harikane et al. (2025) derive stellar mass under the assumption of a Salpeter (Salpeter, 1955) IMF. To ensure consistency we convert these values to the Chabrier IMF by dividing by 1.64 (Madau and Dickinson, 2014).

The IMF describes the relation between mass, light, and the age of stellar populations, defining the ratio of hot stars that dominate the light to cool stars that contribute most of the mass. Changing the IMF therefore rescales the mass-to-light ratio, affecting the measured stellar masses of galaxies.

4.9 Summary and Conclusions

In this chapter, we perform the first kinematic analysis on a sample of galaxies from the Epoch of Reionization.

Table 4.2: Side-by-side comparisons of stellar mass values from literature (COS-2987 and COS-3018 converted to Chabrier IMF from Salpeter IMF), baryonic mass, and our calculated dynamical mass.

REBELS ID	$\log_{10}(M_*/\mathrm{M}_\odot)$	$\log_{10}(M_{bary}/\mathrm{M}_\odot)$	$\log_{10}(M_{dyn}/\mathrm{M}_\odot)$
REBELS-5	$9.1^{0.1}_{0.1}$ [a]	$10.1^{+0.06}_{-0.06}$	$10.0^{+1.6}_{-0.5}$
REBELS-8	$9.0^{0.07}_{0.06}$ [a]	$10.1^{+0.06}_{-0.07}$	$8.9^{+0.1}_{-0.1}$
REBELS-18	$9.4^{0.06}_{0.04}$ [a]	$10.3^{+0.04}_{-0.03}$	$9.7^{+0.1}_{-0.1}$
REBELS-25	$9.0^{0.12}_{0.14}$ [a]	10.4 [b]	11.1 [b]
REBELS-29	$9.4^{0.07}_{0.05}$ [a]	$10.0^{+0.07}_{-0.07}$	$9.2^{+0.2}_{-0.1}$
REBELS-29-2	< 10.1 [c]	<10.4	$10.6^{+0.2}_{-0.2}$
REBELS-38	$9.4^{0.09}_{0.06}$ [a]	$10.5^{+0.05}_{-0.04}$	$9.2^{+0.3}_{-0.2}$
COS-2987	$8.9^{0.1}_{0.1}$ [d]	$9.7^{0.1}_{0.1}$	$9.0^{+0.1}_{-0.1}$
UVISTA-Z-019	$9.2^{0.19}_{0.18}$ [e]	$10.1^{0.05}_{0.05}$	$9.9^{+0.1}_{-0.1}$
COS-3018	$9.3^{0.1}_{0.1}$ [d]	$9.9^{0.05}_{0.05}$	$10.4^{+0.1}_{-0.1}$

[a] Algera et al. (2025), [b] Rowland et al. (2024), [c] Fudamoto et al. (2021), [d] Harikane et al. (2025), [e] Schouws et al. (2022)

We classify disk galaxies according to a set of morpho-kinematic criteria, the results of PVSplit fitting, and the ratio of their maximum rotation velocity to their average velocity dispersion, v/σ.

Only three galaxies pass all five of the morpho-kinematic disk criteria (REBELS-29-2, COS-3018, and REBELS-25 - see Rowland et al. (2024) for this result), but a galaxy is considered a disk according to the morpho-kinematic test if it passes three or more criteria, which all REBELS-HR galaxies do except for COS-2987. Fitting with PVSplit associates both of our dynamically cold disks and one turbulent disk (REBELS-38) with the disk region of the PVSplit parameter space, alongside one misclassified dispersion dominated galaxy (REBELS-18). The v/σ measurements identify two galaxies as dispersion dominated with $v/\sigma < 1$ (REBELS-18, UVISTA-Z-019), two galaxies as dynamically cold with $v/\sigma > 3$ (REBELS-25, REBELS-29-2), and the remaining six as falling within the turbulent disk category with $1 < v/\sigma < 3$.

We test the galaxies showing potential signatures of merging activity to determine whether they are merging systems, and if so whether they are major or minor mergers, by estimating the mass or luminosity ratio for each candidate merger. We identify one major merger (REBELS-29), two minor mergers (REBELS-8, COS-3018) and two galaxies that could contain very minor merging components (REBELS-38, COS-2987).

We find that stellar mass exceeds dynamical mass for three of our ten galaxies, while baryonic (stellar + gas) mass exceeds dynamical mass for seven out of ten galaxies. This could imply that the assumed gas fraction is overestimated; as discussed in Section 4.8, there is a large variation in the conversion factor used to relate gas luminosity to gas mass. The dynamical mass may be considered a more fundamental tracer of the galaxy potential well, as it represents the entirety of the gravitationally interacting matter, and is arguably less reliant on modelling assumptions than the stellar mass. The stellar mass is generally measured from SED fitting and therefore requires assumptions to be made regarding the stellar population models and star formation history, as well as the initial mass function, which is locally calibrated and not necessarily applicable at high redshifts (e.g. Martín-Navarro et al., 2024; Hutter et al., 2025). Scaling relations such as the stellar mass Tully-Fisher relation (Tully and Fisher, 1977), the observed tight correlation between stellar mass

and circular velocity, can provide a useful framework to contextualise stellar mass measurements. Placing our sources on the Tully-Fisher relation would therefore provide useful insight into whether their stellar masses and kinematic properties follow expectation.

- We observe a diverse range of kinematics among the ten REBELS-HR galaxies at $z = 6.5 - 7.7$. We identify two dynamically cold disks (REBELS-25, REBELS-29-2), one major merger (REBELS-29), two dispersion dominated galaxies (REBELS-18, UVISTA-Z-019), one galaxy which appears to be a complex system comprised of multiple clumps (COS-2987), two galaxies having turbulent disk structure with minor merger components (REBELS-8, COS-3018) and two galaxies having turbulent disk structure with no significant merger components (REBELS-5, REBELS-38).

- We find that our fitted velocity dispersions are low compared to the results from literature with which we compare. Our measured σ values are consistent with the scenario of no evolution of velocity dispersion with redshift when viewed in context with cold gas surveys from $z \sim 1 - 4.5$. This is not what would be expected from the CRISTAL disk sample, where the velocity dispersions appear consistent with a relation of increasing σ with redshift. However, both scenarios demonstrate a large scatter.

- Despite the relatively low velocity dispersions recovered from our galaxies, the v/σ ratios are consistent with the relationship of decreasing v/σ with redshift established by cold gas measurements from literature, indicating that our rotational velocities are relatively low.

- Our dynamical masses are lower than would be expected, with the measured dynamical mass being lower than the baryonic mass for seven out of our ten galaxies. We explore potential sources of uncertainty that could explain this unphysical situation. The two dynamically cold disks, alongside one turbulent disk, show dynamical masses higher than their baryonic masses.

We present the first systematic survey of galaxy kinematics in the Epoch of Reionization, utilising high resolution [CII]158μm ALMA observations in synergy with

NIRCam and NIRSpec observations to study typical star-forming galaxies at $z > 6$. We discover an intriguing diversity of kinematics, with a major merger fraction of 0.1, and a disk fraction of 0.6 when cold and turbulent disks are both taken into account. This groundbreaking kinematic sample furthermore acts as a unique resource for future research, as we will consider in the following chapter.

Chapter 5

Conclusions and Outlook

We here summarise the key ideas from this thesis, as well as discussing potential future work that could build upon this foundation.

5.1 Conclusions

In this thesis, we present an investigation into the kinematics of galaxies at $z > 6$, as well as a consideration of the best practice for kinematic analysis based on NIRSpec IFU data, and in comparison to ALMA observations.

In Chapter 2, we create mock NIRSpec observations for two galaxies from the SERRA zoom-in hydrodynamical simulations, and with these we investigate how robustly it is possible to recover dynamical information including rotational velocity, velocity dispersion and dynamical mass from the NIRSpec/IFU. We establish that it is possible to identify disk galaxies in the Epoch of Reionization, along with complex structure arising from non-circular motion when three dimensional information is available, and find that dynamical mass can be measured relatively reliably for axisymmetric systems at $z > 6$.

We go on to perform an analysis of ten observed galaxies at $6 < z < 8$, the REBELS-HR sample. In Chapter 3 we present the morphologies of these galaxies according to all available tracers, including cold ([CII] gas, the FIR dust continuum, rest-optical and rest-UV light, and the Hα and Hβ lines. Among our galaxies we identify potential [CII] halo signatures, most notably in UVISTA-Z-019, and clumpy rest-UV morphologies in numerous sources, interpreted as unevenly distributed star forma-

tion. We perform resolved SED fitting on one such source, COS-3018, associating the regions with highest SFR with the regions of highest rest-UV emission and also FIR emission, suggesting that the star formation in the source may be significantly obscured. We measure the spatial offsets between various emission components in each galaxy, finding no discernible relationship between the UV/dust offset and the global physical properties L_{IR} or f_{obs}.

In Chapter 4 we present the kinematics of the ten REBELS-HR galaxies, describing two dynamically cold disk galaxies, two fully dispersion dominated galaxies with no discernible velocity structures, one major merger, one complex clumpy system, and four turbulent disks of which two appear to host minor merger components. We identify a strong outflow signature in UVISTA-Z-019, and tentative indications of outflows in other galaxies. We find that the velocity dispersion measurements of our galaxies are lower than might be expected from a comparison with literature surveys of cold gas kinematics across redshifts, but our measured v/σ ratios are consistent with a decreasing relation with redshift. Our measured dynamical masses are lower than our baryonic masses for 70% of the galaxies, and we present a discussion exploring uncertainties in our measurements and assumptions that could contribute to this.

The high resolution ALMA observations of the [CII] line emission from the REBELS-HR survey presented in this thesis alongside the dust continuum, rest-optical and -UV light, and Hα and Hβ lines, enabled the first systematic census of kinematics in typical star forming galaxies at the Epoch of Reionization $z > 6$. As complementary ionized gas kinematics become available through JWST IFU observing programmes, in-depth comparison between warm and cold gaseous tracers will become possible on observed galaxies, following our demonstration in Chapter 2 that Hα kinematics can successfully be used to recover kinematic properties.

5.2 Outlook

The project we undertake in this thesis of classifying the cold gas kinematics of galaxies in the Epoch of Reionization lays the groundwork for many possible future projects. These could include a re-analysis of the CRISTAL galaxies (Herrera-

Camus et al., 2025) using the techniques applied to the REBELS-HR sample, to gain an understanding of the extent to which differing analysis assumptions and methodologies affect kinematic results. As we identify a population of turbulent disks in the REBELS-HR sample, we could conduct an analysis of the main driving forces behind this turbulence, comparing with the Krumholz et al., 2018 analytic model to estimate the relative contributions of star formation and gravitational instabilities. We could conduct a systematic analysis of the angular momentum and disk stability, characterised by the Toomre Q parameter (Toomre, 1964) as Swinbank et al., 2017 do with a MUSE and KMOS survey of 400 star forming galaxies at $0.3 < z < 1.7$. We consider two of the many potentially interesting research directions in more detail in the following.

5.2.1 Comparing Cold and Warm Gas Kinematics for Real Epoch of Reionization Galaxies

A central premise of Chapter 2 is that a like-for-like comparison cannot be made between cold and warm gas kinematics, and these tracers provide different information about the galactic environment. Therefore, an obvious extension to the cold gas kinematic analysis of the REBELS-HR galaxies presented in Chapter 4 would be to obtain high-resolution warm gas observations with JWST of the same targets, so as to enable a direct comparison of the dynamical characteristics of the galaxies according to the two most powerful facilities currently available. As REBELS-HR is the first survey to provide kinematic information for a sample of galaxies in the Epoch of Reionization, it represents a unique dataset for this kind of study. COS-2987 has existing JWST NIRSpec/IFS coverage from the Reionization and ISM/Stellar Origins with JWST and ALMA (RIOJA: PID 1840, PIs: J. Alvarez-Márquez and T. Hashimoto) project, and an analysis of its JWST kinematics has already been presented in Usui et al., 2025 and Mawatari et al., 2025. COS-3018 has NIRSpec/IFS observations from the GA-NIFS survey (PID 1217, PIs: S. Arribas and R. Maiolino) and these data have been interpreted by Scholtz et al., 2025 as showing that the galaxy is a merging system. Furthermore, Renske Smit and I are co-PIs on a JWST proposal, which has been ranked in the first quintile of proposals in two previous application cycles, to obtain NIRSpec observations of REBELS-5, REBELS-18,

REBELS-29, REBELS-29-2 and UVISTA-Z-019. If this were to be approved and we were to obtain NIRSpec observations of these galaxies, they would provide the sub-kpc spatial resolution necessary to robustly measure the mass profiles of the galaxies and understand whether centrally concentrated mass profiles are indeed crucial for the formation of early disks. If this proposal is not accepted, however, there is still great potential in comparing public NIRSpec/IFU and archival ALMA data to build a comparative survey of hot and cold gas kinematics across cosmic time.

NIRSpec observations would also support our second science goal of identifying and characterising outflows in the Epoch of Reionization. Among the galaxies targeted in the JWST proposal, the dispersion-dominated UVISTA-Z-019 displays a strong outflow signature in cold gas. However, simulations indicate that outflow mass-loading is dominated by hot, ionized gas (Kohandel et al., 2024) which suggests that by having access to only the cold gas view of outflow candidates, we are missing the main contribution to feedback in these galaxies.

5.2.2 Cataloguing and Characterising Outflows

The REBELS-HR sample is an ideal basis for a systematic search in both the image and UV plane for [CII] halos (Fujimoto et al., 2019; Fujimoto et al., 2020), shedding light on their physical origins, and outflowing gaseous streams, which we can also search for in archival data. Building a survey of confirmed outflows will help in understanding the quenching mechanisms responsible for the existence of the massive quiescent galaxies that have been confirmed spectroscopically up to $z \sim 4$, and according to photometric results may exist at even higher redshifts (e.g. Forrest et al., 2020; Valentino et al., 2020; Carnall et al., 2023b). This would be a major step towards understanding the evolution of galaxies across cosmic time.

5.2.3 The Future of High Redshift Extragalactic Research

We are in a period of unprecedented data quality and availability for Epoch of Reionization galaxy studies, with exciting recent observations revealing massive star forming and quiescent galaxies within the first 1-2 billion years of cosmic time (e.g. Bunker et al., 2023; Carnall et al., 2023a; Eisenstein et al., 2023). The abundance of

such massive galaxies at early times has been interpreted as a challenge to ΛCDM, but could also serve as an indication that locally calibrated modelling assumptions are not universal and scaling relations are not yet established at $z > 6$. The complementarity of the ALMA and JWST observatories has allowed individual galaxies in the Epoch of Reionization to be studied in great detail (e.g. GNz11: Oesch et al., 2016; Bekki and Tsujimoto, 2023; Scholtz et al., 2024; Álvarez-Márquez et al., 2025, and many other references) but this thesis presents the first systematic kinematic census for ten galaxies at $z > 6$. We evidently suffer from insufficient datapoints to constrain scaling relations in the Epoch of Reionization, which limits the reliability of interpreting observations in this redshift range. The stellar mass Tully-Fisher relation has been observed to show only modest evolution between $z = 2$ and $z = 0$, as individual galaxies evolve along the relation: Swinbank et al. (2012) find that the average stellar mass increases by a factor of 2.0 ± 0.4 over this redshift range at fixed circular velocity. Danhaive et al. (2025), studying galaxies between $z = 4 - 6$, find substantial intrinsic scatter within the relation, which they interpret as the relationship only beginning to emerge during this redshift interval. However, the relationship measured by Übler et al. (2017) at $z = 0.9 - 2.3$ is extrapolated to $z \sim 8$ by Wisnioski et al. (2025) who find that even at this early redshift the majority of their data follow the expected relation, with some scatter. Large observing programmes focused on validating scaling relations into the Epoch of Reionization could provide vital context for determining the applicability of such relations and the interpretation of observations.

Following on from Section 5.2.1, large observing programmes to obtain simultaneous cold and warm gas kinematics from a statistically significant population of galaxies at $z > 6$ would provide a more full picture of the internal environments within the target sources and therefore open up a less biased view of formation and evolution processes in the first galaxies to form in the Universe.

Bibliography

Adelberger, E. G. et al., 2011, *Reviews of Modern Physics*, 83, pp. 195–246.

Algera, H. et al., 2025, *arXiv e-prints*, arXiv:2501.10508.

Algera, H. S. B. et al., 2023, MNRAS, 518, pp. 6142–6157.

Alpher, R. A. et al., 1948, *Physical Review*, 73, pp. 803–804.

Álvarez-Márquez, J. et al., 2025, A&A, 695, A250.

Anders, P. and U. Fritze-v. Alvensleben, 2003, A&A, 401, pp. 1063–1070.

Arata, S. et al., 2019, MNRAS, 488, pp. 2629–2643.

Aravena, M. et al., 2024, A&A, 682, A24.

Arcones, A. and F.-K. Thielemann, 2023, A&A Rev., 31, p. 1.

Arjona-Gálvez, E. et al., 2024, A&A, 690, A286.

Arrabal Haro, P. et al., 2023, Nature, 622, pp. 707–711.

Arribas, S. et al., 2024, A&A, 688, A146.

Atek, H. et al., 2024, Nature, 626, pp. 975–978.

Bacchini, C. et al., 2020, A&A, 641, A70.

Baggett, S. et al. (2008). "The wide-field camera 3 detectors". In: *High Energy, Optical, and Infrared Detectors for Astronomy III*. Vol. 7021. SPIE. (2008), pp. 527–537.

Baker, W. M. et al., 2025, MNRAS, 539, pp. 557–589.

Becker, R. H. et al., 2001, AJ, 122, pp. 2850–2857.

Beckwith, S. V. W. et al., 2006, AJ, 132, pp. 1729–1755.

Begeman, K. K. G. (1987). "HI rotation curves of spiral galaxies". PhD thesis. University of Groningen, Netherlands, (1987).

Begley, R. et al., 2024, MNRAS, 527, pp. 4040–4051.

Bekki, K. and T. Tsujimoto, 2023, MNRAS, 526, pp. L26–L30.

Bertin, E. and S. Arnouts, 1996, A&AS, 117, pp. 393–404.

Binney, J. and G. Tabor, 1995, MNRAS, 276, pp. 663–678.

Binney, J. and S. Tremaine, 1987. *Galactic dynamics*.

Birkin, J. E. et al., 2024, MNRAS,

Birkmann, S. M. et al., 2022, *SPIE*, 12180, 121802P.

Blumenthal, G. R. et al., 1984, Nature, 311, pp. 517–525.

Blumenthal, K. A. and J. E. Barnes, 2018, MNRAS, 479, pp. 3952–3965.

Böker, T. et al., 2022, A&A, 661, A82.

Bond, N. A. et al., 2011, ApJ, 729, p. 48.

Bosma, A. (1978). "The distribution and kinematics of neutral hydrogen in spiral galaxies of various morphological types". PhD thesis. University of Groningen, Netherlands, (1978).

Bouché, N. et al., 2015, AJ, 150, p. 92.

Bournaud, F. et al., 2005, A&A, 437, pp. 69–85.

Bournaud, F. et al., 2011, ApJ, 730, p. 4.

Bouwens, R. J. et al., 2015, ApJ, 811, p. 140.

Bouwens, R. J. et al., 2022, ApJ, 931, p. 160.

Bouwens, R. J. et al., 2016, ApJ, 833, p. 72.

Bowler, R. A. A. et al., 2014, MNRAS, 440, pp. 2810–2842.

Bowler, R. A. A. et al., 2017, MNRAS, 466, pp. 3612–3635.

Bowler, R. A. A. et al., 2020, MNRAS, 493, pp. 2059–2084.

Bowler, R. A. A. et al., 2024, MNRAS, 527, pp. 5808–5828.

Boylan-Kolchin, M., 2023, *Nature Astronomy*, 7, pp. 731–735.

Briggs, D. S. (1995). "High fidelity deconvolution of moderately resolved sources". PhD thesis. New Mexico Institute of Mining and Technology, (1995).

Bruzual, G. and S. Charlot, 2003, MNRAS, 344, pp. 1000–1028.

Bunker, A. J. et al., 2023, A&A, 677, A88.

Calzetti, D. (1997). "UV opacity in nearby galaxies and application to distant galaxies". In: *The ultraviolet universe at low and High redshift*. Ed. by W. H. Waller. Vol. 408. American Institute of Physics Conference Series. (1997), pp. 403–412. DOI: 10.1063/1.53764. arXiv: astro-ph/9706121 [astro-ph].

Calzetti, D., 2001, PASP, 113, pp. 1449–1485.

Capak, P. L. et al., 2015, Nature, 522, pp. 455–458.

Cappellari, M. and Y. Copin, 2003, MNRAS, 342, pp. 345–354.

Cappellari, M. et al., 2006, MNRAS, 366, pp. 1126–1150.

Carnall, A. C. et al., 2018, MNRAS, 480, pp. 4379–4401.

Carnall, A. C. et al., 2023, MNRAS, 520, pp. 3974–3985.

Carnall, A. C. et al., 2023, Nature, 619, pp. 716–719.

Carniani, S. et al., 2015, A&A, 580, A102.

Carniani, S. et al., 2018, MNRAS, 478, pp. 1170–1184.

Carniani, S. et al., 2024, Nature, 633, pp. 318–322.

Carniani, S. et al., 2025, A&A, 696, A87.

Carroll, S. M., 2001, *Living Reviews in Relativity*, 4, p. 1.

Castellano, M. et al., 2016, ApJ, 818, p. L3.

Castellano, M. et al., 2022, ApJ, 938, p. L15.

Castellano, M. et al., 2024, ApJ, 972, p. 143.

Ceverino, D. et al., 2017, MNRAS, 467, pp. 2664–2672.

Chabrier, G., 2003, PASP, 115, pp. 763–795.

Chevance, M. et al. (2023). "The Life and Times of Giant Molecular Clouds". In: *Protostars and Planets VII*. Ed. by S. Inutsuka et al. Vol. 534. Astronomical Society of the Pacific Conference Series. (2023), p. 1. DOI: 10.48550/arXiv.2203.09570. arXiv: 2203.09570 [astro-ph.GA].

Chisholm, J. et al., 2022, MNRAS, 517, pp. 5104–5120.

Choi, Y. et al., 2020, ApJ, 902, p. 54.

Cimatti, A. et al., 2020. *Introduction to galaxy formation and evolution: from primordial gas to present-day galaxies*.

Concas, A. et al., 2022, MNRAS, 513, pp. 2535–2562.

Conroy, C., 2013, ARA&A, 51, pp. 393–455.

Conselice, C. J. et al., 2000, ApJ, 529, pp. 886–910.

Conselice, C. J. et al., 2003, AJ, 126, pp. 1183–1207.

Conselice, C. J. et al., 2008, MNRAS, 386, pp. 909–927.

Cowley, W. I. et al., 2017, MNRAS, 467, pp. 1231–1248.

Crain, R. A. and F. van de Voort, 2023, ARA&A, 61, pp. 473–515.

Cresci, G. et al., 2009, ApJ, 697, pp. 115–132.

Curti, M. et al., 2023, MNRAS, 518, pp. 425–438.

Curtis-Lake, E. et al., 2023, *Nature Astronomy*, 7, pp. 622–632.

D'Eugenio, F. et al., 2024, *Nature Astronomy*, 8, pp. 1443–1456.

Dalcanton, J. J., 2009, Nature, 457, pp. 41–50.

Dalmasso, N. et al., 2024, MNRAS, 533, pp. 4472–4484.

Danhaive, A. L. et al., 2025, *arXiv e-prints*, arXiv:2510.14779.

Davies, R. et al., 2011, ApJ, 741, p. 69.

Davies, R. I. et al., 2004, ApJ, 613, pp. 781–793.

Davies, R. I. et al., 2004, ApJ, 602, pp. 148–161.

Dayal, P. and A. Ferrara, 2018, Phys. Rep., 780, pp. 1–64.

Dayal, P. et al., 2024, *arXiv e-prints*, arXiv:2401.11242.

De Blok, W. J. G. et al., 2008, AJ, 136, pp. 2648–2719.

De Graaff, A. et al., 2024, A&A, 684, A87.

De Looze, I. et al., 2014, A&A, 568, A62.

de Vaucouleurs, G., 1948, *Annales d'Astrophysique*, 11, p. 247.

Decataldo, D. et al., 2019, MNRAS, 487, pp. 3377–3391.

Di Teodoro, E. M. and F. Fraternali, 2015, MNRAS, 451, pp. 3021–3033.

Di Teodoro, E. M. et al., 2016, A&A, 594, A77.

Di Teodoro, E. M. (2015). "Kinematics of local and high-z galaxies through 3D modeling of emission-line datacubes". PhD thesis. University of Bologna, Italy, (2015).

Dicke, R. H. et al., 1965, ApJ, 142, pp. 414–419.

Dome, T. et al., 2024, MNRAS, 527, pp. 2139–2151.

Duan, Q. et al., 2025, MNRAS, 540, pp. 774–805.

Efstathiou, G., 2025, *Philosophical Transactions of the Royal Society of London Series A*, 383, p. 20240022.

Einstein, A., 1916, *Annalen der Physik*, 354, pp. 769–822.

Einstein, A., 1915, *Sitzungsberichte der Königlich Preußischen Akademie der Wissenschaften*, pp. 844–847.

Einstein, A., 1917, *Sitzungsberichte der Königlich Preußischen Akademie der Wissenschaften*, pp. 142–152.

Eisenstein, D. J. et al., 2023, *arXiv e-prints*, arXiv:2306.02465.

Ejdetjärn, T. et al., 2022, MNRAS, 514, pp. 480–496.

Ejdetjärn, T. et al., 2024, MNRAS, 534, pp. 135–150.

Eke, V. R. et al., 2005, MNRAS, 362, pp. 1233–1246.

Elbaz, D. et al., 2011, A&A, 533, A119.

Eldridge, J. J. et al., 2017, PASA, 34, e058.

Ellis, G. F. R. and E. R. Harrison, 1974, *Comments on Astrophysics and Space Physics*, 6, pp. 23–27.

Ellison, S. L. et al., 2008, AJ, 135, pp. 1877–1899.

Endsley, R. and D. P. Stark, 2022, MNRAS, 511, pp. 6042–6054.

Endsley, R. et al., 2021, MNRAS, 500, pp. 5229–5248.

Endsley, R. et al., 2023, MNRAS, 524, pp. 2312–2330.

Endsley, R. et al., 2024, MNRAS, 533, pp. 1111–1142.

Epinat, B. et al., 2008, MNRAS, 388, pp. 500–550.

Faisst, A. L. et al., 2022, ApJ, 929, p. 66.

Ferland, G. J. et al., 2017, Rev. Mexicana Astron. Astrofis., 53, pp. 385–438.

Ferrara, A. et al., 2022, MNRAS, 512, pp. 58–72.

Ferrara, A. et al., 2025, A&A, 694, A286.

Ferreira, L. et al., 2022, ApJ, 938, p. L2.

Ferreira, L. et al., 2023, ApJ, 955, p. 94.

Ferreira, L. et al., 2025, MNRAS, 538, pp. L31–L36.

Finkelstein, S. L. et al., 2023, *arXiv e-prints*, arXiv:2311.04279.

Fisher, R. et al., 2025, MNRAS, 539, pp. 109–126.

Fixsen, D. J., 2009, ApJ, 707, pp. 916–920.

Forrest, B. et al., 2020, ApJ, 903, p. 47.

Förster Schreiber, N. M. et al., 2009, ApJ, 706, pp. 1364–1428.

Förster Schreiber, N. M. and S. Wuyts, 2020, ARA&A, 58, pp. 661–725.

Fraternali, F. et al., 2021, A&A, 647, A194.

Fraternali, F. et al., 2002, AJ, 123, pp. 3124–3140.

Frenk, C. S. et al., 1985, Nature, 317, pp. 595–597.

Fudamoto, Y. et al., 2021, Nature, 597, pp. 489–492.

Fudamoto, Y. et al., 2022, ApJ, 934, p. 144.

Fujimoto, S. et al., 2019, ApJ, 887, p. 107.

Fujimoto, S. et al., 2020, ApJ, 900, p. 1.

Gaia Collaboration et al., 2018, A&A, 616, A1.

Gallerani, S. et al., 2018, MNRAS, 473, pp. 1909–1917.

Gelli, V. et al., 2024, ApJ, 964, p. 76.

Genzel, R. et al., 2008, ApJ, 687, pp. 59–77.

Genzel, R. et al., 2020, ApJ, 902, p. 98.

Giavalisco, M. et al., 2004, ApJ, 600, pp. L93–L98.

Giavalisco, M., 2002, ARA&A, 40, pp. 579–641.

Giménez-Arteaga, C. et al., 2024, A&A, 686, A63.

Giménez-Arteaga, C. et al., 2023, ApJ, 948, p. 126.

Ginolfi, M. et al., 2020, A&A, 633, A90.

Girard, M. et al., 2019, A&A, 631, A91.

Girard, M. et al., 2021, ApJ, 909, p. 12.

Glazebrook, K. et al., 1995, MNRAS, 275, pp. L19–L22.

Glazebrook, K. et al., 2017, Nature, 544, pp. 71–74.

Gnedin, N. Y. and P. Madau, 2022, *Living Reviews in Computational Astrophysics*, 8, p. 3.

Gnerucci, A. et al., 2011, A&A, 533, A124.

Grassi, T. et al., 2014, MNRAS, 439, pp. 2386–2419.

Grazian, A. et al., 2012, A&A, 547, A51.

Greif, T. H. et al., 2010, ApJ, 716, pp. 510–520.

Groves, B. A. et al., 2015, ApJ, 799, p. 96.

Gunn, J. E. and B. A. Peterson, 1965, ApJ, 142, pp. 1633–1636.

Guth, A. H., 1981, Phys. Rev. D, 23, pp. 347–356.

Hani, M. H. et al., 2018, MNRAS, 475, pp. 1160–1176.

Harikane, Y. et al., 2024, ApJ, 960, p. 56.

Harikane, Y. et al., 2025, ApJ, 980, p. 138.

Harrison, C. M. et al., 2017, MNRAS, 467, pp. 1965–1983.

Hashimoto, T. et al., 2019, PASJ, 71, p. 71.

Hassan, S. et al., 2018, MNRAS, 473, pp. 227–240.

Hawking, S. W. and G. F. R. Ellis, 1973. *The Large Scale Structure of Space-Time*. Cambridge University Press.

Hawking, S. and W. Israel, 2010. *General Relativity: an Einstein Centenary Survey*.

Hayes, M. J. and C. Scarlata, 2023, ApJ, 954, p. L14.

Hayward, C. C. and P. F. Hopkins, 2017, MNRAS, 465, pp. 1682–1698.

Hennebelle, P. and M. Y. Grudić, 2024, ARA&A, 62, pp. 63–111.

Hernquist, L., 1989, Nature, 340, pp. 687–691.

Herrera-Camus, R. et al., 2018, ApJ, 861, p. 95.

Herrera-Camus, R. et al., 2021, A&A, 649, A31.

Herrera-Camus, R. et al., 2022, A&A, 665, p. L8.

Herrera-Camus, R. et al., 2025, A&A, 699, A80.

Herwig, F., 2005, ARA&A, 43, pp. 435–479.

Hills, R. E. and A. J. Beasley (2008). "The Atacama Large Millimeter/submillimeter Array". In: *Ground-based and Airborne Telescopes II*. Ed. by L. M. Stepp and R. Gilmozzi. Vol. 7012. Society of Photo-Optical Instrumentation Engineers (SPIE) Conference Series. (2008), 70120N, 70120N. DOI: 10.1117/12.787567.

Hodge, J. A. and E. da Cunha, 2020, *Royal Society Open Science*, 7, p. 200556.

Högbom, J. A., 1974, A&AS, 15, p. 417.

Hopkins, P. F. et al., 2009, ApJ, 691, pp. 1168–1201.

Hu, W. et al., 2000, Phys. Rev. Lett., 85, pp. 1158–1161.

Hubble, E. P., 1926, ApJ, 64, pp. 321–369.

Hung, C.-L. et al., 2019, MNRAS, 482, pp. 5125–5137.

Hutter, A. et al., 2021, MNRAS, 503, pp. 3698–3723.

Hutter, A. et al., 2025, A&A, 694, A254.

Hygate, A. P. S. et al., 2023, MNRAS, 524, pp. 1775–1795.

Inami, H. et al., 2022, MNRAS, 515, pp. 3126–3143.

Inoue, A. K. et al., 2014, MNRAS, 442, pp. 1805–1820.

Iyer, K. G. et al., 2025, *arXiv e-prints*, arXiv:2502.17680.

Jacobs, C. et al., 2023, ApJ, 948, p. L13.

Jakobsen, P. et al., 2022, A&A, 661, A80.

Johnson, B. D. et al., 2021, ApJS, 254, p. 22.

Johnson, D. K., 2009. *The Lavender Scare: The Cold War Persecution of Gays and Lesbians in the Federal Government*. University of Chicago Press.

Johnson, H. L. et al., 2018, MNRAS, 474, pp. 5076–5104.

Johnson, J. A. et al., 2020, *Philosophical Transactions of the Royal Society of London Series A*, 378, p. 20190301.

Jones, B. J. T. and R. F. G. Wyse, 1985, A&A, 149, pp. 144–150.

Jones, G. C. et al., 2017, ApJ, 850, p. 180.

Jones, G. C. et al., 2021, MNRAS, 507, pp. 3540–3563.

Jones, G. C. et al., 2024, A&A, 682, A122.

Kartaltepe, J. S. et al., 2023, ApJ, 946, p. L15.

Katz, H. et al., 2019, MNRAS, 487, pp. 5902–5921.

Katz, H. et al., 2022, MNRAS, 510, pp. 5603–5622.

Katz, H. et al., 2024, *arXiv e-prints*, arXiv:2411.07282.

Kennicutt Jr., R. C., 1983, ApJ, 272, pp. 54–67.

Kennicutt Jr., R. C., 1998, ARA&A, 36, pp. 189–232.

Kim, S. et al., 2012, ApJ, 756, p. 28.

Kimble, R. A. et al. (2008). "Wide Field Camera 3: a powerful new imager for the Hubble Space Telescope". In: *Space Telescopes and Instrumentation 2008: Optical, Infrared, and Millimeter*. Ed. by J. M. Oschmann Jr. et al. Vol. 7010. Society of Photo-Optical Instrumentation Engineers (SPIE) Conference Series. (2008), 70101E, 70101E. DOI: 10.1117/12.789581.

Kobayashi, C. and K. Nomoto, 2009, ApJ, 707, pp. 1466–1484.

Kobayashi, C. et al., 2006, ApJ, 653, pp. 1145–1171.

Kobayashi, C. et al., 2020, ApJ, 900, p. 179.

Kohandel, M. et al., 2019, MNRAS, 487, pp. 3007–3020.

Kohandel, M. et al., 2020, MNRAS, 499, pp. 1250–1265.

Kohandel, M. et al., 2024, A&A, 685, A72.

Kohandel, M. et al., 2025, *arXiv e-prints*, arXiv:2505.07935.

Krajnović, D. et al., 2006, MNRAS, 366, pp. 787–802.

Kreilgaard, K. C. et al., 2024, A&A, 692, A57.

Kriek, M. et al., 2009, ApJ, 700, pp. 221–231.

Kroupa, P., 2002, *Science*, 295, pp. 82–91.

Krumholz, M. R. et al., 2018, MNRAS, 477, pp. 2716–2740.

Kulkarni, G. et al., 2019, MNRAS, 488, pp. 1035–1065.

Labbé, I. et al., 2023, Nature, 616, pp. 266–269.

Lambas, D. G. et al., 2012, A&A, 539, A45.

Lambrides, E. L. et al., 2021, ApJ, 919, p. 129.

Lang, P. et al., 2017, ApJ, 840, p. 92.

Laporte, N. et al., 2017, ApJ, 851, p. 40.

Law, D. R. et al., 2007, ApJ, 669, pp. 929–946.

Lawrence, A. et al., 2007, MNRAS, 379, pp. 1599–1617.

Le Fèvre, O. et al., 2020, A&A, 643, A1.

Lee, B. et al., 2013, ApJ, 774, p. 47.

Lee, L. L. et al., 2025, ApJ, 978, p. 14.

Lee, L. L. et al., 2025, *arXiv e-prints*, arXiv:2507.11600.

Lelli, F. et al., 2018, MNRAS, 479, pp. 5440–5447.

Lelli, F. et al., 2021, *Science*, 371, pp. 713–716.

Lelli, F. et al., 2023, A&A, 672, A106.

Lewis, J. S. W. et al., 2022, MNRAS, 516, pp. 3389–3397.

Li, J. et al., 2024, ApJ, 976, p. 70.

Li, Z. et al., 2023, *arXiv e-prints*, arXiv:2310.09327.

Liang, Y. et al., 2025, MNRAS, 536, pp. 2672–2689.

Lightsey, P. A. et al., 2012, *Optical Engineering*, 51, pp. 011003-011003–20.

Looser, T. J. et al., 2024, Nature, 629, pp. 53–57.

Lu, S. et al., 2025, MNRAS, 536, pp. 1018–1034.

Lu, T.-Y. et al., 2024, MNRAS, 528, pp. 4872–4890.

Lupi, A. et al., 2020, MNRAS, 496, pp. 5160–5175.

Lynds, C. R. and A. R. Sandage, 1963, ApJ, 137, p. 1005.

Madau, P., 1995, ApJ, 441, p. 18.

Madau, P. and M. Dickinson, 2014, ARA&A, 52, pp. 415–486.

Madden, S. C. et al., 2020, A&A, 643, A141.

Magnelli, B. et al., 2011, A&A, 528, A35.

Maio, U. et al., 2011, MNRAS, 414, pp. 1145–1157.

Maiolino, R. et al., 2012, MNRAS, 425, pp. L66–L70.

Maiolino, R. et al., 2017, Nature, 544, pp. 202–206.

Marconcini, C. et al., 2024, MNRAS, 533, pp. 2488–2501.

Marian, V. et al., 2020, ApJ, 904, p. 79.

Marrone, D. P. et al., 2018, Nature, 553, pp. 51–54.

Martín-Navarro, I. et al., 2024, A&A, 684, A110.

Maschmann, D. et al., 2023, A&A, 670, A46.

Mashian, N. et al., 2016, MNRAS, 455, pp. 2101–2109.

Mason, C. A. et al., 2015, ApJ, 813, p. 21.

Massey, R. et al., 2010, *Reports on Progress in Physics*, 73, p. 086901.

Mawatari, K. et al., 2025, *arXiv e-prints*, arXiv:2507.02053.

McCracken, H. J. et al., 2012, A&A, 544, A156.

McKee, C. F. and E. C. Ostriker, 2007, ARA&A, 45, pp. 565–687.

McMullin, J. P. et al. (2007). "CASA Architecture and Applications". In: *Astronomical Data Analysis Software and Systems XVI*. Ed. by R. A. Shaw et al. Vol. 376. Astronomical Society of the Pacific Conference Series. (2007), p. 127.

McQuinn, M. et al., 2007, MNRAS, 377, pp. 1043–1063.

Mengel, J. G. et al., 1979, ApJS, 40, pp. 733–791.

Meštrić, U. et al., 2021, MNRAS, 508, pp. 4443–4458.

Milne, E. A., 1933, ZAp, 6, p. 1.

Misner, C. W., 1968, ApJ, 151, p. 431.

Mocák, M. et al., 2010, A&A, 520, A114.

Momcheva, I. G. et al., 2016, ApJS, 225, p. 27.

Moore, B., 1994, Nature, 370, pp. 629–631.

Mowla, L. A. et al., 2019, ApJ, 880, p. 57.

Muñoz, J. B. et al., 2024, MNRAS, 535, pp. L37–L43.

Naidu, R. P. et al., 2022, MNRAS, 510, pp. 4582–4607.

Nakajima, K. and R. Maiolino, 2022, MNRAS, 513, pp. 5134–5147.

Nakazato, Y. et al., 2023, ApJ, 953, p. 140.

Navarro, J. F. et al., 1997, ApJ, 490, pp. 493–508.

Neeleman, M. et al., 2020, Nature, 581, pp. 269–272.

Nelson, E. et al., 2024, ApJ, 976, p. L27.

Newman, S. F. et al., 2013, ApJ, 767, p. 104.

Oesch, P. A. et al., 2016, ApJ, 819, p. 129.

Olsen, K. P. et al., 2021, ApJ, 922, p. 88.

Ormerod, K. et al., 2024, MNRAS, 527, pp. 6110–6125.

Ouchi, M. et al., 2013, ApJ, 778, p. 102.

Pacifici, C. et al., 2023, ApJ, 944, p. 141.

Pallottini, A. et al., 2017, MNRAS, 471, pp. 4128–4143.

Pallottini, A. et al., 2017, MNRAS, 465, pp. 2540–2558.

Pallottini, A. et al., 2019, MNRAS, 487, pp. 1689–1708.

Pallottini, A. et al., 2022, MNRAS, 513, pp. 5621–5641.

Papovich, C. et al., 2001, ApJ, 559, pp. 620–653.

Parlanti, E. et al., 2023, A&A, 673, A153.

Patton, D. R. et al., 2000, ApJ, 536, pp. 153–172.

Patton, D. R. et al., 2013, MNRAS, 433, pp. L59–L63.

Peebles, P., 1993. *Principles of Physical Cosmology*. Princeton University Press.

Peebles, P. J. E., 1984, ApJ, 284, pp. 439–444.

Peebles, P. J. E. and B. Ratra, 2003, *Rev. Mod. Phys.*, 75, pp. 559–606.

Peng, C. Y. et al., 2002, AJ, 124, pp. 266–293.

Pentericci, L. et al., 2016, ApJ, 829, p. L11.

Penzias, A. A. and R. W. Wilson, 1965, ApJ, 142, pp. 419–421.

Perlmutter, S. et al., 1999, Phys. Rev. Lett., 83, pp. 670–673.

Perna, M. (2023). "The JWST/NIRSpec GTO programme "The Physics of Galaxy Assembly: IFS observations of high-z galaxies"". In: *Resolving the Rise and Fall of Star Formation in Galaxies*. Ed. by T. Wong and W.-T. Kim. Vol. 373. IAU Symposium. (2023), pp. 60–62. DOI: 10.1017/S174392132200374X.

Perrin, M. D. et al., 2012, *SPIE*, 8442, p. 84423D.

Perrin, M. D. et al., 2014, *SPIE*, 9143, p. 91433X.

Pierce, J. C. S. et al., 2022, MNRAS, 510, pp. 1163–1183.

Pillepich, A. et al., 2019, MNRAS, 490, pp. 3196–3233.

Pizzati, E. et al., 2020, MNRAS, 495, pp. 160–172.

Planck Collaboration et al., 2016, A&A, 594, A13.

Planck Collaboration et al., 2020, A&A, 641, A1.

Planck Collaboration et al., 2020, A&A, 641, A5.

Polidan, R. S., ed. (1991), 1991. *Hubble Space Telescope overview*. Vol. 29. *29th AIAA Aerospace Sciences Meeting*.

Pontoppidan, K. M. et al., 2016, *SPIE*, 9910, p. 991016.

Pontzen, A. and F. Governato, 2012, MNRAS, 421, pp. 3464–3471.

Pope, A. et al., 2023, ApJ, 951, p. L46.

Posses, A. et al., 2025, A&A, 699, A256.

Posses, A. C. et al., 2023, A&A, 669, A46.

Price, S. H. et al., 2021, ApJ, 922, p. 143.

Price, S. H. et al., 2022, A&A, 665, A159.

Qin, Y. et al., 2017, MNRAS, 472, pp. 2009–2027.

Quai, S. et al., 2023, MNRAS, 519, pp. 2119–2137.

Rauscher, B. J. et al., 2012, *SPIE*, 8453, 84531F.

Ravindranath, S. et al., 2004, ApJ, 604, pp. L9–L12.

Rawat, A. et al., 2009, ApJ, 695, pp. 1315–1326.

Read, J. I. et al., 2016, MNRAS, 459, pp. 2573–2590.

Riess, A. G. et al., 1998, AJ, 116, pp. 1009–1038.

Riess, A. G. et al., 2022, ApJ, 938, p. 36.

Rigby, J. et al., 2023, PASP, 135, p. 048001.

Rizzo, F. et al., 2020, Nature, 584, pp. 201–204.

Rizzo, F. et al., 2022, A&A, 667, A5.

Rizzo, F. et al., 2023, A&A, 679, A129.

Rizzo, F. et al., 2024, A&A, 689, A273.

Rizzo, F. et al., 2021, MNRAS, 507, pp. 3952–3984.

Robaina, A. R. et al., 2010, ApJ, 719, pp. 844–850.

Robertson, B. E., 2022, ARA&A, 60, pp. 121–158.

Robertson, B. E. et al., 2023, ApJ, 942, p. L42.

Rogstad, D. H. et al., 1974, ApJ, 193, pp. 309–319.

Roman-Oliveira, F. et al., 2024, A&A, 687, A35.

Roman-Oliveira, F. et al., 2023, MNRAS, 521, pp. 1045–1065.

Roman-Oliveira, F. et al., 2026, *arXiv e-prints*, arXiv:2601.03338.

Romano, M. et al., 2021, A&A, 653, A111.

Rosdahl, J. et al., 2013, MNRAS, 436, pp. 2188–2231.

Rosdahl, J. et al., 2022, MNRAS, 515, pp. 2386–2414.

Rowland, L. E. et al., 2024, MNRAS, 535, pp. 2068–2091.

Rowland, L. E. et al., 2025, *arXiv e-prints*, arXiv:2501.10559.

Rubin, V. C. et al., 1978, ApJ, 225, pp. L107–L111.

Rubin, V. C. et al., 1980, ApJ, 238, pp. 471–487.

Rubin, V. C. and W. K. Ford Jr, 1970, ApJ, 159, p. 379.

Saha, P. et al., 2024, Space Sci. Rev., 220, p. 12.

Salaris, M. and S. Cassisi, 2005. *Evolution of stars and stellar populations*. John Wiley & Sons.

Saldana-Lopez, A. et al., 2023, MNRAS, 522, pp. 6295–6325.

Salim, S. and D. Narayanan, 2020, ARA&A, 58, pp. 529–575.

Salim, S. et al., 2018, ApJ, 859, p. 11.

Salpeter, E. E., 1955, ApJ, 121, p. 161.

Santini, P. et al., 2017, ApJ, 847, p. 76.

Schaye, J. et al., 2010, MNRAS, 402, pp. 1536–1560.

Schaye, J. et al., 2023, MNRAS, 526, pp. 4978–5020.

Schinnerer, E. et al., 2016, ApJ, 833, p. 112.

Schneider, R. and R. Maiolino, 2024, A&A Rev., 32, p. 2.

Scholtz, J. et al., 2025, MNRAS, 539, pp. 2463–2484.

Scholtz, J. et al., 2024, A&A, 687, A283.

Schouws, S. et al., 2022, ApJ, 928, p. 31.

Schouws, S. et al., 2023, ApJ, 954, p. 103.

Schouws, S. et al., 2024, *arXiv e-prints*, arXiv:2409.20549.

Schouws, S. et al., 2025, *arXiv e-prints*, arXiv:2502.01610.

Schwarzschild, M. and R. Härm, 1962, ApJ, 136, p. 158.

Scoville, N. et al., 2007, ApJS, 172, pp. 1–8.

Scoville, N. et al., 2013, ApJS, 206, p. 3.

Sellwood, J. A., 2014, *Reviews of Modern Physics*, 86, pp. 1–46.

Sellwood, J. A. and K. Spekkens, 2015, *arXiv e-prints*, arXiv:1509.07120.

Sérsic, J. L., 1963, *Boletin de la Asociacion Argentina de Astronomia La Plata Argentina*, 6, pp. 41–43.

Shah, E. A. et al., 2020, ApJ, 904, p. 107.

Shapiro, K. L. et al., 2008, ApJ, 682, pp. 231–251.

Sharma, R. S. et al., 2024, MNRAS, 527, pp. 9461–9479.

Shivaei, I. et al., 2018, ApJ, 855, p. 42.

Shivaei, I. et al., 2022, MNRAS, 514, pp. 1886–1894.

Silk, J., 1977, ApJ, 211, pp. 638–648.

Simmonds, C. et al., 2024, MNRAS, 535, pp. 2998–3019.

Simons, R. C. et al., 2019, ApJ, 874, p. 59.

Smit, R. et al., 2015, ApJ, 801, p. 122.

Smit, R. et al., 2018, Nature, 553, pp. 178–181.

Smithsonian Astrophysical Observatory (2000). *SAOImage DS9: A utility for displaying astronomical images in the X11 window environment*. Astrophysics Source Code Library, record ascl:0003.002. (2000).

Sorba, R. and M. Sawicki, 2018, MNRAS, 476, pp. 1532–1547.

Spilker, J. S. et al., 2022, ApJ, 929, p. L3.

Stanway, E. R. and J. J. Eldridge, 2018, MNRAS, 479, pp. 75–93.

Starobinsky, A. A., 1980, *Physics Letters B*, 91, pp. 99–102.

Stefanon, M. et al., 2017, ApJ, 851, p. 43.

Stefanon, M. et al., 2019, ApJ, 883, p. 99.

Stefanon, M. et al., 2022, ApJ, 927, p. 48.

Steidel, C. C. and D. Hamilton, 1993, AJ, 105, p. 2017.

Stott, J. P. et al., 2016, MNRAS, 457, pp. 1888–1904.

Strait, V. et al., 2023, ApJ, 949, p. L23.

Strandet, M. L. et al., 2017, ApJ, 842, p. L15.

Suess, K. A. et al., 2022, ApJ, 937, p. L33.

Swinbank, A. M. et al., 2012, MNRAS, 426, pp. 935–950.

Swinbank, A. M. et al., 2017, MNRAS, 467, pp. 3140–3159.

Teyssier, R., 2002, A&A, 385, pp. 337–364.

Thielemann, F. .-. et al., 2017, *Annual Review of Nuclear and Particle Science*, 67, pp. 253–274.

Thorp, M. D. et al., 2019, MNRAS, 482, pp. L55–L59.

Tilvi, V. et al., 2013, ApJ, 768, p. 56.

Timmes, F. X. et al., 1995, ApJS, 98, p. 617.

Tinsley, B. M., 1980, Fund. Cosmic Phys., 5, pp. 287–388.

Toomre, A., 1964, ApJ, 139, pp. 1217–1238.

Topping, M. W. et al., 2022, MNRAS, 516, pp. 975–991.

Trac, H. and R. Cen, 2007, ApJ, 671, pp. 1–13.

Treister, E. et al., 2012, ApJ, 758, p. L39.

Treu, T. et al., 2023, ApJ, 942, p. L28.

Truelove, J. K. et al., 1997, ApJ, 489, pp. L179–L183.

Trussler, J. A. A. et al., 2024, MNRAS, 527, pp. 11627–11650.

Tsukui, T. and S. Iguchi, 2021, *Science*, 372, pp. 1201–1205.

Tully, R. B. and J. R. Fisher, 1977, A&A, 54, pp. 661–673.

Turner, O. J. et al., 2017, *arXiv e-prints*, arXiv:1711.03604.

Übler, H. et al., 2017, ApJ, 842, p. 121.

Übler, H. et al., 2019, ApJ, 880, p. 48.

Übler, H. et al., 2024, MNRAS, 533, pp. 4287–4299.

Usui, M. et al., 2025, *arXiv e-prints*, arXiv:2507.02054.

Valentino, F. et al., 2020, ApJ, 889, p. 93.

Vallini, L. et al., 2015, ApJ, 813, p. 36.

Vallini, L. et al., 2018, MNRAS, 473, pp. 271–285.

Vallini, L. et al., 2024, MNRAS, 527, pp. 10–22.

van der Wel, A. et al., 2014, ApJ, 792, p. L6.

van Leeuwen, I. F. et al., 2024, MNRAS, 534, pp. 2062–2085.

Vega-Ferrero, J. et al., 2024, ApJ, 961, p. 51.

Veilleux, S. et al., 2020, A&A Rev., 28, p. 2.

Vizgan, D. et al., 2022, ApJ, 929, p. 92.

Vogelsberger, M. et al., 2014, MNRAS, 444, pp. 1518–1547.

Wang, B. et al., 2024, ApJ, 973, p. L29.

Wang, T. et al., 2025, ApJ, 988, p. L35.

Whitaker, K. E. et al., 2017, ApJ, 850, p. 208.

Whitler, L. et al., 2023, MNRAS, 519, pp. 157–171.

Williams, C. C. et al., 2024, ApJ, 968, p. 34.

Williams, R. E. et al., 1996, AJ, 112, p. 1335.

Wisnioski, E. et al., 2015, ApJ, 799, p. 209.

Wisnioski, E. et al., 2019, ApJ, 886, p. 124.

Wisnioski, E. et al., 2025, MNRAS, 544, pp. 2777–2794.

Witstok, J. et al., 2022, MNRAS, 515, pp. 1751–1773.

Witstok, J. et al., 2023, Nature, 621, pp. 267–270.

Woodrum, C. et al., 2024, *Proceedings of the National Academy of Science*, 121, e2317375121.

Woosley, S. and T. Janka, 2005, *Nature Physics*, 1, pp. 147–154.

Wootten, A. and A. R. Thompson, 2009, *IEEE Proceedings*, 97, pp. 1463–1471.

Wuyts, S. et al., 2016, ApJ, 831, p. 149.

Zanella, A. et al., 2018, MNRAS, 481, pp. 1976–1999.

Zanella, A. et al., 2021, MNRAS, 500, pp. 118–137.

Zanella, A. et al., 2024, A&A, 685, A80.

Zavala, J. A. et al., 2024, ApJ, 977, p. L9.

Zhou, L. et al., 2017, MNRAS, 470, pp. 4573–4582.

Ziparo, F. et al., 2023, MNRAS, 520, pp. 2445–2450.

Appendix A

Appendices relating to Chapter 2.

A.1 The Effect of Masking on Velocity Map Analysis

We created model galaxies with ^{3D}BAROLO using the same parameters as the best-fit models for our galaxies. These models are by definition galaxy disks containing only circular motions. We convolve these model disk galaxies with the mock NIRSpec PSF, and add noise resulting in SNR=5, using these models to create velocity maps. In Figure A.1, an example created using ^{3D}BAROLO is shown for a model disk galaxy to which we apply a selection of different masking restrictions. SNRCUT sets the SNR threshold of the moment map, while GROWTHCUT is a secondary SNR cut used to grow the mask (see Di Teodoro and Fraternali, 2015, for further details). We apply the masking combinations of (a) SNRCUT = 5, GROWTHCUT = 4, (b)SNRCUT = 4, GROWTHCUT = 3 and (c) SNRCUT = 3, GROWTHCUT = 2.8. Although the model contains only circular motions, there is some deviation of the v=0 isophote from a straight line. This illustrates that the masking applied to velocity fields can cause artificial identification (or can bias the identification) of non-circular motions even where they are not present.

A.2 Testing the Assumption of a Thin Disk

We tested the effect of altering the assumed disk thickness on the fitted models. We fitted the mock NIRSpec observations with disk thicknesses of 0.05″ and 0.1″, in

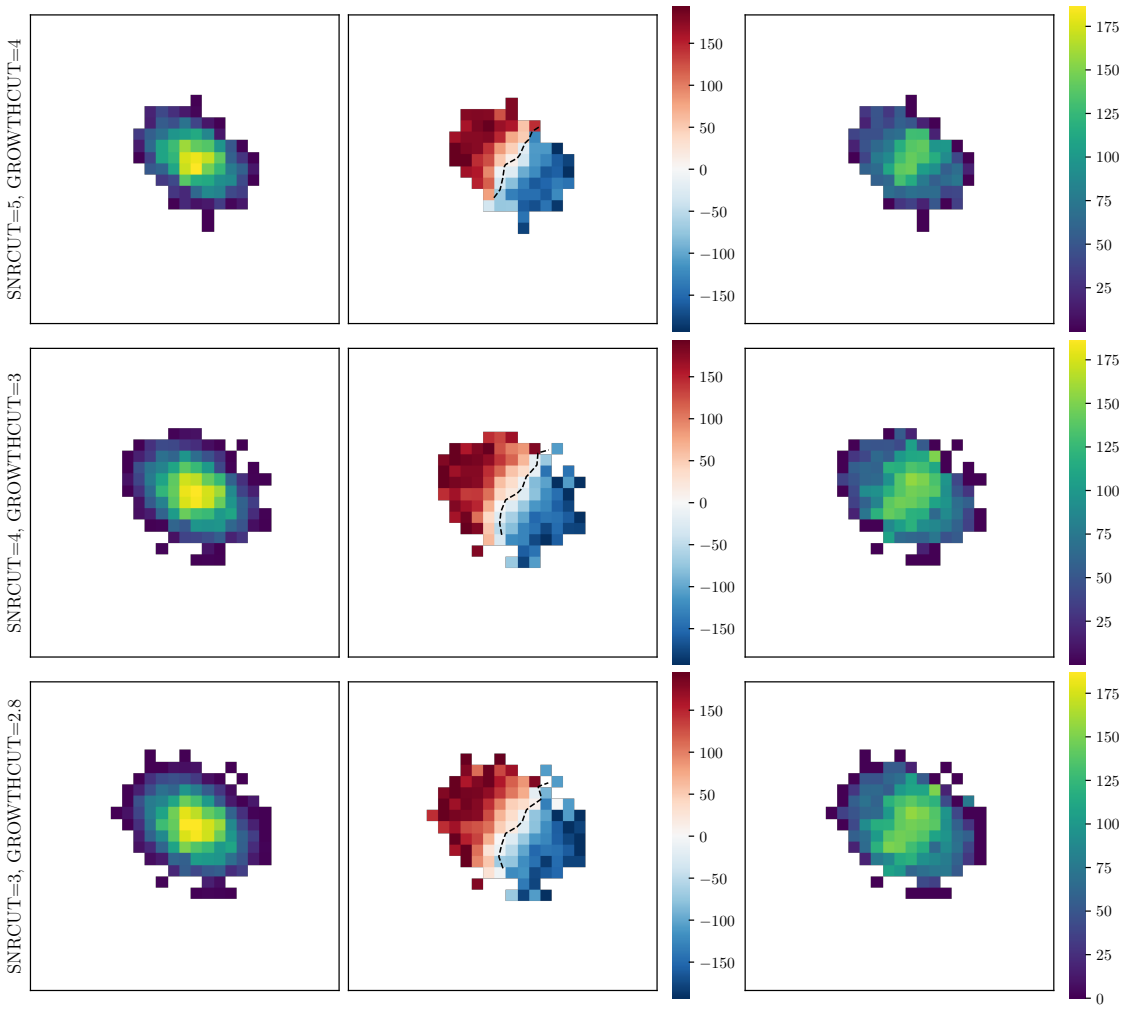

Figure A.1: Moment maps for a symmetric disk model, containing no non-circular motions, with SNR=5, created using ^{3D}BAROLO with GROWTHCUT=4, 3, 2.8.

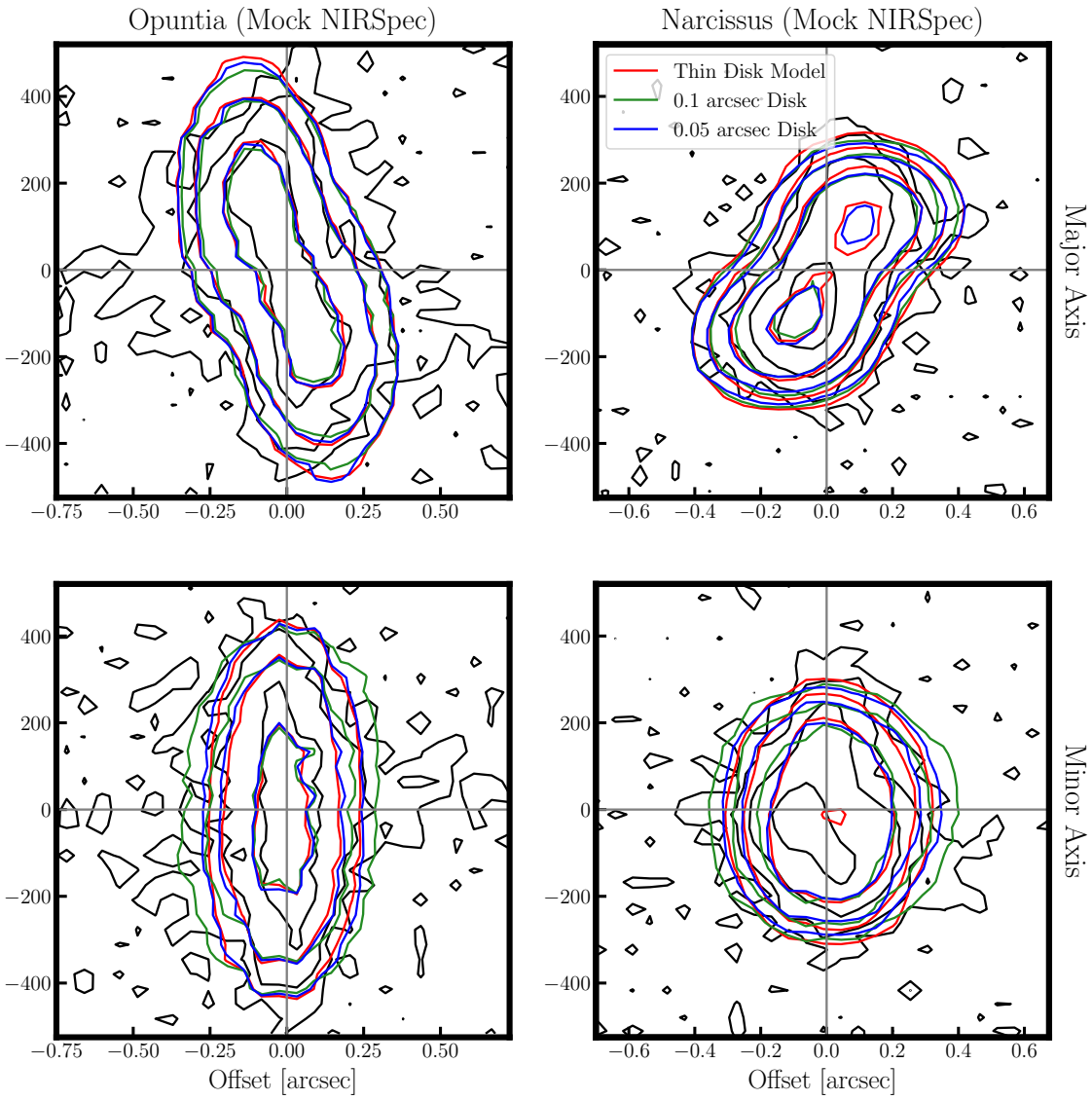

Figure A.2: Fitted models with varied disk thicknesses.

comparison to our assumed thin disk with a thickness of 0.001″. Figure A.2 shows the PV diagrams for the 0.05″ and 0.1″ thick disks, illustrating that variations in the disk thickness have very little impact on the recovered model.

We furthermore implemented a fit where the disk thickness was equal to the galaxy effective radius and we see from Table A.1 that while this does introduce discrepancies in the recovered kinematic measurements, they are still within 1-2σ of the measurements resulting from the thin disk assumption even in this extreme case.

Table A.1: Table showing the effect of increasing the disk thickness to the distance of the outer fitting ring.

Name	$v_{rot,max}$	$\langle\sigma\rangle$	v/σ
Opuntia (thick disk)	313^{+10}_{-13}	120^{+11}_{-11}	$2.6^{+0.9}_{-0.6}$
Narcissus (thick disk)	199^{+26}_{-25}	51^{+9}_{-9}	$3.9^{+2.2}_{-0.9}$
Opuntia (thin disk, reference)	290^{+25}_{-28}	136^{+10}_{-14}	$2.1^{+0.2}_{-0.3}$
Narcissus (thin disk, reference)	193^{+14}_{-17}	62^{+10}_{-11}	$3^{+0.9}_{-0.6}$

Table A.2: The effect of changing the SNR of an observation on the recovered kinematic measurements.

Name	$v_{rot,max}$	σ	v/σ
Opuntia (SNR=3)	290^{+15}_{-12}	139^{+13}_{-16}	$2.1^{+0.8}_{-0.6}$
Narcissus (SNR=3)	189^{+15}_{-19}	64^{+10}_{-10}	$3^{+1.5}_{-0.7}$
Opuntia (SNR=5, reference)	290^{+25}_{-28}	136^{+10}_{-14}	$2.1^{+0.2}_{-0.3}$
Narcissus (SNR=5, reference)	193^{+14}_{-17}	62^{+10}_{-11}	$3^{+0.9}_{-0.6}$
Opuntia (SNR=10)	298^{+8}_{-9}	138^{+12}_{-14}	$2.2^{+0.7}_{-0.6}$
Narcissus (SNR=10)	193^{+12}_{-14}	58^{+9}_{-9}	$3.3^{+1.5}_{-0.9}$

A.3 Channel Maps

Figures A.3-A.6 show channel maps of the Hα emission for the idealised and mock NIRSpec observations of both galaxies, alongside the corresponding channel maps of the disk model fitted by ^{3D}BAROLO.

A.4 Resolving Galaxies at $z > 6$

We test the effect of changing the SNR on the kinematic properties recovered from our mock NIRSpec observations. To do this, we fit the same model with two tilted rings to different realisations of the mock NIRSpec data in which the SNR, as measured in a PSF-sized aperture at the outer edge of the galaxy, has been altered from

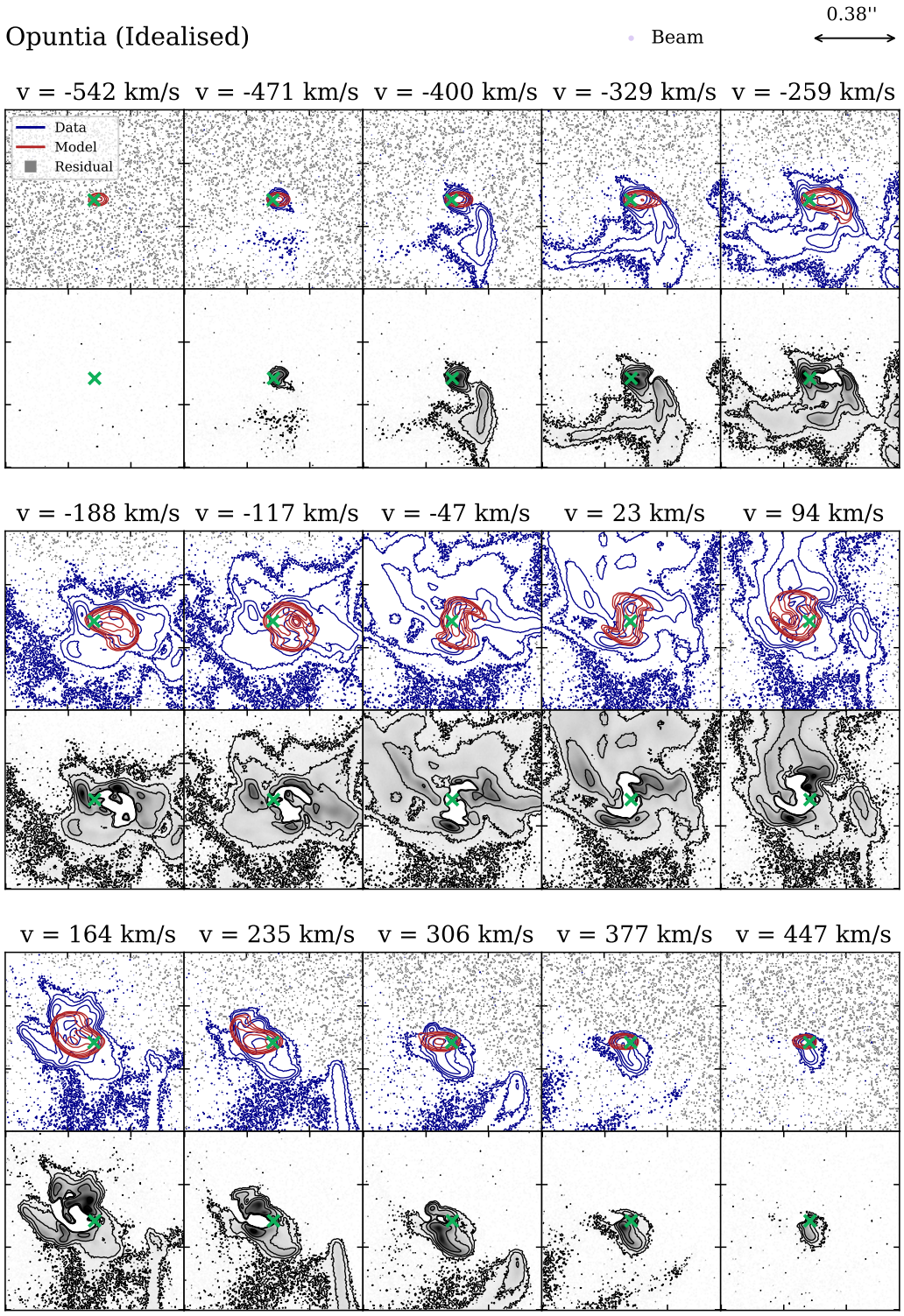

Figure A.3: Representative channel maps for the idealised Opuntia observations (blue contours) and the corresponding model (red contours) alongside the residual (gray with black contours) as fitted by ^{3D}BAROLO. Contours are spaced at $3^n \times \sigma_{\rm RMS}$ starting at n=1, where $\sigma_{\rm RMS}$ is the standard deviation of pure noise channels. The green cross marks the fitted centre of the galaxy.

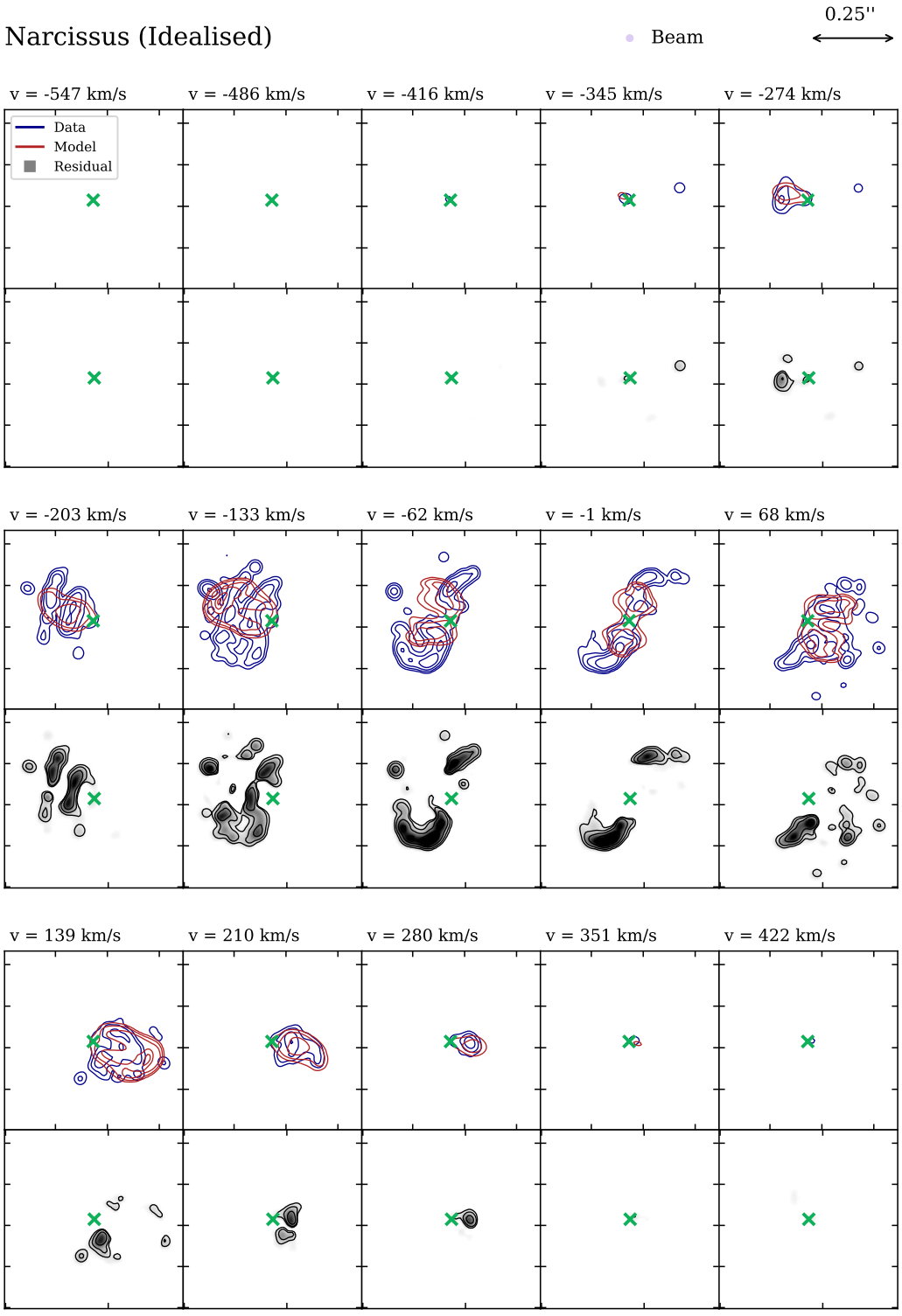

Figure A.4: Channel maps with contour levels $3^n \times \sigma_{\mathrm{RMS}}$ for the idealised Narcissus observations.

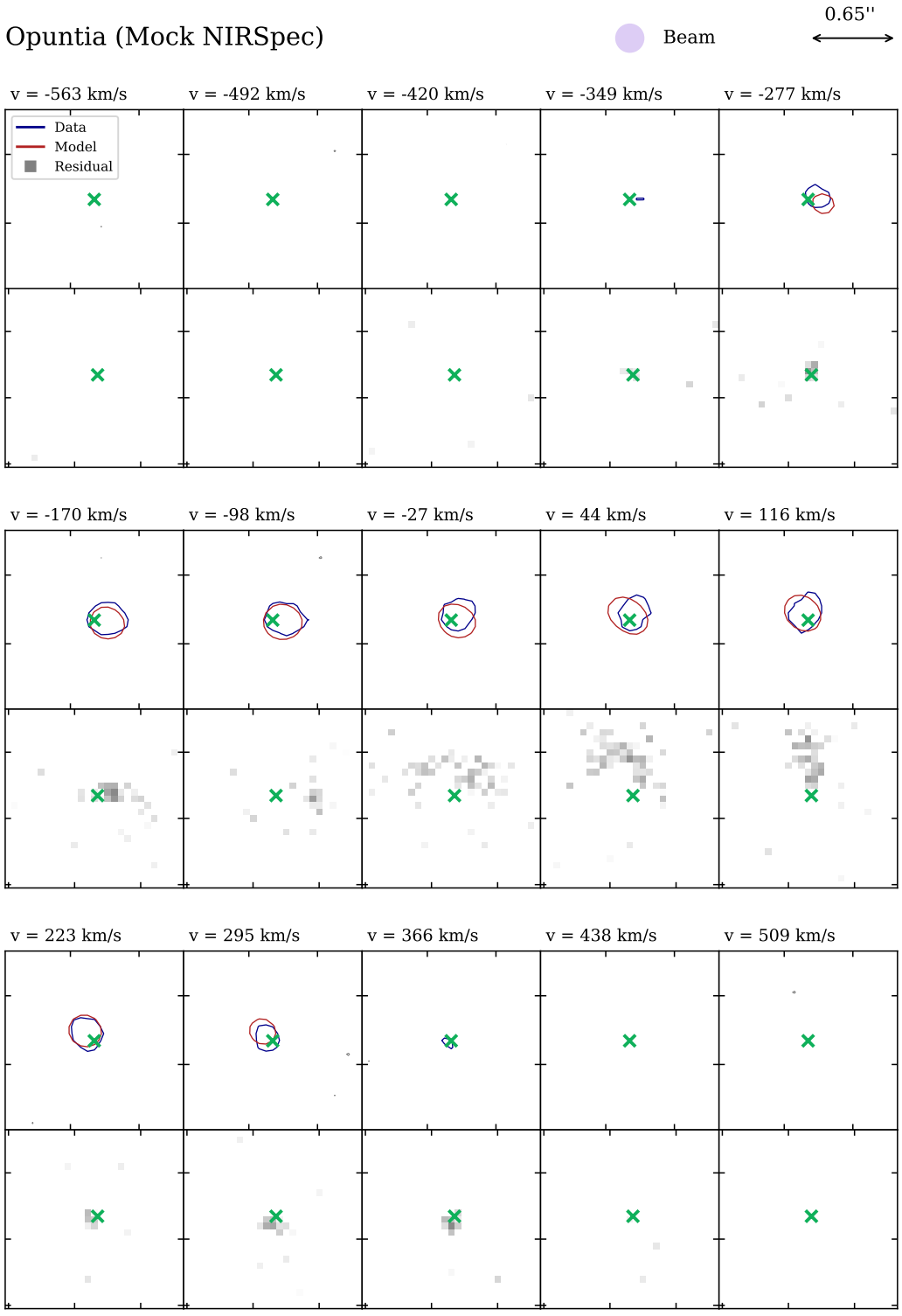

Figure A.5: Channel maps with contour levels $3^n \times \sigma_{\mathrm{RMS}}$ for the mock NIRSpec Opuntia observations.

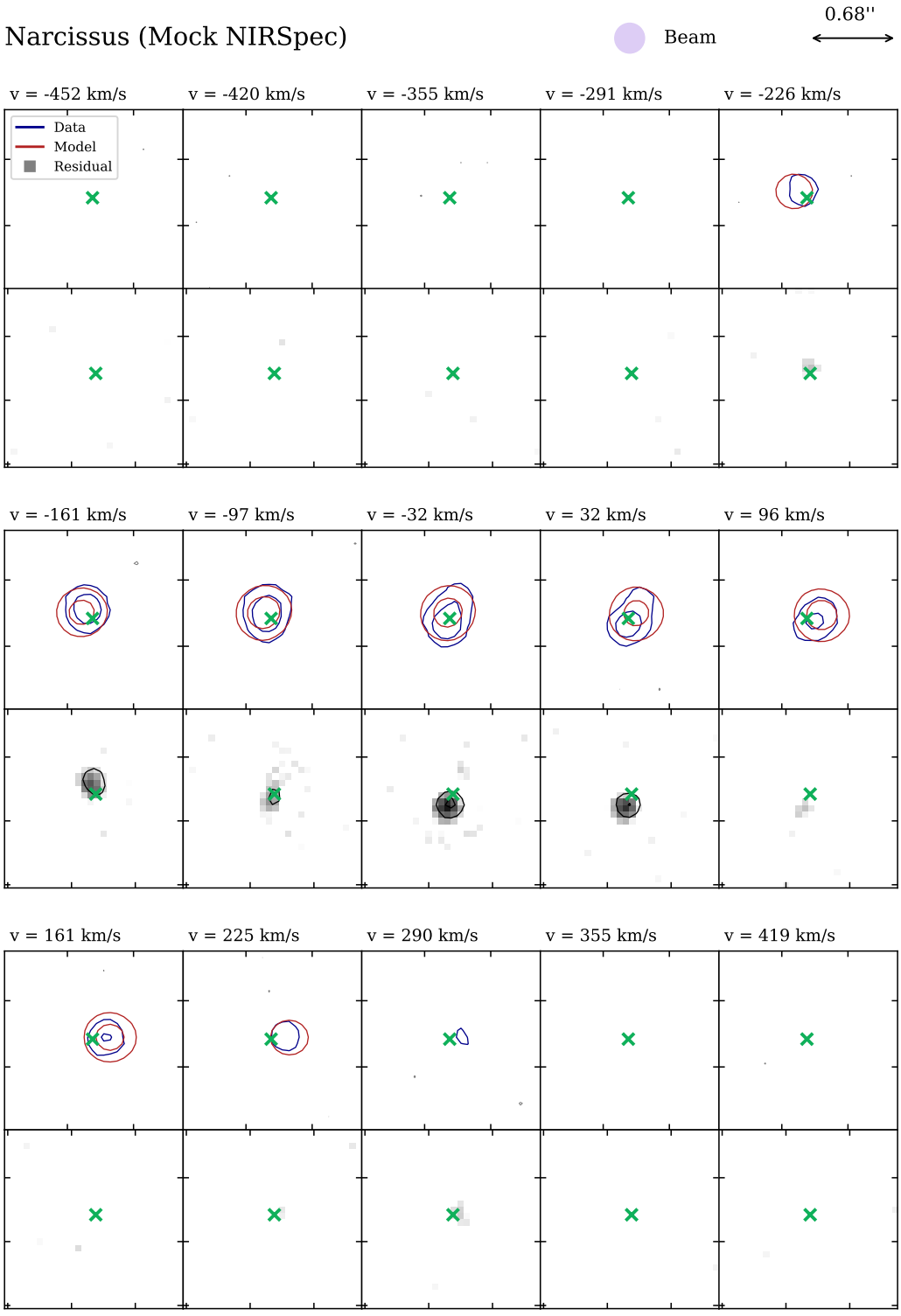

Figure A.6: Channel maps with contour levels $3^n \times \sigma_{\mathrm{RMS}}$ for the mock NIRSpec Narcissus observations.

~ 5 to ~ 3 and ~ 10. The results of this test are shown in Table A.2 along with a reproduction of the results at SNR ~ 5 for reference.

At SNR ~ 10, the increased SNR enables us to fit an additional ring with ^{3D}BAROLO, and so we conduct a further test of factors affecting our measured kinematic properties, this time from increasing the number of independent resolution elements used for fitting from two to three. The v/σ measurements of the realistic mock NIRSpec observations are then $2.2^{+0.2}_{-0.2}$ for Opuntia, an increase within 1σ, and $3.9^{+0.7}_{-0.6}$ for Narcissus, a increase within 1σ. The minor difference indicates that increasing the number of resolution elements is not effective for improving kinematic measurements without any corresponding improvement in spatial resolution.

A.5 Comparison of Disk and Diffuse Emission

Figure A.7 shows the moment-0 map of emission from the idealised galaxy observations, and the disk and diffuse components isolated by masking.

A.6 Double Gaussian Fitting to Mock NIRSpec Spectra

Figure A.8 shows a composite double-Gaussian model fitted to the integrated spectra of the realistic mock NIRSpec observations. This method is a widely employed technique to identify outflows from spectra, particularly where 3D data is not available; if the integrated spectrum is best fit by narrow and broad Gaussian peaks, this is considered evidence of outflows (see discussion in Section 2.5.3). This method would not suggest the presence of outflows in these mock NIRSpec observations, despite non-circular gas contributing significantly to the emission of Opuntia.

A.7 Dynamical Mass Calculation

To evaluate the asymmetric drift correction for the realistic mock NIRSpec observations, we assume that the first term in equation 2.5 goes to zero, as it would not be meaningful to analytically evaluate the relation $\partial ln(\sigma)/\partial R$ when we were able to

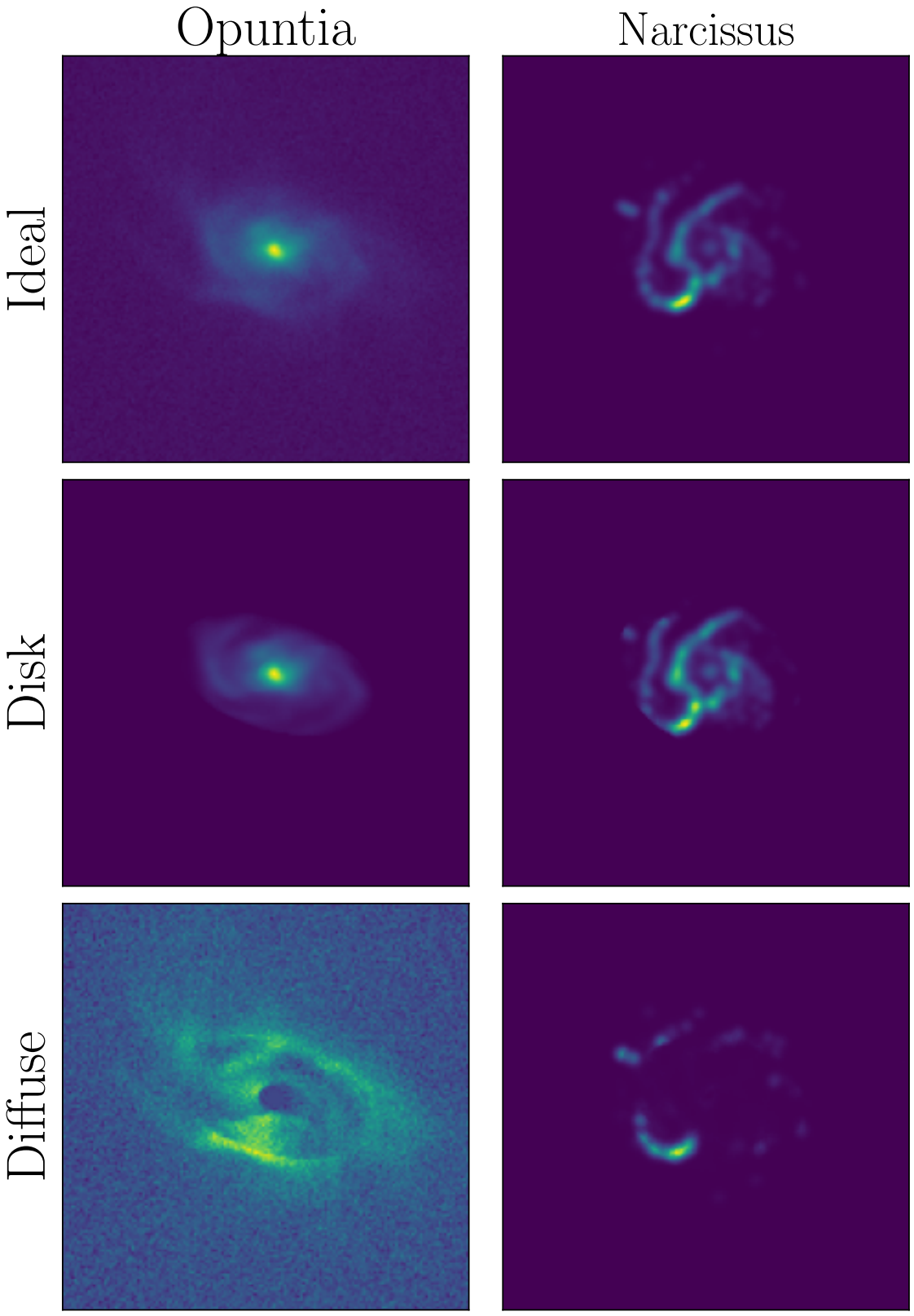

Figure A.7: Moment-0 diagrams of the total idealised galaxy emission (first row), the disk component (second row) and the diffuse component (third row).

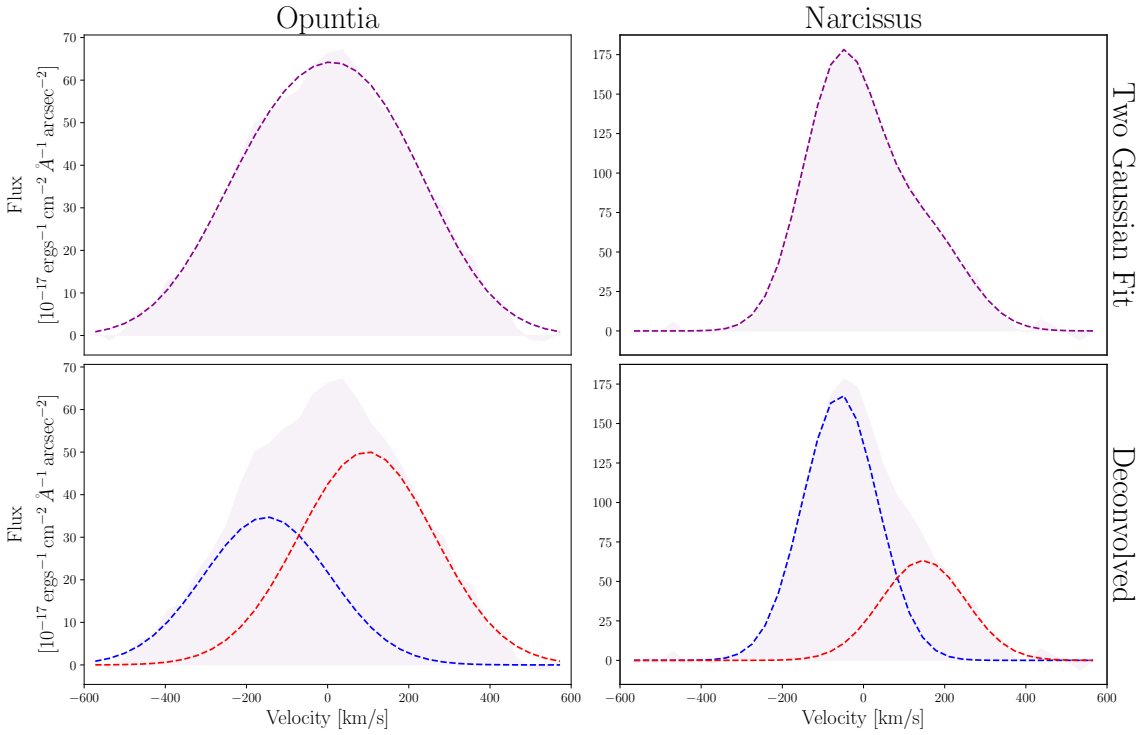

Figure A.8: Integrated spectra of the Opuntia and Narcissus mock NIRSpec observations, fitted with a composite model (top row) consisting of two Gaussian components (second row).

fit only two rings and so have only two data points. Thus, the equation reduces to:

$$v_A^2 = \frac{R\sigma^2}{R_{\text{d, gas}}}$$

We measure $R_{\text{d, gas}}$ by fitting the moment-0 map with a Sérsic profile to determine the effective radius, and then converting this to the scale radius according to $R_{\text{eff}} = 1.68R_d$. We employ the `Sersic2D` from the `astropy` modeling library, which we convolve with the same PSF as the data using the `PetroFit` routine `PSFConvolvedModel2D`. For both galaxies we fix the Sérsic index $n = 1$, assuming an exponential disk, and for Narcissus we additionally fix the central co-ordinates to avoid the fit being skewed by the galaxy's asymmetries.

Appendix B

Appendices relating to Chapter 4.

B.1 Comparing Velocity Measurements Across Fitting Codes

We compare the velocity measurements obtained from 3D fitting (^{3D}BAROLO) and 1D fitting (Dysmalpy).

B.2 Dynamical Mass Calculations for Turbulent Disks

We compare the dynamical mass for the turbulent disk population of the REBELS-HR sample as calculated according to the rotating disk formalism and the dispersion dominated formalism (Table B.2), since turbulent disk galaxies share characteristics of both. We find discrepancies between the two calculations, with the dispersion-dominated calculation sometimes over estimating and sometimes underestimating

Table B.1: Velocity measurements fitted by 3DBarolo and Dysmalpy.

	REBELS-29.2	REBELS-38	COS-3018
Dysmalpy σ [km s^{-1}]	50 ± 3	64 ± 10	54 ± 5
^{3D}BAROLO σ [km s^{-1}]	46^{+6}_{-5}	44^{+5}_{-6}	53^{+6}_{-6}
Dysmalpy $v(r_e)$ [km s^{-1}]	140	13	88
^{3D}BAROLO $v(r_e)$ [km s^{-1}]	202^{+29}_{-27}	58^{+16}_{-16}	137^{+25}_{-20}

Table B.2: Deriving dynamical mass for turbulent disks according to the rotating disk and dispersion dominated formalisms.

Name	$\log_{10}(M_{dyn,rot})$	$\log_{10}(M_{dyn,disp})$
REBELS-5	$10.0^{+1.6}_{-0.5}$	$9.9^{+0.1}_{-0.2}$
REBELS-8	$8.9^{+0.1}_{-0.1}$	$9.3^{+0.2}_{-0.3}$
REBELS-29	$9.2^{+0.2}_{-0.1}$	$9.6^{+0.2}_{-0.2}$
REBELS-38	$9.2^{+0.3}_{-0.2}$	$9.7^{+0.1}_{-0.2}$
COS-2987	$9.0^{+0.1}_{-0.1}$	$9.1^{+0.1}_{-0.2}$
COS-3018	$10.4^{+0.1}_{-0.1}$	$10.0^{+0.1}_{-0.1}$

M_{dyn} relative to the rotation dominated calculation.